UNIVERSITY OF SOUTHAMPTON

FACULTY OF ENGINERING, SCIENCE AND MATHEMATICS

School of Chemistry

AN INVESTIGATION INTO THE ELECTROCHEMICAL PROPERTIES OF NANOSTRUCTURED METALS AND THEIR APPLICATION AS AMPEROMETRIC BIOSENSORS

By

David Andrew Cook

Thesis submitted for the degree of Doctor of Philosophy

April 2005

UNIVERSITY OF SOUTHAMPTON

ABSTRACT

FACULTY OF ENGINERING, SCIENCE AND MATHEMATICS
SCHOOL OF CHEMISTRY

Doctor of Philosophy

AN INVESTIGATION INTO THE ELECTROCHEMICAL PROPERTIES OF NANOSTRUCTURED METALS AND THEIR APPLICATION AS AMPEROMETRIC BIOSENSORS

By David Andrew Cook.

In this work nanostructured materials have been electrodeposited onto conducting substrates using lyotropic liquid crystal phases and assemblies of colloidal particles as templates. These two methodologies offer access to structures with pore sizes in both the mesoporous and macroporous (2 – 50 nm, and > 50 nm respectively, by IUPAC definition) ranges. The unique properties of these materials have been investigated with a view to producing improved amperometric biosensors.

The electrochemistry of hydrogen peroxide, ascorbate and glucose has been investigated using both unstructured and mesoporous platinum, palladium and rhodium microdisc electrodes. It would appear that the Hall mechanism (Hall *et al.* Electrochim. Acta, 43 (5-6), 579, **1998**) of hydrogen peroxide oxidation operates at all three metals, but with improved efficiency at the nanostructures. When modified with a glucose oxidase/polymer matrix, the mesoporous electrodes were able to detect glucose at lower overpotentials and showed greater stability than their unstructured counterparts. Mesoporous platinum and palladium may be used for the direct oxidation of aqueous glucose.

The structure and pore connectivity of macroporous gold deposits is investigated by cyclic voltammetry in sulphuric acid. Values for the area of contact between template spheres and the substrate agree well with those in the literature as measured by scanning electron microscopy. Preliminary results on the ordered immobilisation of histadine tagged green fluorescent protein molecules within macrostructures are reported. Collaboration with another group (Alexander Kuhn, Université Bordeaux, Electrochem. Comm. 5(9), 747, **2003**) has shown that macroporous gold deposits can be decorated with a bioactive mediator to make NADH sensors with a response that is proportional to the surface area of the gold; this work is also summarised here.

Recessed microdisc electrodes were used as substrates for the electrodeposition of mesoporous platinum and macroporous gold. This allowed deposition of thick (up to ~ 10 μm) mesoporous platinum films at increased Faradaic efficiency (~ 66 % compared to ~ 43 % for deposition at similar inlaid microdiscs) without alteration of the electrode geometry.

Contents

Introduction

Experimental

Mesoporous Electrodes

Macroporous Electrodes

Recessed Microelectrodes

Acknowledgments

I would probably need a separate volume to fully thank every individual who has helped me over the last few years. Stopping short of that there are a few people I would like to mention.

MediSense for funding this project, and also for supplying me with glucose oxidase.

Alexander Kuhn and his group for their hospitality and collaboration.

Thanks to everyone in electrochemistry, especially the Bartlett group, who have made me feel so welcome. In particular: Sergio (whose IT skills are matched only by his compulsion to dismantle things), Dr Stuart Evans (who motivated and inspired me through my first year), Dr Peter Birkin (for his ideas and time) and my supervisor, Professor Phil Bartlett (a man of inexhaustible patience and knowledge).

Introduction

1.1 Liquid Crystals (LC)

The two most common phases of condensed matter on Earth are: crystals, which are highly ordered structures with molecules occupying specific lattice points and adopting specific orientations, and liquids, which are completely isotropic. Liquid crystals display properties common to both liquids and crystalline solids. While LC phases are fluid their molecules posses some order induced by the anisotropic nature of the constituent molecules[1]. There are two broad categories of liquid crystal: thermotropic and lyotropic.

1.1.1 Thermotropic Liquid Crystals:

Thermotropic LC are formed by molecules with one axis that is significantly different from the other two. Most commonly these are rod shaped (calamitic) organic molecules which are rigid for at least some portion of their length. Typically calamitic molecules contain 2 or more carbon rings linked directly or by rigid groups and with flexible hydrocarbon chains at each end. Another broad category of anisotropic molecules are disc shaped (discotic) molecules, where one axis is much shorter than the other two. Discotic molecules are often based on flat aromatic centres like benzene, triphenylene or truxene with side groups that resemble calamitic molecules.

The most simple liquid crystal phase is where one molecular axis has a tendency to point along a preferred direction known as the director[2]. This is the nematic phase and has only orientational order. Other phases exist which possess both orientational and positional order; for instance where the centres of mass of the molecules have a tendency to form layers (smectic phases). There are many possible thermotropic phases with varying degrees of order, but the underlying feature is that these phases only exist within a specific temperature range[2].

1.1.2 Lyotropic Liquid Crystals:

In contrast to thermotropic LC (which may consist of a single pure compound or mixtures of compounds) lyotropic LC phases only form when the constituent, anisotropic molecules are dissolved in solvent. The phase behaviour is controlled not only by temperature but also by the concentration of the molecules[3]. The LC molecules must be amphiphilic i.e. having two distinct ends with different solvation properties. Usually these LC are made up of organic molecules with a long hydrophobic, hydrocarbon chain and a hydrophilic headgroup (e.g. soaps and various phospholipids) which will form structures in both polar and non-polar solvents.

At very low concentrations (typically < 1 wt %) the molecules tend to orient themselves at the solvents surface to minimise the interaction of the more hydrophobic group with the liqiud. However, above the critical micelle concentration (CMC) the amphiphiles coalesce to form supramolecular structures. Initially, micelles (in the case of soap molecules) or vesicles (in the case of phospholipids) form. These are usually spherical[1] structures where the amphiphiles have both orientational and some positional order (figure 1 a). In polar solvents (such as water) the hydrophilic head groups of the molecules form the shell of the structure with the hydrophobic chains in the core, away from the solvent. The micelles themselves may also have some positional order being able to pack into cubic structure analogous to the packing of macroscopic spheres.

At higher concentrations other liquid crystal phases may form. The first of these is the hexagonal phase where the molecules form cylinder-like structures. Once again, the hydrophobic portion of the molecule is locked inside the structure, away from the water, and the hydrophilic groups form the surface of the cylinder. The cylinders themselves arrange in a hexagonal array separated by a thin layer of the solvent water (figure 1b).

At even higher amphiphile concentrations a lamellar phase may form where the molecules form bilayers with the hydrophobic groups sandwiched in the middle. These bilayers stack

---

[1] In a mixture of highly polar and slightly polar solvents, under just the right conditions, rod-like, disc-like or biaxial micelles may also form. These anisotropic micelles may themselves arrange into phases resembling the nematic and smectic thermotropic phases.

hydrophilic faces to hydrophilic faces with water in between (figure 1c). At very high surfactant concentration (i.e. more surfactant than solvent) inverse phases form where the hydrophilic groups (along with the remaining water) are inside the structures (figure 1d inverse hexagonal, and 1e inverse micellar).

Note these inverse phases may also be formed if the amphiphiles are dissolved in a non-polar solvent where it is favourable for the hydrophobic groups to be in contact with the medium.

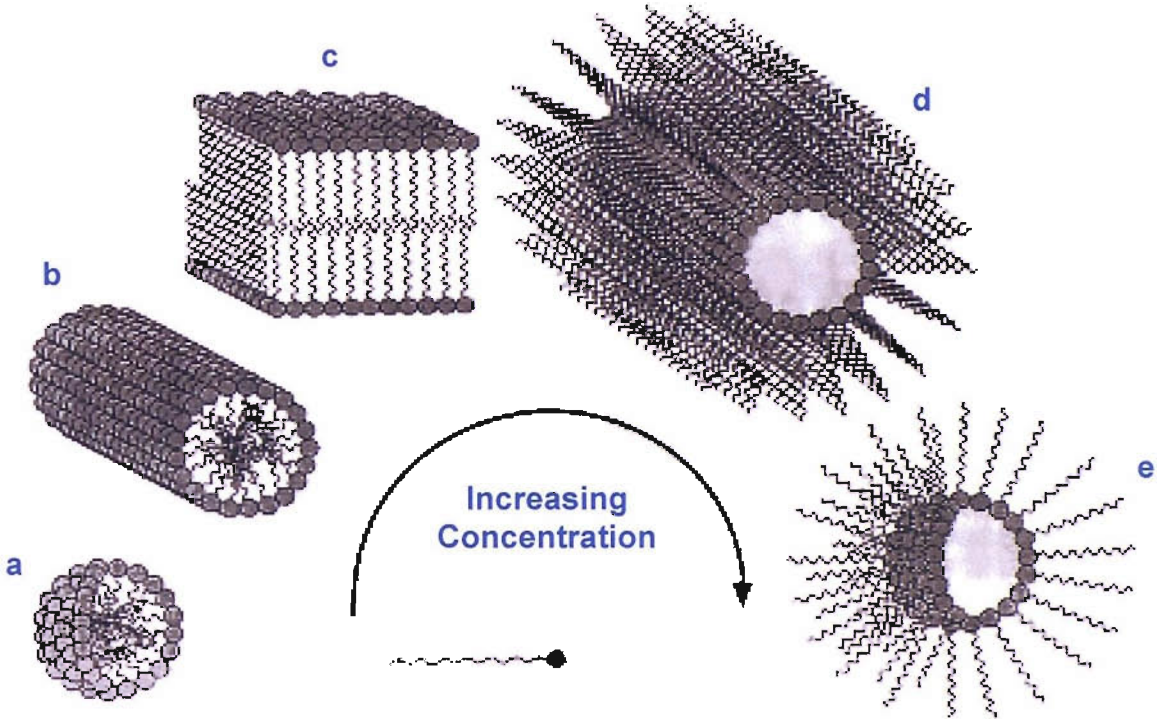

Figure 1. Schematic showing general aggregation of amphiphilic molecules into supramolecular structures[4] when solvated in a polar solvent. Liquid crystal phases obtained: a) micellar, b) hexagonal, c) lamellar, d) inverse hexagonal and e) inverse micellar.

1.1.3 Liquid Crystal Templating (LCT):

In this work surfactant[2] molecules, like those shown in figure 2 were used to form hexagonal, lyotropic LC phases.

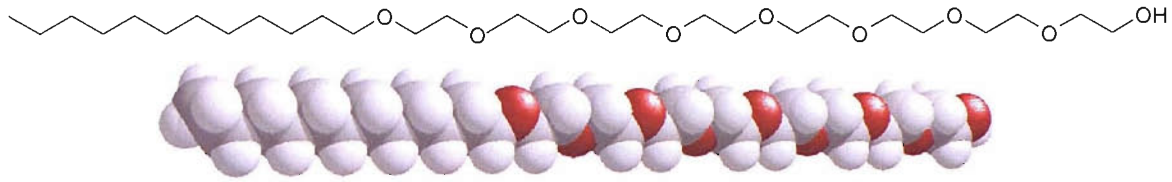

Octaethylene glycol monododecyl ether ($C_{12}EO_8$)

Octaethylene glycol monohexadecyl ether ($C_{16}EO_8$)

Polyoxyethylene(10) cetyl ether (the major constituent of Brij® 56)

Figure 2. Space filling models of the surfactant molecules used as templates to form mesoporous metals. Dark grey spheres = carbon, light grey = hydrogen and red = oxygen. A line diagram for octaethylene glycol monododecyl ether is shown above.

With their hydrophobic alkyl chains and hydrophilic ether headgroups, these molecules are all amphiphilic and will aggregate to form supramolecular structures in water. Note that the conformations shown in the diagram are just for ease of viewing; in solution the molecules will not be straight and the ethylene headgroups in particular will contract due to hydrogen bonding. A phase diagram for octaethylene glycol monohexadecyl ether ($C_{16}EO_8$) is shown in figure 3.

---

[2] A surface active agent. **1950** *American Dyestuff Reporter* XXXIX. 379/3: A new word, Surfactants, has been coined by Antara Products, General Aniline & Film Corporation, and has been presented to the chemical industry to cover all materials that have surface activity, including wetting agents, dispersants, emulsifiers, detergents and foaming agents.

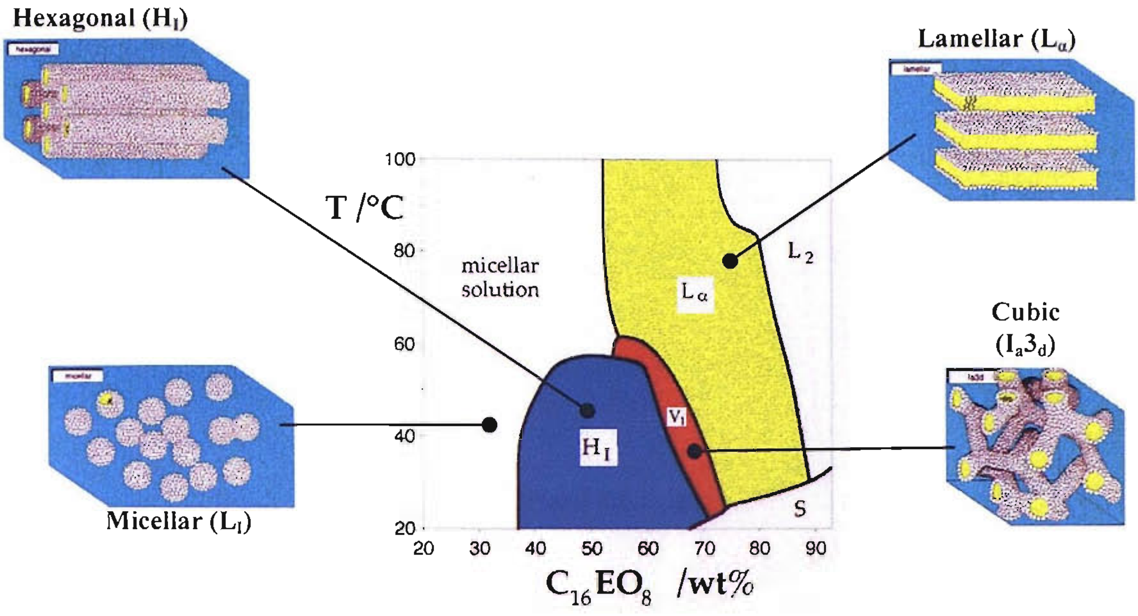

Figure 3. Phase diagram for Octaethylene glycol monohexadecyl ether ($C_{16}EO_8$) in water[5].

The phase diagrams for each of the surfactants shown in figure 2 are quite similar; although Brij56® (which is comprised of a mixture of molecules with slightly varying ethylene oxide chain lengths) was used in this work as it is relatively cheap.

As mentioned earlier, water is excluded from the insides of the structures. Therefore if a solid is generated in the aqueous phase (e.g. by chemical/electrochemical reduction of a metal salt) it grows only in the interstitial spaces between the surfactant aggregates. Then if the surfactant is removed (by dissolution in a large excess of water) the solid that is left behind has an architecture that is the inverse of the LC template; an architecture that can be controlled by the concentration of the surfactant and the temperature. The size of the pores can also be controlled through the choice of surfactant molecule (the pore diameter is typically 10-30 % < double the alkyl chain length[2]) and the addition of swelling agents like heptane.

It is important to note that when metal salts are added to the binary LC mixtures the phase boundaries are perturbed. Figure 4 shows the pseudobinary phase diagram for $C_{16}EO_8$ and water with a fixed concentration of 1.92 M HCPA (hexachloroplatinic acid). The primary effect of the HCPA is to stabilise the more curved phases at higher temperatures[5]. Note that the hexagonal (H_I) phase forms over a broad range of temperatures and surfactant concentrations making it particularly attractive as a template for mesoporous metal deposition.

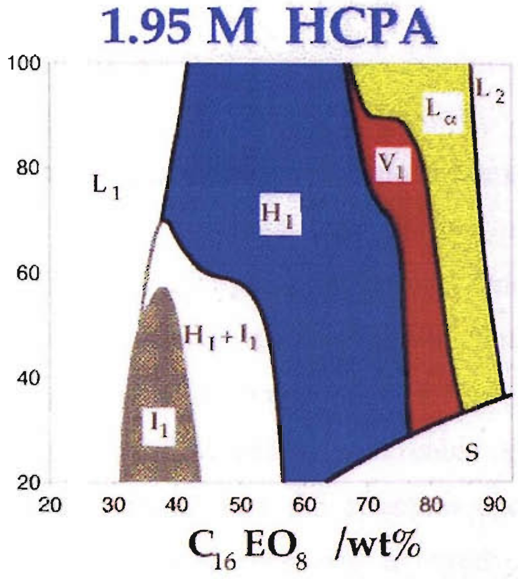

Figure 4. The pseudobinary phase diagram for $C_{16}EO_8$ and water with a fixed concentration of 1.92 M HCPA[5]. Going from miceller (L_I) to miceller cubic (I_I), hexagonal (H_I), cubic (V_I) and lamellar (L_α) with increasing surfactant concentration.

1.2 Mesoporous Materials

1.2.1 Early Nanostructures:

Porous materials such as zeolites are of great interest to chemists because of their potential for application as high surface area catalysts, molecular sieves and solid electrolytes. Zeolite structures occur naturally in many minerals and have been synthesised routinely since the 1950s. They are particularly important in many industrial processes such as selective catalysis but have found broader applications and are now common in many household products like washing powders and water softeners[6].

Zeolites are invariably amorphous or paracrystalline with a narrow range of pore sizes (typically < 1 nm diameter, i.e. microporous). This limits their application for catalysis and size selective separation to quite small molecules. Until recently the materials with the largest pore sizes that could be synthesized were the aluminophosphates ALPO$_4$-8[7] and VPI-5[8] and the gallophosphate cloverite[9], which have pore diameters in the range of 0.8 – 1.3 nm.

1.2.2 The Mobil Method:

A new family of silicate/aluminosilicate mesoporous molecular sieves, designated M41-S, was reported in 1992[10,11]. These materials were formed from the calcination of aluminosilicate gels in the presence of organic surfactants. One of the members of this family, MCM-41 (Mobil composition of matter-41), was found to have a hexagonal arrangement of pores with diameters in the range of *ca.* 1.5 nm to over 10 nm depending on the conditions of its synthesis. Materials with cubic symmetry could also be synthesized, but it was always found that the structure and pore dimensions were intimately linked to the surfactant properties, and a liquid crystal templating (LCT) mechanism was proposed[10].

However it should be noted that the concentration of surfactant used in the synthesis gels was always well below what was needed to form liquid crystal phases (often as low as 1 %). A study of the preparation by Monnier *et al.*[12] attributed the formation of the mesophase and polymerisation of silica to strong interactions between oligomeric silica polyanions and cationic surfactant molecules. This leads to a high density of silica species at the surfactant interface encouraging their polymerisation, and directing the ordering of the silicate encasesd micelles into structures. Support for this mechanism was provided by Cheng *et al.*[13] who showed that ordered mesoporous materials could only be formed if the surfactant concentration was above the CMC.

These materials were of significance because they greatly extended the range of pore sizes previously accessible using zeolites (up to ~ 1.3 nm for some recently discovered metallophosphates[8,9]). M41S materials with larger pore structures were found to have surface areas of > 700 m^2 g^{-1} and hydrocarbon sorption capacities of 0.7 cm^3 g^{-1} and more. There was a great deal of interest in these materials generating many more papers[12,14], and extending the family to include mesoporous metal oxides[15].

1.2.3 True Liquid Crystal Templating (TLCT):

In 1995 Attard *et al.* reported the templating of silica mesostructures using the non-ionic surfactants octaethylene glycol monodecyl ether ($C_{12}EO_8$) and octaethylene glycol monohexadecyl ether ($C_{16}EO_8$) in water to form lyotropic liquid crystalline phases with tetramethyl orthosilicate (TMOS) as the silica precursor[16]. At room temperature and mildly acidic conditions the TMOS was polymerised to form solid silica, and the methanol by-product was removed continuously by performing the reaction under partial vacuum.

In contrast to the mobil method the surfactant is used in much higher concentrations (~50 wt % or more) and true LC phases are formed in the reaction mixture. Also the formation of the mesoporous product is not dependent on the interaction between the surfactant and the silica precursor. The hexagonal (H_I), cubic (V_I) and lamellar (L_α) LC phases were successfully used to form porous silicas of an inverse architecture, with the former two being stable to calcination. This method generates macroscopic, un-cracked monolithic films, unlike the Mobil method which leads to sub-micron powders.

Conformation of the liquid crystal phases was achieved by optical microscopy and transmition electron micrographs (TEM) were used to observe the silica structures. The TEM images showed the hexagonal, cubic and lamellar silicas all had well ordered structures with pore diameters of 2-3 nm and wall thicknesses of 1.2 nm[17].

1.2.4 Advantages of TLCT:

- Unlike the Mobil method TLCT does not rely on charge based interactions between the silica precursor and the surfactant; meaning that the process is independent of the charge and structure of the surfactant amphiphile.
- It is possible to predict the structure of the product from the pre-formed LC phase in the reaction mixture.

- Inorganic precursors have little effect on the LC behaviour; meaning that the binary phase diagram can be used to predict the structure of the product in most cases.
- Lastly the structures are monolithic with no microporosity or interparticle macroporosity unlike the fine powders generated by the Mobil method.

1.2.5 Mesoporous Platinum from TLCT:

Subsequently, mesoporous platinum was produced through chemical reduction of hexachloroplatinic acid (HCPA) and ammonium terachloroplatinate (ATCP), by less noble metals, in the aqueous domains of the H_I phase of a $C_{16}EO_8$ water mixture[18]. The resulting platinum (denoted H_I-Pt) consisted of particles of 90-500 nm in diameter and was shown to be the inverse of the supramolecular architecture of the template around which it was formed (with TEM studies indicating hexagonal arrays of 3 nm diameter pores separated by 3 nm thick walls).

Electrochemical reduction of HCPA in a similar templating mixture was later used to produce thin films of mesoporous platinum on electrode surfaces[19]. This material was denoted as H_I-ePt. Scanning tunnelling microscopy (STM) studies showed these films to be uniform and flat (typical surface roughness of 20 ± 5 nm over a 1 mm^2 area). While TEM imaging revealed cylindrical, nanometre pores of indefinite length, arranged in a hexagonal lattice. It was found that the pore diameter could be varied from ~ 1.75 – 3.5 (± 0.15) nm by using surfactants of different alkyl chain lengths (i.e. $C_{16}EO_8$ or $C_{12}EO_8$ in this case) in combination with varying quantities of hydrophobic swelling agents like n-heptane.

Subsequent studies of H_I-ePt, by Elliott *et al.*[20] found that gold microdiscs plated with this mesoporous platinum had roughness factors of ~ 200 (corresponding to a surface area of 6.45 $m^2\ g^{-1}$ of electrodeposited platinum nanostructure). However cyclic voltammetry in potassium ferricyanide showed that the microelectrodes retained the high rates of mass transport associated with radial diffusion, with increased double layer capacitance due to the large surface areas.

1.2.6 Advances and Applications of TLCT:

This technique has now been used to make a range of mesoporous metals (denoted H_I-eM, where M refers to the metal) like platinum[20-24], tin[25], cobalt[26], nickel[27], rhodium[28], palladium[29,30] and metal alloys[31]; with pore sizes ranging from ~ 1.7 - 4 nm. Pore separations and film thickness can be controlled by careful selection of the deposition conditions (i.e. temperature, surfactant concentration, charge passed during electrodeposition and the type and source of metal ions)[21].

Some of these materials have already found practical applications. Evans *et al.*[32] report the use of H_I-ePt, deposited onto microelectrodes, for catalytic hydrogen peroxide detection (discussed in Chapter 3). Similar microelectrodes have also been used in the non-enzymatic detection of glucose[33] (discussed in Chapter 4), and for measurement of dissolved oxygen[34]. Mesoporous palladium catalyses the oxidation of methane and has been investigated for gas sensor applications[35]. Mesoporous nickel may have applications in the manufacture of more efficient batteries[36] and fuel cells[37,38] and in electrochemical hydrogenation of organics[39]; where in each case performance is closely related to the surface area of the nickel substrate employed. And mesoporous cobalt has proved to display unusual magnetic properties[26] and may find application in new data storage devices. The coercivity of the H_I-eCo phase was found to vary systematically with the size of the pores through a range of three to five times greater than that observed for the bulk, polycrystalline metal.

1.3 Macroporous Materials

These are solids with porous structures that have dimensions larger than 50 nm.

1.3.1 Colloidal Particles:

The fabrication of macroporous metals, discussed in this thesis, relies on the self assembly of monodisperse, colloidal particles as templates. The colloids used in this work were polystyrene latex spheres with diameters of a few hundred to a few microns, although similar spheres may also be formed from other polymers (such as poly(methylmethacrylate) or polyacrylate) using emulsion polymerisation techniques[40]. Monodispersive particles may also be prepared from silica using the Stober method[41]. Aqueous colloidal suspensions of both silica and polymer (often referred to as latexes) particles are now commercially available in a range of sizes; from 20 nm to several microns in diameter.

1.3.2 Self Assembly and Synthetic Opals:

In this work self assembly was achieved simply by allowing the latex spheres to sediment, from an aqueous suspension, onto a flat substrate. The spheres naturally assemble, under gravity, to form close packed crystalline arrays, with a structure analogous to that of the semi-precious gem-stone opal[42,43]. The packing has been observed to be predominantly face centred cubic (fcc)[44]. However the energy difference between fcc and hcp (hexagonal close packed) is less than 10^{-3} k_BT per particle, therefore overall the crystals adopt a random hexagonal close packed structure (rhcp)[45,46]. These synthetic opals contain numerous defects e.g. grain boundaries, stacking faults, dislocations and vacancies[44]. Also sedimentation is not always a viable route to self assembly of very small polymer spheres (< 100 nm) where Brownian motion keeps the particles in suspension. This has led to the development of other methodologies to improve the crystallinity of the structures and allow the coalescence of nanometre sized particles:

1. Careful, controlled drying of thin films[47,48]. As the solvent evaporates (and the thickness of the film decreases below the diameter of the spheres) the shrinking menisci between spheres generate capillary forces which draw the particles towards each other. This lateral immersion force arises from the deformation of the water surface by the protruding particles and is proportional to the square of the particle diameter (r^2, which may be greater than k_BT even for nanometer sized particles). An influx of water from the thicker portions of the film compensates for evaporation around the hydrophilic particles in this drying nucleus. This leads to convection and brings more particles, to the edge of the growing array, which are assembled by the flux of water into the crystal structure[49]. Dushkin *et al.*[47] found that higher evaporation rates gave structures of higher crystallinity. Good self

assembly requires un-restricted motion of the particles within the film (i.e. low friction between the particle and the substrate).

2. Controlled de-wetting of flat, hydrophilic substrates. The substrate is positioned in a colloidal suspension, with its surface perpendicular to the solution surface. Then the substrate is either withdrawn slowly[50] or the solution is allowed to evaporate. Particle monolayers are formed by continuous convective assembly[51]. This method is not to be confused with the Langmuir Blodgett technique; where the particles are assembled at the surface of a liquid and then transferred to the substrate.
3. The Colvin Method[46,52]. Like the de-wetting methods above this involves slowly drawing the substrate out of a colloidal suspension. Unlike the other methods this allows assembly of bulk 3D structures. Colvin *et al.* were able to control the thickness of their particle arrays (from a few sphere layers, to hundreds of layers) by carefully selecting the assembly parameters (i.e. the angle between the substrate and the solution surface, the temperature, particle size, particle concentration and the rate of evaporation/substrate withdrawal).

One of the main driving forces for improving the crystallinity of synthetic opals is to produce effective photonic bandgap materials[53]. A photonic bandgap (PBG) can be defined as a frequency band in a three dimensional dielectric structure in which electromagnetic (EM) waves are forbidden. This is analogous to the electronic bandgap in semiconductors[54,55]. Photonic crystals (PC) offer a unique way of manipulating EM waves and may be exploited for various applications such as: optical integrated circuits[56], thermophotovoltaics[57,58], and novel biological[59] and chemical[60,61] sensors.

However for the purposes of this work the crystallinity of the colloidal arrays is less important; here they serve as templates for the fabrication of macroporous metals. Such materials fall under the broader definition of inverse opals.

1.3.3 Inverse Opals:

Inverse opaline structures are produced by using the colloidal particle arrays (described above) as templates. Firstly the synthetic opal must be infiltrated with a new substance (different from that comprising the spheres), and then the spheres are removed by chemical etching or calcination to leave a network of interconnected spherical voids within the remaining infiltrated material (which may or may not require further processing).

Templates are commonly infiltrated with a concentrated chemical precursor which is then converted into the desired macroporous material e.g. electroless metal deposition[62,63] or sol-gel chemistry[64]. Infiltration may also be achieved by nanoparticle infusion[65], chemical vapour deposition[66,67], electrophoretic deposition[68] or electrochemical deposition[69-76]. This work is concerned with electrochemical deposition, which has certain advantages over the other methods of infiltration. Electrochemical deposition leads to true volume filling of the interstitial space in the template; quite precise control over the thickness of the macroporous deposit is possible by careful monitoring of the potential and current and, lastly, the macroporous structure produced requires no further processing steps.

These materials have potential in applications such as catalysis[77], filters and separators[78], photonic band-gap materials[79,80], micromirrors and possible microlaser applications[81,82], surface enhanced Raman spectroscopy (SERS)[83] or as porous electrodes[84]. Use of macroporous metals as porous electrodes[85] and as "femtolitre beakers" is reported in this thesis.

1.4 Amperometric Biosensors

1.4.1 Main Principles of Amperometric Sensors:

A potential difference is applied between 2 or 3 electrodes in the medium of interest (typically aqueous solution) i.e. working electrode counter electrode and reference (if measuring very small current CE & RE may be same electrode). By applying sufficient potential at the working electrode it is possible to exchange electrons with molecules at the surface (thus reducing or oxidising them).

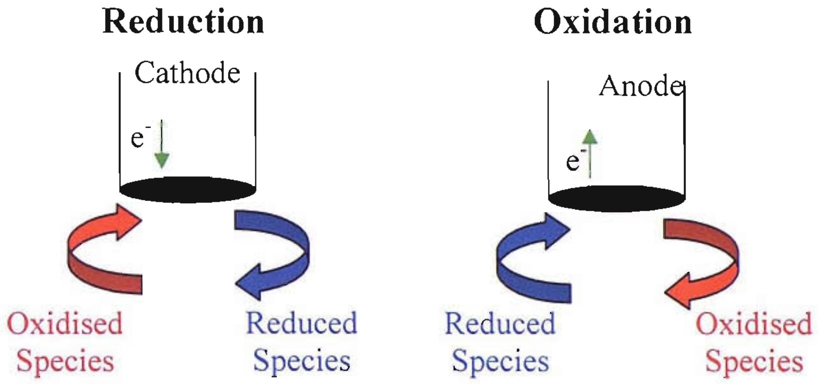

Figure 5. Schematic representation of oxidation/reduction at a working electrode surface.

This transfer of electrons causes a current to flow in the electrode, which is proportional to the number of molecules reacting at the surface per unit time. Provided that certain experimental parameters are known then the concentration of the species can be calculated from the current under mass transport limited conditions:

$$i = nFAk_mc \qquad \mathbf{1}$$

Where:

- i = current generated by reaction (A).
- n = number of electrons involved in the process.
- F = the Faraday constant, 96485 C mol^{-1}.
- A = area of electrode (cm^2).

- k_m = mass transfer coefficient of the species involved (cm s^{-1}).
- c = bulk concentration of analyte the species (mol cm^{-3}).

1.4.2 Microelectrodes:

A microelectrode (or UME, ultra-microelectrode) is defined as an electrode with at least one dimension so small (usually <50 μm) that its properties are a function of size[86]. Microelectrodes were first developed in the late 1940s, and were used by biologists as potentiometric sensors. They designed small electrodes that could be inserted into living organisms with limited tissue damage[87]. It wasn't until the late 1970s that electrochemists began to fully characterize the unique properties of these devices.

The properties of microelectrodes are affected by their size, and differ from those of conventional electrodes. Key differences are seen in:

1. ***The mass transport regime.*** Rapid establishment of diffusion controlled, steady state, limiting current[88]. Note this is only seen if all of the electrode dimensions are of a small enough size e.g. a microdisc of diameter < 50 μm will attain a steady state current rapidly however a micro band electrode of significant length will not attain a true steady diffusion limited state.
2. ***Charging current.*** The double layer capacitance of an electrode is proportional to its surface area, and the time constant of charging is dependent on the overall capacitance ($\tau = RC_{dl}$). Since the surface area of a microelectrode is so small C_{dl} and τ are also very small, meaning that Faradaic information may be obtained after very short times i.e. μs. This facilitates the study of fast electron transfer reactions, and very short-lived species.
3. ***Decreased distortion from iR drop.*** Current is proportional to electrode size (see equation 1), so the smaller the electrode area, the smaller the currents and the lesser the effects of *iR* drop. One advantage of this is that electrochemical reactions may be carried out, at a microelectrode surface, in poorly conducting media, even in the absence of supporting electrolyte[89-91].

It is these properties that make microelectrodes ideal biosensors. Their size means they can be used to acquire data in small volumes without significantly altering the concentration of the analyte and a steady state response is reached in very short times. In the case of a microdisc electrode, at steady state, equation (1) becomes:

$$i_L = 4nFDca \qquad \mathbf{2}$$

Where:

- i_L = limiting current (A).
- D = diffusion coefficient ($cm^2\ s^{-1}$).
- a = radius of the disc (cm).

1.4.3 Biosensors:

Biosensors may be defined as a compact analytical device employing a biological/biologically derived sensing element integrated (or in close contact) with a physiochemical transducer; the aim being to generate a continuous/semi-continuous digital signal that is proportional to a specific chemical/group of chemicals[92].

A biosensor consists of two parts: the receptor, which interacts selectively with the analyte and the transducer, which produces an electrical or optical signal carrying information about the analyte (i.e. presence/concentration of a specific molecule). There are five main transducer types:

- Calorimetric transducers.
- Optical transducers.
- Gravimetric resonator transducers.
- Surface plasmon resonance (SPR) transducers.
- Electrochemical transducers.

This thesis is concerned solely with electrochemical transducers, specifically amperometric cells (although potentiometric or conductimetric cells may also be employed). In amperometry the signal of interest is the current resulting from exchange of electrons between the working electrode and the analyte species; this has the advantage of being linear with analyte concentration.

There are three types of receptor:

- Affinity biosensors: based on specific chemical binding e.g. immunosensors using antigen-antibody reaction.
- Living biosensors: employing micro-organisms or living tissue as receptors.
- Enzymatic (or metabolism) biosensors: where an enzyme is immobilized on or near the transducer and typically the corresponding substrate is the analyte species.

1.4.4 Enzyme Electrodes:

Enzymes are high molecular weight proteins that catalyse biological reactions, and are the most common biomolecule with more than 2500 identified (many of these being commercially available). Their abundance, variety and high specificity for their substrates makes enzymes an attractive receptor for many biosensor applications.

However many enzymes are very easily denatured and can loose their activity in a matter of days or even hours. One key factor in the stability and lifetime of a biosensor is the method used to immobilize the enzyme at the transducer. Immobilisation may be achieved in several ways: encapsulation of free, soluble enzyme at the transducer i.e. within a membrane[93]; polymer entrapment either by physisorption followed by polymerization of a monomer[94] or co-deposition with a conducting polymer[95,96]; enzyme cross-linking[97]; covalent binding[98] or entrapment within the transducer material (e.g. by mixing with a carbon paste[99] or by co-deposition with a conducting material that subsequently acts as the transducer electrode[100]).

The general form of an enzyme substrate reaction is[93]:

$$E + S \underset{k_{-1}}{\overset{k_1}{\leftrightarrow}} ES \overset{k_2}{\rightarrow} E + P \qquad (1)$$

where the irreversible conversion of the substrate (S) to the product (P) occurs through the reversible formation of an intermediate enzyme-substrate complex (ES). The kinetics of this process is described by the Michaelis Menten model:

$$v = -\frac{dc_s}{dt} = \frac{dc_p}{dt} = \frac{v_{\max} c_s}{K_m + c_s} \qquad \mathbf{3}$$

where v is the reaction rate, v_{max} is the maximum rate ($v_{max} = k_2 c_e$, where c_e is the enzyme concentration), c_s is the substrate concentration, c_p is the product concentration and K_m is the Michaelis-Menten constant and may be expressed in terms of the equilibrium constants as:

$$K_m = k_{-1} + \frac{k_2}{k_1} \qquad \mathbf{4}$$

or defined as the concentration of substrate at which the reaction rate is ½ v_{max}. At low values of c_s the reaction is first order (and the reaction rate is linearly dependant on substrate concentration) but at high c_s the rate becomes constant. Figure 6 shows the general form of equation 3.

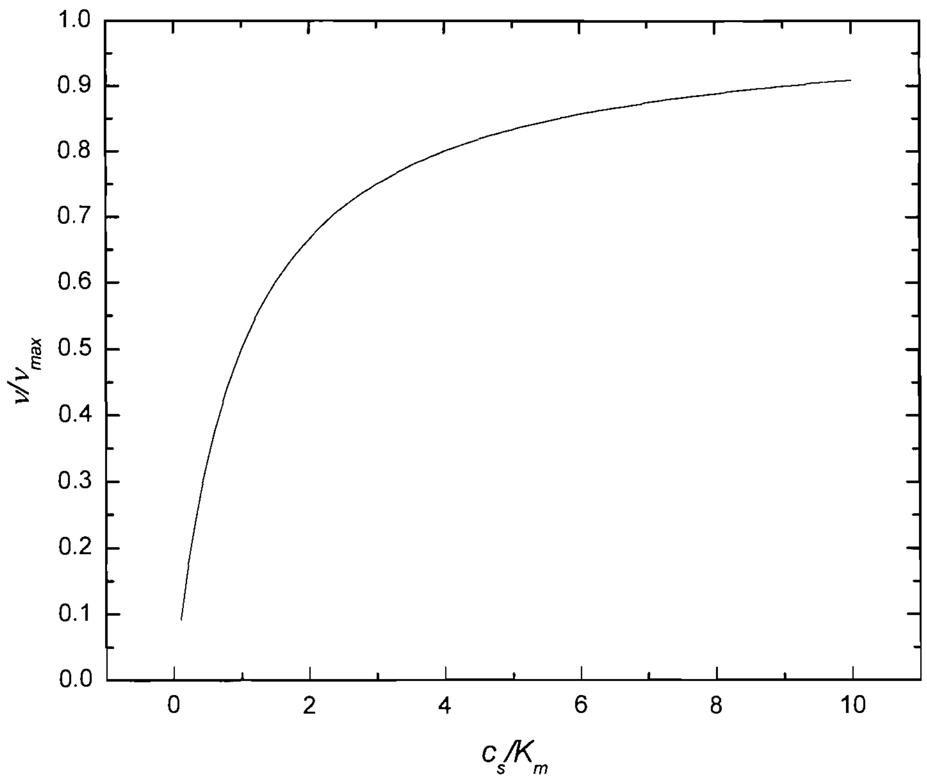

Figure 6. General form of Michaelis-Menten equation. Normalised reaction rate versus substrate concentration normalized with respect to K_m.

Oxidase enzymes employ molecular oxygen as an electron acceptor and generate hydrogen peroxide as a byproduct of the overall substrate reaction (water is often also consumed by the reaction)[93]:

$$S + O_2 + (H_2O) \xrightarrow{\text{Oxidase}} P + H_2O_2 \tag{2}$$

Thus hydrogen peroxide is the detected species in many enzymatic biosensors. The electrochemistry of hydrogen peroxide is discussed in Chapter 3. One such oxidase enzyme is glucose oxidase (Gox) which is employed in many glucose biosensors.

Glucose is a short chain carbohydrate molecule of empirical formula $C_6H_{12}O_6$. Because there are two asymmetric arrangements of the alcohol groups, with respect to the carbon chain, there are two possible stereoisomers[93] (figure 7).

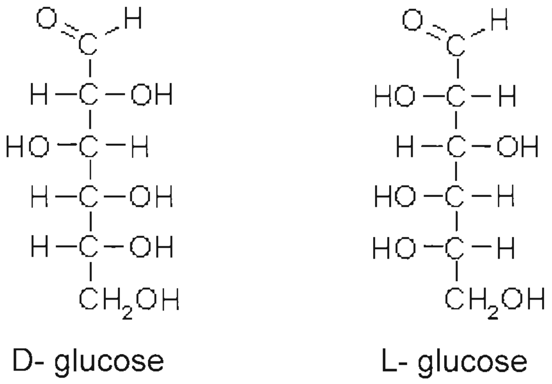
D- glucose L- glucose

Figure 7. The two stereoisomers of glucose.

At physiological pH the alcohol of the number 5 carbon (conventionally the carbons are numbered 1-6 starting from the carbonyl) can attack the aldehyde group and the molecule exists as a ring structure. Both the D and L sterioisomers will cyclise to form two distinct ring anomers, distinguished by the position of the alcohol group on the number 1 carbon (figure 8). At 25 °C the ratio of the two anomers is 37 % α to 63 % β. Note that five membered rings may also form in much smaller proportions.

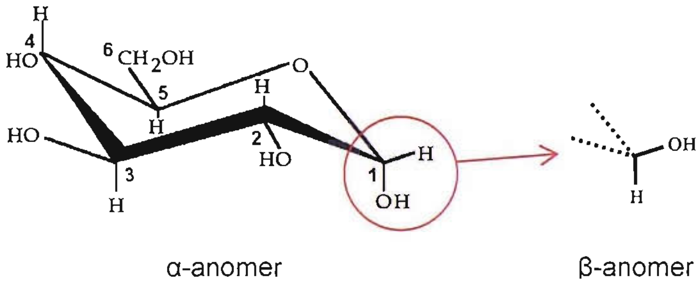

α-anomer β-anomer

Figure 8. The two anomers of the cyclic (six memberd ring) glucose molecule.

Glucose oxidase selectively oxidizes β-(D)- glucose according to the scheme below:

$$C_6H_{12}O_6(\beta\text{-D-glucose}) + \text{FAD(present in glucose oxidase)} + H_2O \rightarrow FADH_2 + C_6H_{12}O_7(\text{gluconolactone}) \quad (3)$$

The gluconolactone may go on to form gluconic acid and the active, FAD/$FADH_2$, redox centre of the Gox is re-oxidised by molecular oxygen in solution:

$$O_2 + FADH_2 \rightarrow FAD + H_2O_2 \qquad (4)$$

Thus amperometric hydrogen peroxide detection may be used as a means of glucose mesurement.

1.5 Glucose Detection

1.5.1 Diabetes:

Currently the main market for biosensors is in medicine with the vast majority of commercial sensors being for glucose analysis. This is hardly surprising, with around 1.8 million people in the UK alone (approximately 3 %) diagnosed with diabetes; there is great impetus for the development of effective blood glucose sensors.

Diabetes is characterized by the body's inability to absorb glucose into its cells and turn it into energy. This process is regulated by insulin, a hormone produced in the pancreas.

There are two types of diabetes[101]:

- Type 1: Where the patient is insulin dependent due to a malfunction of the pancreas. It is unclear why, but for some reason the insulin producing cells of the pancreas are destroyed in a sort of auto-immune reaction, possibly brought on by viral infection. The onset of type 1 diabetes is quite quick, with symptoms usually developing over a few weeks, and generally occurs early on in life.
- Type 2: This is where the body becomes less sensitive to the insulin it produces. The symptoms of type two diabetes generally develop in later life. Its onset is slower, the symptoms less severe and can usually be controlled with good diet or a combination of diet and tablets.

Healthy fasting blood glucose levels range between 3.6 and 6.4 mM, but in a diabetic are $\geq$ 7.8 mM and may reach as much as 30 mM in cases of extreme hyperglycemia. If the condition is not managed properly the long term risks include, kidney, nerve, heart and artery damage and blindness. If left untreated many sufferers would die.

Diabetics need to check their blood glucose levels up to 4 times a day in order to properly maintain a healthy concentration. This is done by analysis of a blood droplet using a commercially available glucose sensor/testing kit.

1.5.2 A Brief History of Glucose Sensors:

The use of a glucose oxidase modified electrode for the detection of glucose was first proposed by Clark and Lyons in 1962[102]. In this early sensor Gox was held close to the electrode surface using a semipermeable dialysis membrane and the glucose concentration was inferred from the rate of oxygen consumption[103]. The first commercial sensor to employ this technology was the Yellow Spring Instruments, model 23YSI analyzer launched in 1975[104]. It was shown in 1973 that blood glucose could also be determined by amperomertic monitoring of hydrogen peroxide[105], which is a product of the reaction between Gox, glucose and oxygen.

Glucose sensors that use molecular oxygen to mediate the reaction between glucose and Gox are referred to as first generation glucose sensors. These generally rely on hydrogen peroxide oxidation to monitor the glucose concentration, and are subject to errors in measurement due to other blood species (such as acetaminophen, ascorbic and uric acid) which are electroactive in the same range. Common strategies for reducing the effects of interferent species include the use of permselective membranes, which exclude the interferents based on their size, charge or polarity[106,107]. These films will often also exclude surface active macromelecules leading to increased stability and sensor lifetime.

Another problem with first generation glucose sensors is their dependence on oxygen. Fluctuation in oxygen tension may cause errors in the measurement signal, and the reaction between Gox and glucose is restricted by the amount of O_2 available in solution (the concentration of dissolved oxygen in blood is often an order of magnitude less than that of glucose[104]). Some strategies that have been employed to overcome this problem include: the use of semipermeable films to restrict the flux of glucose to the sensor[108]; the use of an oxygen rich carbon paste transducer[109] and sensors based on glucose dehydrogenase (GDH)[110]. However the most common solution is to introduce an artificial redox mediator to do the job of the dioxygen molecule.

Glucose sensors which employ an artificial mediator are classified as second generation sensors. A good mediator should operate at low overpotentials to help reduce the effects of interferents. MediSense (formerly Genetics International) was the first company to exploit this technology commercially when they produced the first personal glucose meter in 1987. The electrode consisted of a disposable screen printed strip with a carbon working electrode, infiltrated with Gox and a ferrocene mediator, and a silver/silver chloride reference electrode. A drop of blood is applied to the strip which is then inserted into a portable meter which applies a potential to the working electrode and calculates the blood glucose concentration from the resulting current transient. The majority of commercial glucose meters are still based on this technology.

A great deal of effort has gone into producing sensors which require smaller and smaller blood droplets for measurement (glucose readings can now be obtained from droplets of less than a microlitre which means that samples can be taken from the arm instead of the fingers[104]) and in reducing the analysis time. However the future would seem to be in sensors that could provide continuous blood glucose monitoring. If such a sensor could be combined in a closed-loop system with a means of automatic insulin delivery it could offer very tight glyceamic control; acting as an artificial pancreas.

There are many problems to be overcome before a viable artificial pancreas can be realized, particularly if such a device is intended to be implanted into the body. Any mediator used would need to be of low toxicity and low solubility in case of leaching into the blood system. Indeed all of the materials comprising the sensor would have to be non-toxic and of good biocompatibility. The device would need to be small and employ an enzyme with long-term stability (ideally on the order of months or longer). One would need to be able to recondition and calibrate the sensor *in vivo*. Overall, the device would have to be small, safe, accurate and convenient.

Some success has already been achieved with subcutaneous monitoring using implantable "needle-type" electrodes which can be operated for a few days and then replaced by the patient[111]. There have also been advances in non-invasive monitoring like the Cygnus Inc. GlucoWatch® biographer[112], which uses reverse iontopheresis to collect glucose through the skin.

1.6 Thesis Overview

This work is concerned with: 1) the further development and characterization of the mesoporous, H_I-eM, metal phases and macroporous, inverse opal structures; 2) application of these materials in fabricating amperometric biosensors, which exploit their unique properties.

In Chapter 3 the properties of mesoporous, and polished, platinum (H_I-ePt), palladium (H_I-ePd) and rhodium (H_I-eRh) microelectrodes are reviewed briefly before comparing their electrochemical response to hydrogen peroxide, ascorbate and glucose. The three metals were also modified with glucose oxidase to make 2nd generation glucose sensors. Conclusions are drawn about the suitability of each metal for direct hydrogen peroxide and glucose detection, and for enzyme mediated glucose measurement.

Chapter 4 is concerned with assembly of latex spheres at electrodes for the subsequent deposition of macroporous metals. Sedimentation and electrophoresis was used to assemble spheres (ranging in size from hundreds of nanometers to 5 μm diameter) onto various substrates and the structure of the opaline deposits is discussed. The structure of macroporous gold films, deposited onto platinum discs, are investigated electrochemically by cyclic voltammetry in sulphuric acid. It has been shown that these macroporous gold electrodes may be modified with redox mediators for the catalytic oxidation of NADH[85], and this work is summarized here. Lastly, larger (5 μm) spheres were used to deposit arrays of tiny metal cups (femtolitre beakers) for the directed immobilization of protein molecules.

In Chapter 5 recessed microdisc electrodes are used to deposit thick films of mesoporous platinum with greater efficiency and without altering the geometry of the substrate electrode. These mesoporous deposits have been characterized using environmental scanning electron microscopy (ESEM) and cyclic voltammery in sulphuric acid and ruthenium hexamine solutions. Recessed microdiscs were also used for the electrophoretic assembly of 500 nm diameter polystyrene spheres and subsequent deposition of macroporous gold. The recess seems to help confine the spheres after assembly so that a useful template is formed.

Experimental

2.1 Solutions and Reagents

All solutions were prepared using deionised water (Whatman Still+ purification system, resistivity > 10 MΩ cm) and all compounds were used as received (unless otherwise stated): Alumina powders (Buehler). Hydrogen peroxide (30 %, unstabilised, A.C.S., Fluka) standardised by titration with sodium thiosulphate[113] (0.1000 *N* volumetric standard, Aldrich). Brij® 56 (Aldrich). Ammonium tetrachloropalladate (99.995 + % purity, Aldrich). Rhodium trichloride (99 % purity, Alfa Aesar). Hexachloroplatinic acid hydrate (HCPA, 99.9 % purity, Aldrich). n-Heptane (99 % purity, Lancaster). D(+)-Glucose (ARISTAR, BDH). Buffer solutions were prepared from 0.2 M $NaH_2PO_4.H_2O$ & 0.2 M $Na_2HPO_4.12H_2O$ (99 %, BDH). And the pH of the solution was verified using a Corning model 145 pH meter. Phenol (Aldrich, purified by cold finger distillation). Glucose oxidase (lyophilised powder, from aspergillus niger, 157,500 U g^{-1}, Sigma). 2-deoxy-D-glucose (Grade III, SIGMA). L-ascorbic acid (99+ % ACS reagent, ALDRICH). Aqueous colloidal suspensions of polystyrene latex sphere particles were obtained from Duke Scientific. Gold 25 plating bath (Technic Inc.). Silver Paint (RS). Slow-set epoxy resin (Struers, Epofix Kit). Quick-set epoxy resin (RS). Ruthenium hexaamine trichloride (99 %, STREM chemicals). KCl (>99.5 %, BDH). 1 M sulphuric acid (diluted from concentrated sp. gr. 1.84 acid, > 95 %, BDH).

2.2 Electrodes

2.2.1 Working Electrode Fabrication:

The majority of the working electrodes used in this work were platinum disc electrodes. These were constructed by sealing wires (of appropriate diameter) in soda glass pipettes, and polishing to expose a smooth disc of metal. Electrical contact to a standard copper wire was made using an indium solder.

Evaporated nickel, and gold slides were also used as working electrodes for the deposition of macroporous metals in Chapter 4. Here the slides were cut to size with a diamond cutting tool, the working area was defined using nail polish as a mask and electrical contact to a standard copper wire was made using silver paint (the contact was protected in a blob of quick-set epoxy resin).

0.5 mm silver disc electrodes were made by sealing silver wires in slow-set epoxy resin. The working face was polished to reveal a smooth silver disc. Electrical contact was made to a standard copper wire with a spot of solder before sealing in the resin.

2.2.2 Preparation of Platinum Microelectrodes:

Before conducting any depositions or experiments, electrodes were polished on Buehler microcloths using alumina slurries of 1 μm and then 0.3 μm particle sizes. Then cycled in 1 M H_2SO_4 (25 °C, purged with argon) between -0.65 V and +0.85 V vs SMSE until a stable voltammogram was obtained.

2.2.3 Ancillary Electrodes:

Most of the electrochemical experiments were performed in a thermostated glass cell using a standard three electrode arrangement. Both saturated calomel (SCE) and saturated mercury mercurous sulphate (SMSE) electrodes were used as reference electrodes. Platinum gauze and porous carbon were both used as counter electrodes. Details of the electrodes and experimental conditions are given with each of the results shown in Chapters 3 to 5.

2.3.4 Recessing of Platinum Microdisc Electrodes:

25 μm polished platinum microdiscs, sealed in soda glass, were recessed by potential stepping from -5 V (0.1 s) to +5 V (0.1 s) vs a sacrificial carbon electrode in a solution of 60 % saturated $CaCl_2$, 36 % H_2O and 4 % HCl. Pulses were applied continuously from a PPR1 waveform generator, or in 10 s bursts from an Autolab PGSTAT30 potentiostat/galvanostat.

2.3 Mesoporous Metal Deposition

2.3.1 Plating Mixtures:

The templating solutions were mixtures of: ***a***) HCPA (hexachloroplatinic acid, 29 % w/w), water (29 % w/w) and Brij® 56 (42 % w/w); ***b***) ammonium tetrachloropalladate (12 % w/w), heptane (2 % w/w), water (39 % w/w) and Brij® 56 (47 % w/w); or ***c***) rhodium trichloride (12 % w/w), heptane (2 % w/w), water (39 % w/w) and Brij® 56 (47 % w/w). For platinum, palladium and rhodium depositions respectively.

2.3.2 Procedure:

The deposition mixture was spread onto the platinum gauze and the working electrode was inserted into the templating solution along with an SCE reference electrode (fig 2 below). Note, a little of the plating mixture was also applied to the surface of the working electrode before inserting into the bulk solution. This was particularly important for depositions onto recessed microdiscs where the solution had to be worked into the recess to get good even plating.

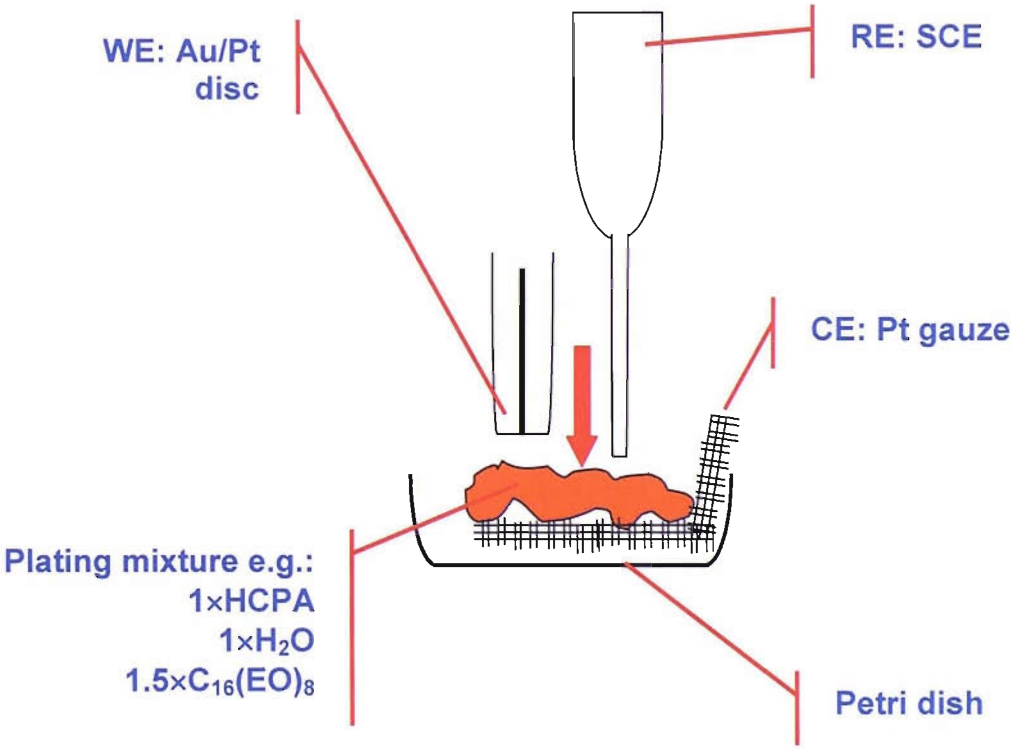

Figure 2. Schematic of equipment used to electrodeposit mesoporous metals.

The working electrode was held at -0.1 V (for platinum or rhodium deposition) or +0.1 V (for palladium deposition) vs SCE until the desired charge had been passed. After deposition the electrodes were rinsed with deionised water and then transferred to a beaker of stirred, deionised water, to dissolve the plating mixture.

Cyclic voltammetry in 1 M sulphuric acid, before and after deposition, was used to establish an increase in surface area and to help clean the electrode surface in preparation for experimentation. Mesoporous electrodes were stored in distilled water.

2.4 Gox Electrodes

2.4.1 Enzyme Immobilisation:

Electrodes were stood (for 15 min at open circuit potential) in a solution of 3.15 mg cm^{-3} glucose oxidase, 50 mM phenol and 0.1 M TEATFB[3] in 0.1 M sodium phosphate buffer (pH=7.0). Before applying the following potential step regime: 0.0 V (20 s), +0.9 V (8 min) and 0.0 V (20 s) (potentials measured vs. SCE).

After modification electrodes were washed with, and stored in, 0.1 M, pH 7.4 sodium phosphate buffer (storage temperature = 4 °C).

2.4.2 Preparation of Glucose Solution:

Typically 5 M solutions were made by dissolving powdered glucose in distilled water or phosphate buffer (pH 7.4) and stirring for a minimum of 2 h to allow the anomers to equilibrate.

2.4.3 Calibration of Gox Electrodes:

Gox modified working electrodes were held at +0.2 V vs SMSE (this potential was chose to allow oxidation of the Gox/glucose reaction product, hydrogen peroxide, as detailed with results in Chapter 3) in a 0.1 M solution of sodium phosphate buffer (pH 7.4), theromostated at 25 °C in a water jacketed glass cell, with a platinum gauze counter

---

[3] Tetraethylamonium terafluoroborate, used as an electrolyte.

electrode. The background current was allowed to stabilise for 20 min before adding 25-50 μl aliquots of concentrated glucose solution (1-5 M in the same phosphate buffer, as detailed in Chapter 3). The solution was stirred during additions using a magnetic stirrer. After addition the stirring was stopped and measurement was made for 3 min before the next glucose aliquot added.

2.5 Macroporous Metals

2.5.1 Template Self Assembly by Sedimentation:

Aqueous suspensions of spherical, colloidal, particles (of polystyrene latex) were contained at the working electrode substrates within Teflon® rings. The rings were 7 mm in diameter (with a 4 mm diameter hole) and 6 mm high and were attached to the substrates using nail polish (figure 3). In each case the volume and concentration of sphere suspension was calculated to give the required number of particle layers in the dried template.

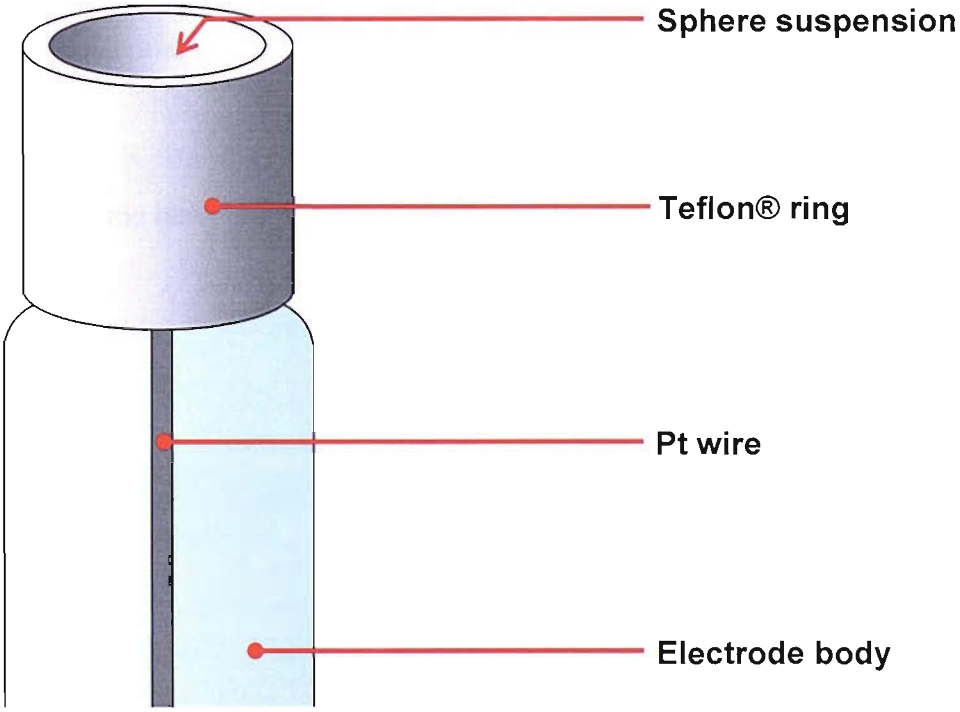

Figure 3. Schematic showing procedure for immobilising spheres at the 0.5 mm diameter platinum disc electrodes.

Once the colloidal suspension was in place on the substrate, samples were maintained in an atmosphere of 100 % humidity, at lab temperature (to prevent evaporation), until the particles had settled (typically 1-2 days for larger spheres i.e. 5 μm diameter, or for up to a week for smaller spheres i.e. 100-600 nm diameter). Then the water was allowed to evaporate under normal laboratory conditions.

In a few cases the templates were heated, to ~90 °C for 1 min, after drying, but typically they were used without any further processing.

2.5.2 Deposition of macroporous metals:

Gold was deposited from a, cyanide free, commercial plating solution: the Gold 25 plating bath supplied by Technic Inc.. The bath was used at 25 °C in a water jacketed glass cell with platinum gauze counter electrode and SCE reference. For deposition onto silver and gold substrates a potential of -0.94 V vs SCE was applied but -0.85 V for deposition onto platinum and -0.9 V for deposition onto nickel.

Platinum was deposited from an aqueous solution of 50 mM HCPA with no additional electrolyte. A potential of -0.05 V vs SCE was applied for deposition onto gold and silver substrates.

After deposition the latex templates were removed by dissolving in THF (15 min).

Mesoporous Electrodes

3.1 Overview

Due to its application in the treatment and management of diabetes there is much interest in the amperometric measurement of glucose[104]. Direct oxidation/reduction of glucose is not a simple well defined process; it requires high overpotentials and usually leads to poisoning at conventional electrodes. Consequently amperometric glucose measurement is often preformed vicariously via the oxidation or reduction of hydrogen peroxide, which is a by-product of the catalytic reaction between glucose and glucose oxidase (GOx). This reaction proceeds by a "ping-pong" mechanism[114]:

$$C_6H_{12}O_6(\beta\text{-D-glucose}) + \text{FAD(present in glucose oxidase)} + H_2O \rightarrow$$
$$\text{FADH}_2 + C_6H_{12}O_7(\text{gluconolactone})$$

$$O_2 + \text{FADH}_2 \rightarrow \text{FAD} + H_2O_2$$

One method of glucose detection involves immobilising glucose oxidase at an electrode surface (usually by electrodeposition of a polymer film[94], figure 1). In the presence of glucose this generates hydrogen peroxide which can then be measured by applying a constant overpotential to the electrode (usually an anodic overpotential, as reduction of hydrogen peroxide occurs in the same potential window as oxygen reduction).

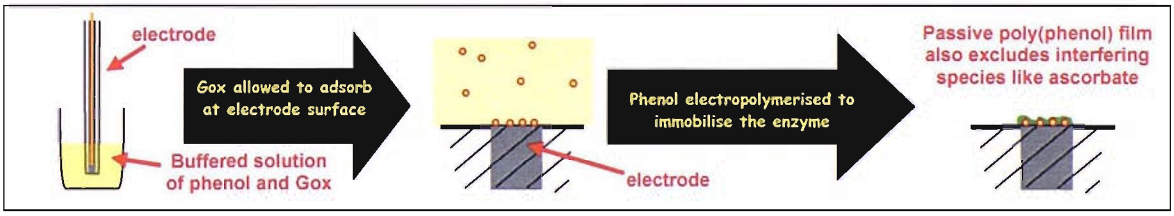

Figure 1. Procedure for glucose oxidase entrapment in poly(phenol) film as reported by Bartlett and Caruana[94].

There is a great deal of literature on glucose sensors that operate using this principle. However, while this method works well under laboratory conditions, common problems are encountered when trying to make measurements *in-vivo* or in whole blood samples; problems such as stability of the enzyme, response time and interference from other electroactive species like ascorbate, uric acid and acetoamidophenol[115].

Recently it was discovered that mesoporous platinum catalyses the redox chemistry of hydrogen peroxide[32]. Mesoporous (H_I-ePt) platinum microelectrodes showed good reproducibility and high accuracy of measurement over a wide range of hydrogen peroxide concentrations while maintaining the high rates of mass transport expected at conventional microelectrodes. The catalytic activity of such electrodes means that the oxidation of hydrogen peroxide occurs at much lower potentials i.e. 0 V vs saturated mercury mecurous sulphate reference electrode (Hg/Hg_2SO_4 sat. K_2SO_4, referred to as SMSE) compared to +0.4 V at normal polished platinum. At such low potentials the interference from species like ascorbate might be reduced. Also the increased surface area means that a broader range of glucose concentrations could be measured and the effects of electrode fouling could be reduced.

This chapter extends the work conducted by Evans *et al.*[32] to include other mesoporous platinum group metals. Cyclic voltammetry was used to investigate the redox chemistry of hydrogen peroxide and attempts made to explain the differences and similarities between platinum, palladium and rhodium in terms of the metal oxidation state using the mechanism proposed by Hall *et al.*[116-120].

The suitability of the three metals for glucose detection (both directly and using the method described above) was also investigated.

3.2 Preparation and Characterisation of Electrodes

3.2.1 Electrodeposition of Mesoporous Metal Films:

Platinum and palladium microdiscs were fabricated by sealing 25 μm diameter wires in soda glass and polishing to a fine mirror finish using a 0.3 μm alumina slurry on a Buhler microcloth.

Platinum microdiscs were also modified with thin films of mesoporous platinum, palladium and rhodium by electroreduction of the appropriate metal salt from an aqueous solution containing the non-ionic surfactant Brij® 56 (full descriptions of the process are available for platinum[19,21,23], palladium[29] and rhodium[35]). The proportions were chosen such that the amphiphilic molecules of the surfactant form a hexagonal structure, which acts as a template, directing the deposition of the metal. It is possible to form other lyotropic crystalline phases depending on the relative concentrations of the components and the temperature of the mixture; the correct phase is identified by microscopy using polarised light.

A current time transient for the deposition of mesoporous rhodium is shown below. The shape and magnitude of the current are fairly typical of that seen for each of the metals deposited onto platinum microdiscs. There is an initial spike in the current (not recorded) due to the charging of the electrode surface. This falls away rapidly since the surface area of the microdisc is very small.

The transient after the double layer charging is more complicated, and a complete description of the evolving current goes beyond the scope of this work. Suffice to say these features seem common to each of the mesoporous metals when deposited onto microelectrodes in this way.

This differs from mesoporous metal growth on macroelectrodes where a much larger charging current is seen initially which then slowly decreases with time as the metal salt is depleted (NB a limiting current is never obtained since the solution is too viscous to allow convection).

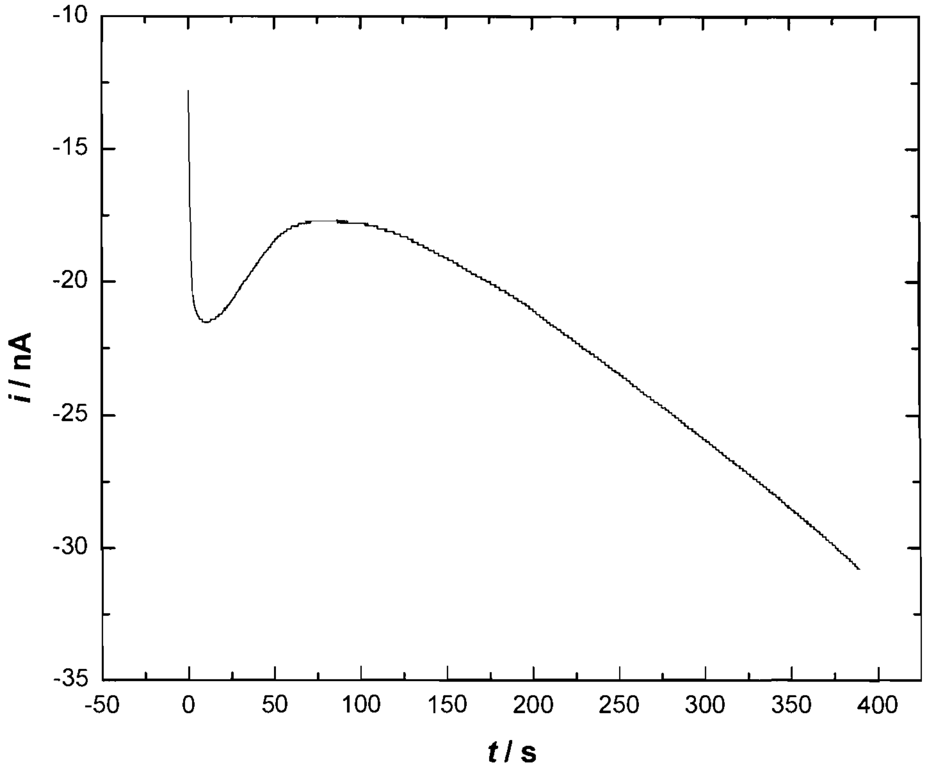

Figure 2. Chronoamperometry for deposition of mesoporous rhodium onto a 25 μm polished platinum disc. Deposition potential of -0.09 V vs SCE applied after pulsing the working electrode to +0.6 V for 1 s. Plating mixture consisting of $RhCl_3$, Brij® 56, n-heptane and water (12, 47 and 39 and 2 % by weight respectively).

In each case current was applied until sufficient charge had been passed to deposit a film of approximately half a micron thickness (for platinum $Q = 15.7$ μC, palladium $Q = 5$ μC, rhodium $Q = 8.68$ μC). The charge required for platinum is considerably higher; due to the use of the platinum(IV) complex the Faradaic efficiency is much lower. This is particularly true at microelectrodes where diffusion is fast and the first reduction product (Pt(II)) can be lost before complete reduction to Pt(0).

After deposition the surfactant was removed by soaking the electrode in a stirred beaker of water. The metal that remains has an architecture that is the inverse of the hexagonal template. Electrodes were stored in deionised water at room temperature.

3.2.2 Characterisation of Mesoporous Metal Films by Voltammetry in Acid:

Cyclic Voltammetry in 1 M sulphuric acid was the first step in the characterisation of the mesoporous electrodes since this not only provides information about the surface area and structure, but also removes any vestigial surfactant and generally cleans the nanopores. Below are example voltammograms for mesoporous platinum[20], palladium[24,29] and rhodium[35].

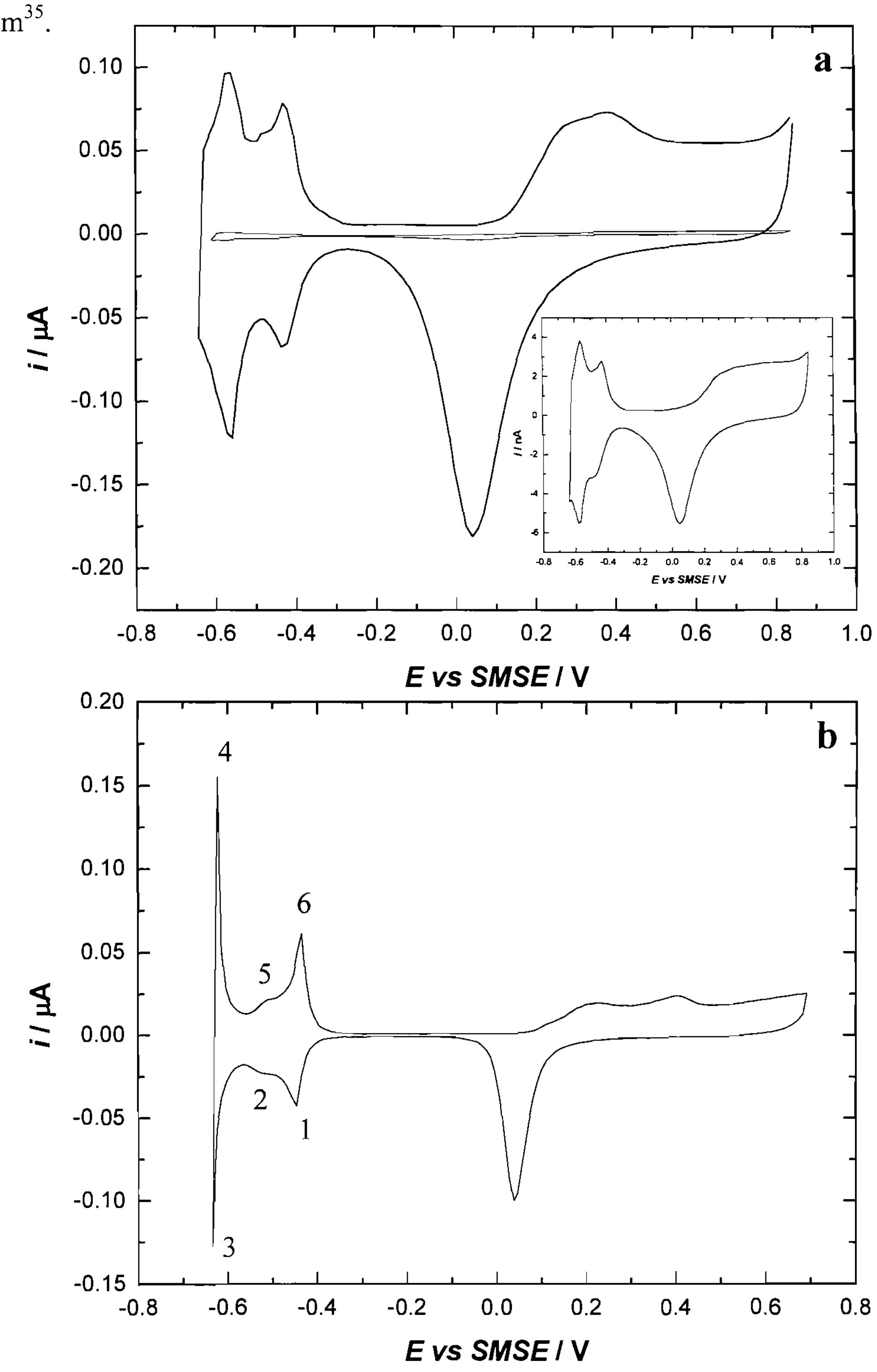

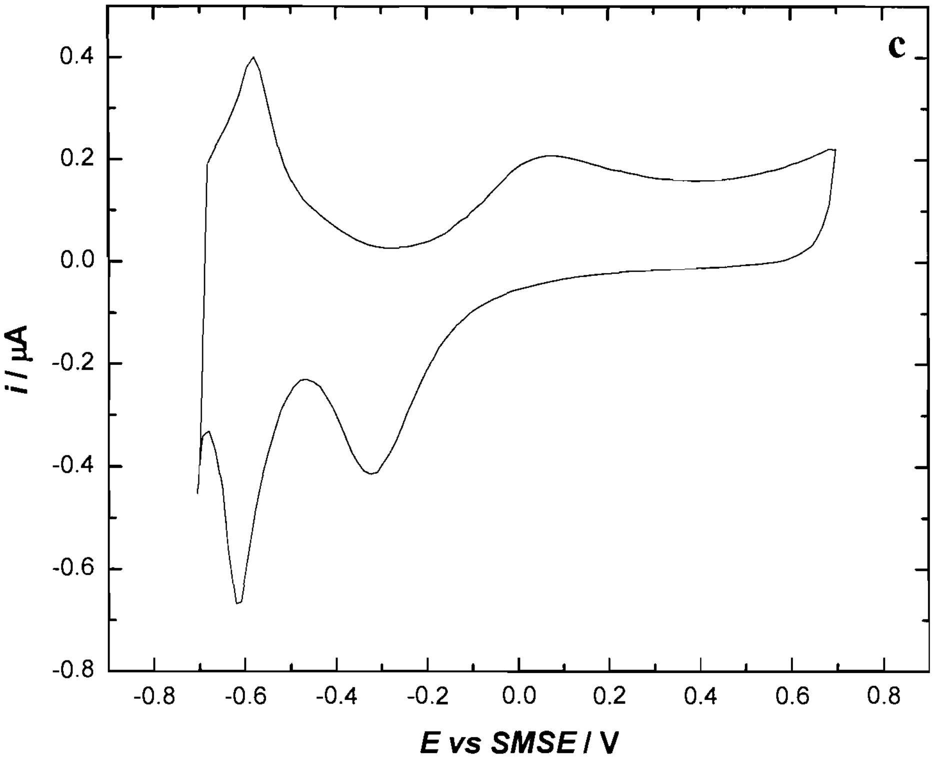

Figure 3. Cyclic voltammetry in 1 M sulphuric acid, 25 °C purged with argon. All WE = 25 µm diameter platinum discs. a) Thick line: modified with a half micron deposit of mesoporous platinum sweep rate = 200 mV s^{-1}. Thin line (and inset) unmodified, polished platinum disc. b) Modified with a half micron deposit of mesoporous palladium, sweep rate = 20 mV s^{-1}. c) Modified with a half micron deposit of mesoporous rhodium, sweep rate = 200 mV s^{-1}.

For thin mesoporous films such as these it takes 20-30 cycles to fully clean the structure and obtain reproducible voltammograms. The first thing to note is the increased magnitude of the currents recorded at the mesoporous electrodes, e.g. 180 nA for the oxide stripping peak recorded at nanostructured platinum compared to 5.5 nA for a polished electrode of the same size. This is because the main features of the voltammogams are due to surface processes so the high currents reflect the high surface areas of the nanostructured deposits.

The features of the mesoporous platinum voltammogram are essentially the same as those of polycrystalline platinum (see inset figure 3a). On the anodic sweep, starting at the negative potential limit of -0.65 V, the first features are for the desorption of hydrogen from the platinum surface. This is mirrored on the cathodic sweep in the same potential range (-0.3 to -0.65 V) by hydrogen adsorption. There appear to be two peaks for the adsorption (and corresponding desorption) of hydrogen, which are much better resolved for the mesoporous platinum. In fact there are actually three convoluted peaks for the adsoption/desoption processes, corresponding to adsorption/desorption on different crystal planes[121,122].

Continuing the anodic sweep beyond hydrogen desorption the current falls and is constant between ≈ -0.2 V and +0.1 V. This background current is due to double layer charging of the electrode surface. The current increase at + 0.2 V is due to oxidation of the platinum surface. If the potential is taken beyond the positive limit of + 0.85 V the bulk oxide may form and electrolysis of the solution would begin with evolution of oxygen. When the cathodic sweep begins there is a delay before the platinum oxide is reduced (most of the reduction charge being passed between + 0.3 V and - 0.1 V). This is unusual for a surface process, where oxidation and reduction generally occur in the same potential window having symmetrical anodic and cathodic voltammetry (see hydrogen adsorption/desorption). It is thought that this asymmetry in the platinum oxidation and reduction is due to exchange of platinum and oxygen atoms in the oxide film[123].

The mesoporous palladium voltammetry (figure 3b) differs from the platinum mainly in that hydrogen adsorption/desorption is complicated by absorption of hydrogen into the bulk metal. There is a very sharp pair of peaks at - 0.45 V (denoted as 1 and 6 in figure 3b) with a smaller broader pair at - 0.52 V (2 and 5) and then the reduction current increases rapidly at the cathodic limit associated (3) with the anodic peak at - 0.625 V (4) (NB voltammetry of unstructured palladium is broader and unresolved in this region). A more complete discussion of the mesoporous palladium voltammetry has been presented by Bartlett *et al.*[29], where the peaks are assigned as follows:

- Peaks 1 and 6, due to hydrogen adsorption and desorption respectively.
- Peak 2, reduction of protons leading to formation of the α–hydride phase.
- Peak 3, further absorption of hydrogen forming the β–hydride phase.

- Peak 4, oxidation of the β–hydride phase.
- Peak 5, oxidation of the α–hydride phase.

As for platinum, the voltammetry for mesoporous rhodium is essentially the same as that of unstructured rhodium[28]. Oxidation occurs at a slightly lower overpotential than at platinum or palladium and shows a similar shape and similar delay in the stripping peak on the cathodic sweep. However the exact position of the rhodium oxide stripping peak depends, to some extent, on the acid concentration, sweep rate and the number of previous cycles. Once again the peak pair towards the lower potential limit (-0.625 V) is due to hydrogen adsorption and desorption. While adsorbed hydrogen is thought to exist in two distinguishable forms, these are not resolved in dilute (< 5 M) acid and only the weakly adorbed hydrogen is seen.

The surface areas of the electrodes were estimated from the voltammograms. In the case of platinum this was calculated from the charge under the hydrogen desorption peaks using the conversion factor 210 μC cm^{-2} [20]. For palladium and rhodium the charge under the oxide stripping peaks was used (conversion factors 424[124] and 660[28] μC cm^{-2} respectively). This gives roughness factors of 77, 173 and 156 for the (platinum, palladium and rhodium respectively) electrodes in figure 4 above which is typical for films of this thickness with a continuous hexagonal structure.

For a perfect hexagonal array of cylindrical pores the volumetric surface area (f) can be calculated, from equation 1, as follows[22]:

$$f = 4\pi r/\sqrt{3}(2r + w)^2 \qquad \mathbf{1}$$

Where r = pore radius (1.25 nm), and w = wall thickness (2.5 nm) then $f = 0.36 \times 10^7$ cm^2 cm^{-3}. Hence the deposition efficiencies were estimated from the observed surface areas as 43 %, 87 % and 96 % for platinum, rhodium and palladium respectively. The Faradaic efficiency for H_I-ePt deposition has previously been estimated as 75 %[21]. One of the reasons for the low efficiency is the use of a platinum(IV) salt in the plating mixture; this means that reduction to platinum metal proceeds via a platinum(II) intermediate as described by Gollas *et al.*[23]. Diffusion of the intermediate Pt(II) away from the electrode reduces the plating efficiency, and this is exacerbated at microdiscs due to their increased rate of mass transport as reported by Elliott *et al.*[20].

3.2.3 Characterisation of Mesoporous Metal Films by ESEM:

A Philips XL30 environmental scanning electron microscope was used to image the surface of the mesoporous electrodes.

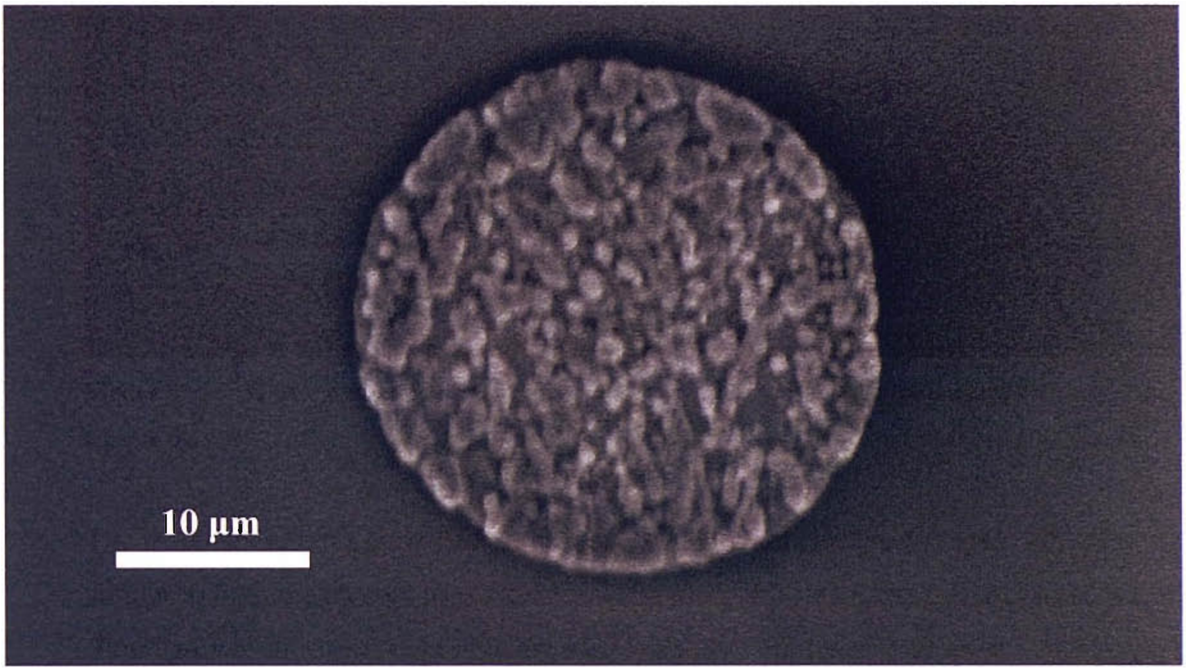

Figure 4. ESEM image of a 25 μm polished platinum disc after deposition of a mesoporous rhodium film. Charge passed = 6 μC.

The result shown in figure 4 for a mesoporous rhodium electrode is quite typical and very similar to both the mesoporous palladium and platinum electrodes (although the palladium films grown in these experiments were slightly smoother and more uniform). It is important to note that the diameters of the electrodes are altered by deposition of the nanostructured films. For the electrode depicted above ∅ = 28.3 μm compared to 25.5 μm for the polished platinum substrate. In general the observed diameters of the polished platinum microdiscs used here were between 25 and 26.5 μm. However the diameter of the mesoporous films increases with the deposition charge. This is due to the edge effect seen at microelectrodes and discussed in more detail in Chapter 5.

For mesoporous palladium and rhodium films of around half a micron height the increase in electrode diameter was about 2-3 μm (this is born out by voltammetry in ruthenium hexaamine which was also used to investigate the electrode diameters before and after deposition 3.2.4). The deposition efficiency of mesoporous platinum was a lot lower than expected and consequently the films were often thinner than 0.5 μm, and the increase in diameter was less (0.5-1 μm).

3.2.4 Characterisation of Mesoporous Metal Films by Voltammetry in Ruthenium Hexaamine Solution:

The mass transport limited current at a microdisc (i_L) scales linearly with the radius (a) of the electrode (equation 2):

$$i_L = 4nFDca \qquad \mathbf{2}$$

Where:

D = the diffusion coefficient of redox species.
n = the number of electrons involved in the reaction (1e$^-$ for $Ru(NH_3)_6^{+3}$ to $Ru(NH_3)_6^{+2}$).
F = Faraday constant (96485 C mol^{-1}).
c = the concentration of the redox species.

Therefore voltammetry of simple, reversible, one-electron redox species such as ruthenium hexamine and ferrocene carboxylic acid can be used to estimate the radius of a microdisc electrode.

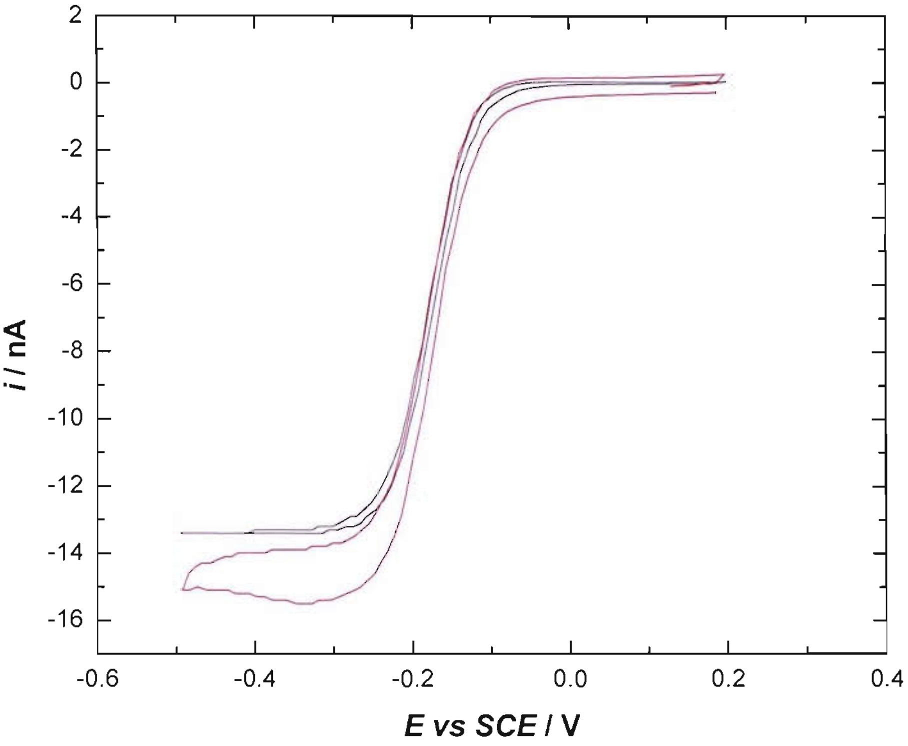

Figure 5. cyclic voltammetry in 3.1 mM ruthenium hexaamine/0.2 M potassium chloride solution (purged with argon for 20 minutes, *T*=25 °C). Sweep rate = 5 mV s^{-1}. **Black line**: WE = polished platinum microdisc, 25 μm diameter. **Red line**: WE = polished platinum microdisc, 25 μm diameter with 0.5 μm mesoporous platinum film.

The hysteresis for the mesoporous electrodes is always greater due to their high surface areas and therefore increased charging currents. However there is an additional current seen on the cathodic sweep, which causes a peak at -0.35 V. This is discussed in detail in Chapter 5. The limiting currents were taken at -0.45 V. This was estimated for the mesoporous electrode by subtracting the charging current (i.e. the plateau of the anodic sweep at +0.1 V) from the anodic current observed at -0.45 V. By comparison of the currents recorded at mesoporous electrodes, with those recorded at two polished electrodes (a = 12.5 μm) the diameters of the mesoporous deposits could be calculated from the difference.

3.3 Hydrogen Peroxide Electrochemistry

3.3.1 Comparison of Mesoporous and Polished Pt:

Below are cyclic voltammograms recorded with mesoporous and polished platinum microdiscs in 5 mM hydrogen peroxide in 0.1 M sodium phosphate buffer (pH 7.4). The voltammogram recorded at the mesoporous electrode is typical and very reproducible; whereas voltammograms recorded at polished platinum are not stable or reproducible. This is because the degradation of hydrogen peroxide at platinum (and indeed most other substrates[125]) is very sensitive to poisoning.

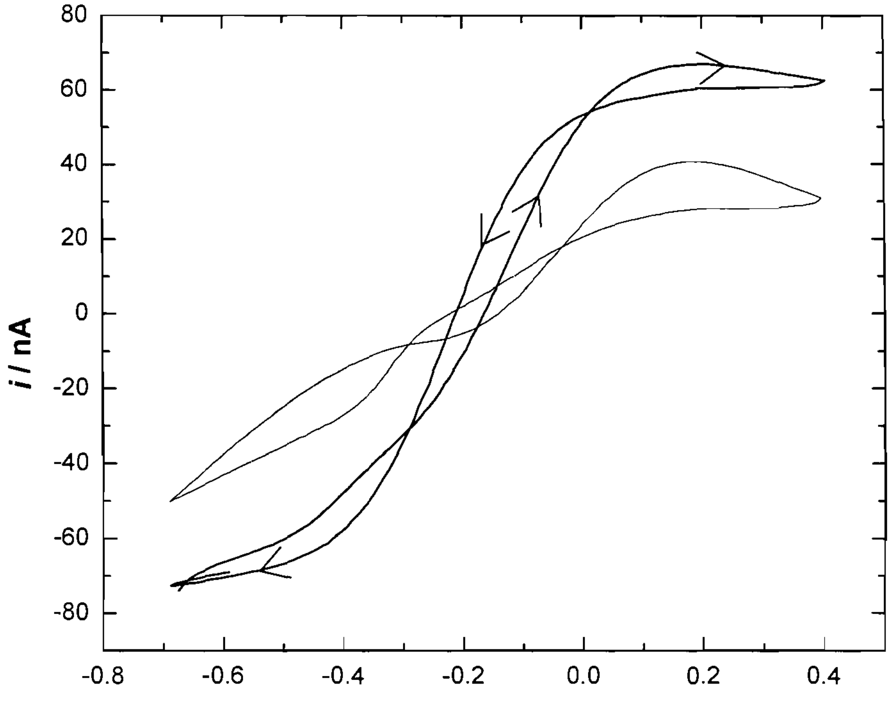

Figure 6. Cyclic voltammetry in 5 mM hydrogen peroxide, 0.1 M sodium phosphate buffer pH 7.4, $T = 25$ °C. Sweep rate = 2 mV s^{-1}. The direction of the sweep is indicated by the arrows on the thick line. **Thin line**: WE = polished platinum microdisc, 25 μm diameter. **Thick line**: WE = polished platinum microdisc, 25 μm diameter with 0.5 μm mesoporous platinum film.

It is important to note that the decomposition of hydrogen peroxide at platinum is a chemical process and the current is due to oxidation and reduction of the metal surface. In fact there are two simultaneous chemical reactions occurring:

$H_2O_2 \rightarrow 2e^- + O_2 + 2H^+$ (1)

$H_2O_2 + 2H^+ + 2e^- \rightarrow 2H_2O$ (2)

Where the current is zero (E = -0.2 V vs SMSE) the two processes are proceeding at equal and opposite rates. At potentials more positive than -0.2 V, reaction 1 becomes more favourable and dominates, and at potentials more negative reaction 2 is favourable.

3.3.2 The Hall Mechanism:

The hysteresis in the voltammogram is unusual in that the cathodic and anodic sweeps cross over each other. The reason for this becomes clearer by considering the mechanism of hydrogen peroxide breakdown at a platinum surface as proposed by Hall *et. al.*[120] which is similar to that previously proposed for palladium[126]:

$H_2O_{2(bulk)} \rightarrow H_2O_{2(surface)}$ (3)

$H_2O_2 + Pt(OH)_2 \rightleftharpoons Pt(OH)_2.H_2O_2$ (4)

$Pt(OH)_2.H_2O_2 \rightarrow Pt + 2H_2O + O_2$ (5)

$Pt + 2H_2O \rightarrow Pt(OH)_2 + 2H^+ + 2e^-$ (6)

The ratio of oxidation to reduction of hydrogen peroxide (reaction 1 and 2 respectively) is dependant on the surface state of the platinum; with the oxidised platinum surface ($Pt(OH)_2$) being conducive to hydrogen peroxide oxidation (reaction 5) and the un-oxidised (Pt(0)) surface being conducive to hydrogen peroxide reduction. However the oxidised platinum surface, represented by Hall *et. al.* as $Pt(OH)_2$, is likely to be the "place exchange oxide"[123]. Therefore the oxide stripping is delayed by the exchange of the atoms at the electrode surface (see figure 3) and this leads to continued hydrogen peroxide oxidation at a lower overpotential on the cathodic sweep. This is what causes the anodic and cathodic volatmmograms to cross over each other.

3.3.3 Hydrogen Peroxide Calibration Curves:

The current response of mesoporous and polished platinum microdiscs to increasing hydrogen peroxide concentration is shown in figure 7.

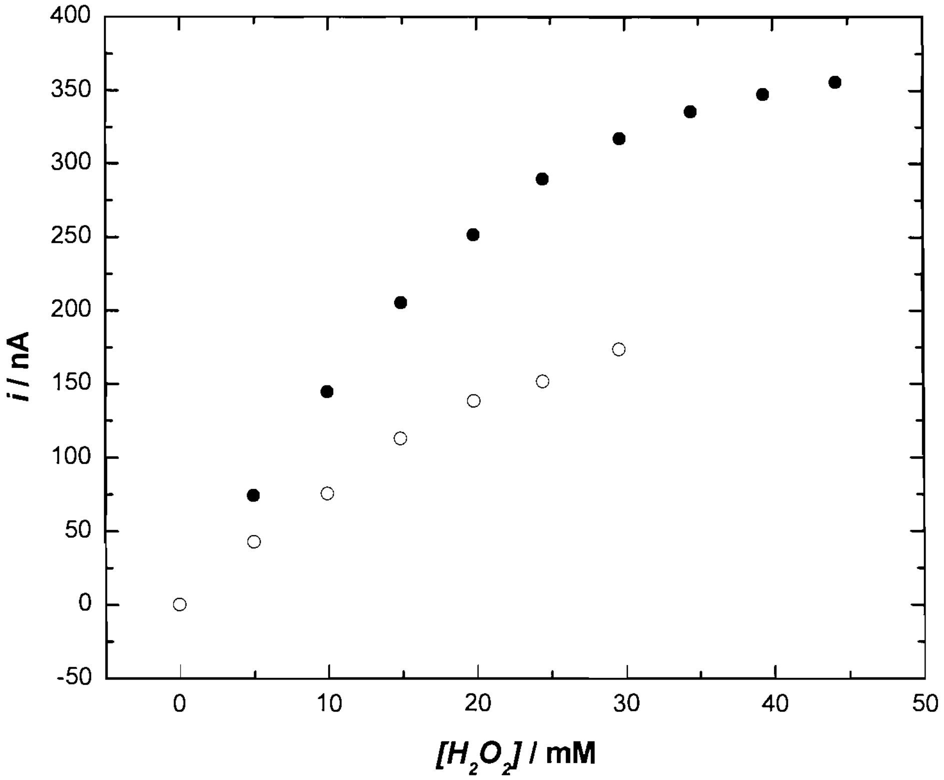

Figure 7. Calibration curve obtained from chronoamperometry in 10 ml 0.1 M sodium phosphate buffer, pH 7.4, *T*=25 °C. WE held at 0 V vs SMSE for 20 min before aliquots of 2.5 M hydrogen peroxide were added at three minute intervals (solution stirred during addition). •) WE = polished platinum microdisc, 25 µm diameter with 0.5 µm mesoporous platinum film. o) WE = polished platinum microdisc, 25 µm diameter.

As implied by the Hall mechanism the oxidation of hydrogen peroxide is limited at higher concentrations by the number of available platinum sites. However the current response is only linear over a low concentration range (< 10-15 mM hydrogen peroxide) even at the mesoporous electrode which has approximately 100 times the surface area of its polished counterpart[4]. This is explained by Hall *et al.*, who suggest that the oxidation of hydrogen peroxide is inhibited by two competing side reactions:

---

[4] Note that in the work of Evans *et al.*[5] the increased linear range for the mesoporous electrode was even more pronounced due to the fact that there experiments were performed in argon purged solutions.

1) Competitive binding of dioxygen to the Pt(II) binding sites.

$Pt(OH)_2 + O_2 \rightleftharpoons Pt(OH)_2.O_2$ (7)

2) Reversible protonation of the Pt(II)/H_2O_2 complex, where the protons are the product of reaction (5).

$Pt(OH)_2.H_2O_2 + H^+ \rightleftharpoons Pt(OH)_2.H_2O_2.H^+$ (8)

For polished and mesoporous platinum electrodes of the same diameter in the same solution of hydrogen peroxide the voltammetric currents observed are consistently lower for the polished electrodes. This can also be explained by the Hall mechanism. Consider the steps (3-6) involved in hydrogen peroxide oxidation:

$H_2O_{2(bulk)} \rightarrow H_2O_{2(surface)}$ (3)

Mass transport of hydrogen peroxide; controlled in this case by diffusion to the electrode surface.

$H_2O_2 + Pt(OH)_2 \overset{K_1}{\rightleftharpoons} Pt(OH)_2.H_2O_2$ (4)

Adsorption of hydrogen peroxide, where the adsorption constant K_1 is given by equation 3:

$$K_1 = \theta_{Pt(OH)_2H_2O_2} / [H_2O_2]\theta_{Pt(OH)_2} \qquad \textbf{3}$$

Where θ_i refers to the fractional surface coverage of the species i.

Following adsorption, the complex undergoes internal electron transfer and the products are released back into solution:

$Pt(OH)_2.H_2O_2 \xrightarrow{k_2} Pt + 2H_2O + O_2$ (5)

The observed current is due to the electrochemical regeneration of the Pt(II) site:

$Pt + 2H_2O \xrightarrow{k_3} Pt(OH)_2 + 2H^+ + 2e^-$ (6)

If a sufficiently anodic potential is applied at the electrode then step 6 is very fast (the proportion of Pt (0) sites approaches zero) and therefore not rate limiting. The steady state rate (j) will be determined by the internal electron transfer and break down of the surface complex (equation 4).

$$\Rightarrow j = k_2 N \theta_{Pt(OH)_2.H_2O_2} \qquad \mathbf{4}$$

where N is the number of binding sites per m^2.

For a mesoporous platinum electrode with a roughness factor of 100 there will be 100 times more surface sites and the rate of oxidation will be much faster and less sensitive to poisoning. In this case it is diffusion of hydrogen peroxide to the electrode surface that is the limiting factor.

3.3.4 Reduction of Hydrogen Peroxide:

There have been many studies of hydrogen peroxide reduction at monovalent metals (such as silver[127] and copper[128-131]) where the mechanism proposed involves oxidation of the metal during chemical decomposition of hydrogen peroxide, followed by electrochemical reduction of the metal. In the case of copper cathodes hydrogen peroxide reacts chemically with Cu(I) surface oxide to produce Cu(II) and water and the Cu(II) is then electrochemically reduced back to Cu(I):

$Cu_2O + H_2O_2 \rightarrow 2CuO + H_2O$ (9)

$2CuO + H_2O + 2e^- \rightarrow Cu_2O + 2OH^-$ (10)

There would appear to be no such broadly accepted mechanism published for the reduction of hydrogen peroxide at platinum metals (although this is also a well established method for amperometric measurement at platinum[132] and palladium[133]). There is however a lot of literature on the reduction of aqueous dioxygen at platinum, where hydrogen peroxide is widely believed to be an intermediate product. Anderson and Albu[134,135] have performed an analysis of activation energies for the reduction of oxygen to water, and propose intermediates which they have found to be energetically stable:

$$\text{Pt-O}_2 + \text{H}^+ + \text{e}^- \rightarrow \text{Pt-OOH} \qquad (11)$$

Surface specific adsorption of dioxygen is followed by a one electron reduction.

$$\text{Pt-OOH} + \text{H}^+ + \text{e}^- \rightarrow \text{Pt-OHOH} \qquad (12)$$

Reduction of dioxygen complex to the intermediate hydrogen peroxide.

$$\text{Pt-OHOH} + \text{H}^+ + \text{e}^- \rightarrow \text{Pt-OH} + \text{H}_2\text{O} \qquad (13)$$

Increased stability of Pt-OH relative to free ·OH lowers the activation energy of this 1 electron reduction step.

$$\text{Pt-OH} + \text{H}^+ + \text{e}^- \rightarrow \text{Pt-OH}_2 \qquad (14)$$

Formation of platinum oxide (analogous to that involved in hydrogen peroxide oxidation, reactions 5 and 6).

In the case of hydrogen peroxide reduction we are really only concerned with steps 13 and 14. Where step 13 would start with the surface specific adsorption of hydrogen peroxide at Pt(0). Anderson and Albu propose adsorption of hydrogen peroxide to platinum through bonding to one of the hydrogen peroxide oxygens.

Since the reduction of hydrogen peroxide is thought to be a chemical process then perhaps reactions 13 and 14 should be thought of as internal electron transfers within the platinum-hydrogen peroxide complex (as in reaction 5 for oxidation). The catalytic cycle can then be completed by electrochemical reduction of the platinum oxide (product of reaction 14):

$$\text{Pt-OH}_2 + 2e^- \rightarrow \text{Pt(0)} + H_2O \qquad (15)$$

This is analogous to the mechanism, proposed by Hall *et al.*, for hydrogen peroxide oxidation.

3.3.5 Comparison of Platinum and Palladium:

As already discussed above, oxidation of hydrogen peroxide at platinum and palladium are believed to occur through similar mechanisms. The voltammetry of these two metals in hydrogen peroxide solution is consequently very similar. Figure 8 shows a typical voltammogram for mesoporous palladium in hydrogen peroxide (condition as in figure 6).

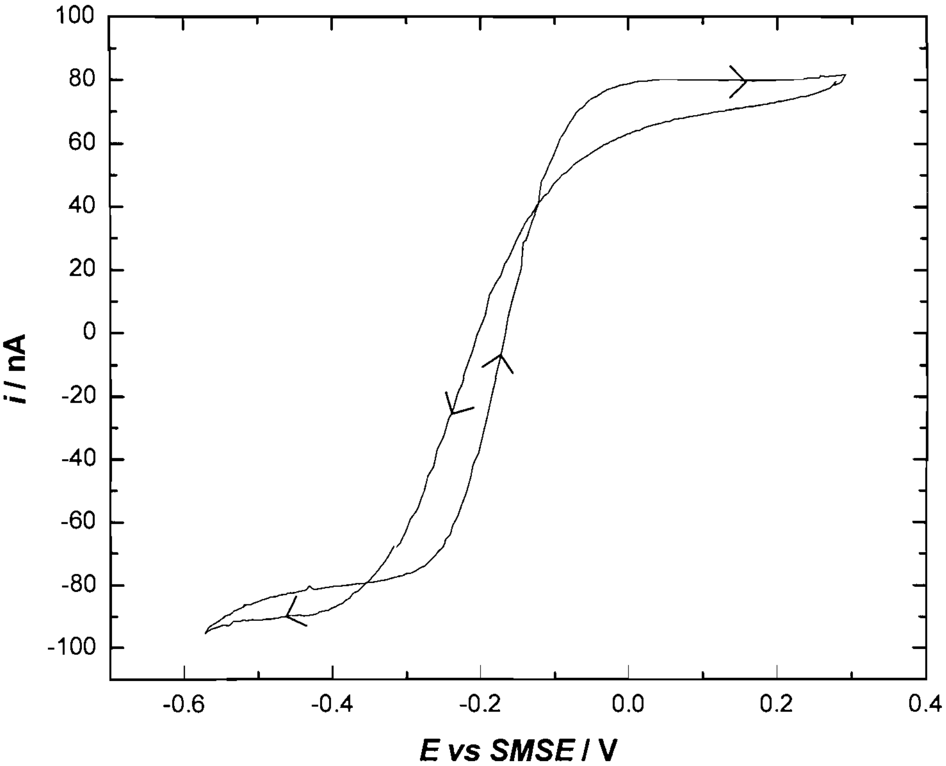

Figure 8. Cyclic voltammetry in 5 mM hydrogen peroxide, 0.1 M sodium phosphate buffer pH 7.4, T = 25 °C. Sweep rate = 2 mV s^{-1}. WE = polished platinum microdisc, 25 μm diameter with 0.5 μm mesoporous palladium film.

The similarities between mesoporous platinum (figure 6) and palladium (figure 8) voltammetry in hydrogen peroxide are striking. Both metals show increased catalytic currents and stable response due to high specific surface area. Also the significant features of the voltammograms occur at similar potentials (potential of zero current ≈ -0.19 V for both, positive plateau ≈ +0.02 V and +0.15 V for palladium and platinum respectively). The limits of oxide formation and stripping were investigated by cycling mesoporous platinum and palladium microelectrodes in 0.1 M phosphate buffer (figure 9).

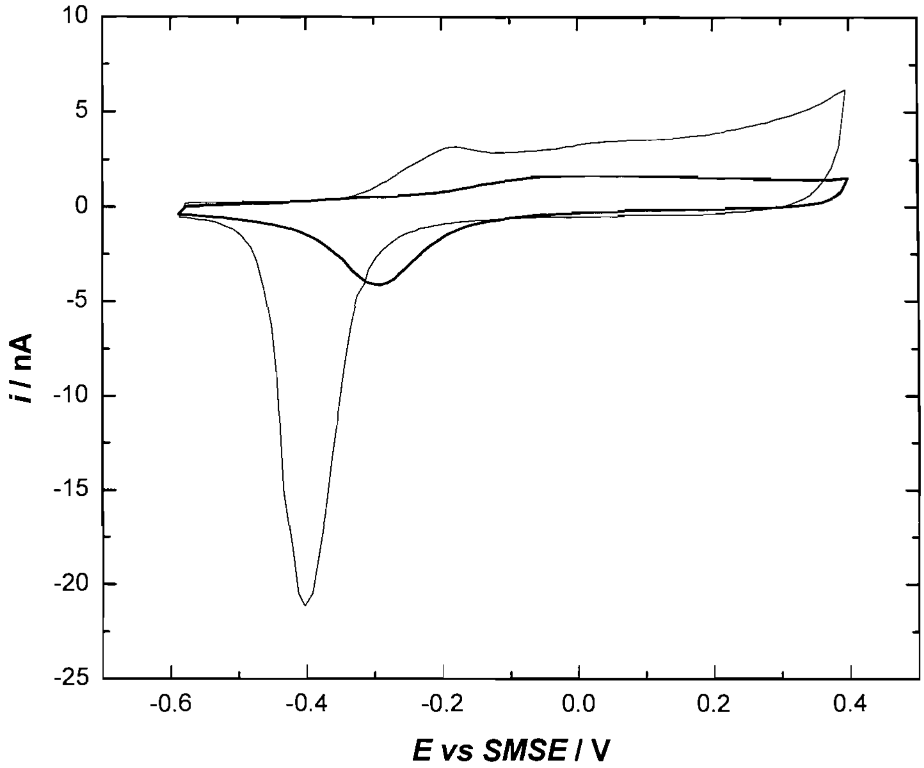

Figure 9. Cyclic voltammetry in 0.1 M sodium phosphate buffer, purged with argon, pH 7.4, T = 25 °C. Sweep rate = 5 mV s^{-1}. **Thin line**: WE = polished platinum microdisc, 25 μm diameter with 0.5 μm mesoporous palladium film. **Thick line**: WE = polished platinum microdisc, 25 μm diameter with 0.5 μm mesoporous platinum film.

Figure 9 shows that metal oxide formation and stripping occurs within the same potential window as oxidation and reduction of hydrogen peroxide (at both platinum and palladium electrodes). The palladium oxide stripping peak is shifted by approximately -0.1 V relative to platinum. The potentials at which the hysteresis, in the hydrogen peroxide voltammetry, cross over are also shifted by -0.1 V for palladium (figure 8) relative to platinum (figure 6); giving weight to the theory that the difference between anodic and cathodic sweeps in hydrogen peroxide is due to the changing oxidation state of the electrode surface.

3.3.6 Comparison of Platinum, Palladium and Rhodium:

Mesoporous palladium and platinum require similar overpotentials to oxidise hydrogen peroxide. This is because hydrogen peroxide oxidises by forming a complex with the metal oxide, and palladium and platinum both start to oxidise at similar potentials. By employing another metal, which oxidises and reduces at different potentials, it might be possible to alter the potentials for the hydrogen peroxide electrochemistry. This could be beneficial in eliminating interference from species such as ascorbate.

With this in mind mesoporous rhodium was investigated. The use of high surface area rhodium for the electrocatalytic detection of hydrogen peroxide has been reported[100]. However in this study rhodium and glucose oxidase were co-deposited onto a carbon fibre microelectrode (7 μm diameter by 5 mm length) to generate the high surface area, catalytic substrate. As far as is known, mesoporous rhodium has previously never been used for hydrogen peroxide electrochemistry.

Hydrogen peroxide voltammetry was recorded at a 25 μm mesoporous rhodium electrode. Initially the same potential range as used for platinum and palladium was employed (figure 10). Two things immediately stand out about the rhodium voltammetry. Firstly there is no clearly defined current plateau for either the oxidation or reduction of hydrogen peroxide. Secondly the hysteresis does not cross over at any point; indicating that the oxidation state of the metal surface is the same throughout.

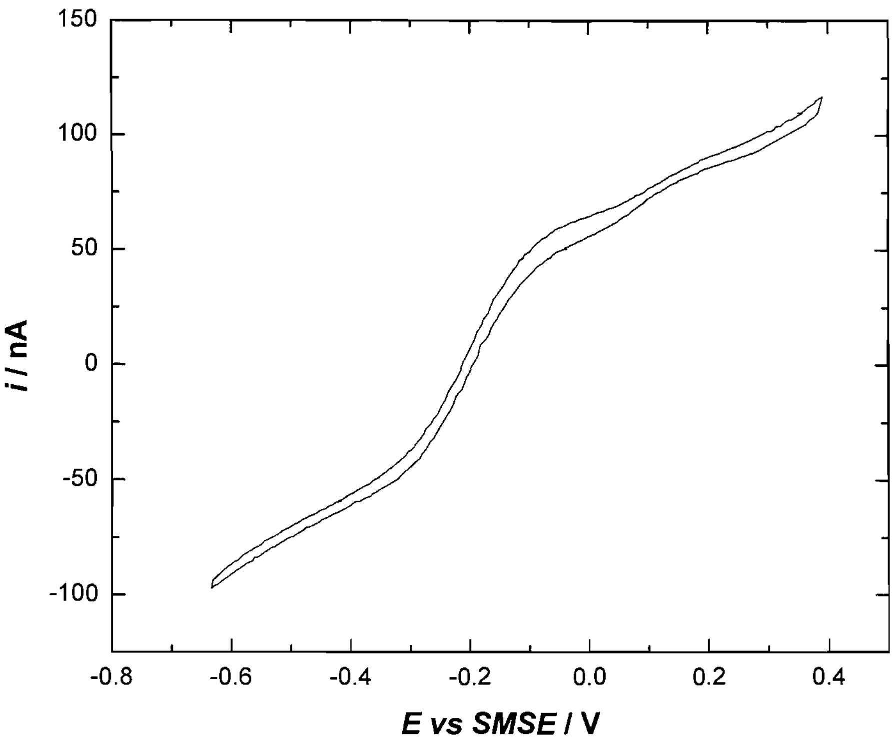

Figure 10. Cyclic voltammetry in 5 mM hydrogen peroxide, 0.1 M sodium phosphate buffer pH 7.4, $T = 25$ °C. Sweep rate = 2 mV s^{-1}. WE = polished platinum microdisc, 25 μm diameter with 0.5 μm mesoporous rhodium film.

It can be seen from experiments in buffer solution (in the absence of hydrogen peroxide) that while rhodium oxidation does occur within the limits of the hydrogen peroxide voltammogram (~ -0.2 V), significant oxide reduction does not (figure 11). In fact there is no discernable cathodic current until ~ -0.5 V.

By extending the limits of the potential sweep in hydrogen peroxide it is possible to alter the surface of the rhodium and a hysteresis cross-over is observed (figure 12). Also, on the subsequent anodic sweep, the plateaus are now well defined and reproducible.

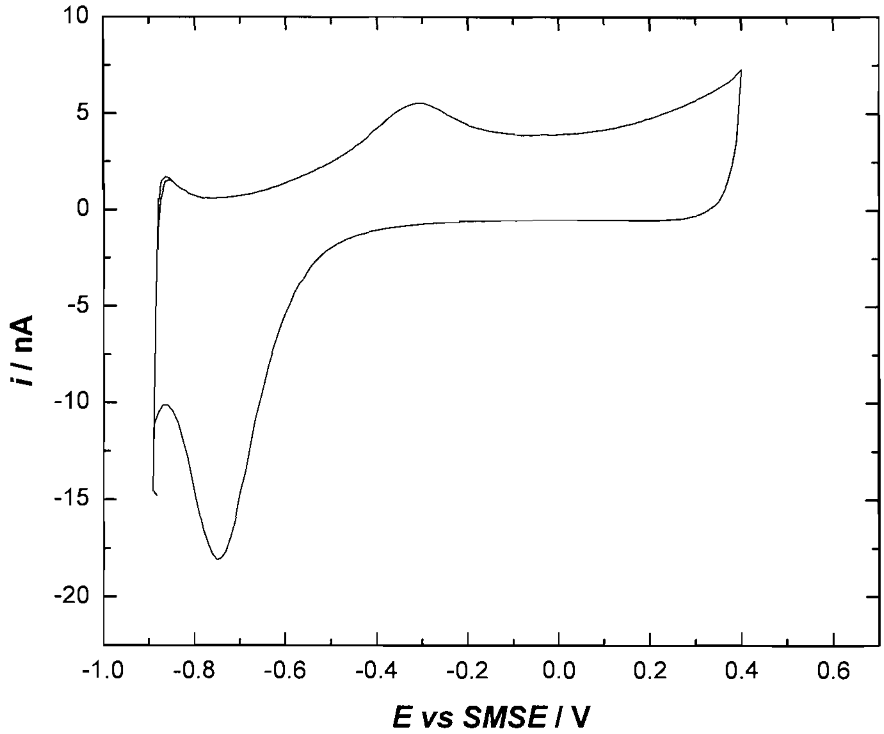

Figure 11. Cyclic voltammetry in 0.1 M sodium phosphate buffer, purged with argon, pH 7.4, T = 25 °C. Sweep rate = 5 mV s^{-1}. WE = polished platinum microdisc, 25 μm diameter with 0.5 μm mesoporous rhodium film.

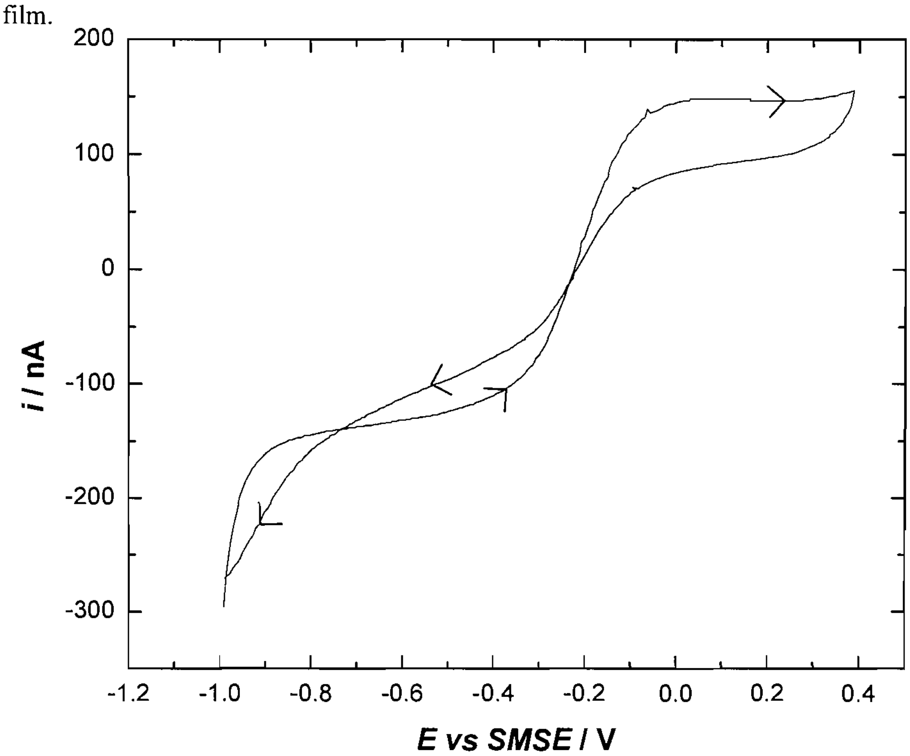

Figure 12. Cyclic voltammetry in 5 mM hydrogen peroxide, 0.1 M sodium phosphate buffer pH 7.4, T = 25 °C. Sweep rate = 2 mV s^{-1}. WE = polished platinum microdisc, 25 μm diameter with 0.5 μm mesoporous rhodium film.

3.3.7 Conclusions:

Mesoporous platinum, palladium and rhodium all show improved hydrogen peroxide electrochemistry (in terms of current, and stability) over their unstructured counterparts (although results are not show for unstructured rhodium, they follow the same pattern as for platinum and palladium). This improvement would seem to be directly related to the increased surface area of these materials.

There is significant evidence to suggest that the degradation of hydrogen peroxide at the electrodes is a chemical process, dependant on the oxidation state of the metal surface (i.e. with a metal oxide being conducive to hydrogen peroxide oxidation, and the metal(0) surface being conducive to reduction), and that the currents observed in the experiments are due to oxidation/reduction of the metal.

Therefore employing a metal with a low oxidation potential should allow hydrogen peroxide oxidation at low overpotential, and this could be beneficial in reducing the effects of interferents. However the metals investigated here all oxidise hydrogen peroxide at similar potentials, so none would seem to offer any obvious advantage for hydrogen peroxide measurement.

3.4 Ascorbate Electrochemisrty

Detection of hydrogen peroxide in biological media such as whole blood is complicated by the presence of other redox species like ascorbate and uric acid (blood concentrations ≈ 50 μM and 400 μM respectively[136]). These all oxidise within the same potential window as hydrogen peroxide at platinum electrodes. It is hoped that the improved catalytic activity seen for hydrogen peroxide oxidation at mesoporous metals will make these interferent species less significant.

3.4.1 Mesoporous and Polished Platinum Voltammetry:

Ascorbic acid is present as the L-ascorbate anion in aqueous solution at pH 7.4. This undergoes a two electron transfer from the platinum surface to form the intermediate dehydro-L-ascorbic acid, which through condensation of water, cyclises to form the final product 2,3-diketogluconic acid (scheme 1[137]).

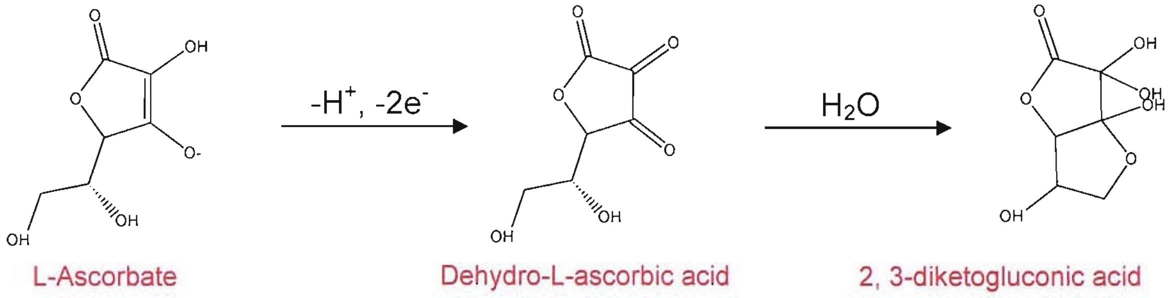

Scheme 1. Reaction scheme for the oxidation of L-ascorbate, and subsequent hydration of the intermediate product.

Figure 13 below shows voltammograms recorded at mesoporous and polished platinum microelectrode in ascorbate solution. This confirms that the oxidation of ascorbate coincides with that of hydrogen peroxide. This result is fairly typical although in some cases the oxidation wave begins somewhat more steeply and reaches a plateau over this range. The results are very sensitive to the state of the metal surface and the age of the ascorbate solution.

The factors affecting the shape of the voltammetry go beyond the scope of this work. However it is worth noting that the oxidation current is not maintained during the cathodic sweep and that there appears to be a wave between -0.35 and -0.45 V (more pronounced at the mesoporous electrode). It is likely that, as with hydrogen peroxide voltammetry, the oxidation state of the metal plays some role in these features. It could be that the place exchange platinum oxide is being formed and this is less efficient at ascorbate oxidation. It is therefore worth noting that the wave, observed between -0.35 and -0.45 V in the cathodic sweep coincides with platinum oxide stripping (see figure 9).

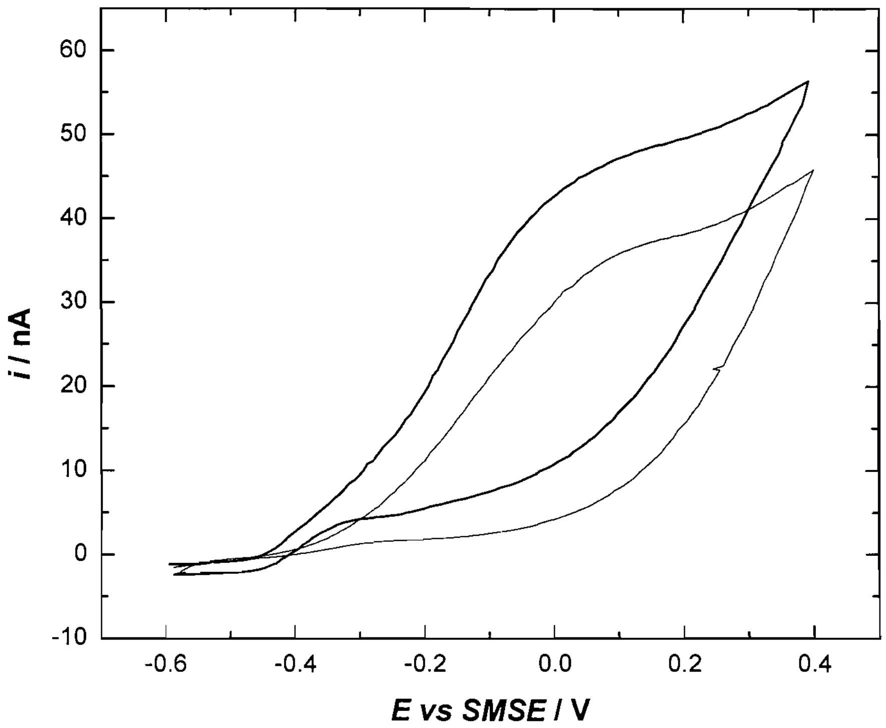

Figure 13. Cyclic voltammetry in 10 mM L-ascorbate, 0.1 M sodium phosphate buffer, pH 7.4, $T = 25$ °C. Sweep rate = 2 mV s^{-1}. **Thin line**: WE = polished platinum microdisc, 25 μm diameter. **Thick line**: WE = polished platinum microdisc, 25 μm diameter with 0.5 μm mesoporous platinum film.

The current response for the mesoporous electrode is slightly greater and initially it was considered that there might be some additional electrochemical process responsible for this e.g. the further oxidation of the intermediate dehydro-L-ascorbic acid or the 2,3-diketogluconic acid product.

This experiment was repeated with mesoporous and polished electrodes ranging in size from 5 μm to 50 μm and the ratio of the limiting currents was never consistent between electrode pairs. So the electrodes were measured using chronoamperometry in ruthenium hexamine solution, and it was found that the current discrepancies between the waves corresponded to the differences in the real radii of the electrode pairs.

It is therefore likely that the higher currents at mesoporous electrodes are simply due to the increased radii of the nanostructured film (see equation 1, 3.2.4 above). To test this idea further chronoamperometry in solutions of varying ascorbate concentration was recorded at mesoporous and polished microelectrodes, ranging in size from 5 to 50 μm (diameter). A plot of i_L versus electrode radius × ascorbate concentration ($a \times c$) was made (figure 14).

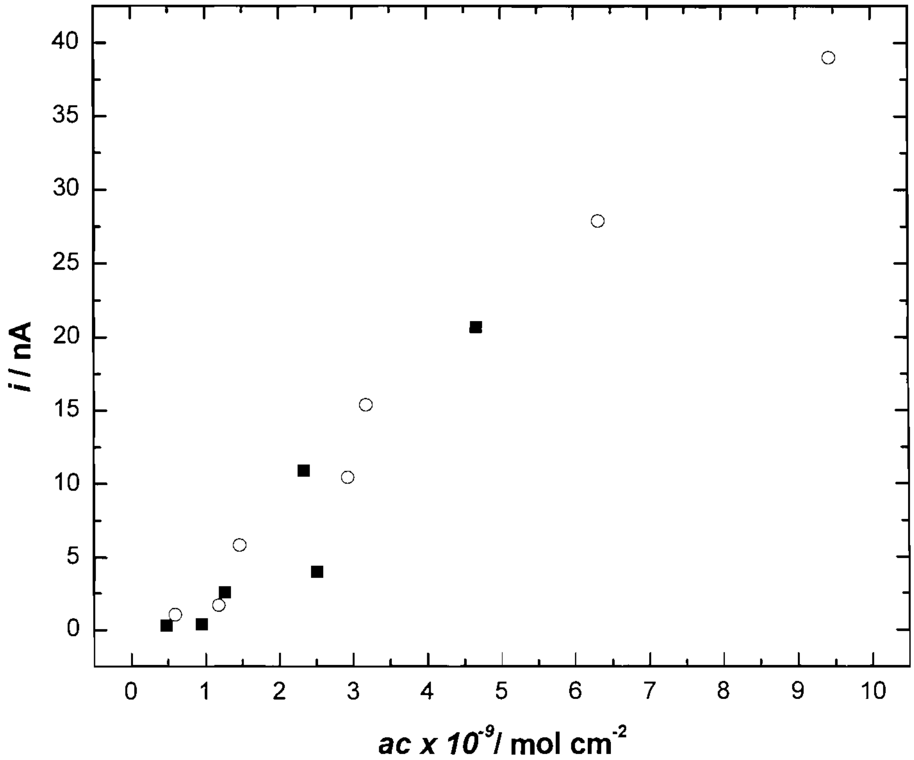

Figure 14. Mass transport limited current for ascorbate oxidation (recorded at microdisc electrodes of various diameters) vs electrode radii (a estimated from ruthenium hexamine voltammetry) × ascorbate concentration. Solution was 0.1 M sodium phosphate buffer, pH 7.4, T=25 °C. Electrodes held at a potential of +0.2 V vs SMSE until current stabilised before adding 50 μL aliquots of 0.2 M L-ascorbte to make desired concentrations.

The gradient of the regressions, for the two sets of data, are roughly the same (4.41 A mol^{-1} cm^2 for the mesoporous electrodes and 4.95 A mol^{-1} cm^2 for the polished electrodes); implying the same number of electrons are involved, in the oxidation processes, at both mesoporous and polished electrodes.

Assuming that the oxidation is a two electron process, it is possible to calculate (from equation 1) the diffusion coefficient for ascorbate in 0.1 M sodium phosphate buffer (pH=7.4, T=25 °C). This gives 5.7×10^{-6} cm^2 s^{-1} from the data recorded at the mesoporous electrodes and 6.4×10^{-6} cm^2 s^{-1} from the data recorded at the polished electrodes. These values are in reasonable agreement to the value of D reported by Bartlett and Wallace[137] ($5.0 \pm 0.4 \times 10^{-6}$ cm^2 s^{-1} for ascorbate in citrate/phosphate buffer of pH=7.0).

3.4.2 Mesoporous and Polished Palladium Voltammetry:

As for hydrogen peroxide, the oxidation of ascorbate at palladium is shifted to slightly less anodic potentials, compared to platinum. The shape of the voltammetry is essentially the same, with the oxidation current 'switching off' on the cathodic sweep. A similar cathodic wave is also seen at the mesoporous electrode between -0.35 and -0.5 V, which again coincides with metal oxide stripping (see thin line figure 9).

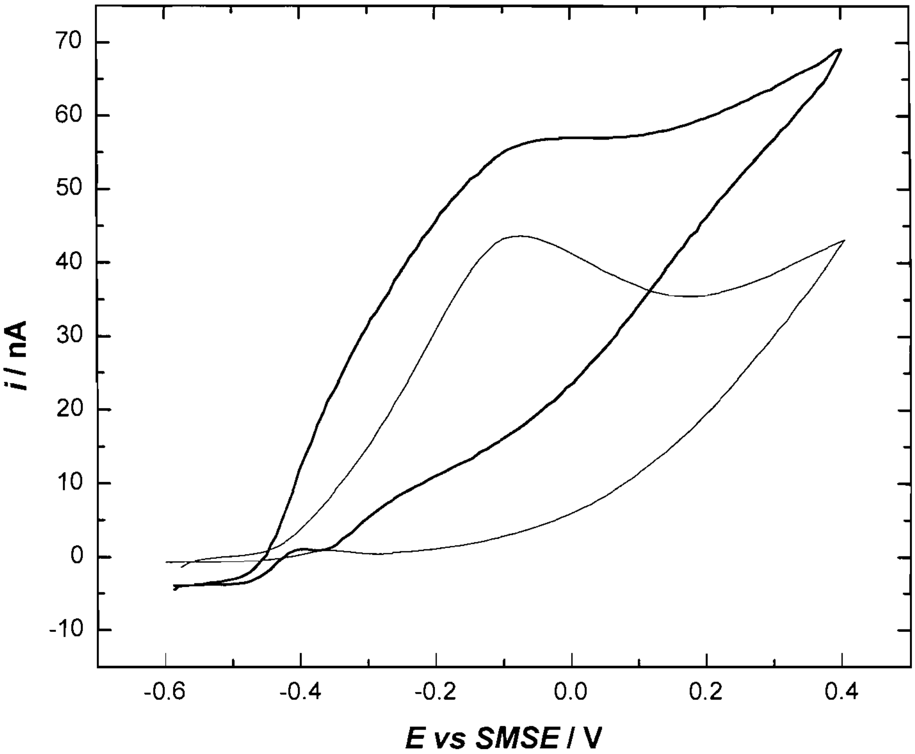

Figure 15. Cyclic voltammetry in 10 mM L-ascorbate, 0.1 M sodium phosphate buffer, pH 7.4, $T = 25$ °C. Sweep rate = 2 mV s^{-1}. **Thin line**: WE = polished platinum microdisc, 25 μm diameter. **Thick line**: WE = polished platinum microdisc, 25 μm diameter with 0.5 μm mesoporous palladium film.

There is some difference between the mesoporous and polished metal (figure 15) in that the current at the mesoporous electrode is significantly greater than that at the polished electrode. Assuming D for ascorbate is 6×10^{-6} cm^2 s^{-1} (estimated by combining the values obtained from the plots on figure 13) and taking the radius of the electrodes to be

12.5×10^{-4} cm; then substitution into equation 2 gives an expected limiting current of 59 nA. this coincides well with the plateau on the mesoporous voltammogram at around -0.05 V vs SMSE. The maximum current at the polished electrode is somewhat lower (~ 44 nA) and this is also much less stable, decaying with each sweep.

3.4.3 Mesoporous and Polished Rhodium Voltammetry:

Once again the current at the mesoporous electrode is significantly greater than that at the polished electrode (figure 16). However the current is now strongly dependent on potential even at the mesoporous electrode. The response at both the nanostructured and polished rhodium electrodes decreased with each sweep in ascorbate solution. No plateau for ascorbate oxidation is seen at more positive potentials (only ever rising current due to electrolysis of water).

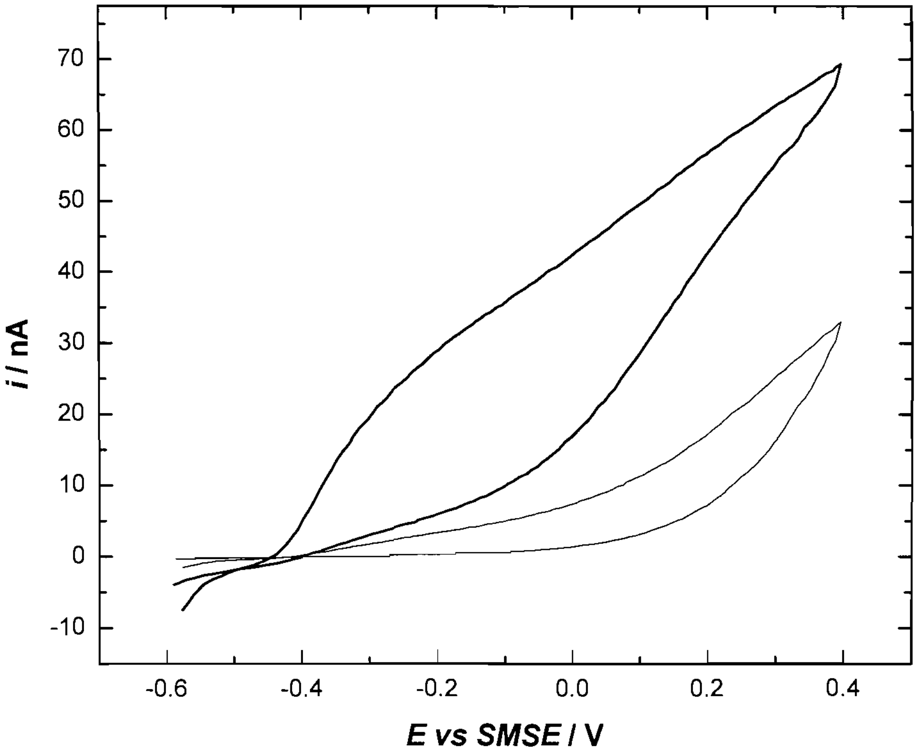

Figure 16. Cyclic voltammetry in 10 mM L-ascorbate, 0.1 M sodium phosphate buffer, pH 7.4, $T = 25$ °C. Sweep rate = 2 mV s^{-1}. **Thin line**: WE = polished platinum microdisc, 25 μm diameter. **Thick line**: WE = polished platinum microdisc, 25 μm diameter with 0.5 μm mesoporous rhodium film.

It would seem that, as for platinum and palladium electrodes, rhodium oxide is less efficient at ascorbate oxidation than Rh(0). Referring back to figure 11, it is clear that rhodium remains oxidised over the potential range used for ascorbate voltammetry here; so this helps explain why the current decreases with successive cycles. It also explains why there is no cathodic wave as seen for platinum (-0.35 and -0.45 V) and palladium (-0.35 and -0.5 V).

3.4.4 Conclusions:

Mesoporous platinum, palladium and rhodium all oxidise ascorbate over the same potential range as hydrogen peroxide; once again there would seem to be no obvious advantage to using one of these materials over the others (at least in terms of glucose detection).

3.5 Glucose Electrochemistry

3.5.1 Non-enzymatic Glucose Detection:

Direct amperometric detection of glucose at platinum[138-140] suffers from two main drawbacks. Firstly the kinetics of glucose oxidation are very sluggish and this leads to low currents; often negligible in the presence of inteferents such as ascorbate or acetamidophenol. Secondly the response is not stable with time due to poisoning of the electrode surface by adsorption of intermediate species.

However it has been shown that the H_I-ePt material can be used to catalyse the electrochemistry of glucose. Park *et al.*[33] reported non-enzymatic glucose detection using mesoporous platinum with sensitivities (dependent on surface area) of 9.6 μA cm^{-2} mM^{-1}, linear response range of approximately 10 mM (normal physiological range 3-8 mM) and good reproducibility in the presence of high chloride ion concentration.

Measurements were made at + 0.4 V vs Ag/AgCl (i.e. + 0.843 V vs SMSE), and while ascorbic acid and acetamidophenol are also oxidisable at this potential, it was found that

0.1 mM (typical physiological concentration 0.1 mM) of each gave negligible current responses compared to the glucose.

In this work direct oxidation of glucose at mesoporous and polished platinum was also studied. Cyclic voltammetry indicated that mesoporous platinum shows a significant response to glucose in the potential range -0.2 to 0 V vs SMSE. At these potentials interference from ascorbate might be further reduced.

Polished and mesoporous platinum microelctrodes were held at potentials ranging from -0.15 to 0 V vs SMSE in 10 ml of 0.1 M sodium phosphate buffer for 20 minutes (sufficient time for the background current to stabilise) before addition of glucose and ascorbate. Figure 17 shows the current time plot for one such experiment.

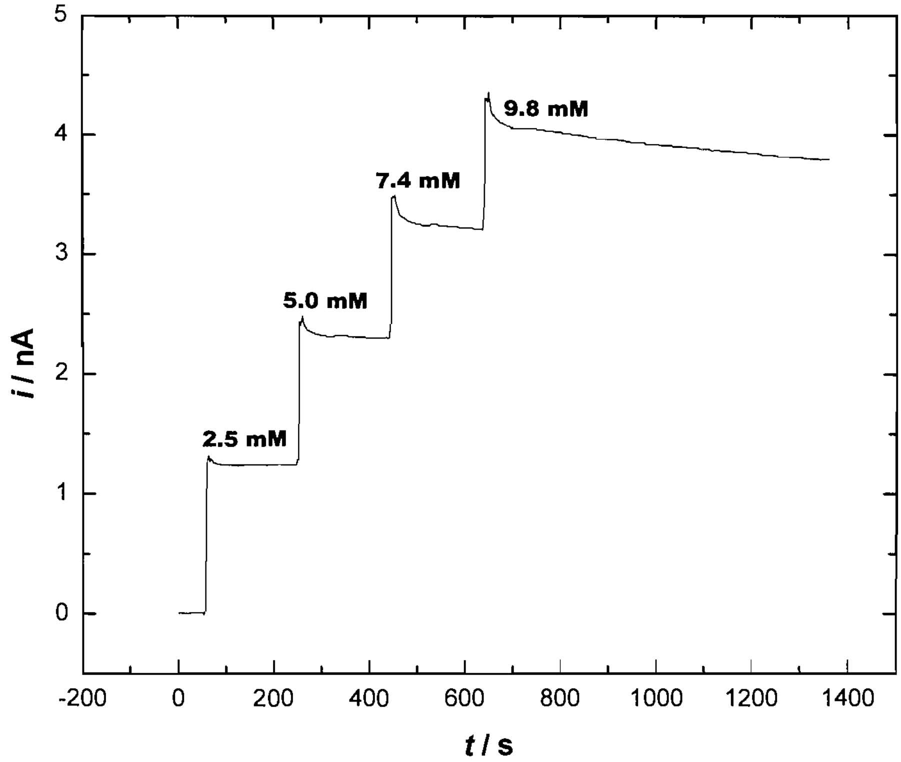

Figure 17. Chronoamperometry in 10 ml 0.1 M sodium phosphate buffer, pH 7.4, *T*=25 °C. WE = 25 μm polished platinum disc with a ~1 μm mesoporous platinum film; held at -0.1 V vs SMSE for 20 minutes before 50 μl aliquots of 0.5 M glucose were added at three minute intervals (solution stirred during addition). Plot corrected for background current -0.41 nA. Glucose concentrations are marked on the plot.

The response of the mesoporous electrode ranged from 440 to 180 pA mM^{-1} of glucose (decreasing at more cathodic potentials). While the ascorbate response at these potentials is reduced from the diffusion limited value it was found to be significant 8.0 – 6.8 nA mM^{-1} ascorbate (typical physiological concentration 0.1 mM).

In each case the current decays with time after addition of glucose showing that poisoning is still a factor with mesoporous platinum. Electrodes were cycled in the buffer (two cycles: -1 to +0.6 V vs SMSE at 50 mV s^{-1}) before the start of each experiment in order to refresh the platinum surface and minimise the effects of poisoning. If experiments were repeated without cleaning the electrode the current response was typically 17-20 % of that for the clean platinum (though this current is more stable). Current decay is also apparent in the current time transients published by Park *et al.* although this is not discussed in their paper. Results are summarised in table 1 below.

E / V	i_{glucose} / pA mM^{-1}	$i_{\text{background}}$ / pA	$i_{\text{decrease over 3 min}}$	$i_{0.1\text{ mM AA}}$ / pA
0.00	440	150	8.8 %	800
-0.05	490	10	8.4 %	770
-0.10	390	-410	3.3 %	720
-0.15	180	-1590	4.0 %	680

Table 1. Current response of a 25 μm diameter mesoporous platinum electrode to glucose and ascorbic acid (AA) at different potentials (measured vs SMSE).

Figure 18 shows a current time transient for glucose oxidation at polished platinum. As reported by Park *et al.* the response of polished platinum to glucose is much less (~ 0.4 - 6.9 %) and is negligible in comparison to the ascorbate current (also shown).

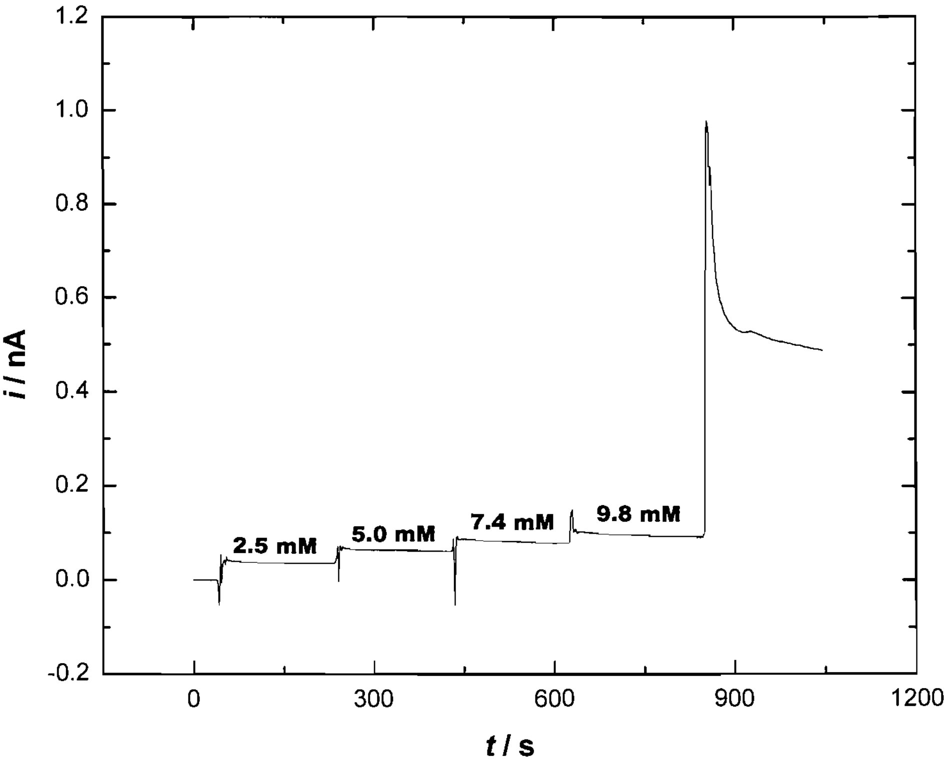

Figure 18. Chronoamperometry in 10 ml 0.1 M sodium phosphate buffer, pH 7.4, T=25 °C. WE = 25 μm polished platinum disc; held at -0.1 V vs SMSE for 20 minutes before 50 μl aliquots of 0.5 M glucose were added at three minute intervals (solution stirred during addition). Addition of 50 μL 0.02 M ascorbate also shown at t = 850 s (i.e. [ascorbate] = 0.1 mM). Background current <0.1 pA. Glucose concentrations are marked on the plot.

The ascorbate response is relatively more significant at the polished electrode due to the low glucose oxidation currents. The unstructured platinum surface is also more sensitive to poisoning and once again the current decreases with time. Results are summarised in table 2.

E / V	i_{glucose} / pA mM^{-1}	$i_{\text{background}}$ / pA	$i_{\text{decrease over 3 min}}$	$i_{0.1\text{ mM AA}}$ / pA
0.00	1.59	2.30	13.3 %	585
-0.05	9.03	2.40	10.4 %	650
-0.10	8.15	<0.1	10.2 %	528
-0.15	12.45	-4.4	8.5 %	400

Table 2. Current response of a 25 μm diameter polished platinum electrode to glucose and ascorbic acid (AA) at different potentials (measured vs SMSE).

3.5.2 Mesoporous and Polished Platinum Voltammetry:

Cyclic voltammetry in phosphate buffer solution containing different concentrations of glucose was used to compare the general response of platinum, palladium and rhodium. Voltammograms at mesoporous and polished platinum microelectrodes are shown in figure 19.

Oxidation of glucose is influenced by many factors including electrolyte composition, pH and temperature; although oxidation at platinum always proceeds in three distinct regions on the anodic voltammogram[141]: the hydrogen region (-0.5 to -0.65 V), the double layer region (-0.4 to -0.2 V) and the platinum oxide region (>-0.2 V). The exact mechanism of glucose oxidation at platinum is unclear although techniques such as Fourier transform infrared reflectance (FTIR) spectroscopy[139] and surface capacitance measurements[142] have provided some insight into the possible intermediates.

What is generally accepted is that the initial chemisorption and dehydrogenation of glucose is linked with the adsorption of hydrogen and that the primary oxidation product is gluconolactone[139-142].

The peaks in the double layer region (-0.3 V) and the platinum oxide region (+0.08 V) are attributed to further oxidation of adsorbed intermediates. This leads to other products including carbon monoxide which poisons the metal, eventually leading to a reduction in response.

The voltammograms for the mesoporous and polished electrodes are essentially the same; although the glucose oxidation currents at mesoporous platinum are more pronounced. Also, the current in the hydrogen region, for polished platinum, is somewhat suppressed at the highest glucose concentration of 20 mM. This might suggest that, once again, increased surface area has a positive influence in reducing the effect of poisoning.

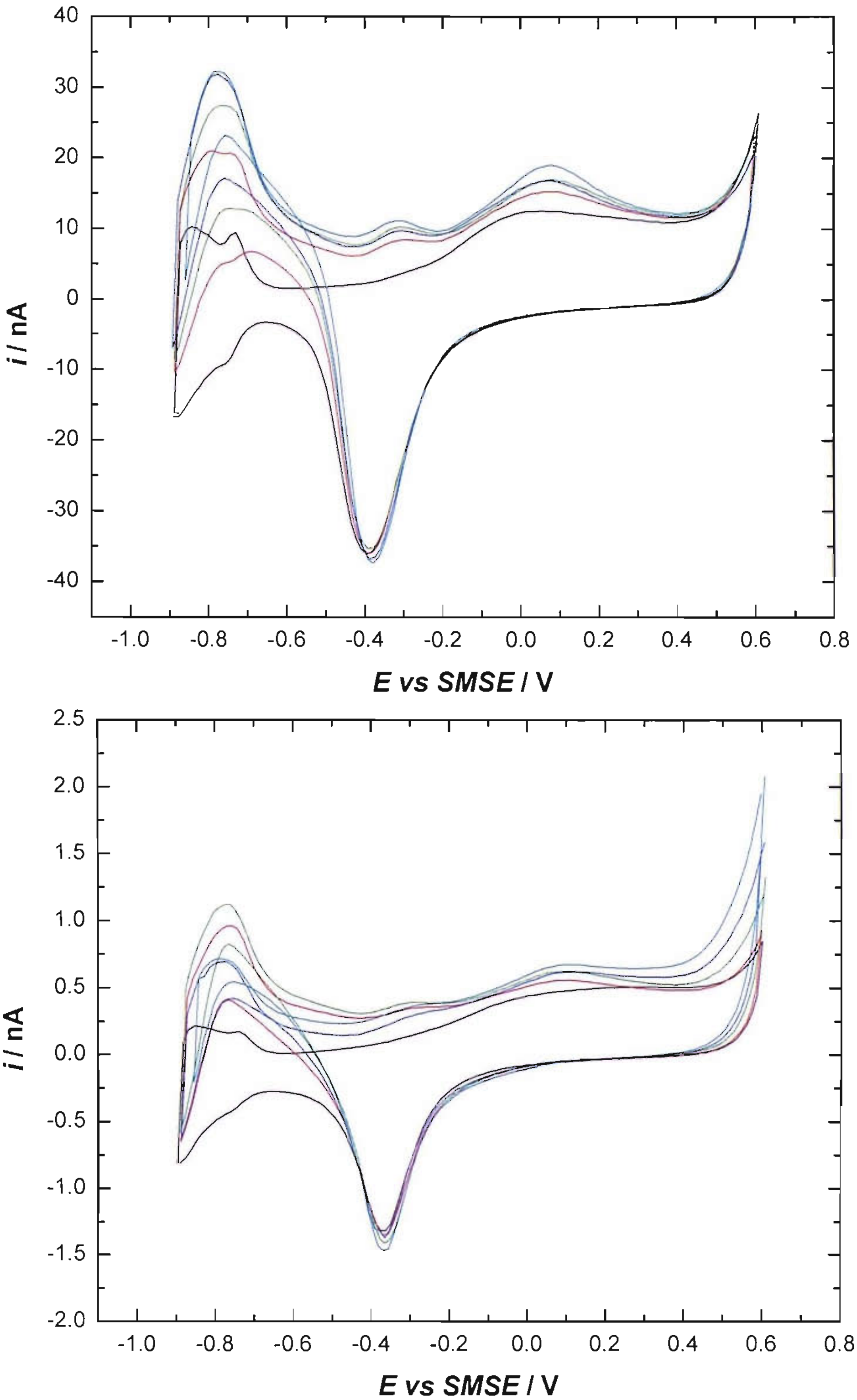

Figure 19. Cyclic voltammetry in 0.1 M sodium phosphate buffer, purged with argon, pH 7.4, T = 25 °C. Sweep rate = 50 mV s^{-1}. **Top**: WE = polished platinum microdisc, 25 μm diameter with 0.5 μm mesoporous platinum film. **Bottom**: WE = polished platinum microdisc, 25 μm diameter. Coloured lines correspond to different glucose concentrations: (—) = 0 mM, (—) = 5 mM, (—) = 10 mM, (—) = 15 mM, (—) = 20 mM.

3.5.3 Mesoporous and Polished Palladium Voltammetry:

Glucose voltammetry at palladium is quite different from that at platinum. Firstly, there is a complete lack of any peak in the double layer region (figure 20). Also, while there is some increase in current in the palladium oxide region as glucose concentration is increased, the peak here is much less pronounced than in the platinum voltammetry (figure 19).

Once again the current in the hydrogen region, for the polished microdisc, is somewhat suppressed at the highest glucose concentration of 20 mM.

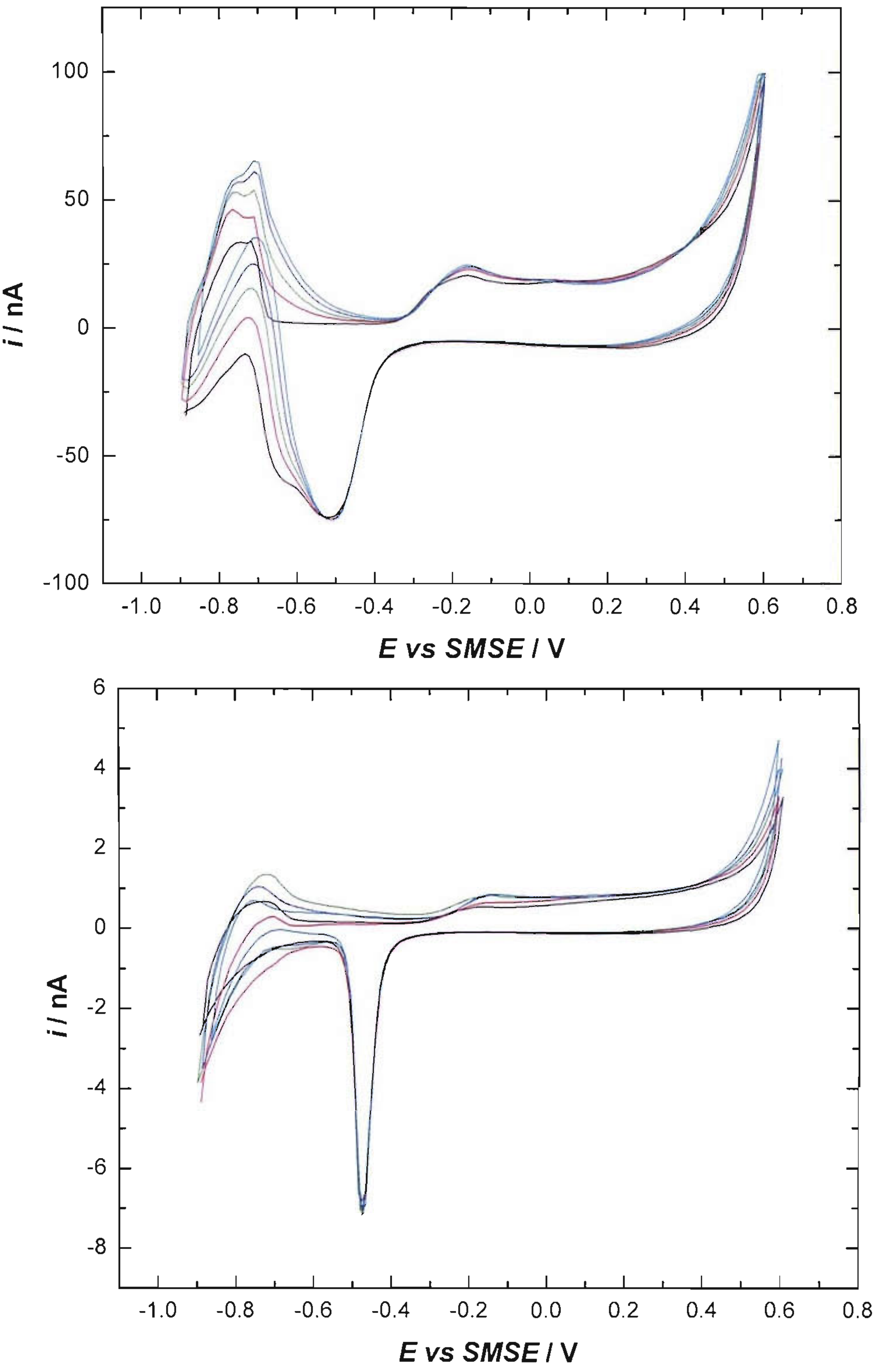

Figure 20. Cyclic voltammetry in 0.1 M sodium phosphate buffer, purged with argon, pH 7.4, T = 25 °C. Sweep rate = 50 mV s^{-1}. **Top**: WE = polished platinum microdisc, 25 μm diameter with 0.5 μm mesoporous palladium film. **Bottom**: WE = polished palladium microdisc, 25 μm diameter. Coloured lines correspond to different glucose concentrations: (—) = 0 mM, (—) = 5 mM, (—) = 10 mM, (—) = 15 mM, (—) = 20 mM.

3.5.4 Mesoporous and Polished Rhodium Voltammetry:

The voltammetry of rhodium in buffer over this potential range (-0.9 to + 0.6 V vs SMSE) is almost featureless, and the current decreases rapidly with successive sweeps and increasing glucose concentration. It would seem that glucose undergoes no electrochemistry in this range either, but merely serves to poison the rhodium surface.

3.5.5 Conclusions:

Mesoporous platinum and palladium both catalyse glucose oxidation and reduce the effects of piosoning. Reducing the overpotential did not help to eliminate the effect of ascorbate; indeed the ascorbate oxidation current becomes more significant at the lower potentials tried here.

Unlike the hydrogen peroxide detection, there would appear to be a definite advantage to using mesoporous platinum (over palladium, which is itself preferable to rhodium) for the direct oxidation of glucose. None the less poisoning of the electrodes is still an issue and it is worthwhile investigating the potential of mesoporous platinum, palladium and rhodium for enzyme based sensing.

3.6 Modification with Glucose Oxidase

3.6.1 Polymerisation of Phenol on Platinum:

Entrapment of glucose oxidase in electropolymerised phenol has been studied by Arrigan and Bartlett[143]. Scanning force microscopy was used to investigate the topology of the poly(phenol) and GOx/poly(phenol) composite on highly ordered pyrolytic graphite (HOPG). A "nanodozing" technique[144] was employed to estimate the thickness of the polymer films as 3 ± 1.2 nm and 7.4 ± 0.8 nm for enzyme free and enzyme composite polymers respectively. These measurements were performed *ex situ* and therefore do not reflect the thickness of the films in solution where they would be expected to swell.

One question worth considering is how phenol will polymerise on mesoporous platinum. There would seem to be two extreme possibilities: 1) polymerisation at the surface blocking the pores or 2) polymerisation throughout the structure (figure 21).

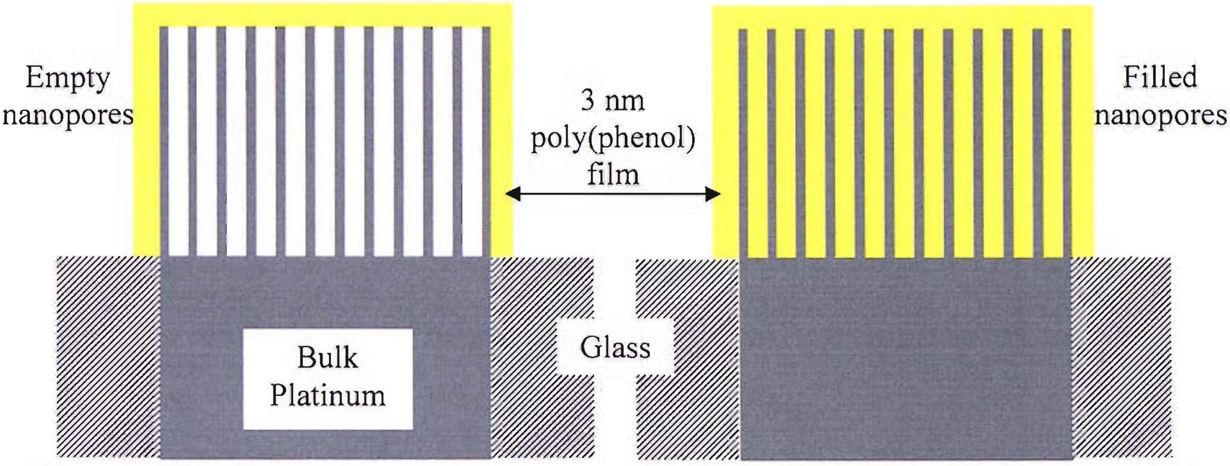

Figure 21. Cross-sectional diagram of mesoporous platinum covered with poly(phenol) film. **Left**: polymerisation outside the structure only. **Right**: polymerisation inside the pores.

Phenol has an approximate diameter of 0.56 nm[145] and is therefore small enough to diffuse into the mesostructure. With the deposition solutions containing only 50 mM phenol, complete filling of the pore (with poly(phenol) will be dependent on diffusion of extra phenol from the bulk. This will become more hindered as the deposition continues. A case somewhere between the two extremes (depicted above) might therefore be expected, with the film inside the pores being less dense as you progress down the pore, and possibly incomplete in places.

In order to investigate these possibilities poly(phenol) films were electrodeposited onto one mesoporous and one polished electrode (figure 22).

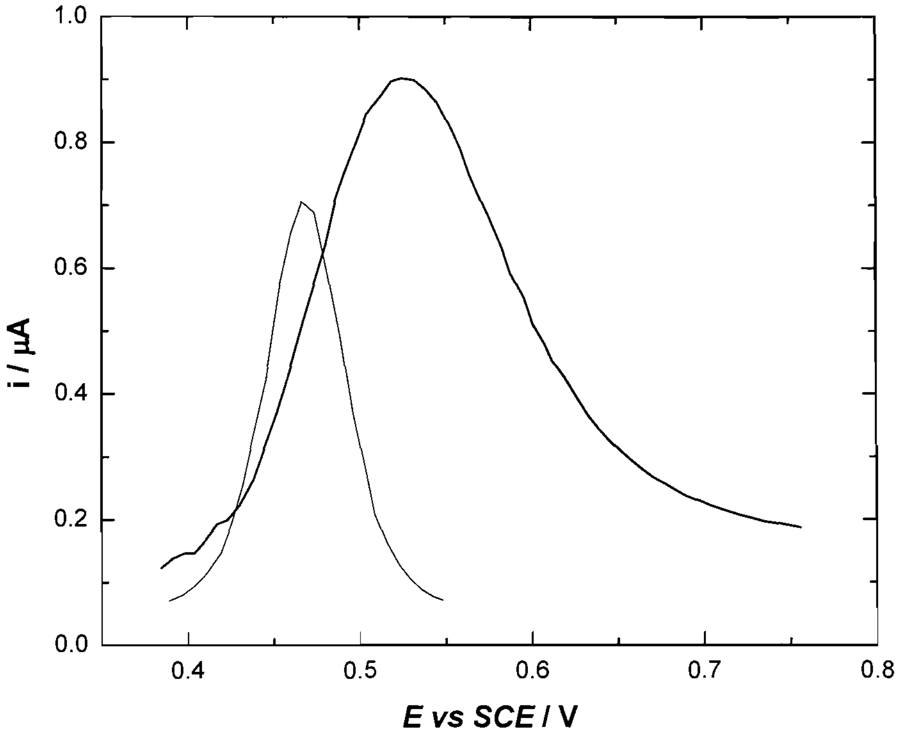

Figure 22. Voltammetry in 45 mM Phenol, 0.1 M sodium phosphate buffer, pH 7.4, $T = 25$ °C. Sweep rate = 10 mV s^{-1}. **Thick line**: 0.5 mm diameter polished gold disc with 1 µm mesoporous platinum film. **Thin line**: 0.5 mm diameter polished platinum disc.

Polymer films were deposited by voltammetry at 10 mV s^{-1}; under these conditions almost all of the charge is passed on the first sweep. The charges for passivation of the two electrodes were compared:

- Q_{pol} = phenol polymerisation charge required to passivate the polished electrode = 4.80 µC
- A_{pol} = the surface area of the polished electrode = 1.963×10^{-3} cm^2.
- A_{meso} = the surface area of the mesoporous electrode = 0.19 cm^2.

$\Rightarrow$ Q_{pas} = charge required to passivate a given surface area = 2.44 mC cm^{-2}

⇒ Predicted Q_{meso} = charge required to passivate the mesoporous electrode = $Q_{pas} \times A_{meso}$ = 2.44 mC × 0.19 cm^2 (surface area estimated from cyclic voltammetry in acid see above).

⇒ Predicted Q_{meso} = 464.5 µC

- However polymer film cannot reach full 3 nm thickness over most of electrode surface due to diameter of pores (2.5 nm).

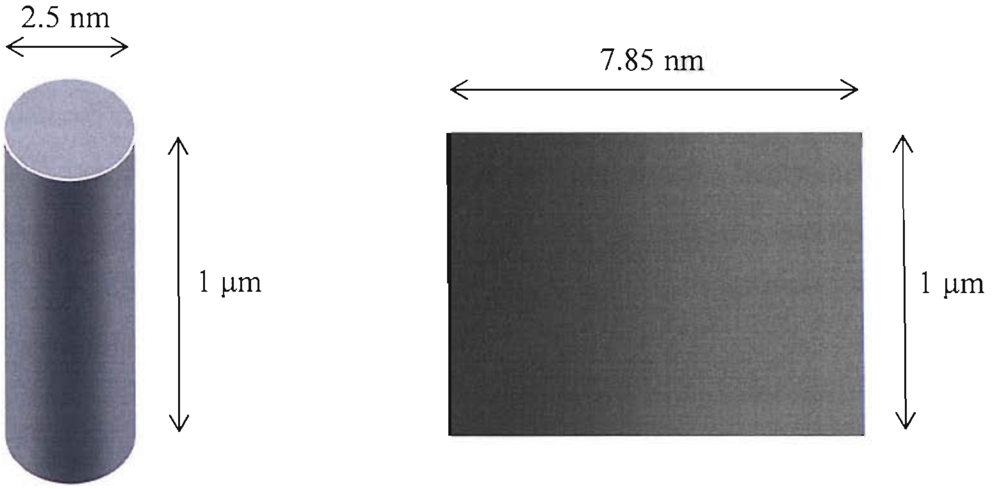

Figure 23. Schematic showing same surface area as a cylinder and laid flat. Note cylinder has a defined volume while, in theory, any thickness of polymer could be deposited onto the flat surface to give potentially infinite volume.

- The surface area of the pores laid flat (figure 24 above) is 7.85 × 10^{-11} cm^2 µm^{-1}.
- Therefore for a 3 nm polymer film grown over this area the volume of polymer is 2.355 × 10^{-17} cm^3.
- The volume of the closed pore is only 4.909 × 10^{-18} cm^3.
- Therefore the percentage of polymer that can be deposited onto the full mesoporous surface is 4.909 × 10^{-18} cm^3/2.355 × 10^{-17} cm^3 × 100 = 20.9 %.
- Predicted Q_{meso} for passivation of the mesoporous electrode becomes:
- 464.5 µC × 0.209 = 97 µC.

The observed charge for the passivation of the mesoporous electrode (Q = 16.55 µC) is much less than 97 µC; suggesting that the pores are not completely filled with polymer but are merely capped at the top with some limited growth inside. This may be advantageous when the mesoporous electrodes are modified with the GOx/poly(phenol) matrix since the hydrogen peroxide (produced during reaction with glucose) will not have to diffuse through large amounts of polymer to access the extra platinum surface area.

3.6.2 Modification of Mesoporous and Polished Platinum with GOx/poly(phenol) Matrix:

Firstly it is important to note that glucose oxidase is too large to fit into the pores of the nanostructured metals. The approximate dimensions of the enzyme dimer are 0.7 × 0.55 × 0.8 nm [114], compared to the pore diameter of 2.5 nm. So it is likely that the coverage of the mesoporous electrodes will be the same as for the polished microelectrodes studied before[94]. However the interaction of the glucose oxidase with the nanostructure may differ from its interaction with polished platinum.

Figure 24 shows the response of: a) a 25 μm mesoporous platinum disc modified with a GOx/poly(phenol) film and b) a 25 μm polished platinum disc modified with a GOx/poly(phenol) film, to increasing glucose concentration.

While efforts were made to reproduce the modification procedure described by Caruana[146] (see experimental section) the currents obtained during calibration here are somewhat less than those reported by Caruana (i.e. approximately half). Also the stability of the polished GOx/poly(phenol) electrode is very poor. Caruana's electrode showed a small drop in activity over the first 7 days with very good stability thereafter (up to 40 days); while here the current response of the polished GOx/poly(phenol) electrode is less that 10 % after only 8 days.

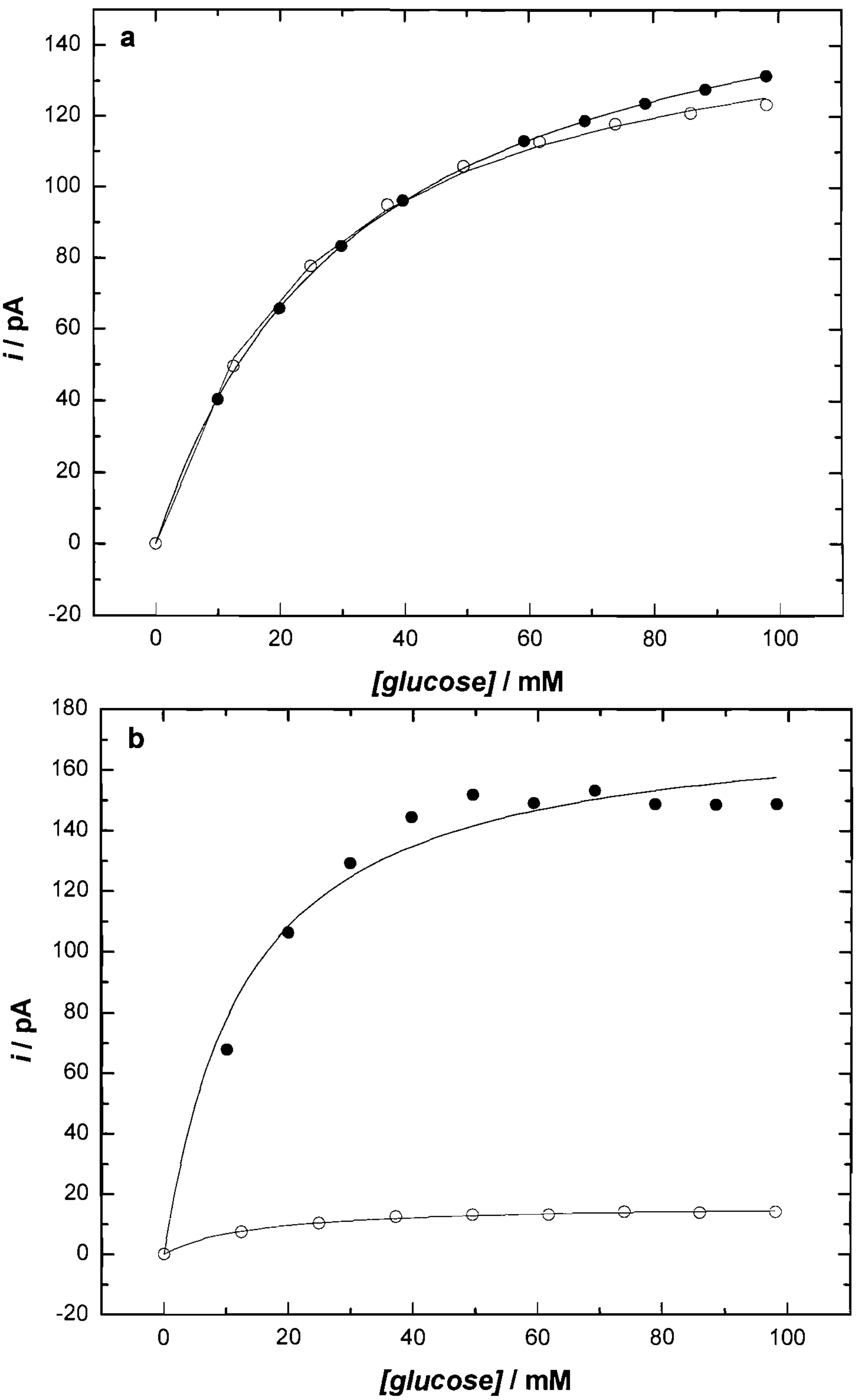

Figure 24. Chronoamperometry in 10 ml 0.1 M sodium phosphate buffer, pH 7.4, *T*=25 °C. WE held at 0.2 V vs SMSE for 20 min before aliquots of 5 M glucose were added at three minute intervals (solution stirred during addition). a) WE = polished platinum microdisc, 25 μm diameter with 0.5 μm mesoporous platinum film. b) WE = polished platinum microdisc, 25 μm diameter. •) data recorded on day of modification. ○) data recorded on day 8. Lines are regression data from equation.

The same concentration of active enzyme was used (as determined by absorbance at 450 nm) and the activity of the enzyme employed here was comparable to that described by Caruna (≥ 140 units mg^{-1} determined by MediSense procedure, and ≥ 2000 U/ml by Beckman method compared to 157-210 units mg^{-1}). The enzyme activity may have some bearing on the lower currents obtained in this work.

Also the enzyme adsorption time is very important; too short and maximum coverage will not be achieved, too long and the enzyme may become denatured and less active. Electrodes were left in the growth solution for the recommended 15 minutes prior to electropolymerisation; however, it is unknown if this is also the optimum time for the structured electrode.

Lastly in this study the measurement potential used to acquire the calibration plots was +0.2 V vs SMSE compared to + 0.9 V vs SCE used by Caruana (i.e. + 0.5 V vs SMSE). The reason for choosing this lower potential was in order to take advantage of the catalytic hydrogen peroxide oxidation at the mesoporous platinum, in the hope that this might help reduce the effect of interfering species. However this potential would seem to be less than ideal for operation of the polished electrode, and is possibly responsible for the greatly decreased stability. The reduced currents observed at the polished electrode on day 8 are probably due to a loss of sensitivity to hydrogen peroxide rather than a decrease in enzyme activity.

Equation 5 was derived in order to describe the general behaviour of these enzyme electrodes[147]:

$$j_s = \frac{kK_A a_\infty e_\Sigma k_{cat} K_S s_\infty l}{k_{cat} K_S s_\infty + kK_A a_\infty K_S s_\infty + kK_A a_\infty K_M} \qquad \textbf{5}$$

Where j_s is the rate of consumption of the substrate (glucose), a_∞ and s_∞ are the bulk concentrations of the mediator (oxygen) and substrate respectively, K_A and K_S are the partition coefficients of a and s between the solution and the polymer film, l is the thickness of the film, e_Σ is the total enzyme coverage, k describes that rate of enzyme mediator reaction and k_{cat} and K_M are the characteristic enzyme rate constants.

- When $kK_A a_\infty K_S s_\infty$ is dominant then the limiting reaction is the rate at which the enzyme is re-oxidised by the mediator.
- When $k_{cat} K_S s_\infty$ is dominant then the enzyme substrate reaction is limiting.
- At low substrate concentration (when $kK_A a_\infty K_S s_\infty$ is not dominant) where $K_S s_\infty < K_M$, $kK_A a_\infty K_M$ in the denominator is dominant so j_s is proportional to s_∞. As the bulk concentration of substrate is increased ($K_S s_\infty > K_M$) either $kK_A a_\infty K_S s_\infty$ or $k_{cat} K_S s_\infty$ become limiting. In both cases j_s is then independent of s_∞.

The calibration plots in figure 24 were analysed using equation 5 and the kinetic data, in table 3, was extracted by regression in Origin 6.0 (OriginLab®). In order to achieve this equation 5 was simplified by combining certain terms to give equation 6:

$$i_s = \frac{a s_\infty}{b s_\infty + c} \qquad \mathbf{6}$$

$i_s = nFAj_s$

$a = nFAkK_A a_\infty e_\Sigma k_{cat} K_S l$

$b = k_{cat} K_S + kK_A\, a_\infty K_S$

$c = kK_A\, a_\infty K_M$.

This was rewritten as equation 7 which could be plotted in origin to extract the constants 1, 2 and 3.

$$i_s = \frac{a_1 s_\infty}{b_1 s_\infty + 1} \qquad \mathbf{7}$$

Where $a_1 = a/c$ = constant 1, $b_1 = b/c$ = 1/constant 3 and constant 2 = a_1/b_1.

Constant 1 $\frac{\alpha K_S k_{cat} e_{\Sigma} l}{K_M}$ /cm s^{-1}	Constant 2 $\frac{\alpha K_S k_{cat} e_{\Sigma} l}{(1 + k_{cat} / kK_A a_{\infty})}$ /mol cm^{-2} s^{-1}	Constant 3 $\frac{K_M}{K_S (1 + k_{cat} / kK_A a_{\infty})}$ /mmol dm^{-3}
25 μm mesoporous Pt electrode modified with GOx/poly(phenol).		
Day 1:		
5.60×10^{-6} ($\pm 0.03 \times 10^{-6}$)	185×10^{-12} ($\pm 0.007 \times 10^{-12}$)	33.2 (± 0.3)
Day 8:		
6.53×10^{-6} ($\pm 0.22 \times 10^{-6}$)	167×10^{-12} ($\pm 0.3 \times 10^{-12}$)	26 (± 1)
25 μm polished Pt electrode modified with GOx/poly(phenol).		
Day 1:		
14.66×10^{-6} ($\pm 2.02 \times 10^{-6}$)	188×10^{-12} ($\pm 4 \times 10^{-12}$)	13 (± 2)
Day 8:		
1.21×10^{-6} ($\pm 0.10 \times 10^{-6}$)	17×10^{-12} ($\pm 0.1 \times 10^{-12}$)	14 (± 1)

Table 3. Kinetic parameters for non-linear least squares fits of data (figure 25) to equation 5 along with the errors generated by the algorithm. NB constant 3 = constant 2/constant 1.

For the mesoporous platinum microdisc, there is little change in the constants between day 1 and day 8; showing that the enzyme is stable, within the polymer matrix, over this timescale. On day 1, constant 2 for the polished electrode agrees well with that for the mesoporous electrode, while constant 1 is approximately three times larger and constant 3 is three times smaller. This suggests that the GOx/poly(phenol) films on the two electrodes are similar (i.e. similar amount of glucose oxidase entrapped, similar thickness of poly(phenol) and similar permeability of glucose and hydrogen peroxide through the film), but for some reason K_M for the enzyme-substrate complex is different. Lastly, the stability of the polished electrode is lower. By day 8, constants 1 and 2 have fallen to around 10 % of their initial values; this might indicate that the coverage of active enzyme has decreased or could be due to a reduction in hydrogen peroxide response (effectively a change in α).

3.6.3 Comparison of Platinum, Palladium and Rhodium Metal Microdiscs Modified with GOx/poly(phenol) Matrix:

Mesoporous and polished palladium and rhodium microdiscs were modified using the same procedure employed for the platinum electrodes in 3.5.3 above. A different source of glucose oxidase was used (lyophilised powder 157,500 U/g) and the concentration was calculated to give the same number of active units per ml of deposition solution. However the kinetic parameters obtained from the glucose curves (table 4 bellow) were very different from those calculated for the platinum electrodes (table 3 above); so two platinum microdiscs (one polished and one mesoporous) were also modified using the new enzyme and deposition solution in order to make a comparison of kinetic parameters between metals.

Constant 1	Constant 2	Constant 3
$\frac{\alpha K_S k_{cat} e_\Sigma l}{K_M}$	$\frac{\alpha K_S k_{cat} e_\Sigma l}{(1 + k_{cat} / kK_A a_\infty)}$	$\frac{K_M}{K_S(1 + k_{cat} / kK_A a_\infty)}$
/cm s^{-1}	/mol cm^{-2} s^{-1}	/mmol dm^{-3}
Polished Pt:		
1.38 × 10^{-6} (± 0.16 × 10^{-6})	32 × 10^{-12} (± 9 × 10^{-12})	24 (± 3)
H_I-ePt:		
1.63 × 10^{-6} (± 0.01 × 10^{-6})	70 × 10^{-12} (± 1 × 10^{-12})	43 (± 1)
Polished Pd:		
-	-	-
H_I-ePd:		
1.09 × 10^{-6} (± 0.06 × 10^{-6})	26 × 10^{-12} (± 3 × 10^{-12})	24 (± 2)
Polished Rh:		
0.50 × 10^{-6} (± 0.03 × 10^{-6})	10 × 10^{-12} (± 2 × 10^{-12})	19 (± 2)
H_I-eRh:		
1.59 × 10^{-6} (± 0.04 × 10^{-6})	37 × 10^{-12} (± 2.34 × 10^{-12})	23 (± 1)

Table 4. Kinetic parameters for non-linear least squares fits of calibration data to equation 5. All electrodes were 25 μm in diameter and modified with the GOx/poly(phenol) matrix.

The best calibration curves were obtained for the platinum electrodes and once again the mesoporous platinum not only gave a higher current response but also showed the best fit to equation 2 with the smallest errors. The polished palladium electrode gave the worst fit to the equation and it was impossible to obtain any meaningful kinetic parameters as the current decayed rapidly after the first glucose addition. The mesoporous palladium electrode was better, showing a response comparable to that of the platinum electrode, although with slightly more error in the fitting to equation 2. For the rhodium electrodes, once again the greater current response and best fit were seen for the mesoporous electrode. Unlike the platinum electrodes the polished rhodium did not display currents comparable to its mesoporous counterpart.

Electrodes were stored in sodium phosphate buffer (pH 7.4, T=4 °C) for 7 days before repeating the calibration experiments. The kinetic data is presented in table 5.

Constant 1 $\dfrac{\alpha K_S k_{cat} e_\Sigma l}{K_M}$ /cm s^{-1}	Constant 2 $\dfrac{\alpha K_S k_{cat} e_\Sigma l}{(1+k_{cat}/kK_A a_\infty)}$ /mol cm^{-2} s^{-1}	Constant 3 $\dfrac{K_M}{K_S(1+k_{cat}/kK_A a_\infty)}$ /mmol dm^{-3}
Polished Pt:		
0.40×10^{-6} ($\pm$ 0.08×10^{-6})	9×10^{-12} ($\pm$ 7×10^{-12})	21 (± 10)
$\mathrm{H_I}$-ePt:		
2.07×10^{-6} ($\pm$ 0.02×10^{-6})	93×10^{-12} ($\pm$ 3×10^{-12})	45 (± 1)
Polished Pd:		
-	-	-
$\mathrm{H_I}$-ePd:		
4.22×10^{-6} ($\pm$ 0.19×10^{-6})	112×10^{-12} ($\pm$ 12×10^{-12})	27 (± 2)
Polished Rh:		
1.54×10^{-6} ($\pm$ 0.73×10^{-6})	9×10^{-12} ($\pm$ 9×10^{-12})	6 (± 2)
$\mathrm{H_I}$-eRh:		
14.30×10^{-6} ($\pm$ 6.00×10^{-6})	42×10^{-12} ($\pm$ 32×10^{-12})	3 (± 1)

Table 5. Kinetic parameters for non-linear least squares fits of calibration data to equation 5. After storing electrodes for 7 days in sodium phosphate buffer (pH 7.4, T = 4 °C). All electrodes were 25 μm in diameter and modified with the GOx/poly(phenol) matrix.

Once again, the mesoporous platinum is more stable than the polished platinum electrode, with little change in the constants over 7 days; the decrease in constants 1 and 2 again, point towards a loss of active enzyme from the polished platinum surface or a change in α.

However the constants for the other electrodes are significantly changed by day 7. The rhodium electrodes show a drop in constant 3 with a concurrent increase in constant 1, indicating that the enzyme substrate binding constant (K_M) is decreased. Meanwhile there appears to be a marked increase in constants 1 and 2 at the palladium electrode.

3.6.4 Conclusions:

It is possible to immobilise Gox at polished and mesoporous platinum, palladium and rhodium microelectrodes, using the method described by Caruana[146]. However the enzyme electrodes reported here show lower current response to glucose and less stability. The kinetic data would seem to suggest that this is due to a decrease in the electrode response to hydrogen peroxide.

In each case the mesoporous electrodes are able to operate more efficiently, and with greater stability at lower overpotentials, than the polished electrodes.

3.7 Summary

Decomposition of hydrogen peroxide, at platinum group metals, is a continuous chemical process involving both oxidation and reduction reactions (1 and 2). The balance of these reactions can be perturbed by electrochemically altering the oxidation state of the substrate. A surface dependent mechanism for the reduction of hydrogen peroxide at platinum group metals has been proposed. This mechanism is analogous to that previously reported by Hall *et al.*[120] for hydrogen peroxide oxidation at platinum.

Hydrogen peroxide voltammetry is reproducible at the mesoporous platinum, palladium and rhodium microelectrodes but not at the polished electrodes. A gradual decrease in current is seen with continuous cycling of polished electrodes and there are no plateaus in the voltammetry. Hydrogen peroxide electrochemistry is dependent on the number of available metal binding sites and is therefore very sensitive to poisoning. The high specific surface areas of the mesoporous electrodes make the effects of poisoning less significant.

The cross-over of anodic and cathodic voltammograms can be explained by the place exchange of atoms in the oxidised metals.

Ascorbate oxidation would also seem to be affected by the oxidation state of the electrode, although this was not investigated in any depth. Oxidation of ascorbate occurs within the same potential window as hydrogen peroxide oxidation and is therefore likely to interfere with glucose measurement at the enzyme modified electrodes. The mesoporous electrodes have no advantage over the polished electrodes with respect to reducing ascorbate oxidation.

Direct amperometric determination of glucose at mesoporous platinum is possible because of its very high specific surface area. A range of potentials offer viable glucose detection and can be selected such that ascorbate oxidation does not occur or that the current for this is negligible.

Only two of the three regions, associated with glucose oxidation at platinum, are seen in the palladium voltammograms. This may indicate that the mechanism of oxidation and the intermediate products formed are different. It should still be possible to make direct glucose measurements at mesoporous palladium; although polished palladium shows very low currents which decrease at higher glucose concentrations (much like polished platinum).

Neither mesoporous nor polished rhodium electrodes show any voltammetric features that might be attributed to glucose oxidation. In both cases the normal rhodium oxidation, reduction and hydrogen adsorption features, observed for voltammetry in sodium phosphate buffer, were poisoned with each increase in glucose concentration.

It has been possible to modify mesoporous and polished platinum, palladium and rhodium microdiscs with a GOx/poly(phenol) matrix for the mediated detection of glucose. The success of this process is strongly dependent on several factors including the source, age and activity of the enzyme, the pH of the deposition solution and the duration of the polymerisation reaction. Also the calibration curves are dependent on the applied hydrogen peroxide oxidation potential; so it has not been possible to reproduce the high currents or level of stability reported by Caruana[146]. However the mesoporous electrodes are able to operate at lower potentials than their polished counterparts with much greater stability and fit the predicted response more closely.

Macroporous Electrodes

4.1 Overview

The main benefit of the mesoporous metal films, discussed in the last chapter, was their high specific surface areas. Larger metal structures are also of interest as biosensors. While increasing the size of the structure lowers the specific surface area of the materials other possibilities can be exploited; such as the decoration of the structure with bioactive molecules or immobilisation of enzymes/proteins within their own unique micro environment/reaction vessel.

The dimensions of the nanostructures discussed in this chapter range from hundreds of nanometres to several microns and were all prepared from templates consisting of polystyrene latex spheres immobilised on conducting substrates. Spheres are available, as monodisperse aqueous suspensions, in sizes ranging from 20 nm to several microns in diameter.

Templates are typically assembled at a conducting substrate by evaporation of the water to leave behind a close packed array of spheres; once dried the template can safely be transferred to the deposition solution without disrupting the structure of the template. Polymers or metals can be deposited into the interstitial spaces, and the spheres are then removed by dissolving in toluene or THF to leave behind a macroporous structure with an architecture that is the inverse of the original polystyrene template (figure 1).

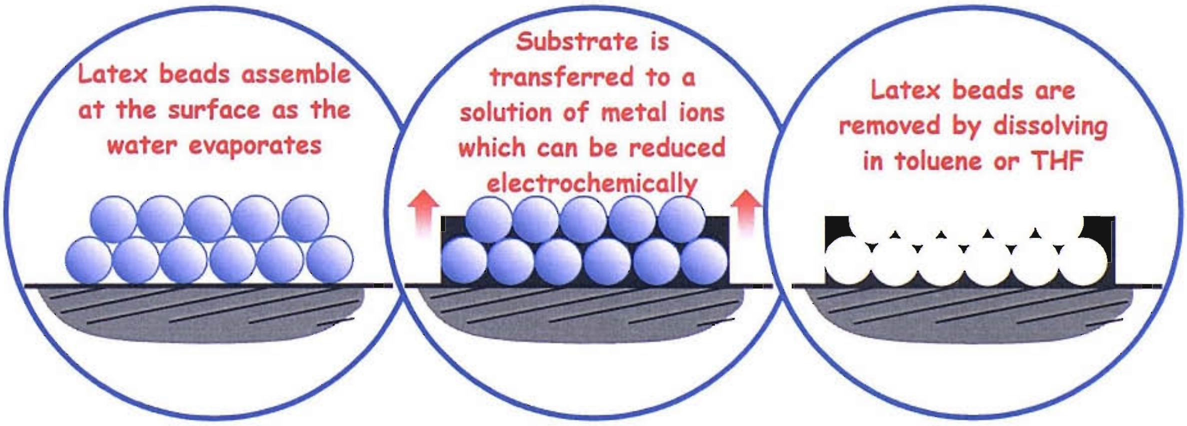

Figure 1. Schematic of main steps in production of nanostructured films from polystyrene latex spheres.

4.2 Template Preparation

4.2.1 Self Assembly by Sedimentation:

Where the substrate is an evaporated gold or nickel slide, self assembly of the template was simply a matter of confining the aqueous sphere suspension at the surface; allowing the solid to sediment and then evaporating the water. This process is much faster and more reliable for larger spheres (> 1 μm) since they are heavy and less affected by Brownian motion than the nanospheres.

In the case of evaporated gold slides this process can be assisted by modification of the surface with a cystamine (thiol) layer prior to adding the sphere suspension. This gives the gold surface a net positive charge (due to the amino groups) improving its wetability and, possibly, helping to keep the spheres (which are covered in negative sulphate groups) in place once the template is dried and during subsequent metal deposition.

While it is easy to template and deposit on slides covered with evaporated metal films, these do not make the most practical electrodes. In this work the templating procedure was used to try and deposit structured films onto platinum disc electrodes (made by sealing 0.5 mm diameter platinum wires into glass, and polishing); these are robust and have a well defined geometric area. Template assembly at polished platinum disc electrodes sealed in glass suffers from two main problems:

1. Positioning the electrode such that the polished face is perfectly horizontal. This is very hard to judge and invariably spheres deposit more thickly on one side of the polished face than the other.
2. Bevelling at the circumference of the electrode face due to polishing. This leads to thinner sphere deposits at the centre (where the platinum disc is located, figure 2).

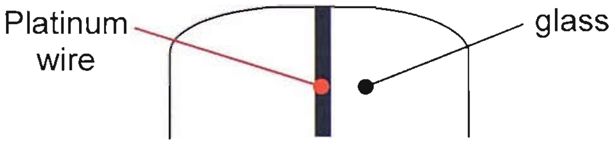

Figure 2. Cross sectional representation of platinum disc electrode, showing effect of polishing on face.

It is also worth considering that glass is somewhat more hydrophilic than platinum (contact angles <5° [50] and ≈68° respectively). This will certainly affect the assembly of the spheres if the water evaporates too fast and sedimentation is incomplete. For smaller spheres (1000 - 500 nm) very long times are required for complete sedimentation (as much as a week for a solution depth of 4 mm). However if several layers of spheres have managed to deposit before the water level gets too low then the structures seem to be quite stable.

4.2.2 Characterisation of Self Assembled Templates:

The spheres themselves are colourless although templates generally appear as white coatings over the substrate. If the sphere size is of the same order of magnitude as the wavelength of visible light then films often appear opalescent. This opalescence is stronger the thinner and more highly ordered the deposit. For instance slow sedimentation onto gold slides gives much more reflective and colourful deposits than were seen on the platinum disc electrodes.

The origin of this iridescence is thin film interference[148] for monolayer deposits of spheres (analogous to an oil film on water) and Bragg scattering[40] is also possible for ordered multilayers. There are many natural examples of structural colour[149] but the closest analogy to the structures described here is the semi-precious gem stone opal[46] (layers of hexagonally packed silica particles held together primarily by Van der Waals interactions and, possibly, also by preferential sedimentation of minerals at the contact points between particles).

The packing of the spheres, and therefore regularity of the template structure, is improved not only for slower sedimentation but also for larger spheres. In this work some 5 micron diameter spheres were used, and while these sediment relatively quickly (due to their weight and the reduced effect of Brownian motion) the deposits were found to be very regular and close packed. Also the template deposits were found to be highly opalescent (figure 3). While the spheres themselves are not of a similar size to the wavelength of light spaces within the regular close packed structure are, and this is what causes the diffractive effects.

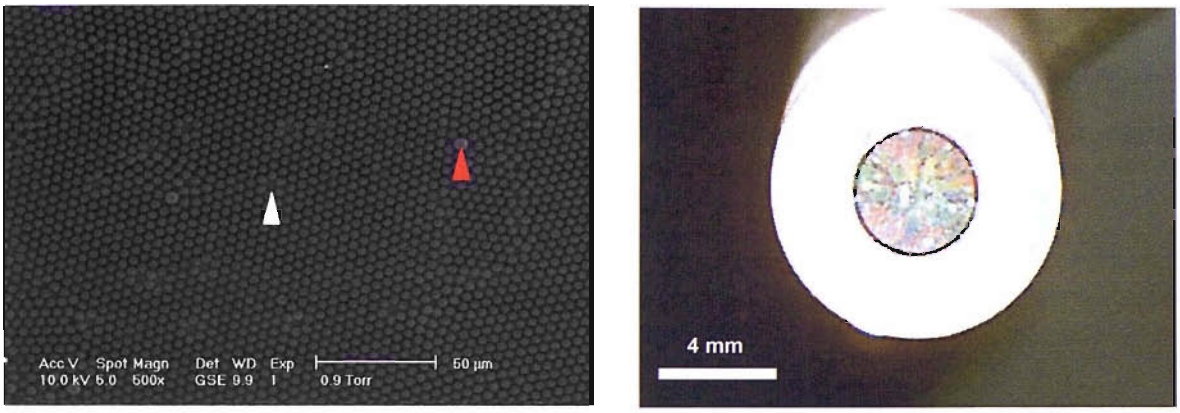

Figure 3. Images of single layers of 5 µm polystyrene latex spheres immobilised at surfaces. **Left**: ESEM image taken with a Philips XL30 ESEM, spheres immobilised at an evaporated nickel slide. Two defects are marked on the image: a void (white flag) and a large sphere (red flag). **Right**: low resolution digital image of spheres immobilised at 4 mm diameter polished nickel disc (opalescent area). Taken with an Intel Digital Blue™ QX3+ microscope.

Packing of the 5 µm spheres was almost invariably hexagonal with crystal domains ranging in size from 0.01-0.02 mm^2 with very few defects. Figure 3 is not an ideal representation of the templates in general since the size of the spheres used here was somewhat variable (in fact two spheres in the image clearly stand out as larger than the others). The spheres used were provided by Alfa Aesar and did not have the guaranteed size distribution of those provided by Duke Scientific; which were used in the experiments in section 4.7 (size distribution = 0.05 µm with standard deviation 1.0 %, mean diameter = 4.996 µm ± 0.035 µm).

Larger particles like this disrupt the regular packing of the array[51] and lead to smaller domain sizes and defects like the voids apparent in figure 3.

For spheres much smaller than 500 nm it was impossible to tell how efficient the packing was since the resolution of the microscope was too low. However what was apparent was that films of these small spheres look cracked like a dry riverbed (Figure 4). There has been some debate over the mechanisms that govern cracking in thin films[150,151]. Most models predict crack spacing by balancing the elastic energy released during fracture with the free energy required to form the new surfaces.

Lee and Routh[152] propose a mechanism controlled by hydrodynamic forces in drying sediment (like the one reported here). The transverse stresses are the result of capillary pressure between particles. This pressure is inversely proportional to particle size and results in a high density of cracks for the films of small spheres (such as those in figure 4).

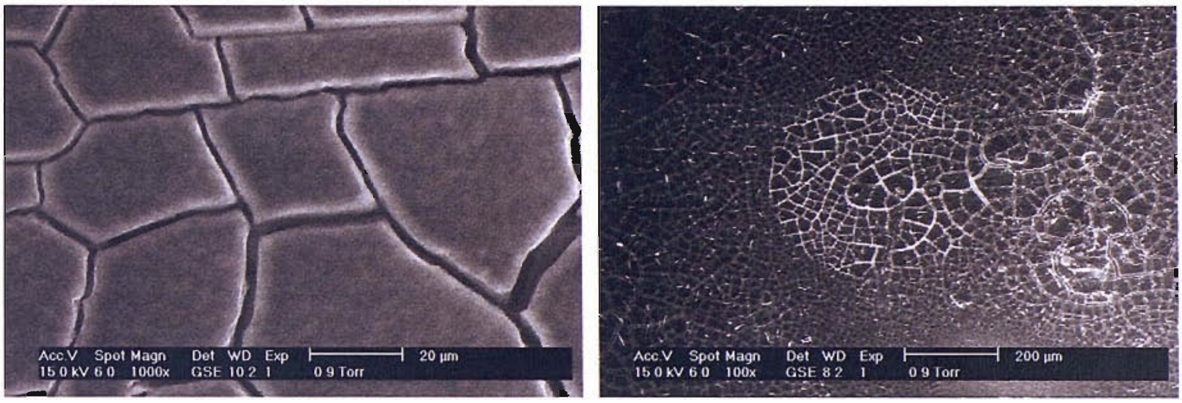

Figure 4. ESEM images of a 0.5 mm diameter polished platinum disc (sealed in glass) covered with 100 nm polystyrene latex spheres. Deposition by sedimentation from 60 µL of 0.3 % (weight of solids) suspension in water confined on electrode in a 4 mm diameter Teflon ring stuck to electrode with varnish. After sedimentation water was allowed to evaporate at room temperature. **Left**: 10 × magnification of right hand image.

It should be noted that it is possible to assemble well ordered arrays of nanometre sized spheres (i.e. diameters 20 - 500 nm) by means other than sedimentation. These include:

4. Careful, controlled drying of thin films[47,48].
5. Controlled de-wetting of flat, hydrophilic substrates[50,51].
6. The Colvin Method[46,52].

and are discussed in more detail in Chapter 1 (section 1.3.2).

Films, such as the one imaged in figure 4, are not particularly useful as templates for the deposition of structured metals. It is impossible to calculate the charge required to electrodeposit a given thickness of metal due to the uncertainty in the packing efficiency and the relatively huge cracks in the film. Films consisting of larger spheres 400-600 nm were much less cracked; although there was still some shrinkage during drying, this led to much less significant defects in the structure. Larger spheres also have the advantage of being much easier to image (figure 5).

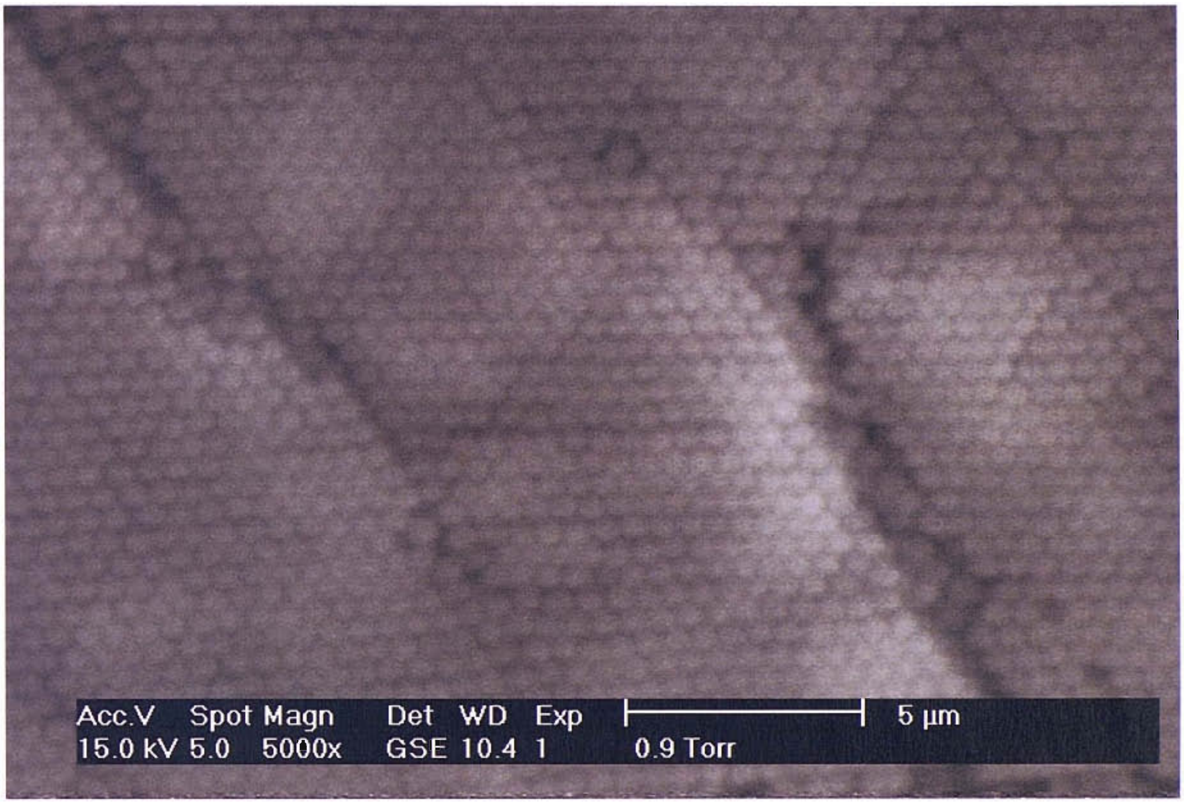

Figure 5. ESEM images of a 0.5 mm diameter polished platinum disc (sealed in glass) covered with 600 nm polystyrene latex spheres. Deposition by sedimentation from 60 µL of 0.3 % (weight of solids) suspension in water confined on electrode in a 4 mm diameter Teflon ring stuck to electrode with varnish. After sedimentation water was allowed to evaporate at room temperature. 5000 × magnification.

Figure 5 shows 600 nm spheres deposited over a 4 mm diameter onto a 0.5 mm diameter platinum disc sealed in glass. The suspension was allowed to settle for approximately 3 days before allowing the electrode to dry. The hexagonal patterns of spheres visible on the surface of the film suggest that the bulk structure is probably, predominantly close packed. It is thought that sedimented synthetic opals adopt a predominantly face centred cubic geometry (fcc, where every third layer lies above the first i.e. ABCABC...) with 10 – 20 % stacking faults[44].

While this is the most energetically stable configuration[45] the energy difference between face centred cubic (fcc) and hexagonal close packed (hcp, where every other layer lies above the first i.e. ABABAB...) structures is $\leq 10^{-3}$ k_BT per particle. So under normal sedimentation conditions, at room temperature, both hcp and fcc structures may form. Therefore, overall, these synthetic opals are random close packed structures (rhcp).

Not all of the template surface appears as hexagonal arrays of spheres; there are also areas with a distinctly square arrangement. These areas represent two different crystal planes of the fcc bulk lattice[40,50]: the hexagonal array is the (111) plane and the tetragonal array is the (100) plane. Orientation of the (111) crystal plane parallel to the substrate surface is energetically, slightly more favourable than the (100) plane.

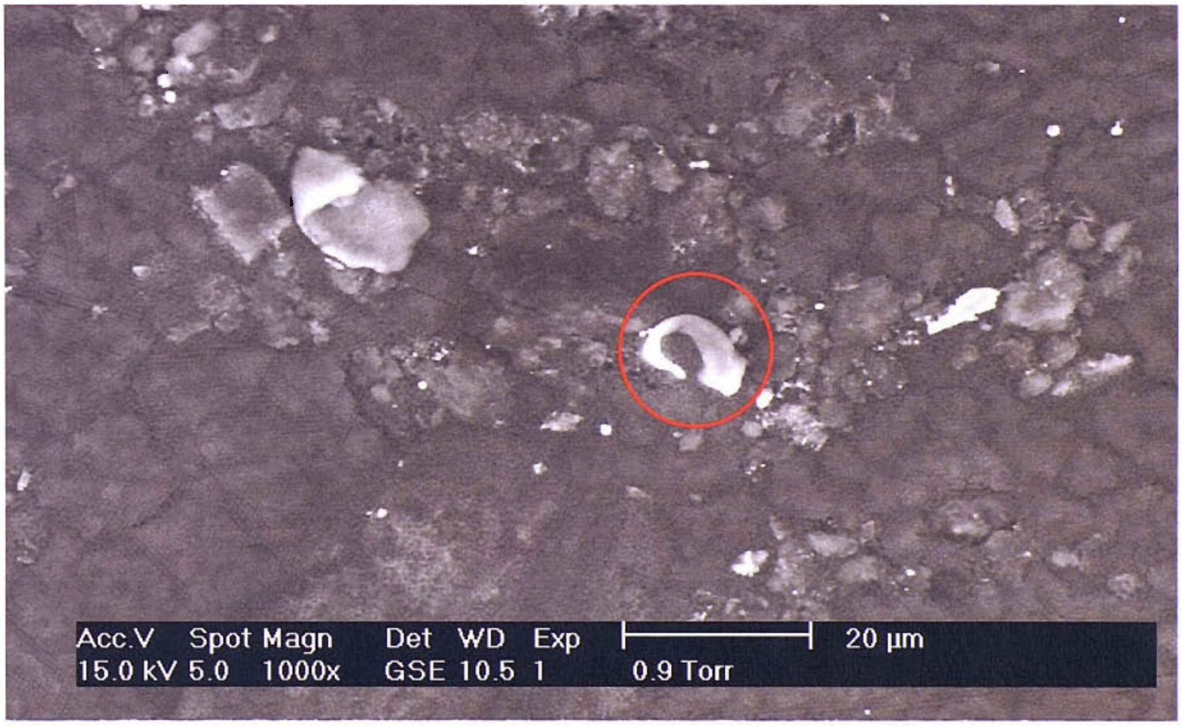

Figure 6. ESEM images of a 0.5 mm diameter polished platinum disc (sealed in glass) covered with 600 nm polystyrene latex spheres. Deposition by sedimentation from 60 µL of 0.3 % (weight of solids) suspension in water confined on electrode in a 4 mm diameter Teflon ring stuck to electrode with varnish. After sedimentation water was allowed to evaporate at room temperature. Red circle marks one of several foreign particles in the film.

Figure 6 gives an impression of the general topology of a sedimented deposit of 600 nm polystyrene spheres. Although the magnification is quite low, it is just possible to make out individual spheres and the patterns they form. It is not possible to measure the thickness of the film, but is clearly not uniform over the whole 4 mm deposit. Figure 6 shows that the film is inhomogeneous and in this case there is also some debris on the surface (probably shavings of Teflon left over from the machining of the tubes used to immobilise the spheres, one is marked on the image by a red ring); although this affects the subsequent deposition of the macroporous metal very little.

4.2.3 Conclusions:

Despite some practical difficulties it was possible to assemble polystyrene latex spheres at the surface of the platinum disc electrodes (as well as evaporated gold and nickel slides) by sedimentation. While it was not possible to investigate the bulk structure of these deposits, the surface topology and particle arrangement suggests that the assemblies are predominantly random close packed structures (as has been reported in the literature).

As reported by Lee and Routh[152] the templates assembled from the smaller spheres (e.g. < 500 nm diameter) are more prone to cracking.

4.3 Electrophoretic Deposition of Polystyrene Latex Spheres

Since the polystyrene spheres are covered in surface sulphate groups (designed to prevent aggregation in the aqueous suspensions), they can be precipitated at a conducting surface by applying a positive potential. One of the earliest accounts of this technique is by Richetti *et al.*[153,154] who examined the electric field effects on dilute suspensions of 1 μm polystyrene latex spheres in thin cells, consisting of parallel, conducting slides (glass substrates with an indium tin oxide coating).

As well as greatly reducing the template assembly time electrophoresis has the added advantage that the spheres are only deposited at the conducting portion of the substrate which means less wastage.

4.3.1 Electrophroetic Deposition of Polystyrene Latex Spheres at Polished Platinum Microelectrodes:

Two 25 μm polished platinum disc electrodes were positioned in a 0.026 % (solid weight) aqueous suspension of 500 nm spheres. One was connected to a potentiostat and held at +5 V vs Pt gauze (A) while the other remained at open circuit potential (B). After 15 minutes both electrodes were removed from the solution. It was noted that the droplet on the tip of electrode B was clear, whereas the droplet on A was cloudy.

Upon drying B appeared as it did before entering the solution, but A had a white cone like mound on its surface (approximately half a millimetre high at its peak). Closer inspection revealed that, while this mound covered the entire face of the glass, there was a tiny pin hole at the centre. High magnification images showed that there was only sparse and random adhesion of particles to the surface of B (figure 7) and that the hole in A's deposit extended all the way to the, still bare, platinum surface (figure 8).

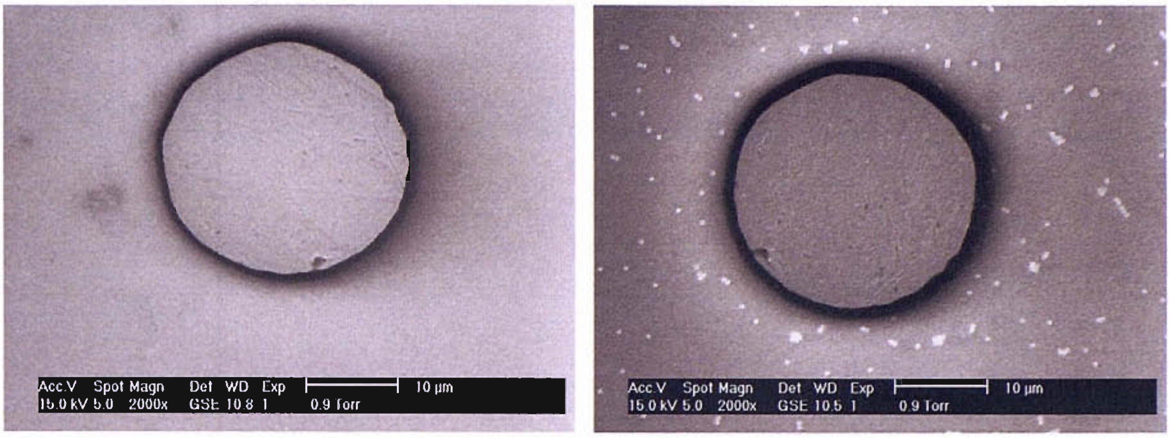

Figure 7. ESEM images of electrode B (25 µm polished Pt sealed in glass). **Left**: after polishing. **Right**: after standing in 0.026 % colloidal suspension of 500 nm polystyrene beads for 15 minutes.

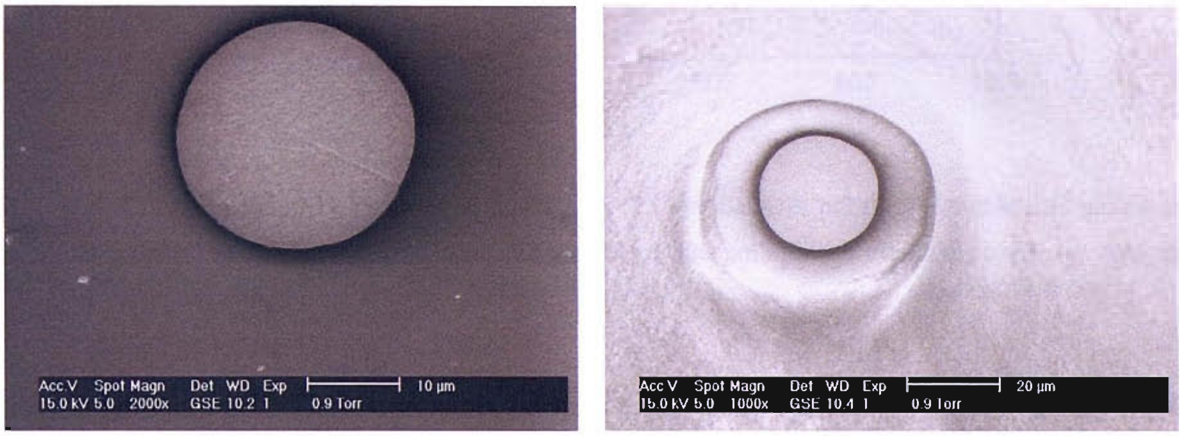

Figure 8. ESEM images of electrode A (25 µm polished Pt sealed in glass). **Left**: after polishing. **Right**: after applying +5 V vs Pt gauze in 0.026 % colloidal suspension of 500 nm polystyrene beads for 15 minutes.

Figure 8 shows that the only place spheres were not deposited onto electrode A was on the platinum itself. This is probably because the overpotential was too high, and bubbles of oxygen were formed at the platinum as water was electrolysed. Small currents are expected during electrophoresis due to water oxidation but significant gas bubble formation is not observed below current densities of ≈ 100 µA cm^{-2} [155]. The current time transient recorded for electrophoresis of spheres onto A (figure 9) shows very high current density (rising over 10 minutes to 7.92 A cm^{-2}) and several spikes which are probably due to bubbles leaving the electrode surface.

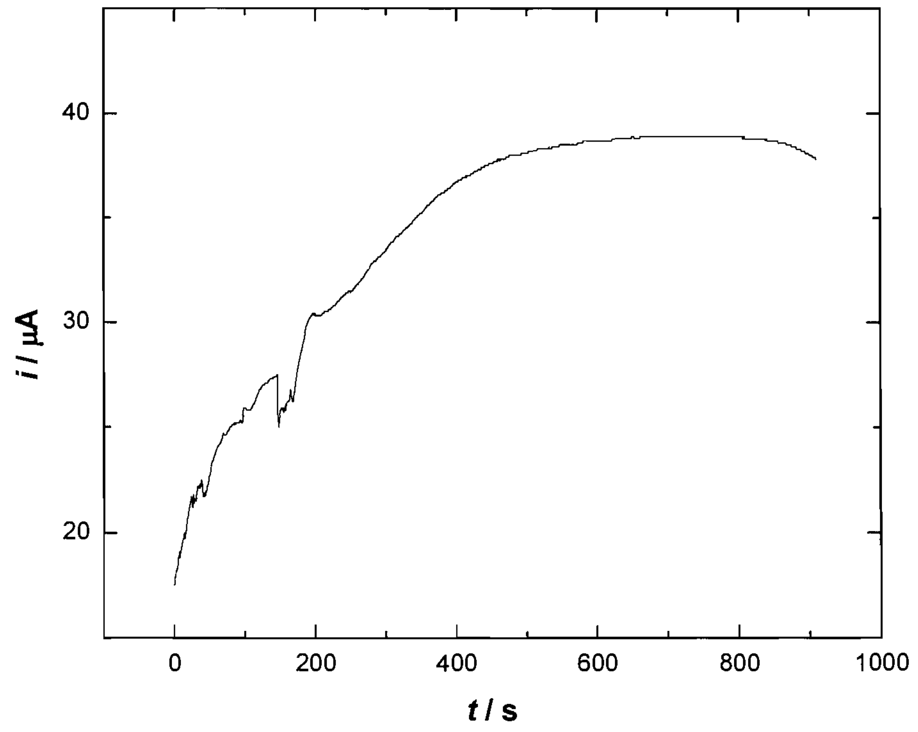

Figure 9. Chronoamperomery recorded at electrode A (25 μm diameter polished platinum disc sealed in glass) in a 0.026 % (solid weight) aqueous suspension of 500 nm spheres. Applied potential + 5 V vs platinum gauze counter/pseudo reference electrode.

Other, lower, potentials were investigated for the electrophoresis of polystyrene latex spheres (figure 10). For the electrodes polarised at + 1 and + 2 V very little current flowed. When the potential was increased to + 3 or + 4 V significant current was observed, and, upon removal from the colloidal suspension, the droplet on the end of the electrode was noticeably cloudy. The spike in the current seen at roughly t = 100 s for the electrode polarised at + 4 V suggests that electrolysis is still occurring.

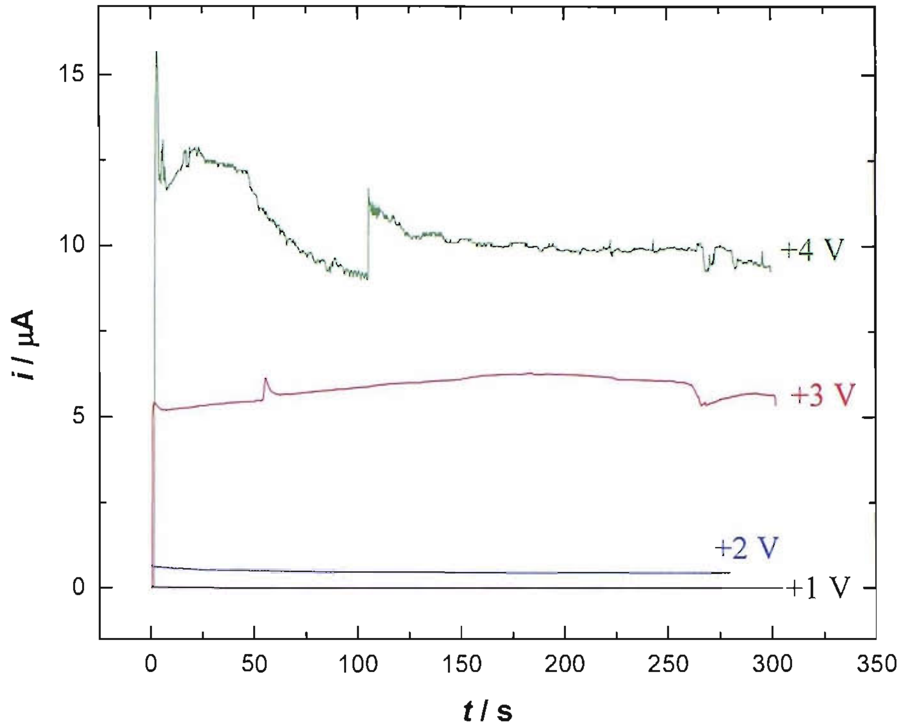

Figure 10. Chronoamperomery recorded at 25 μm diameter polished platinum disc electrodes, in a 0.012 % (solid weight) aqueous suspension of 500 nm spheres. Applied potentials: + 1, + 2, + 3 and + 4 V (black, blue, red and green lines respectively) vs platinum gauze counter/pseudo reference electrode.

The electrodes were imaged by ESEM after electrophoresis. For the electrodes held at potentials + 1 and + 2 V there appeared to be only random adhesion of the spheres to the surface (as in figure 7). The two electrodes held at + 3 and + 4 V show a high concentration of spheres on and around the platinum surface (figure 11). Closer inspection suggests that there is less long range order (compared with sedimented spheres) due to the speed at which they are deposited on the electrode.

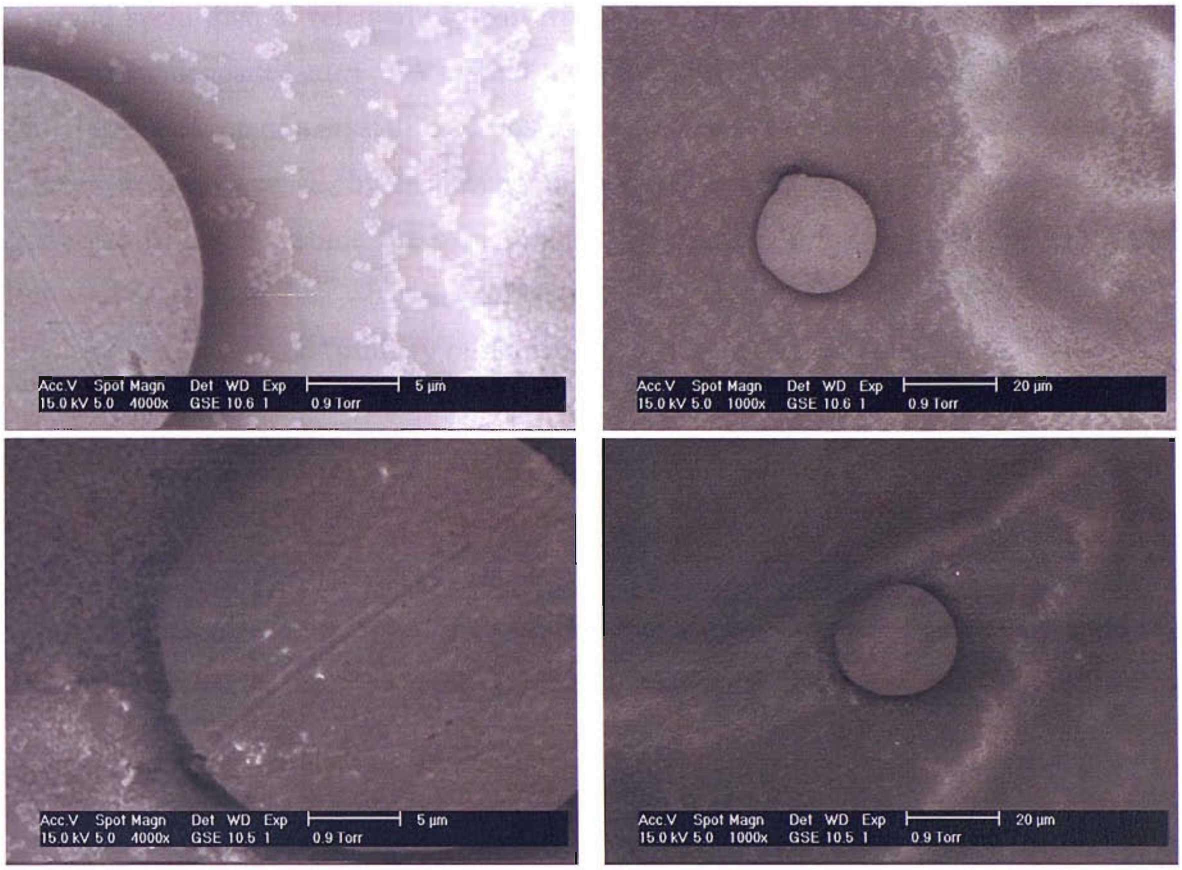

Figure 11. ESEM images of 25 µm polished Pt discs after chronamperometry in 0.012 % x 500 nm bead suspension. **Top**: images of the same electrode after applying a potential of + 3 V vs Pt for 5 minutes. **Bottom**: of an electrode that was held at + 4 V vs Pt for 5 minutes. The 1000 × images (right) show the broader distribution of the spheres.

It is also worth noting that the spheres are still not covering the platinum surface despite the fact that bubble formation is reduced. This is perhaps due to the movement of spheres after electrophoresis as the water droplet dries. Natural Brownian motion is responsible for some sphere motion, but more important are the capillary forces exerted as the water droplet retreats. It was found that this could be minimised by performing the electrophoresis in a more volatile solvent (this means faster drying of the deposit and less time for sphere movement) and by recessing the electrode slightly to help confine the spheres. This is discussed more in Chapter 5.

It would seem that, at relatively low overpotentials, the particles remain mobile (unlike the spheres deposited at + 5 V). This mobility could be advantageous for assembly; allowing formation of a crystalline deposit. It should be possible to permanently attach the spheres to the electrode by increasing the attractive force (i.e. by applying a higher overpotential) to overcome the steric repulsion between the spheres and the electrode. Hayward *et al.* state that: when the attractive electrostatic force exceeds that due to steric repulsion, entry into the "primary minimum" creates a permanent bond[155].

4.3.2 Conclusions:

Electrophoresis may be used to assemble charged, polystyrene latex spheres at platinum microdiscs. The deposits are less even and appear less ordered than those formed by the slower process of sedimentation. Careful selection of the electrode potential is required; such that the spheres are sufficiently attracted to the substrate without causing electrolysis of the solvent.

4.4 Cyclic Voltammetry in Metal Plating Solutions

In this work structured deposits of platinum and gold were deposited onto substrates of silver, gold, platinum and nickel. Cyclic voltammetry, of each substrate, was performed in: a) a 50 mM aqueous solution of hexachloroplatinic acid (HCPA) and b) a commercial gold plating bath, in order to establish suitable deposition potentials. Platinum voltammetry in the gold plating bath is given as an example below.

4.4.1 Platinum Voltammetry in Gold Plating Bath:

Only during the first cycle does the electrode behave as a platinum surface; the second voltammogram is the same as that of a gold working electrode in this solution. There is little change in the voltammetry on subsequent cycles indicating that the electrode is covered with gold.

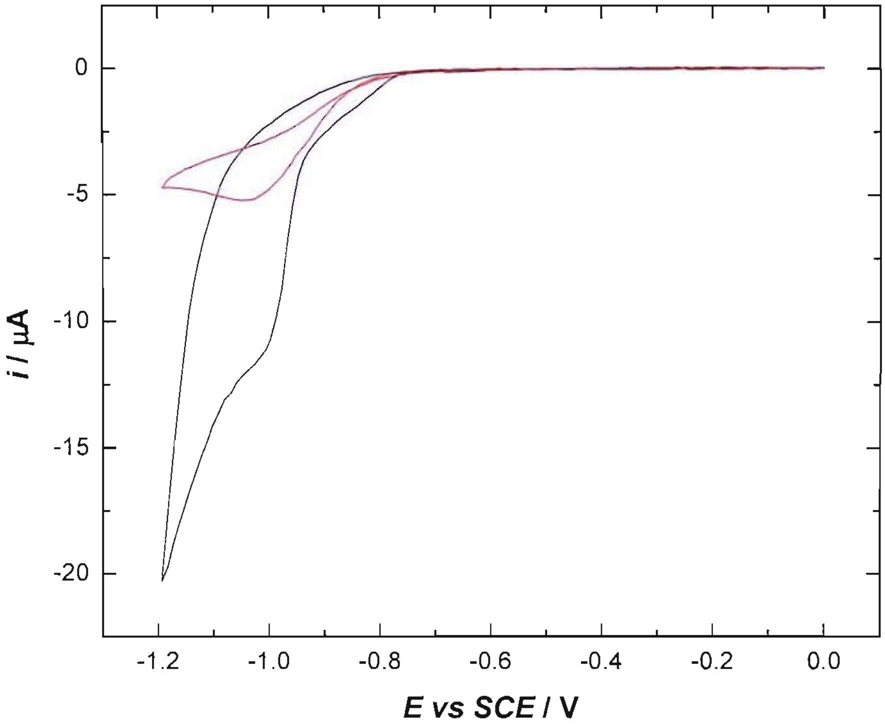

Figure 12. Cyclic voltammetry recorded in commercial gold plating bath (Techni gold 25), T=25 °C. Sweep rate = 20 mV s^{-1}. WE = 0.5 mm diameter polished platinum disc. **Black line**: 1st cycle. **Red line**: 2nd cycle.

There would appear to be three waves occurring on the 1st cathodic sweep. While the solution is not de-aerated none of these are in the right potential range to be due to oxygen reduction (the half wave potential for oxygen reduction being -0.4 V vs SMSE at platinum in phosphate buffer of pH=7.0[34], which translates to a potential of about -0.13 V vs SCE in a solution with a pH of 9.23).

The first wave between -0.8 and -0.9 vs SCE is due to reduction of Au(I) to Au metal. However before this process becomes diffusion controlled it is overlapped by another. It seems likely that the second wave is due to hydrogen adsorption at the platinum surface followed closely by hydrogen evolution. On the second cycle (red line figure 12) there is a single wave, between - 0.9 and - 1.2 V, due to gold reduction on the newly formed (during the first cycle) gold surface.

When voltammetry is performed between 0 V and -0.9 V then a peak in the current can be seen on the anodic sweep (at about -0.8 V) which is reminiscent of hydrogen desorption (figure 13).

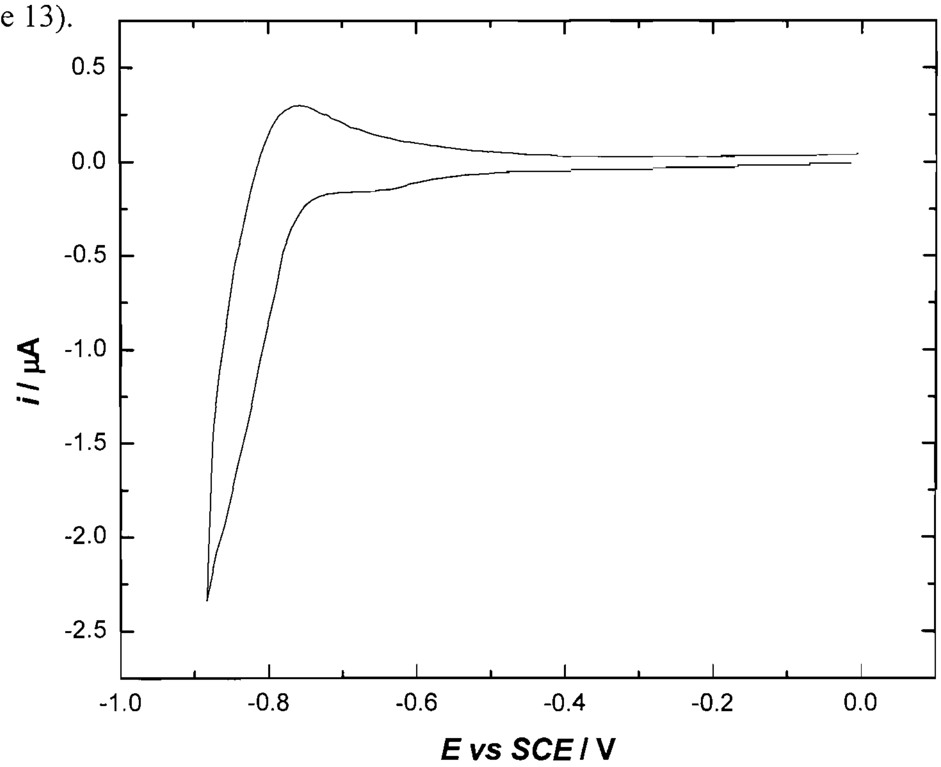

Figure 13. Cyclic voltammetry recorded in commercial gold plating bath (Techni gold 25), *T*=25 °C. Sweep rate = 20 mV s^{-1}. WE = 0.5 mm diameter polished platinum disc.

4.4.2 Conclusions:

For gold deposition onto silver and gold substrates a potential of -0.94 V vs SCE is required, but -0.85 V for deposition onto platinum and -0.9 V for deposition onto nickel. Platinum may be deposited from an aqueous solution of 50 mM HCPA with no additional electrolyte. A potential of -0.05 V vs SCE is required for deposition onto gold and silver substrates.

Electroplating of gold onto platinum at ≤ -0.9 V vs SCE is complicated by hydrogen evolution. This disrupted the template during deposition of macroporous gold, leading to unstructured films. For this reason macroporous gold films could only be deposited onto platinum at potentials more positive than -0.85 V vs SCE. It was found that, once a thin layer of gold had been established, the potential could be safely increased to -0.9 V; since no hydrogen adsorption occurs at gold and there is no hydrogen evolution at this potential.

4.5 Deposition of Macroporous Gold onto Platinum Disc Electrodes

All nanostructured metals reported in this section were deposited through templates that were assembled from sedimented spheres. Certain assumptions had to be made about the coverage of spheres and their packing in order to estimate the charge required to deposit films of specific thickness over a given electrode area. These assumptions and key steps in the calculations are detailed in the appendix A.

4.5.1 Current Transients for Deposition:

Figure 14 shows a current time transient recorded for the deposition of gold onto a 0.5 mm diameter platinum disc covered with close packed 500 nm latex beads.

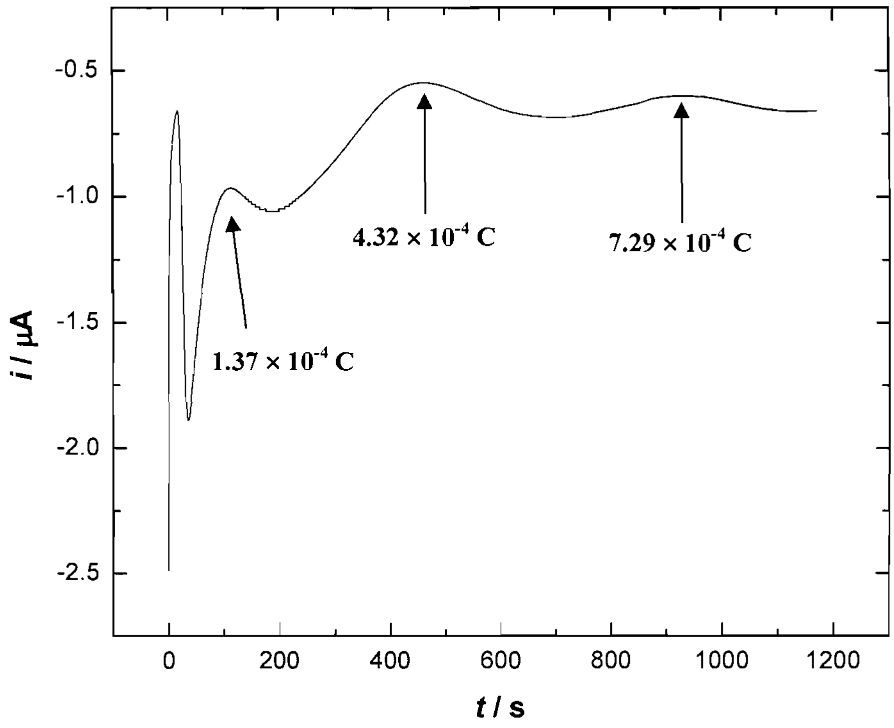

Figure 14. Chronoamperometry in Techni Inc Gold 25 plating bath, T = 25 °C. WE = 0.5 mm diameter polished platinum disc covered with close packed 500 nm latex spheres. WE was soaked in solution for 10 min before applying potential of -0.85 V vs SCE. Charge passed = 8.65 × 10^{-4} C.

Initially the current spikes and drops sharply due to the double layer charging of the platinum. Then it rises as the nucleation of gold centres begins. However after this the current does not stabilise, but increases and decays periodically. It seems likely that this oscillation in current is caused by the changing surface area of the gold as it grows through the template. This phenomenon has been reported, by Sumida *et al.*, for nickel deposition through a close packed array of spheres[74].

In this case the current minima on the transient should correspond to gold thicknesses that are half way up a layer of spheres (i.e. the points in the structure where metal growth is most restricted and the exposed surface area is minimised). The charges passed, at each of these current minima, are marked on figure 14, and agree well with the theoretical values for gold deposits at the half way points on the 1st, 2nd and 3rd sphere layers (table 1).

Gold Thickness / nm	Number of sphere layers	Estimated Q / C	Observed Q / C	Faradaic Efficiency %
250	0.5	1.85×10^{-4}	1.37×10^{-4}	135
658	1.5	3.86×10^{-4}	4.32×10^{-4}	88
1066	2.5	6.44×10^{-4}	7.92×10^{-4}	88

Table 1. Charge estimated to give gold thickness corresponding to half layers of sphere compared to charge passed at each of the current minima on figure 14.

There seems to be pretty good agreement between the theoretical and observed values in the bulk template. However, the observed charge in the 1st half layer is somewhat less than expected (despite the fact that the difference in packing efficiency at the surface and in the bulk lattice was taken into account).

4.5.2 Characterisation of Macrostructures by ESEM:

The gold films, deposited onto platinum in this way, tend to appear either opalescent (red or green depending on lighting and viewing angle) or gold coloured to the naked eye depending on how open the cavities are at the surface. The exact shape of the openings becomes complicated for gold depositions above the first half sphere layer (where they are circular)[71].

Viewed under an optical microscope, using white light, many different crystalline regions are visible on the electrode surface. Separate crystal domains show up, at 80 × magnification, as differently coloured patches on the gold film. These appear to be a few micron in size, which was confirmed by ESEM (figure 16).

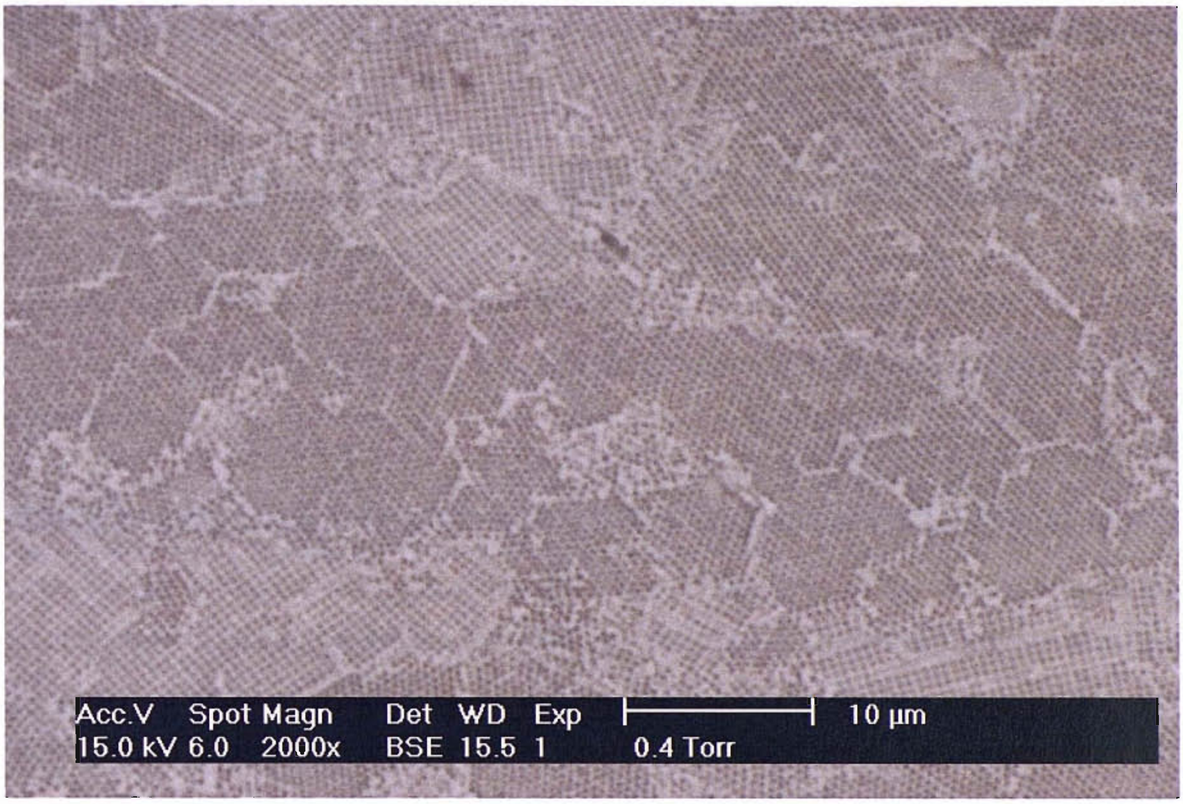

Figure 16. ESEM of gold macrostructure deposited onto a polished platinum disc of 0.5 mm diameter. Cavities are 500 nm diameter. Film thickness is 750 nm.

Crystal domains typically range from 40-100 μm^2. This is somewhat smaller than the domain sizes of 150 μm^2 and more reported by Bartlett *et al.*[70] who employed a similar sedimentation method to form the template (confinement within a Teflon ring for 2-3 days at 100 % humidity) and spheres of similar sizes (diameters of 500 and 750 nm). However Bartlett *et al.* did use evaporated gold slides as the substrate for their depositions and it might be the relative flatness (compared to the polished electrodes used here) that gives improved crystalinity.

The cavities appear to be arranged primarily in a hexagonal pattern over the surface of the electrode, but as much as 40 % of the surface adopts a square pattern. As mentioned earlier in section 4.2.2, the hexagonally arranged pores correspond to the (111) crystal planes in the original template and the square arrangement the (100) planes. Unfortunately the resolution of the Philips XL30 ESEM used to image the electrodes was not good enough to see the connectivity to the underlying cavities; as this would help confirm the bulk structure of the gold. In the work reported by Bartlett *et al.*[70] the connectivity can be seen: within the hexagonally arranged cavities, three smaller pores (marking the contact points between the spheres in the original template) are visible, in a triangular arrangement. High resolution images of (100) planes have been published by Xu *et al.*[76]. Four smaller pores are visible within the 300 nm diameter cavities and they adopt a square arrangement.

Bartlett *et al.*[70] were also able to view the bulk structure of the inverse opals they produced, by fracturing the slide substrates. Their results suggest that the sedimentation process leads to an entirely hexagonal close packed structure. From the film thickness and the charge passed during deposition they were able to calculate a void volume fraction of 60 ± 7.15 %; slightly less than the 74.05 % expected for perfect close packing. They suggest that the presence of domain boundaries account for this discrepancy; although it is also possible that other packing arrangements also exist within the structure such as body centred cubic arrangements (packing efficiency 68.02 %). Given the similarities in template sedimentation and infiltration methods employed in this work it seems safe to assume that the gold structure reported here have similar properties to those reported by Bartlett *et al.*

For an electrode where the template was very good (as in figure 16) the whole of the platinum disc is covered with gold; more than 90 % of this will appear as open structure in the ESEM images and the deviation in thickness is no more than a spheres diameter. However, sometimes the gold deposits show large areas without any structure. This can happen if the template is damaged or lost from a portion of the electrode (in this case these areas represent bulk, unstructured gold deposits). Or, as mentioned above (4.2.1), the spheres sometimes sediment less heavily on one side of an electrode and where the template is thinner it may be completely covered by even a thin deposit of gold (in this case there is likely to be open structure beneath the gold surface, figure 17).

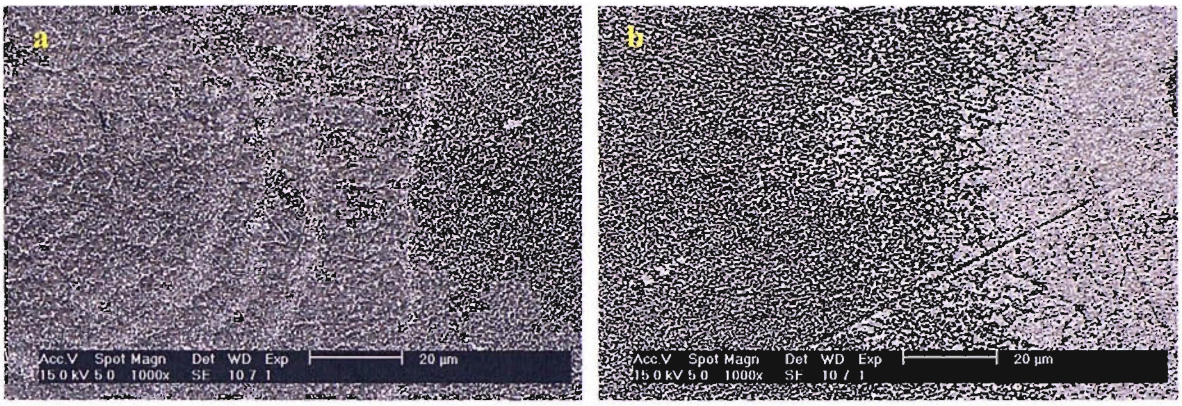

Figure 17. a) ESEM of gold macrostructure deposited onto a polished platinum disc of 0.5 mm diameter. Cavities are 500 nm diameter. Film thickness is 750 nm. **b)** the same electrode imaged just to the right of where the left-hand image ends.

Towards the far right of figure 17a the structure is starting to close as gold has been deposited very close to the top of the template. On the right-hand side of figure 17b the gold has completely covered the template, and is almost flat. It should be noted that for a gold film of approximately 750 nm, as imaged above, the surface topology of the platinum substrate is quite apparent; scratches of 1 µm and 0.3 µm across (corresponding to the particle sizes of the alumina slurries used to polish the platinum electrode) can be seen criss-crossing the surface in figure 17b.
Higher magnification images do not show the normal hexagonal and square arrangements of cavities because the gold has been grown to the limit of the template and in some places beyond.

It was difficult to deposit any gold films of greater than 1250 nm thickness (i.e. 2.5 × 500 nm spheres thick) that were completely structured. This was due to the problems encountered when trying to assemble thick, uniform sphere templates on electrodes of this type (described in 4.2.1).

4.5.3 Cyclic Voltammetry in Sulphuric Acid:

Cyclic voltammetry of platinum electrodes covered with thin films of structured gold show features for both metals (figure 18)[21,156]. The anodic current between 0.6 and 1.1 V is due to formation of gold oxide, which is accompanied by a characteristic stripping peak at 0.45 V on the cathodic sweep (analogous to that for platinum, palladium and rhodium in Chapter 3). Peaks for platinum oxide stripping (-0.01 V) and hydrogen adsorption/desorption (-0.35 to -0.6 V) are also present; although it is not possible to make out any current increase for platinum oxidation.

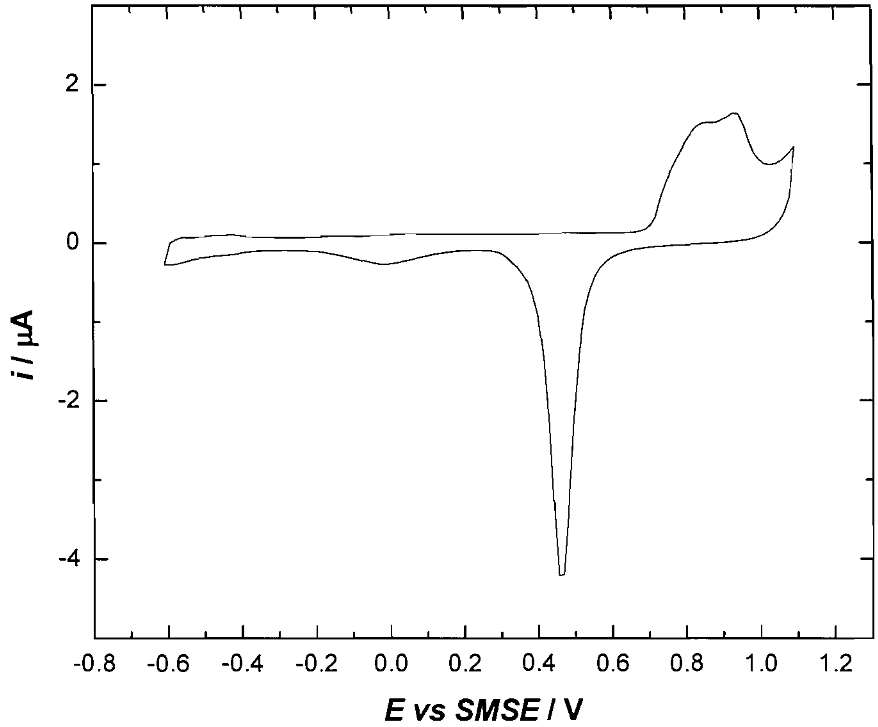

Figure 18. Cyclic voltammetry in 1 M sulphuric acid, $T = 25$ °C, purged with argon for 20 minutes. WE = 0.5 mm diameter polished platinum electrode with 250 nm thick deposit of structured gold (cavity diameter = 500 nm, i.e. ½ sphere layer). Sweep rate = 200 mV s^{-1}.

Many samples were made with gold deposits ranging in thickness from 250-1250 nm (i.e. 0.5-2.5 × 500 nm spheres height). These were cycled in acid; then sonicated in the same acid (in order to displace any pockets of air within the structure) and then cycled once again. Voltammograms recorded before and after sonication were the same; indicating that the gold structure wets readily. Addition of a surfactant to the acid was also used to try and improve wetting, with much the same result.

Therefore it is possible that the platinum features, seen in the sulphuric acid voltammetry (figure 18), are due to bare platinum where the spheres made contact with the substrate electrode. However, exposed platinum may also be due to flaws in the structure: where the gold deposition solution failed to penetrate the template or where the gold may have been damaged.

From the voltammetry it is possible to estimate the surface area of platinum exposed (see Chapter 3) and assuming the packing efficiency of spheres is approximately 85 % (this seems reasonable since packing of spheres at a two dimensional surface has a spatial efficiency of 91 % and 79 % for hexagonal and square arrangements respectively) it was possible to calculate the area of contact for each sphere. For well structured, continuous gold deposits values typically range from 4.12×10^{-10} cm^2 to 5.39×10^{-10} cm^2 corresponding to platinum discs of 230 nm and 260 nm diameter respectively (although values as high as 1.66×10^{-9} cm^2 and as low as 7.85×10^{-10} cm^2 were obtained). These values are less than the cross-sectional area of a 500 nm diameter sphere (1.96×10^{-9} cm^2) suggesting that the platinum features, in the acid voltammetry, are mainly due to contact with the template rather than defects in the structure.

The diameter of these contact points, between the structure and the substrate, were measured by Bartlett *et al.*[82]. Scanning force microscopy of gold cavities, electrodeposited onto evaporated gold slides, showed that 10 % of the central area of the cavities was flat. This contact disc was found to scale with the radius of the template spheres down to r = 100 nm. The contact disc area, between the template spheres and the platinum substrate, was estimated electrochemically (as described above) for several of the electrodes modified here. The results are summarised in Table 2.

Sphere d / nm	Sphere cross-section / cm^2	Area of contact / cm^2	% of flat surface
200	3.14×10^{-10}	1.13×10^{-11}	3.6
500	1.96×10^{-9}	4.12×10^{-10}	21.0
500	1.96×10^{-9}	5.39×10^{-10}	27.5
500	1.96×10^{-9}	4.80×10^{-10}	24.5
600	2.83×10^{-9}	2.78×10^{-10}	9.8

Table 2. Comparison of contact area, between template spheres and substrate (as calculated by cyclic voltammetry), with sphere cross-sectional area.

The percentage of flat surface at the bottom of the cavities reported above, differs slightly from that reported by Bartlett *et al.*[82]. It is important to note that the measurement of 10 % reported by Bartlett *et al.* is based on direct observations made with SEM and scanning force microscopy on samples deposited onto relatively flat substrates (evaporated gold slide compared to the polished electrode used here); whereas the areas of contact were estimated here by cyclic voltammetry of electrodes (electrodes with intrinsic surface defects such as holes and scratches which can increase the amount of exposed platinum).

The gold surface area can also be calculated from the acid voltammetry. Unlike the platinum surface area (which is understandably always within the same range), the gold surface area increases with the deposition charge. However the measured surface areas rarely match the theoretical values. For a good quality structured film the gold surface area should be significantly less than the total surface area of the template spheres. This is because of the points of contact between the spheres where gold does not deposit. These windows between the main cavities would appear to be of the same order of magnitude as the contact points between the spheres and the substrate (table 3).

Deposition Q / C	Sphere layers	Surface area from voltammetry / cm^2	Total sphere surface area / cm^2	ΔSurface area / cm^2	Window diameter / nm
2.9×10^{-4}	1.25	2.79×10^{-3}	8.84×10^{-3}	6.05×10^{-3}	258

Table 3. Estimation of contact window between 500 nm gold pores deposited onto a polished platinum electrode.

4.5.4 Conclusions:

Macroporous gold was successfully deposited onto polished platinum disc electrodes using 500 nm polystyrene latex spheres as a template. The current transients for gold reduction show a periodic oscillation which seems to correspond to variation in conducting surface area as the gold grows through the regular layers of spheres.

Upon removal of the template the gold deposits appear opalescent to the naked eye and ESEM images show regular arrays of hemispherical cavities in both square and hexagonal arrangements. While the connectivity of the pores is not visible (due to limitations in the resolution of the microscope) it is thought that the two arrangements represent the (100) and (111) planes of a close packed lattice of spherical voids (analogous to the particle array of the templates discussed in 4.2.2).

Cyclic voltammetry in sulphuric acid suggests that the gold structure is open (with cavities interconnected at the points where the original polystyrene spheres made contact with each other) and readily accessible to the aqueous acid solution. Furthermore the acid voltammetry provides a measure of gold and platinum surface areas which in turn allow for an estimation of the area of contact between spheres, and between the spheres and the platinum substrate. This varies from approximately 4 to 28 % of the cross-sectional area of the spheres and is in reasonable agreement to the contact areas of 10 % measured by scanning force microscopy[82].

4.6 Application of Macroporous Gold Disc Electrodes

This work was conducted in collaboration with Alexander Kuhn and his group at the University of Bordeaux[5]. Three macroporous gold electrodes with 500 nm cavities and film thickness of 1/2, 3/2 and 5/2 spheres were prepared and characterised here at the University of Southampton. These were sent to the Kuhn group in Bordeaux where the results described in the following section were obtained by Samia Ben-Ali. Full details of this work have been published elsewhere[85].

4.6.1 Catalysis of NAD$^+$ / NADH Electrochemistry:

Nicotinamide adenine dinucleotide (NAD$^+$/NADH) is a cofactor for approximately 300 enzymes, and is of great interest in the development of dehydrogenase based biosensors. However, high overpotentials are needed to drive the electrochemistry of NAD$^+$/NADH at most substrates. One method for overcoming this problem is to use mediators which catalyse the redox chemistry of NAD$^+$/NADH[157-159].

Recently a new family of redox mediators based on a nitrofluorenone skeleton has been developed[160-162]. These molecules form monolayers on various electrode materials like glassy carbon, gold or platinum. In this work the response of macroporous gold electrodes, to NAD+/NADH, was tested after decorating their surfaces with (4-carboxy-2,5,7-trinitro-9-fluorenylidene)malononitrile (figure 19).

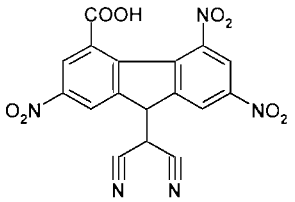

Figure 19. Catalyst: (4-carboxy-2,5,7-trinitro-9-fluorenylidene)malononitrile.

---

[5] Laboratoire d'Analyse Chimique par Reconnaissance Moléculaire, ENSCPB, Université Bordeau I, 16 Avenue Pey Berland, 33607 Pessac, France.

4.6.2 Cyclic Voltammetry in Sulphuric Acid:

Along with ESEM imaging this was used initially to assess the presence and quality of the gold structure. This was then repeated in Bordeaux after shipping to confirm that the gold layers were not damaged. Figure 20 (recorded in 0.5 M sulphuric acid) indicates that the whole surface of the porous gold film is accessible. Estimates of the surface area were made for each electrode from the charge under the gold stripping peaks (using the conversion factor of 386 μC cm^{-2} [124]). These were: 2.5, 8.6 and 20.9 $\times 10^{-3}$ cm^2 (for the ½, 3/2 and 5/2 sphere height deposits respectively).

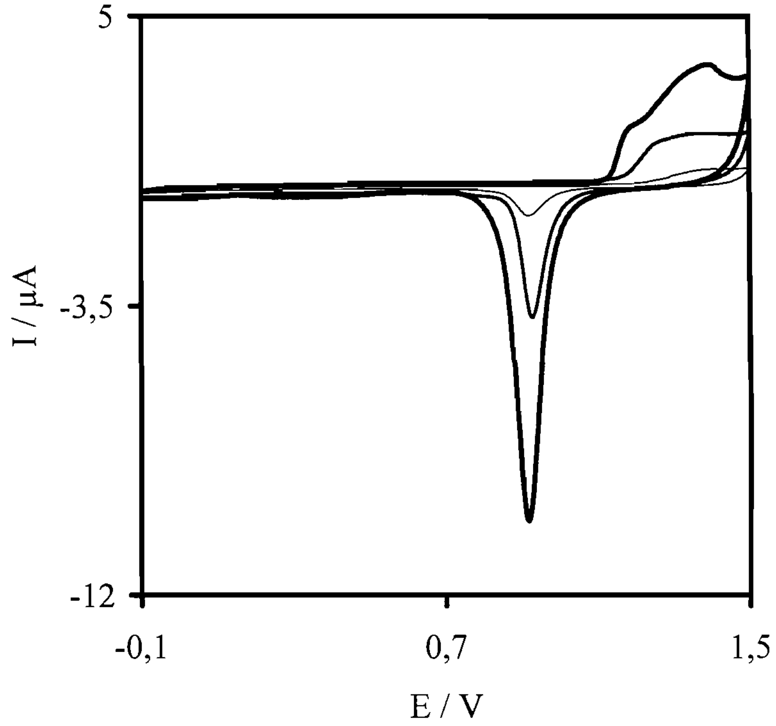

Figure 20. Cyclic Voltammetry in 0.5 M sulphuric acid purged with nitrogen for 15 min. Sweep rate = 100 mV s^{-1}. Ambient temperature 20 ± 2 °C. RE = commercial Ag/AgCl (3 M KCl). WE = 0.5 mm diameter polished platinum discs with macroporous gold deposits of 250 nm (thin line), 750 nm (medium line) and 1250 nm (thick line) thickness (i.e. 1/2, 3/2 and 5/2 × 500 nm diameter sphere deposits).

4.6.3 Electrode Modification with (4-carboxy-2,5,7-trinitro-9-fluorenylidene) malononitrile:

Figure 21 shows the characteristic peak for the 2 electron, 2 proton reversible R-NO/R-NHOH redox couple. This actually represents the convolution of two nitroso/hydroxylamine couples on each molecule of the catalyst. The peaks were integrated to calculate the charge and, thus, the surface coverage of the mediator. A similar result was obtained for each electrode: 2.9×10^{-11}, 3.0×10^{-11} and 2.1×10^{-11} mol cm^{-2} (1/2, 3/2 and 5/2 spheres gold deposits respectively); once again indicating that the whole of the gold surface is accessible, and that a monolayer of the molecule is formed in each case.

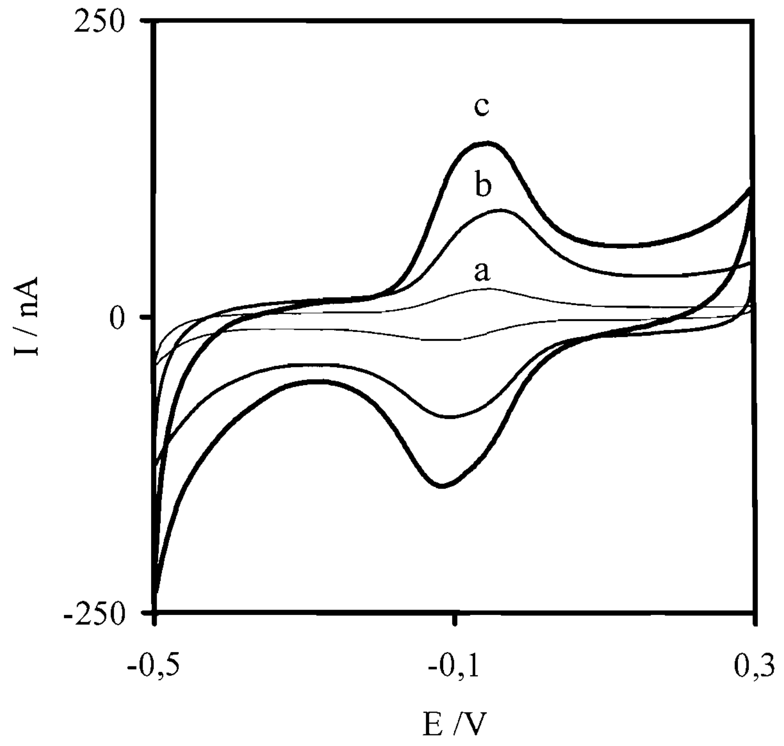

Figure 21. Cyclic Voltammetry in 0.1 M Tris buffer, ambient temperature 20 ± 2 °C, pH 8, purged with nitrogen for 15 min. WE = 0.5 mm diameter polished platinum discs with macroporous gold deposits of 250 nm (thin line a), 750 nm (medium line b) and 1250 nm (thick line c), after modification of electrodes with (4-carboxy-2,5,7-trinitro-9-fluorenylidene)malononitrile. Potentials reported vs Ag/AgCl, 3 M KCl. Sweep rate = 100 mV s^{-1}.

4.6.4 Mediation of NAD^+ / NADH Electrochemistry and Effect of Calcium ions:

As has previously been shown for polished gold electrodes[160,162], the presence of the nitroso mediator catalyses the oxidation of NADH (the overpotential is reduced by more than 500 mV, figure 22 A). Comparison of the three electrodes by voltammetry in 3.2 mM NADH/0.1 M Tris pH 8 shows that the catalytic increase in the current depends on the thickness of the gold deposit (figure 22 B). The ratios of the currents (taken at +100 mV vs Ag/AgCl) for the 5/2 and 3/2 sphere electrodes to the ½ sphere electrode (3.4 and 6.8 respectively) correlate well with the expected increases.

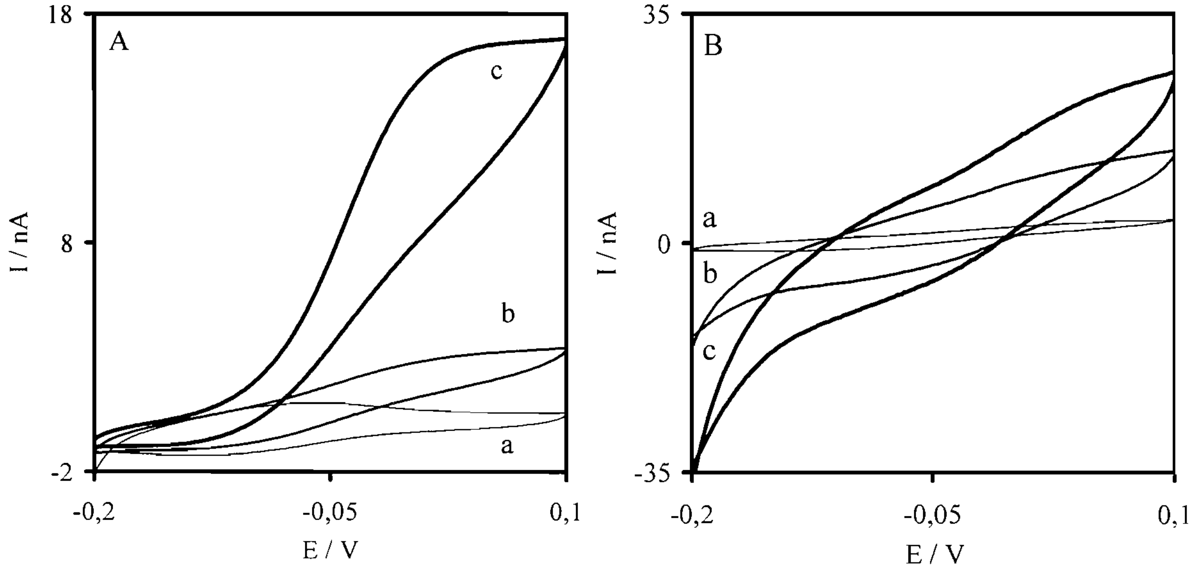

Figure 22. A) Cyclic voltammogram of ½ sphere, mediator modified electrode in (a) 0.1 M Tris pH 8, (b) in the presence of 3.2 mM NADH and (c) in the presence of 3.2 mM NADH and 0.2 M $CaCl_2$. B) Comparison of the catalytic currents in the presence of 3.2 mM NADH for 1/2, 3/2 and 5/2 sphere electrode (a, b and c respectively). Sweep rate = 10 mV s^{-1}, potentials reported vs Ag/AgCl, 3 M KCl.

Lastly addition of Ca^{2+} ions leads to an increase in the catalytic current of more than 500% (figure 22). Once again the ratios of the currents agree well with the predicted values (3.5 and 6.4). It is thought that the current increase is due to the temporary formation of a ternary complex (between the carboxyl group of the mediator, the calcium ions and the phosphate groups of the coenzyme), which facilitates charge transfer[85].

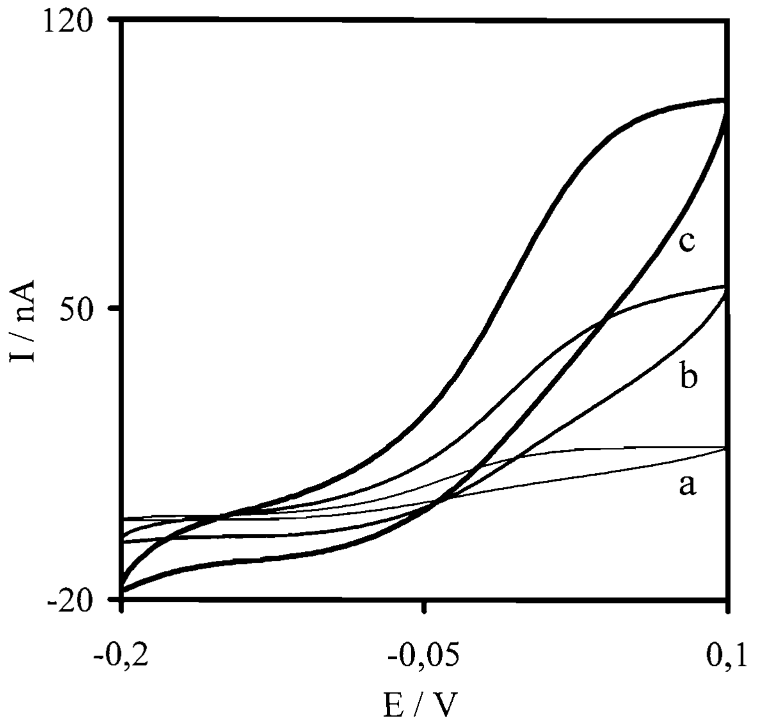

Figure 23. Cyclic Voltammetry in 3.2 mM NADH / 0.2 M $CaCl_2$ / 0.1 M Tris buffer, pH 8, purged with nitrogen for 15 min, ambient temperature 20 ± 2 °C. Comparison of the catalytic currents for 1/2, 3/2 and 5/2 sphere electrode (a, b and c respectively). Sweep rate = 10 mV s^{-1}, potentials reported vs Ag/AgCl, 3 M KCl.

4.6.5 Conclusions:

It has been demonstrated that macroporous gold electrodes can be modified on their entire inner surface with a redox mediator belonging to the nitrofluorenone family. The amount of adsorbed molecule increases linearly with the number of pores and the nitrofluorenone derivative acts as a very efficient mediator for the electrocatalytic oxidation of NADH freely diffusing from the outside into the pores.

The catalytic currents can be enhanced further by addition of Ca^{2+} ions. The electrode with the thickest (1250 nm, 5/2 spheres thick) modified, porous gold layer shows an increase in catalytic current of more than one order of magnitude compared to a modified, polished gold electrode of similar geometric area. It should be possible to produce gold films of greater thicknesses or with smaller pores and thus even greater surface areas.

4.7 Femtolitre Beakers

5 μm spheres were deposited onto conducting substrates (including polished platinum and silver along with evaporated gold and nickel slides) by sedimentation and then dried to form the templates for deposition of macroporous films. Metals were deposited to a height of ≤ 2.5 μm before dissolving the template in THF, to leave "cups" with volumes in the order of 30 femtolitres.

It might be possible to use such structures as arrays of discrete reaction vessels, immobilising bioactive molecules like proteins within the cups. There are several possible ways this could be achieved: for instance by thiol attachment where one or both of the metals comprising the cup is gold or by complexation with the metal surface through histidine residues attached to the protein. Depending on the metals that constitute the cup molecules could be immobilised indiscriminately over the structure or discretely; either on the substrate exposed at the bottom or on the metal plated on top.

It is known that histidine tagged proteins will complex to Ni(II) (and other 2+ metal ions) through the imidazole residues[163] (figure 24).

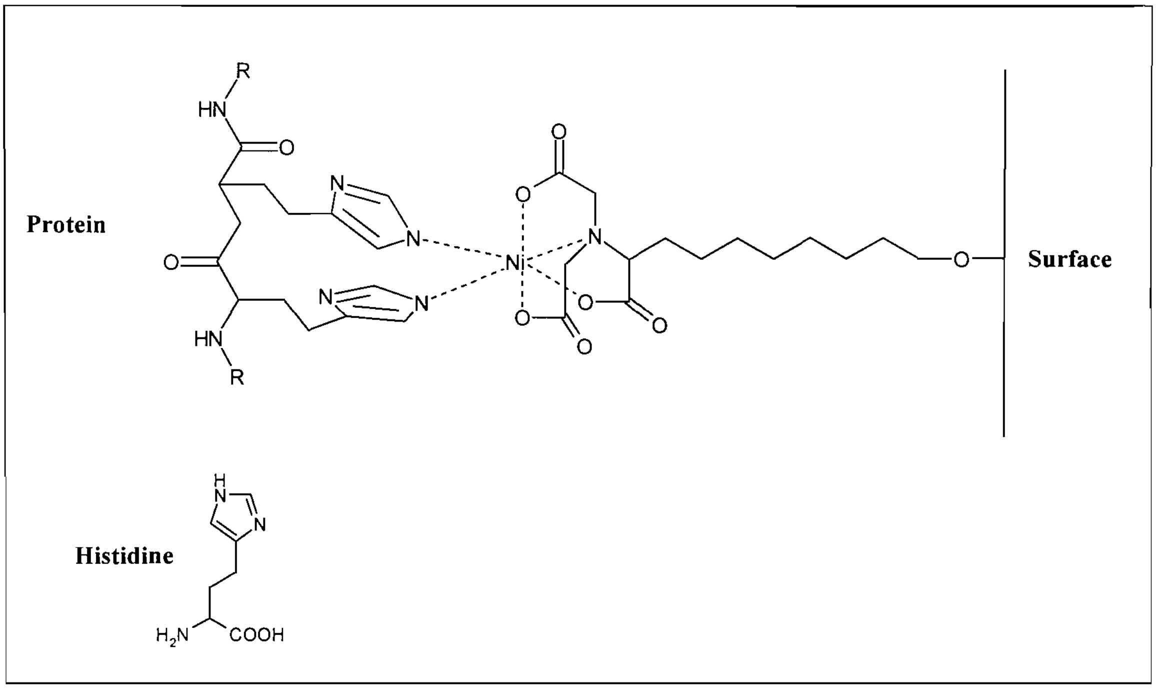

Figure 24. Histidine tag transition metal ion coordination.

Nickel was therefore chosen as a substrate for the femtobeakers and enhanced green fluorescent protein (EGFP[164,165]) was used as a test protein. EGFP has a β-barrel structure and three of its residues covalently bond in the centre to form a fluorophore (figure 25) which emits a green wavelength when excited by blue light (400 – 500 nm wavelength). In this work the outer structure of the EGFP was modified with a 6-histidine tag by site directed mutagenesis. It is hoped that these histidine residues will anchor the molecule to Ni(II) ions at the electrode surface.

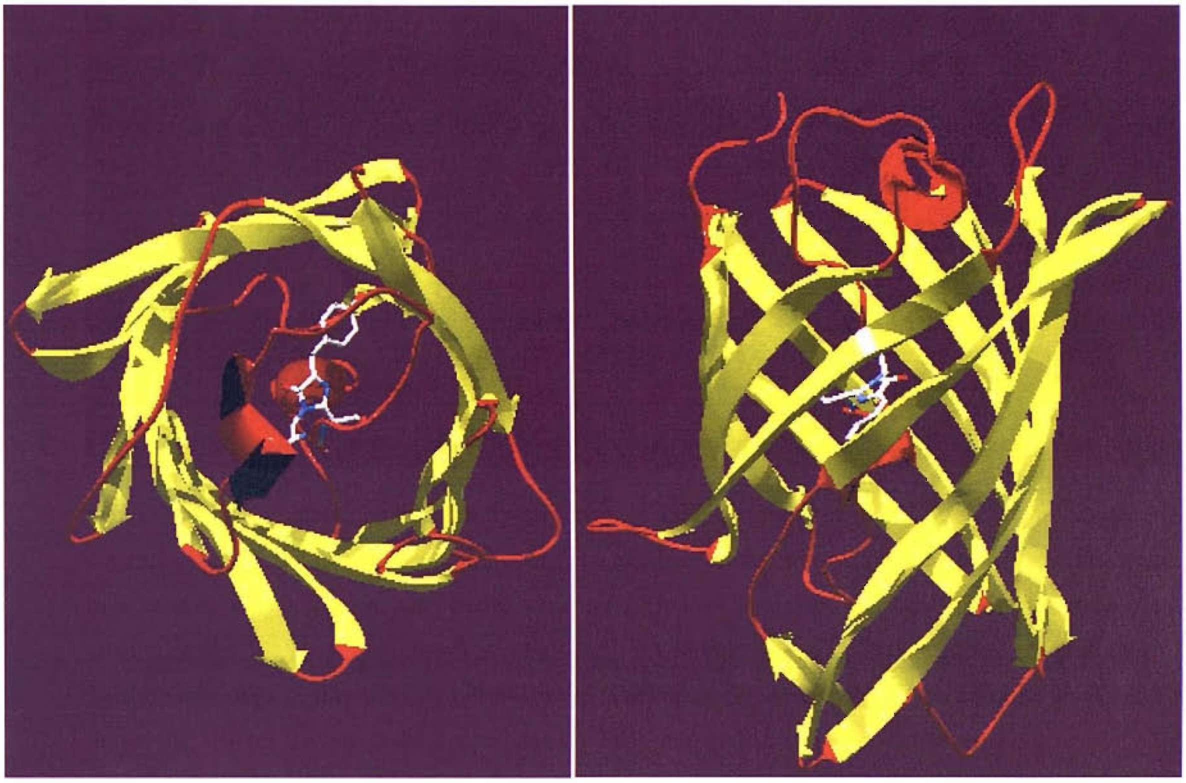

Figure 25. Image showing the tertiary structure of GFP modelled in Swiss-PdbViewer software (using crystallographic data reported by Palm *et al.*[166]) and edited using POV-RAY. The structure is made up of 11 beta strands which form a beta barrel structure (a hollow cylinder) through which is threaded a helix containing the chromophore (shown in a ball and stick representation). NB the crystallographic data for the GFP mutant used in this work is not available. The molecule used in this work contains F64L and S65T mutations, wheres the one in the image has only F64L and no histadine tag. However this does not affect the secondary structure or the site of the chromaphore.

4.7.1 Deposition of Macroporous Gold onto Nickel:

The templated nickel electrodes were not pre-soaked in the plating bath for 10 minutes prior to applying the deposition potential. This was unnecessary since the aqueous gold solution could easily permeate the monolayer of large spheres (in fact when electrodes were left to soak for up to 10 minutes the template was often lost). Figure 26 below shows a typical current time transient for the deposition of gold onto a 4 mm diameter polished nickel disc covered in 5 μm spheres.

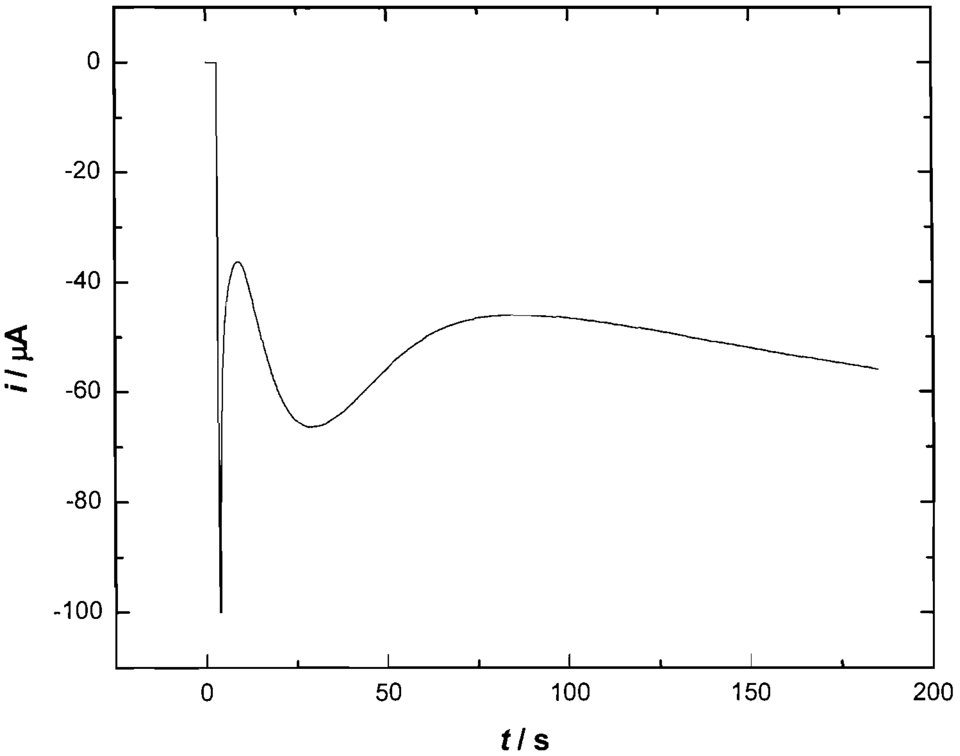

Figure 26. Chronoamperometry for deposition of macroporous gold. Solution is Techni Inc Gold 25 plating bath, T = 25 °C. WE = 4 mm diameter polished nickel disc covered in 5 μm polystyrene latex spheres. Applied potential = -0.9 V vs SCE. Charge passed = 9.44 mC (i.e. approximately ¼ sphere height deposit).

The deposition transient in figure 26 looks very similar to the initial portion of the transient for gold reduction through 500 nm spheres onto platinum, shown if figure 14 (although, a much higher current is observed here due to the larger surface area of the substrate electrode). There is a similar peak in the transient after the initial charging current. However since gold was never deposited to a thickness of more than $^1/_2 d$ (d = template sphere diameter) oscillations in the current are not apparent.

4.7.2 Characterisation of Macroporous Gold onto Nickel:

Upon removal of the template spheres the electrode surface appeared gold coloured and opalescent. The electrode was imaged using the Philips XL30 ESEM (figure 27). The left hand image would seem to suggest that there are nickel dots of approximately 1.6 μm diameter exposed beneath the gold deposit. However this could simply be a feature of the SEM detector arrangement. The gold structure acts like an array of tiny parabolas collecting and reflecting the electrons back to the BSE detector positioned directly above the sample surface. Indeed switching to the secondary electron detector (left hand image) which is not positioned above the sample, the structure would appear to be continuous, with no exposed substrate beneath the gold.

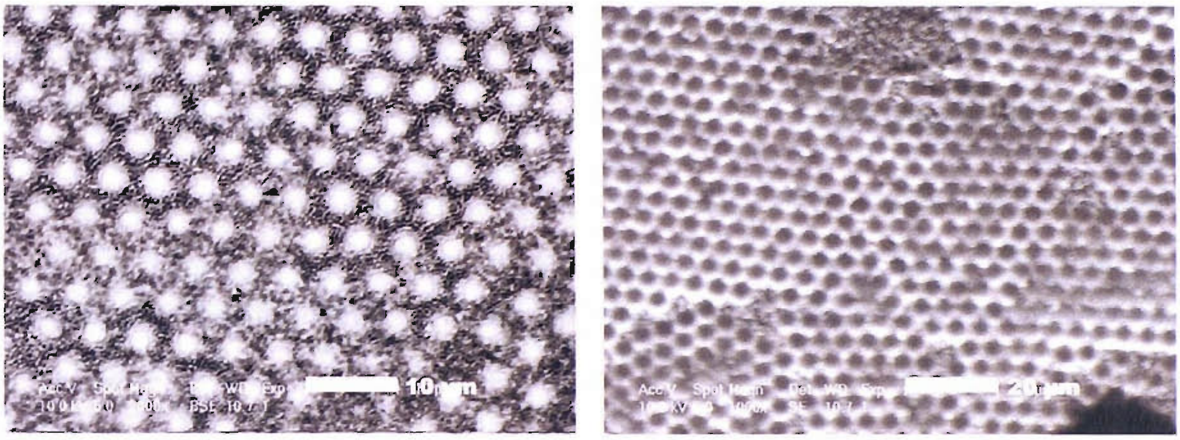

Figure 27. SEM of 5 μm gold structure deposited onto a 4 mm diameter polished nickel disc. Accelerating voltage 10 keV. **Left**: BSE detector, scale bar = 10 μm. **Right**: SE detector, scale bar = 20 μm.

The centres of the cups also appear brighter when viewed under white light impinging at 90° to the surface (figure 28). The pattern of light around the central spots would normally appear as a continuous ring for reflection unpolarised light, but this image was taken through a collinear polariser using plane polarised light. The simulation for polarised light reflecting from a surface in this way is shown to the right, and agrees well with the experimental observation.

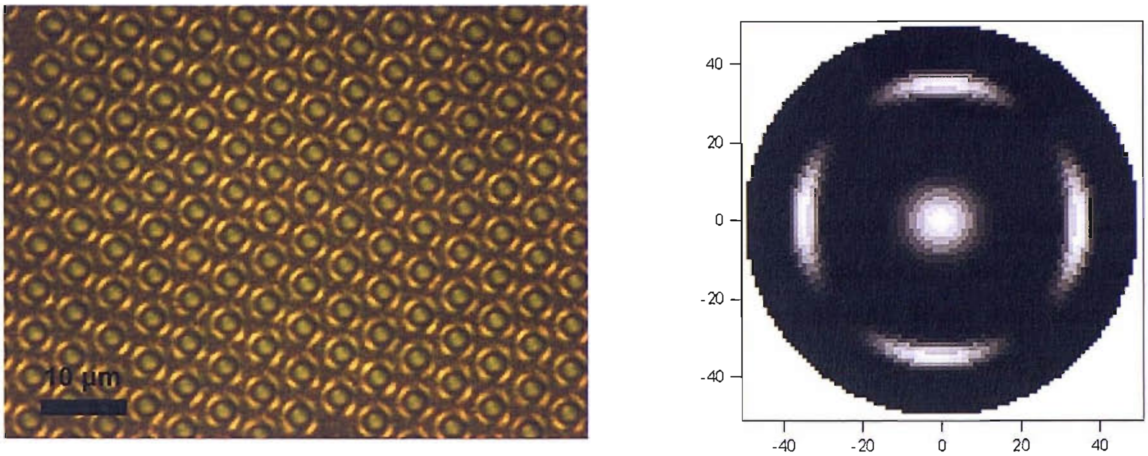

Figure 28. Left: image of 5 μm gold structure deposited onto an evaporated nickel slide, taken with an episcopic differential interference contrast microscope and a CCD camera, an X-Cite 120 metal halide source was used to illuminate the sample with plane-polarised white light. **Right**: simulation of reflected light intensity for polarised light entering a hemispherical cavity at 90° to the opening as viewed through collinear polariser.

The optical properties of similar "micromirror" structures have been reported by Bartlett *et al.*[71,81]. At each interface the light picks up a twist in linear polarisation due to the out-of-plane reflection geometry. Collinear polarisers only permit reflections that preserve the polarisation state, such as the single reflection off the bottom of the cavity[71].

The pattern of reflected light from the structure suggest that the gold really does form smooth, bowl like shapes at the nickel surface, but is still not possible to tell how much, if any, of the nickel is exposed at the bottom. In order to investigate this further 5 μm gold structures were deposited onto some evaporated nickel slides that could be fitted into the sample chamber of a more powerful SEM machine.

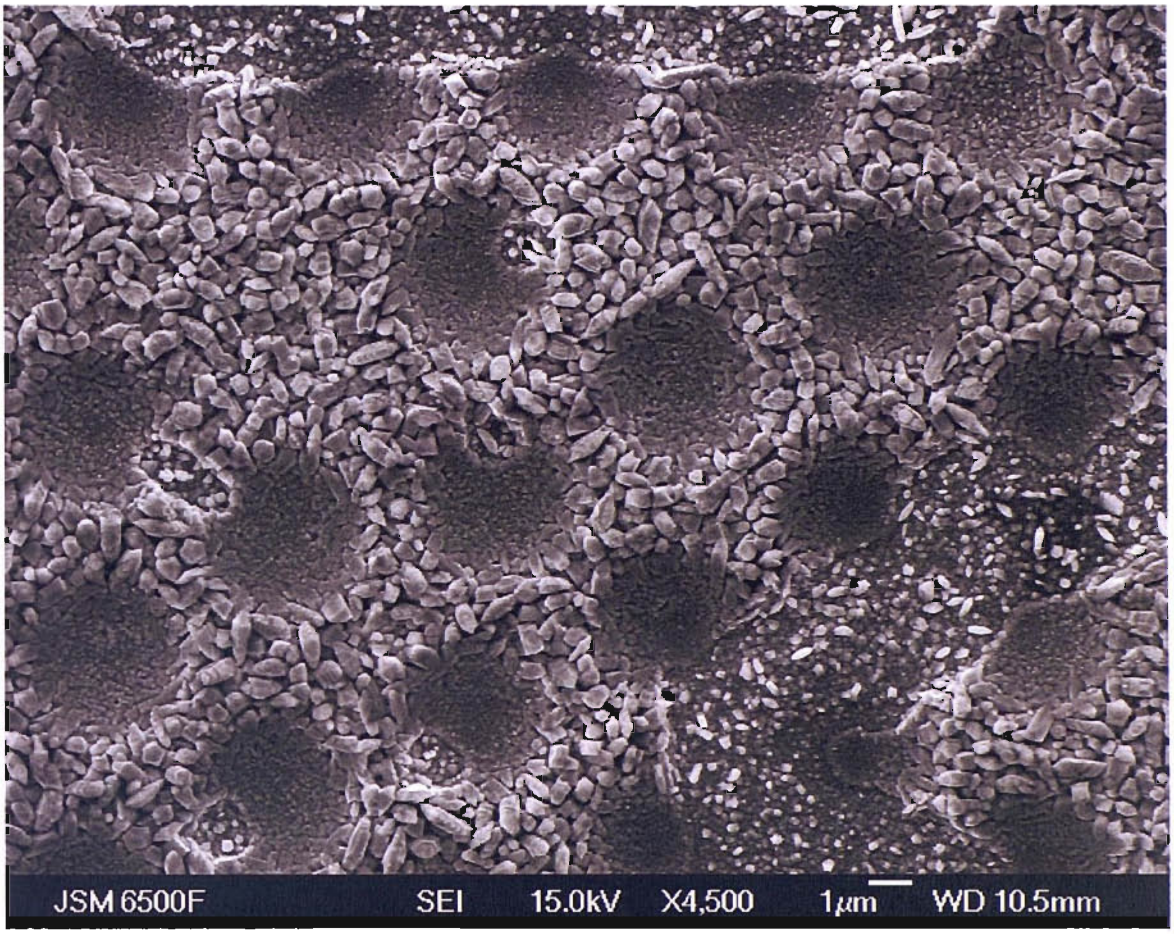

Figure 29. SEM image of a nickel slide with 5 μm gold structure. Experimental area was a disc of 5.7 mm diameter, defined using nail varnish. Charge passed for gold deposition = 0.241 C estimated to give a 2.5 μm gold layer (i.e. ½ a sphere height).

Figure 29 is an SEM image on one such slide taken with a JSM 6500F thermal field emission scanning electron microscope. The high resolution of figure 29 shows that the gold is quite rough in between the cavities and is composed of quite large crystals which are smoother where they have grown in contact with the spheres. There is no obvious distinction between the nickel and the gold over most of the structured film; although the gold is certainly very thin at the bottom of the cavities. EDX spectra recorded on these samples does show some nickel peaks. However this does not prove that the nickel is exposed since silicon peaks are also present; so it would seem that the x-rays are easily able to penetrate the thin layers of metal.

Voltammetry of the nickel-gold surface, in 1 M sulphuric acid, was used to help establish if the nickel was exposed and to see if the gold could be etched to expose more (figure 30).

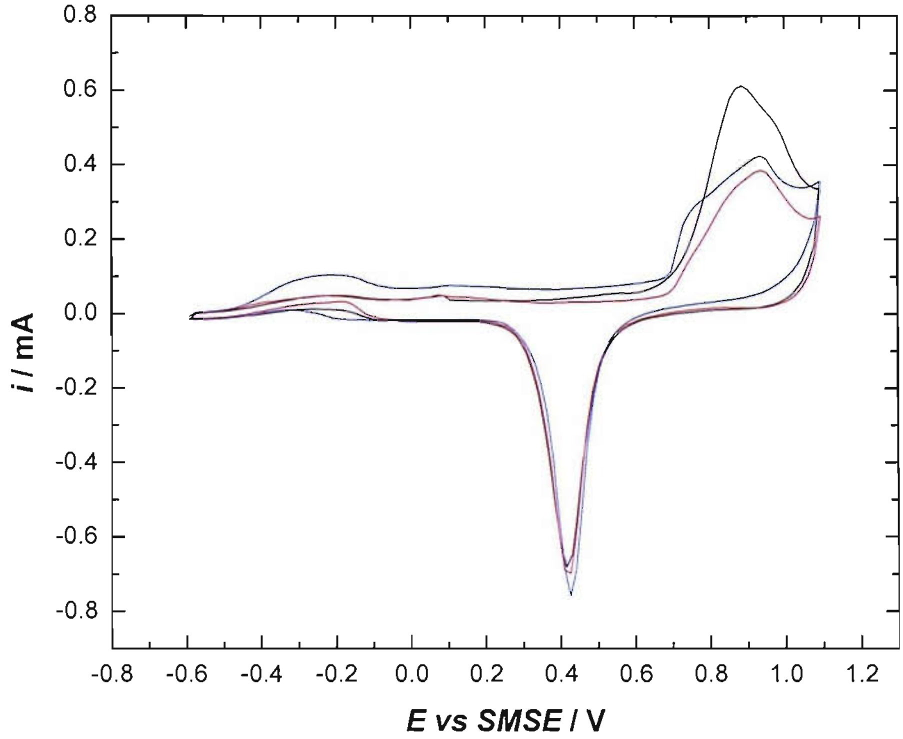

Figure 30. Cyclic voltammetry in 1 M sulphuric acid, *T* = 25 °C, purged with argon. 24 cycles. Sweep rate = 200 mV s^{-1}. Working electrode 5.7 mm diameter nickel disc with 5 μm macroporous gold structure deposited to approximately 2.5 μm thickness. — = 1st sweep, — = 2nd sweep, — = 24th sweep.

The voltammetry shows predominantly gold features, but with an extra peak at -0.25 V due to nickel oxidation[167]. This does not confirm that nickel is exposed at the bottom of the gold cavities as there may be flaws in the insulation of the nickel slide (that the structure was deposited on) or damage to the structure itself. The nickel peak was found to increase in size with cycling (blue line); although this is more likely to be due to the loss of insulation over the nickel slide rather than etching of the gold, since the gold surface area remains the same.

SEM imaging of the structure after the acid voltammetry does seem to show that the gold has been slightly dissolved to leave areas of exposed nickel. However EDX of most of these supposed nickel dots show no nickel peaks. Viewed under an optical microscope it becomes clear that not only the gold but also much of the nickel has been eroded during the acid voltammetry. Figure 31 shows that, when lit from below, light pours through the holes in the nickel layer.

Figure 31. Evaporated nickel slide with structured gold deposit of 5.7 mm (defined by masking with nail polish prior to gold deposition) diameter and 2.5 µm thickness. Structure was 5 µm diameter cavities. Taken with an Intel Digital Blue™ QX3+ microscope.

The amount of nickel exposed at the bottom of the structure might also be increased by improving the contact of the template spheres with substrate prior to gold deposition. So templated slides were heated to the glass transition temperature of the polystyrene latex for a short time (~90 °C for 1 minute) in order to make the spheres sticky[168]. Once the template had cooled the gold was deposited in the same way.

SEM images of these samples do show a clear break in the gold structure where the spheres were in contact with the substrate (figure 32). However, when compared to bare substrate (top right), the nickel still seems to have crystals of gold on it (left, top and bottom images). Much of the structure is interrupted by regions where the spheres seem to have melted into each other (bottom right). This is due to the poor temperature control of the oven used to heat the samples.

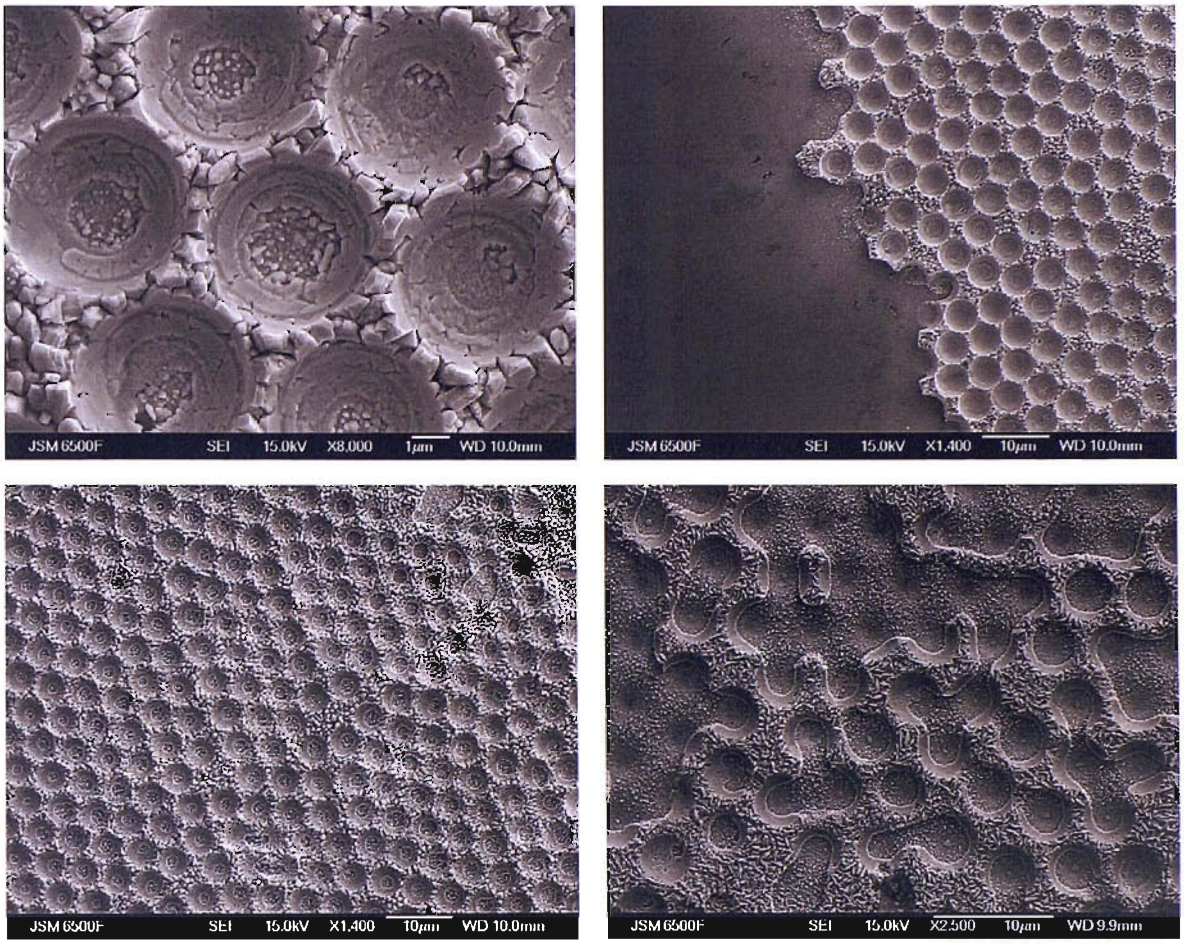

Figure 32. SEM images of a nickel slide with 5 μm gold structure. Experimental area was a disc of 5.7 mm diameter, defined using nail varnish. Spheres fixed prior to gold deposition by heating to ~90 °C for one minute. Charge passed for gold deposition = 0.241 C estimated to give a 2.5 μm gold layer (i.e. ½ a sphere height). Images taken with a JSM 6500F thermal field emission scanning electron microscope.

4.7.3 Immobilsation of his-tagged EGFP at Macroporous Surfaces:

5 μm structures of gold and platinum were deposited onto silver, nickel and gold substrates. These were soaked in a 50 μM his-tagged EGFP / 50 mM Tris buffer pH 8 at 4 °C overnight, and then removed, rinsed, and soaked in 50 mM Tris buffer pH 8 at 4 °C for 1 hour.

Samples were carefully dried and imaged using an episcopic differential interference contrast microscope and a CCD camera. Observations were as follows:

Gold structure on evaporated nickel slides:

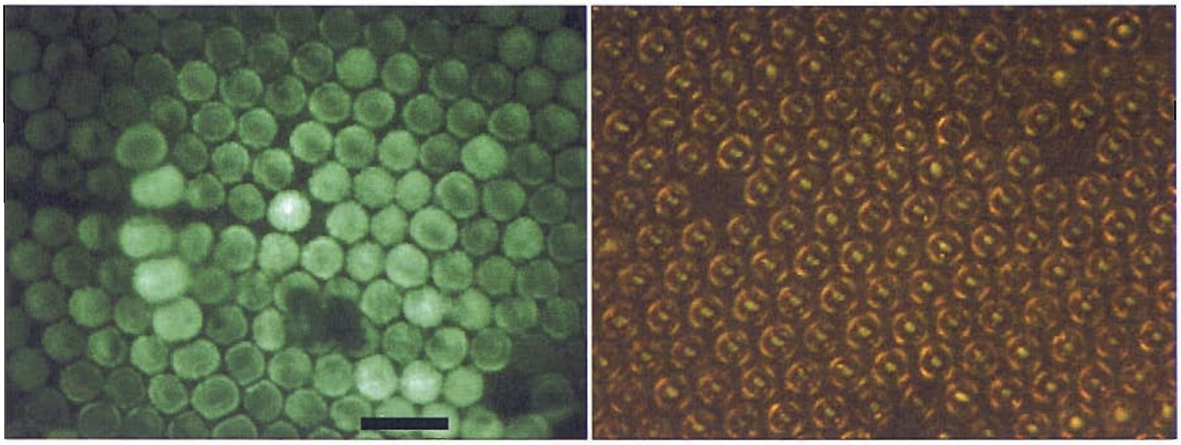

Figure 33. Digital images of 5 μm gold cups electrodeposited onto an evaporated nickel slide. Taken with an episcopic differential interference contrast microscope and a CCD camera, after soaking the sample in 50 μM his-tagged EGFP / 50 mM Tris buffer pH 8 at 4 °C overnight, and washing in 50 mM Tris buffer pH 8 at 4 °C for 1 hour. **Left**: blue light (λ = 400-500 nm) source impinging at 90° to sample. Scale bar = 10 μm. **Right**: polarised white light source (X-Cite 120 metal halide source) at 90° to sample. Same scale.

Figure 33 shows images of one of the samples that was soaked in the EGFP solution. When viewed under normal light (figure 33 right) the sample appears the same as before (figure 28), but under UV irradiation portions of the sample light up green. This is only the case for samples that were soaked in the his-tagged EGFP; samples soaked in blank tris buffer only, appear black under UV, reflecting little or no light. This suggests that the green colour is emitted from the chromophore of the EGFP as it is excited by the UV radiation.

However it is not possible to tell from this result how the EGFP is immobilised on the structure. It could simply be a residue of randomly, and weakly, adsorbed protein molecules on both the gold and the nickel; it may be bonded to the gold through thiol groups on the protein or it could genuinely be through complexation of the histadine to nickel ions at the bottom of the cavities. If the EGFP is randomly adsorbed on the surface of the electrode it would most likely be denatured and would not be UV active.

The path of light originating at the bottom of a hemispherical bowl (i.e. EGFP attached to nickel inside the gold structure) was simulated using the Raytrace simulation program (figure 34).

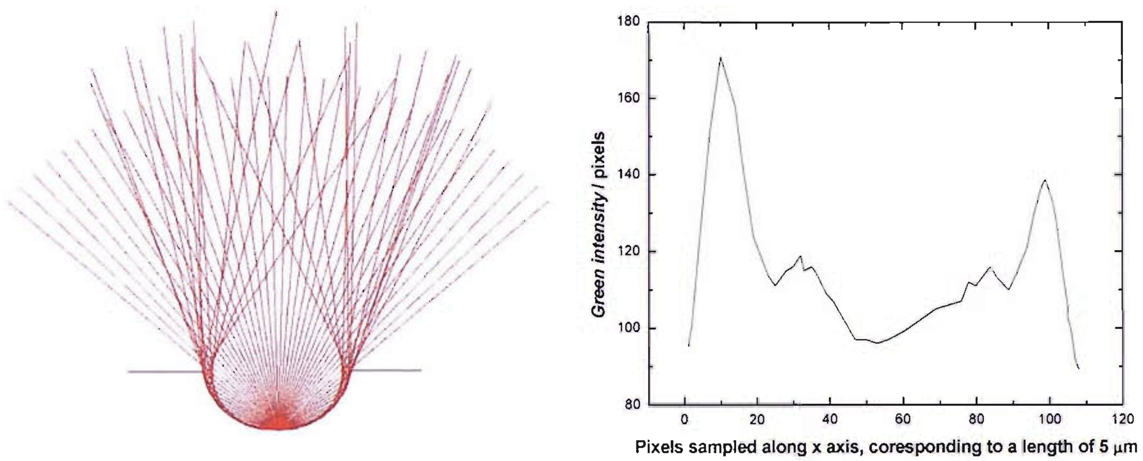

Figure 34. **Left:** Raytrace simulation of light source in the bottom of a reflective hemispherical bowl. **Right:** typical result showing the change in green colour intensity across one of the 5μm cavities as imaged in figure 33. This was achieved by analysis of figure 33a in SigmaScan® Pro. Lines were defined that bisected the 5 μm cavities, and the number of green pixels across these lines were plotted against the line length in origin.

This theoretical, 2D slice of structure suggests that there should be two rings of slightly greater intensity for the light emitting from each cavity: one at the very circumference of the hemisphere, and one just inside this. Referring back to figure 33, most of the cavities do seem to show two intense rings of light in these positions. The right-hand image in figure 34 shows how the green light intensity varies across one of the 5 μm cavities. This suggests that the EGFP, or at least the active EGFP, is located at the bottom of the cavities, and gives some weight to the theory that it is bound to the nickel through the histidine residue.

In order to establish whether the EGFP was bound to the gold or the nickel these experiments were repeated with new combinations of substrate and structure metals. These results are described below.

Gold structure on evaporated gold slides:

Under polarised white light, both before and after treatment with the EGFP solution, these samples show the same reflective pattern as for the gold on nickel samples. When viewed under UV the samples generally appeared black and featureless; although a few of the samples that had been modified with EGFP did show very faint greenish patches which appear to follow the pattern of the structure.

Gold structure on polished silver:

Once again these structures showed a similar reflective pattern to the gold on nickel samples when viewed under polarised white light. After treatment in the EGFP solution they did show some areas of green fluorescence, although this was much weaker than with the gold on nickel samples. Again the fluorescence seems to follow the pattern of the structure with the light emitting from the bottom of the cavities (figure 35). This is not so surprising since histidine is also known to complex with silver ions.

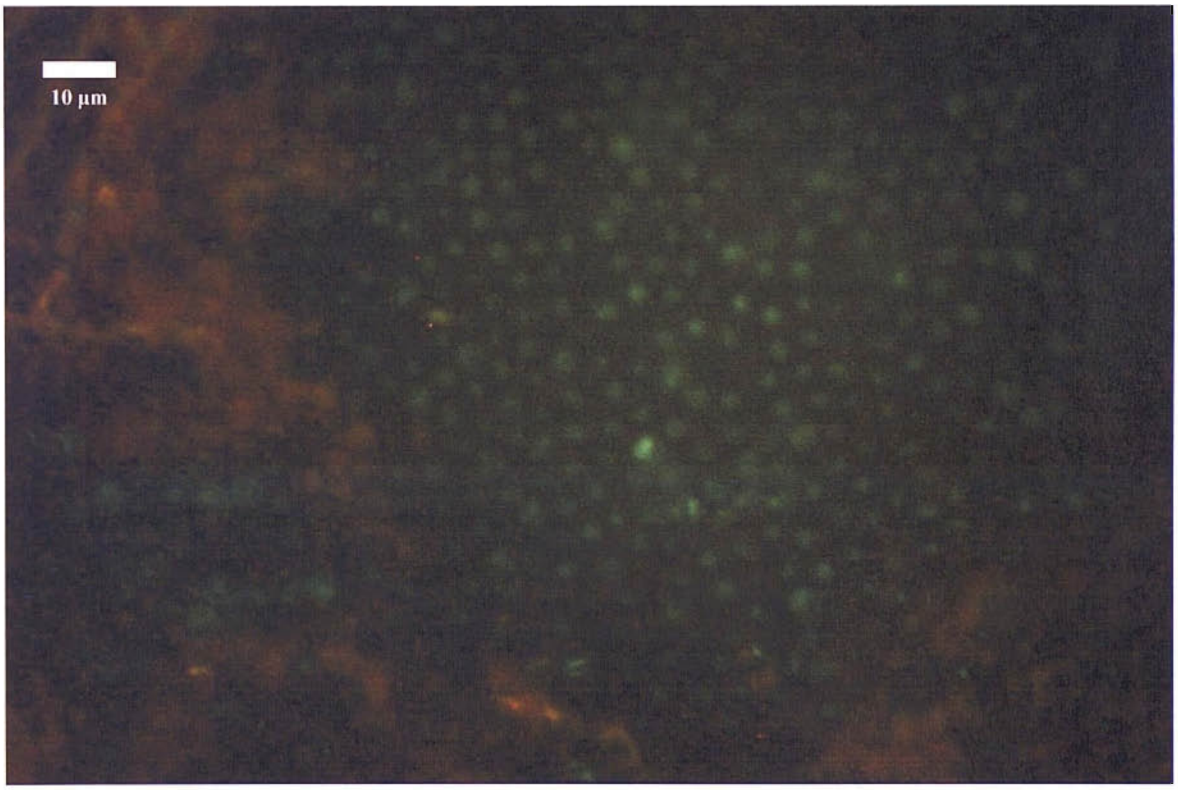

Figure 35. Digital images of 5 μm gold cups electrodeposited onto a polished silver disc. Taken after soaking the sample in 50 μM his-tagged EGFP / 50 mM Tris buffer pH 8 at 4 °C overnight, and washing in 50 mM Tris buffer pH 8 at 4 °C for 1 hour. UV light source at 90° to sample.

Platinum structure on evaporated gold slides:

The results were almost exactly the same as for the gold structure deposited onto evaporated gold slides.

Platinum structure on polished silver:

No meaningful results were obtained for these samples as the platinum films were found to be very mechanically unstable and peeled off of the silver.

4.7.4 Conclusions:

Macroporous gold and platinum was deposited onto nickel, gold, and silver substrates using close packed 5 μm polystyrene latex spheres as a template. Deposition to half sphere height was used to fabricate arrays of tiny cups on the substrates. These cups behave as reflective micromirrors under white light although ESEM at high magnification and fine resolution shows that they are not perfectly smooth.

Where the substrate metal is different from the deposited metal it is possible to form microcups with two distinct surfaces. Electrochemistry/chemistry might be performed preferentially on the parabola of the deposited material or at the microdot of substrate exposed at the bottom of the cup. Preliminary experiments reported here suggest that it is possible to selectively immobilise his-tagged EGFP at nickel (and perhaps to a lesser degree silver) dots at the bottom of 5 μm diameter gold cups.

4.8 Summary

Polystyrene latex spheres of 0.5 and 5 μm have been successfully assembled by sedimentation from aqueous suspension, at evaporated nickel and gold slides and also at polished platinum and silver disc electrodes. The quality of the packing is better for longer sedimentation times and for the larger spheres. The contact between the spheres and the substrate can be improved by heating the spheres to their glass transition temperature for a short time. Once dried, these spheres can be used to electrodeposit structured films of gold and platinum.

It has been demonstrated that macroporous gold electrodes can be modified on their entire inner surface with a redox mediator belonging to the nitrofluorenone family. The amount of adsorbed molecules increases linearly with the number of pores and the nitrofluorenone derivative acts as a very efficient mediator for the electrocatalytic oxidation of NADH freely diffusing from the outside into the pores. The catalytic currents can be enhanced further by addition of Ca^{2+} ions. The electrode with the thickest (1250 nm, 5/2 spheres thick) modified, porous gold layer shows an increase in catalytic current of more than one order of magnitude compared to a modified, polished gold electrode of similar geometric area. It should be possible to produce gold films of greater thicknesses or with smaller pores and thus even greater surface areas. Lastly it would seem from more recent experiments (not shown here) that the NAD^+ produced at these electrodes is enzymatically active.

The structured metal films from the 5 μm diameter sphere templates reflect light as tiny smooth hemispherical bowls. A tiny portion of the substrate remains exposed at the bottom of the hemispheres. Active his-tagged EGFP can be immobilized exclusively at the bottom of these hemispheres if the substrate electrode is able to complex with the histadine (i.e. nickel or silver).

Recessed Microelectrodes

5.1 Overview

As demonstrated in chapter 3 high surface area microelectrodes can be fabricated by electrodepositing a thin film of nanostructured metal onto the surface. However these films, while perfectly stable during most electrochemical procedures, are not mechanically very robust. Care must be taken not to touch the electrode surface as this can easily damage the mesostructure or displace the film altogether. In some cases the films simply fail to adhere to the electrode surface properly and are displaced during electrode rinsing between experiments (figure 1).

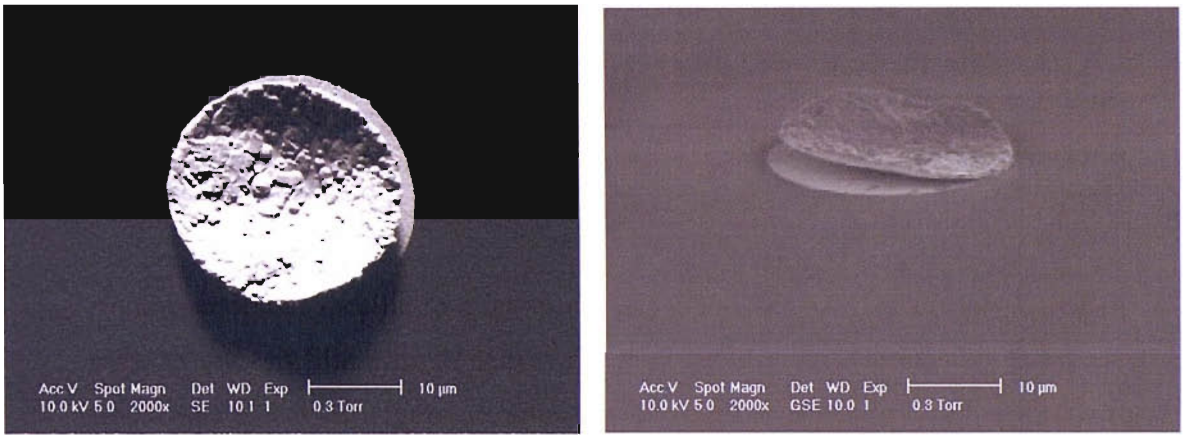

Figure 1. SEM images of a 25 µm polished platinum disc with a 1.3 µm H_I-ePt film taken with a Philips XL30 ESEM. **Left**: viewed perpendicular to gun. **Right**: viewed at 74° to gun and rotated 180°.

Another problem specific to microelectrodes is the high current density at the edge. This leads to uneven film growth and overspill of the deposit altering the geometric surface area of the electrode. Figure 2 shows how the radii of several (25 µm diameter) polished platinum microdiscs vary with deposition charge for electroplating with H_I-ePt films i.e. the radius appears to be proportional to the square root of the charge. Here the radii were estimated by cyclic voltammetry in ruthenium hexamine solution (see section 3.2.4) and were found to agree well with observations made by ESEM.

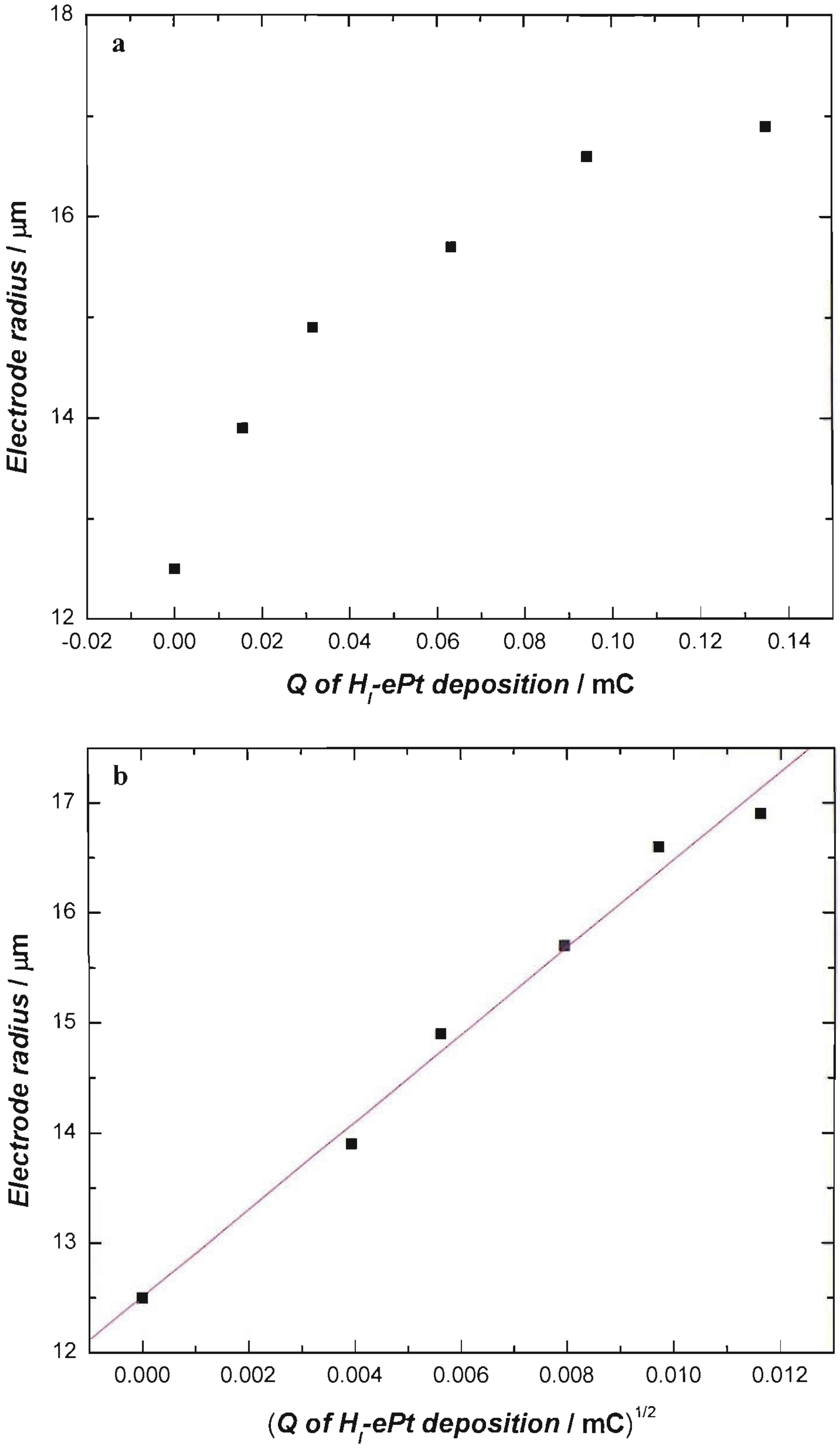

Figure 2. **a)** Plot of electrode radius (as determined by voltammetry in ruthenium hexamine solution) vs charge passed during H_I-ePt deposition. **b)** plot of electrode radius vs square root of charge.

The intercept value of 12.51 μm, from the linear regression in figure 2b, is as expected for the bare polished microdisc. This relationship shows that the mesoporous platinum films grow out radialy much faster than they increase in thickness.

In this work platinum microelectrodes have been electrochemically etched, to produce uniform recessed discs, with some degree of control over the depth. The cavities were then filled with lyotropic liquid crystalline phases in order to deposit thick nanostructures. Since the subsequent metal deposition occurs within the confines of the cavity there is no change in the geometry of the electrode. Also since most (or in some cases all) of the structure is below the level of the insulator it is protected from incidental knocks and scratches, this should make it mechanically more robust than a mesoporous film deposited onto a polished electrode.

Recessed microdiscs might also be advantageous for the immobilization of polystyrene latex spheres (to act as templates for deposition of macroporous films). In Chapter 4 polystyrene latex spheres were deposited at electrodes by electrophoresis. However it was found that the spheres had a tendency to wander away from the conducting surface during drying. It should be easier to confine the spheres at the electrode if its surface is recessed. Some preliminary results for macroporous gold deposition at recessed platinum microdiscs are reported here.

5.2 Recessing of Platinum Microdiscs

The method for recessing platinum microdiscs reported in this section cannot be found in the primary literature. Most of the interest in recessed microdiscs is concerned with modelling the effects of shallow recesses on electrodes that are mass produced by photolithography[169,170] (where the recess is inherent to the fabrication procedure). Other areas of interest include dissolved oxygen[171-173], pH[174] and glucose[175] sensors where recessed microdiscs have an advantage over inlaid electrodes in that they are less sensitive to solution flow rate.

5.2.1 Current Time Transients for Recession:

Aggressive potential pulsing, to ± 5 V vs a sacrificial carbon reference/counter electrode, was used to rapidly oxidise and reduce the platinum surface. This is done in an acidified calcium chloride solution (60 % saturated $CaCl_2$, 36 % H_2O, 4 % HCl). It seems likely that the high chloride concentration facilitates etching by forming soluble complexes with the oxidised platinum. There would appear to be no literature on recessing platinum microdiscs by electrochemical etching and this method is actually reported for the etching of microwires to produce fine points for SECM (scanning electrochemical microscopy) tips[176]. A typical current time transient for this process is given in figure 3.

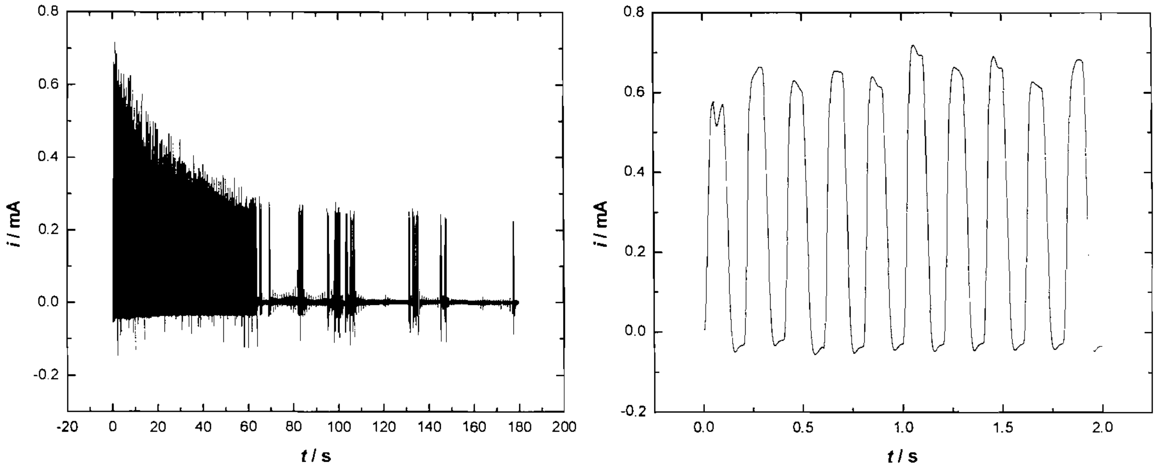

Figure 3. Current time plot for a potential pulsing experiment to recess a platinum microdisc. **Left**: the full 180 s of data. **Right**: the first 2 s expanded to show some detail. WE = 25 μm polished platinum disc set in glass; CE/RE = vitreous carbon. Solution = 60 % saturated $CaCl_2$, 36 % H_2O, 4 % HCl by volume, $T = 20 \pm 2$ °C. Applied potentials ± 5 V (each pulse for 0.1 s). Potentials applied from and recorded using an Autolab potentiostat/galvanostat and the accompanying Gpes manager software.

Figure 3 shows the current time transient for a 180 second etching experiment. High currents are recorded during both the positive and negative potential pulses (although the currents for platinum oxidation are by far the greater of the two). The currents may decay during the course of the experiment as bubbles are formed at the electrode surface. The current is also suppressed by platinum waste fouling the electrode surface; a black scum can often be seen clouding the solution below the electrode. The currents and rate of etching can be improved by tapping the electrode gently to remove bubbles and the platinum products that build up on the surface; although this does become more difficult as the recess deepens.

A strong correlation between recess depth and charge passed has been observed for electrochemical etching of carbon fibre microdiscs[172], and a similar relationship is expected for the platinum etching here. The charge passed during several of the recessing experiments was estimated from the current peaks (as in figure 3) and this was found to correlate quite well with the observed recess depth (figure 4).

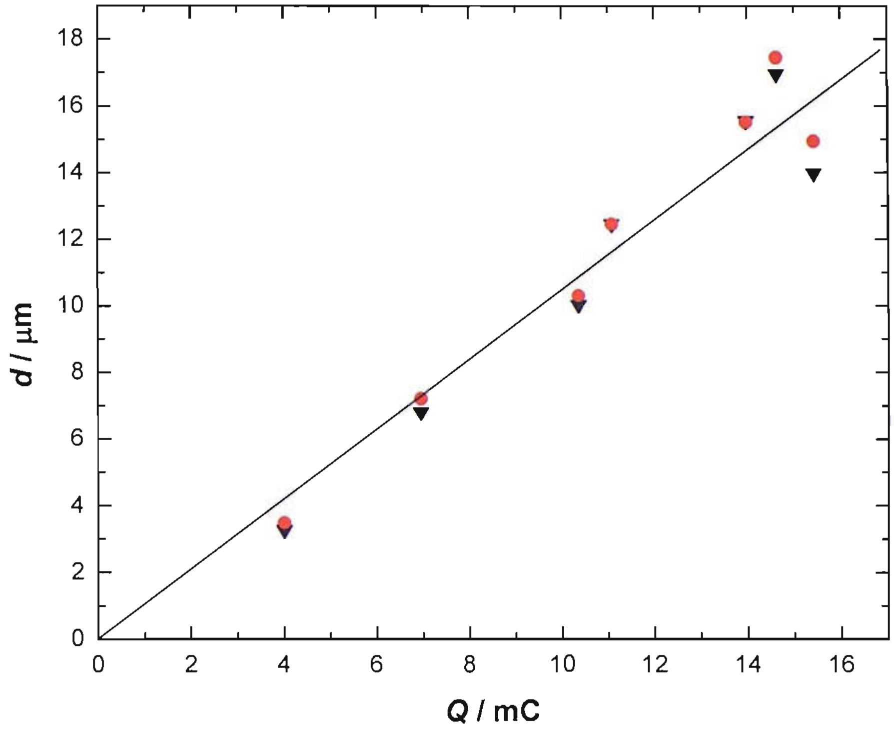

Figure 4. Plot of recess depth (*d*) versus charge passed during etching process (charge taken as the sum under all peaks both positive and negative). **Red circles**: depth as estimated from ESEM measurements (detailed in section 5.2.4). **Black triangles**: depth as estimated from cyclic voltammetry in ruthenium hexamine solution, using the Bartlett method (detailed in section 5.2.4). **Line**: linear regression of data (r = 0.97, SD = 1.2, gradient = 1060 µm C^{-1}). All working electrodes were polished 25 µm diameter platinum discs set in glass.

From the gradient of the slope in figure 4 it was estimated that the charge passed to dissolve each platinum atom was ~ 2.61×10^{-17} C. This suggests that most of the charge is not associated with platinum oxidation (since a charge of 2.61×10^{-17} C per atom would imply that the oxidation was a ~ 160 electron process). A large portion of the total charge is due to electrolysis of water, some is non-Faradaic double layer charging current and some is no doubt due to oxidation and reduction of products (i.e. platinum salts) trapped in the recess. Nonetheless the total charge correlates quite well with the recess depth over this range.

In this work electrodes were recessed in batches (four to ten electrodes etched in the same solution one after another) where each electrode was pulsed in the etching solution for a different time (10-240 seconds typically) and then the depth of the recesses were estimated later (methods for this are described in 5.2.4). However figure 4 suggests that it should be possible to recess electrodes to a specified depth (with some accuracy) by monitoring the total charge passed during etching.

Some recessing experiments were also performed using a PPR1 waveform generator and a homemade current follower. However it was not possible to record the charge passed, or the exact currents during these experiments due to the limitations of the current follower.

5.2.2 Characterisation by ESEM:

The recess depths obtained in this work were relatively shallow (typically less than the diameter of the microdiscs, 25 μm) so it was possible to image the platinum surfaces before and after etching. The Phillips XL30 ESEM was used to view the electrodes as bulky samples can be easily manipulated and moved in the large vacuum chamber. Also the wet mode allows imaging of the non-conducting glass substrate around the electrode.

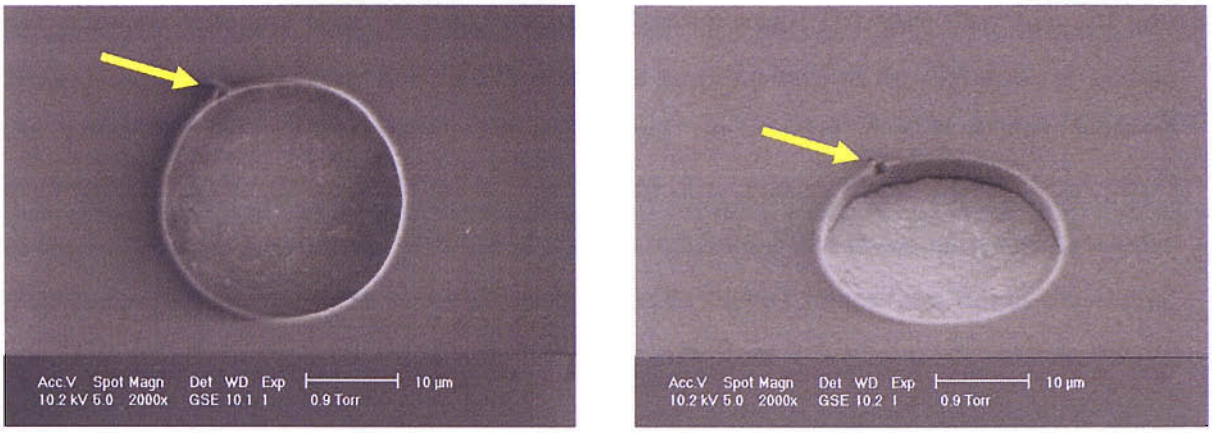

Figure 5. 25 µm Pt disc sealed in glass, recessed by approximately 3 µm. **Left:** electrode surface perpendicular to the electrode beam. **Right:** sample tilted by 41°.

When the microdisc electrodes are made, tiny bubbles are often trapped against the platinum wire as it is sealed in the glass. These are often exposed during etching, and one is visible in the images above (arrows).

Figure 5 shows a typical etching result. Tilting and rotating the samples in the ESEM shows that the platinum is recessed evenly with the glass around it being stripped clean.

Bond *et al.* report the chemical etching of gold microdiscs in aqua regia[177]. Gold microwires of 25 µm diameter were sealed in soda glass and polished (in a similar procedure to that used to fabricate the platinum microelectrodes in this work). These were etched in a stirred solution of one part analytical grade HCl to three parts nitric acid for 5-30 minutes. The depths of the recesses were measured to an accuracy of ± 10 µm by polishing away the glass from one side of the microwire and viewing under a calibrated microscope. Bond *et al.* also found that while the surface of the electrode was roughened there was no obvious convex or hemispherical shape caused by the etching.

This is unlike the case observed for electrochemical recessing of carbon microfibres. Morita *et al.* report the electrochemical etching of carbon fibre microelectrode arrays[172,173]. These were fabricated by extruding 1000, 6.93 µm diameter, high strength carbon fibres through an epoxy resin. After curing these composites were set in a polyethylene tube and fixed in place with more epoxy resin. The tube was then cut into sections with one end being polished to make the working face of the electrode array and the other bonded to a standard electrical lead for contact during electrochemical experiments. Etching was achieved by application of a constant current (> 800 mA cm^{-2}) in a solution of 2 M sulphuric acid/0.2 M sodium sulphate. SEM imaging of the electrodes after recessing showed the carbon fibres to be bullet shaped rather than flat at the etched end. The length of the bullet tips was found to range from 2.5-13 μm (depending on the overall length of the recess)[173].

5.2.3 Characterisation by Cyclic Voltammetry in Sulphuric Acid:

Occasionally electrodes needed sonicating to get the solution into the recess, but the voltammetry of polished and recessed platinum microdiscs is quite similar (figure 6). The acid voltammetry suggests that the platinum remains smooth and even during the etching process. The roughness factor (i.e. the observed surface area/the theoretical surface area, for a perfectly smooth electrode of the same dimensions) for the electrode in figure 6 was calculated as 1.9 and 1.8 before and after etching respectively.

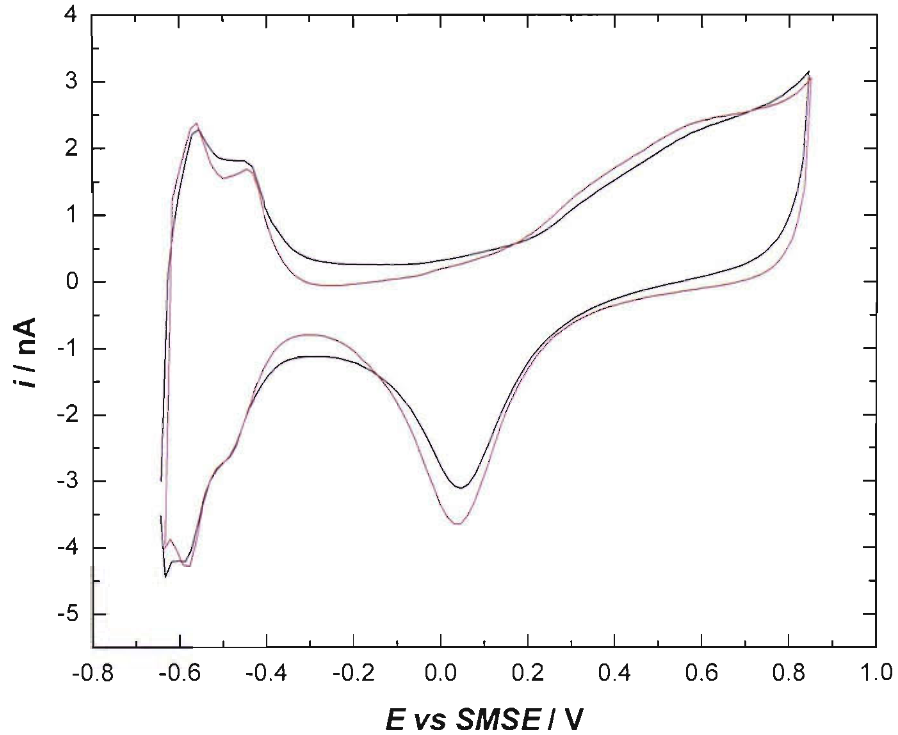

Figure 6. Cyclic voltammetry in 1 M sulphuric acid, T = 25 °C, purged with argon for 20 minutes. Sweep rate = 200 mV s^{-1}. **Red line**: WE = 25 μm polished platinum disc. **Black line**: WE = same electrode after etching (recess ≈ 3 μm).

5.2.4 Estimation of Recess Depth:

The recess depth was estimated by three methods: one using the images obtained from the ESEM and the other two based on electrochemical measurements. These three methods were compared in order to establish which was the most practical and accurate.

1. **Trigonometry on ESEM images:**

This was achieved by recording two images of the electrode: one at 90° with the disc perpendicular to the electron beam and one after tilting the stage to some angle that exposes the inside wall of the recess (figure 7).

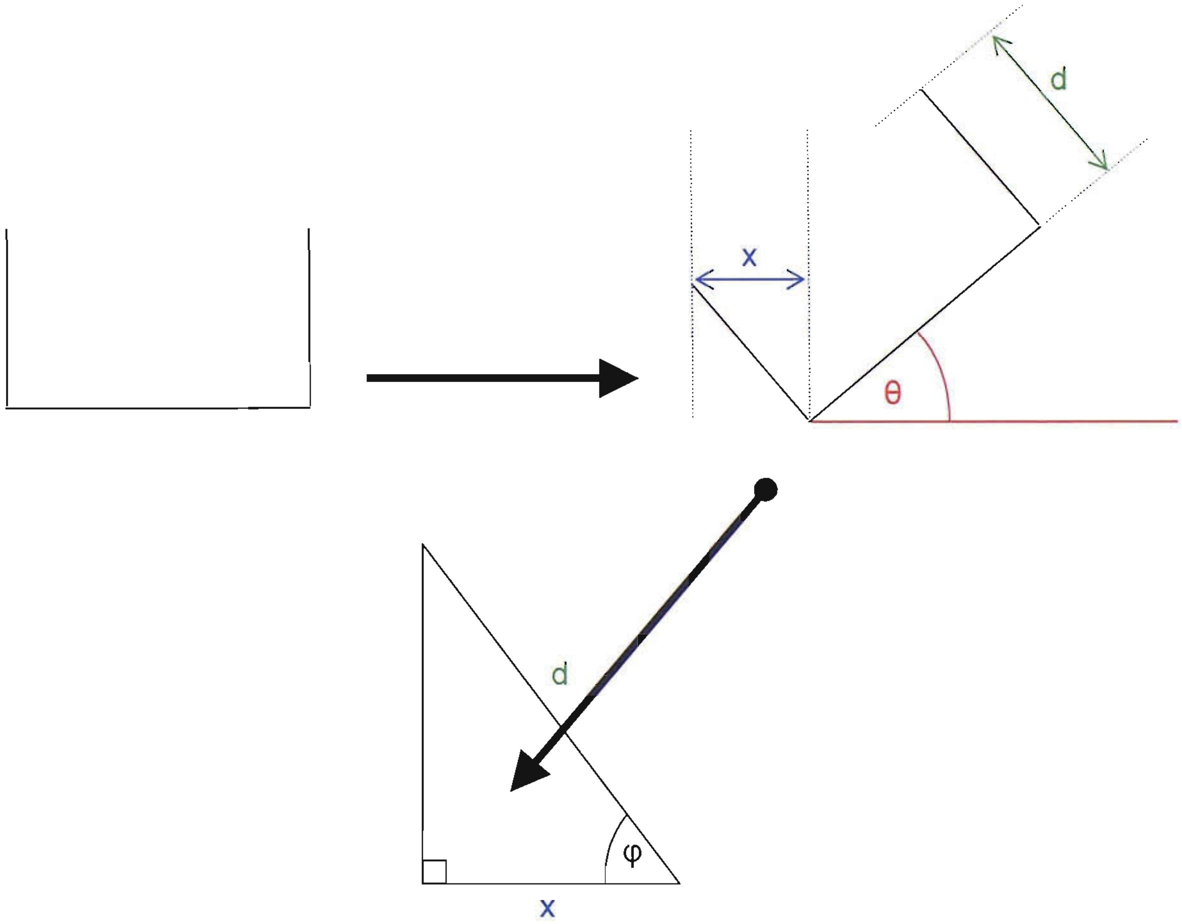

Figure 7. Schematic illustrating the trigonometry used to estimate the recess depth of platinum.

Where:

θ = the angle to which the sample is tilted in the SEM.

x = the length of recess wall exposed (as seen in the SEM image).

d = depth of the recess.

φ = 180°-90°-θ.

Therefore since:

$$\cos\phi = \frac{adjacent}{hypotenuse} \qquad \mathbf{1}$$

Then:

$$d = \frac{x}{\cos\phi} \qquad \mathbf{2}$$

2. Bond method:

The behaviour of recessed and inlaid microdisc electrodes (of identical radii) under chronoamperometric conditions was compared theoretically and experimentally by Bond *et al.*[177]. The situation for a sudden change in electrode potential, at t = 0, from equilibrium to a value sufficient for mass transport controlled oxidation/reduction was considered. Starting with the solution for steady state current at an inlaid microdisc (equation 3):

$$i = 4nFc^{b}Da \qquad \mathbf{3}$$

Where:

D = the diffusion coefficient of redox species.

n = the number of electrons involved in the reaction.

F = Faraday constant (96485 C mol^{-1}).

c^b = the bulk concentration of the redox species.

a model for a recessed disc (of similar dimensions and under similar conditions) was developed.

It was assumed that the concentration of the redox species (R) is uniform across the mouth of the recess and denoted c^m. This value (c^m) will differ from the bulk concentration of R (c^b) if the solution is quiescent but will be the same for a stirred solution. Bond *et al.* assume that there must be a linear concentration profile of R in the recess for a steady state to exist within. If the concentration of R is zero at the electrode surface and c^m at the mouth of the recess, then:

$$\frac{i}{\pi n F a^2} = D\frac{dc}{dx} = D\frac{c^m}{L} \qquad \textbf{4}$$

Where: L = is the recess depth (d) divided by electrode radius (a). Diffusion from the bulk to the recess mouth must mimic steady-state diffusion to an inlaid disc, as given by equation 3 but with c^b replaced by c^b- c^m:

$$i = 4nF(c^b - c^m)Da \qquad \textbf{5}$$

Equations 4 and 5 relate to the same current and may be solved to give the concentration of R at the pore mouth:

$$c^m = \frac{4Lc^b}{4L + \pi a} \qquad \textbf{6}$$

Hence the steady-state current at the recessed disc is:

$$i = \frac{4\pi n F c^b D a^2}{4L + \pi a} \qquad \textbf{7}$$

Therefore the recess depth (d), of a microdisc, can be calculated by comparison of its steady-state current to the steady-state current of a similar inlaid electrode using:

$$f_{ss} = \frac{\pi}{4L + \pi} \qquad \textbf{8}$$

Where:

f_{ss} = is the steady-state flux (from $i_{L\ recessed}/i_{L\ inlaid}$), and,

L = is the recess depth (d) divided by electrode radius (a).

This works best for deep recesses where $L \geq 1$ (as explained below).

3. Bartlett method:

The main shortfall of the Bond equation is in their assumption of a uniform concentration profile across the recess mouth. By calculating the near steady-state concentration profiles across the recess mouth for a range of depths Bartlett *et al.*[178] were able to show that for an L of 2 the concentration change across the recess mouth is about 10 % and varies quite gradually, while for an L of 0.1 or 0.025 (typical values seen for the shallow recesses produced by photolithography) the change in concentration is much greater and the profile alters sharply from the disc centre to the recess edge. Therefore the theoretical steady-state mouth concentration, c^m, derived by Bond *et al.*[177] (equation 6), indicates a lower overall mouth concentration for the shallow recesses, but does fit better for the deeper recesses.

Although Bond *et al.* do make the shortfalls of their model clear; it has been inappropriately applied to shallow, recessed, arrays[179-181] and single microelectrodes[182] by several workers. Consequently some efforts have been made to model such electrodes more accurately by finite element methods (FEM)[183]. In 1997 Ferrigno *et al.*[184] employed a commercial FEM package to numerically simulate the chronoamperometric response of recessed and protruding microdiscs, under transient and steady-state conditions (the purpose of this work was primarily to overcome the problems inherent to numerical simulation of the chronoamperomertic response of inlaid microdiscs i.e. the singularity at the electrode edge due to the conflicting Neumann and Dirichlet boundary conditions[169,185,186]).

Bartlett *et al.* found that the model proposed by Ferrigno *et al.*[184] shows considerable discrepancy between theoretical and experimental results and attribute this to instabilities in the mesh during refinement. Bartlett *et al.* provide a better model based on custom made FEM simulation software, using a more stable hopscotch algorithm[187]. This gives a more accurate prediction of transient and steady-state responses at both deep and shallow recessed microdiscs. From the approximate analytical expressions they provide it is possible to calculate the recess depth, *d*, of an electrode from its chronoamperomertic response (equation 9).

$$f_{ss} = \frac{1}{1 + A_1 L + A_2 L^2 + A_3 L^3 + A_4 L^4} \qquad \mathbf{9}$$

where:

$A_1 = 1.9352$, $A_2 = -3.5009$, $A_3 = 0$, and $A_4 = 0$ for $0 < L < 0.1$.

$A_1 = 1.6843$, $A_2 = -1.3237$, $A_3 = 1.7116$, and $A_4 = -0.7585$ for $0.1 < L < 1.0$.

Equation 9 has been plotted in figure 8.

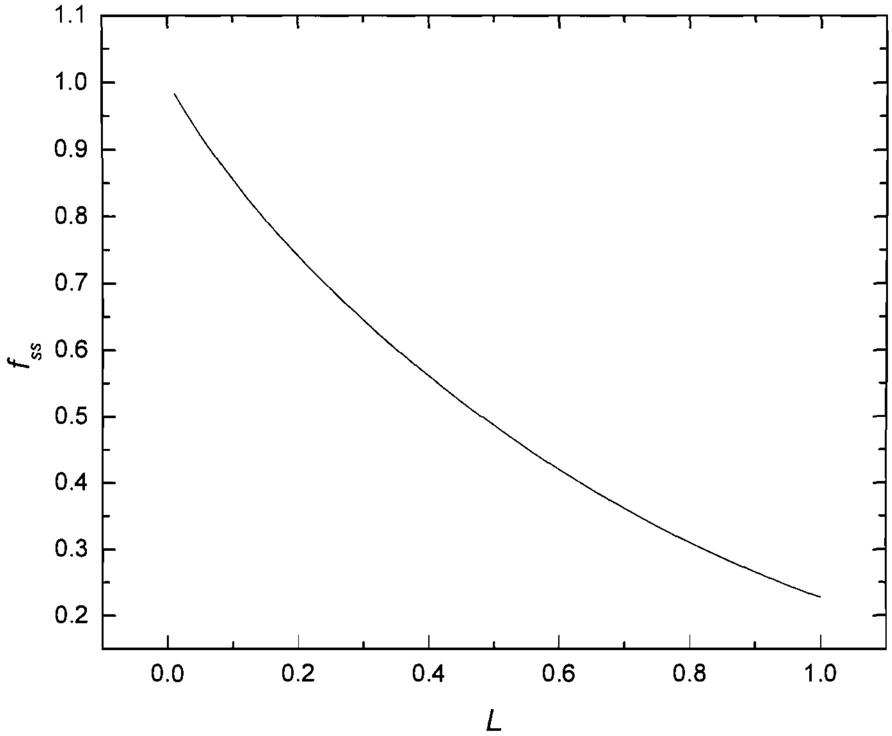

Figure 8. Curve fitted steady state flux calculated from the 4th order polynomial expression (eqn 9) for $0.1 < L < 1.0$.

Determination of f_{ss}:

The current response of the electrodes to ruthenium hexamine was calculated before and after recessing by voltammetry in solutions of three concentrations. f_{ss} was calculated from eqn (10).

$$f_{ss} = \frac{i_{L-recessed}}{i_{L-inlaid}} \qquad \textbf{10}$$

Typical examples of the results obtained before recessing are shown in figure 9 (results obtained after recessing are essentially the same but show correspondingly lower currents).

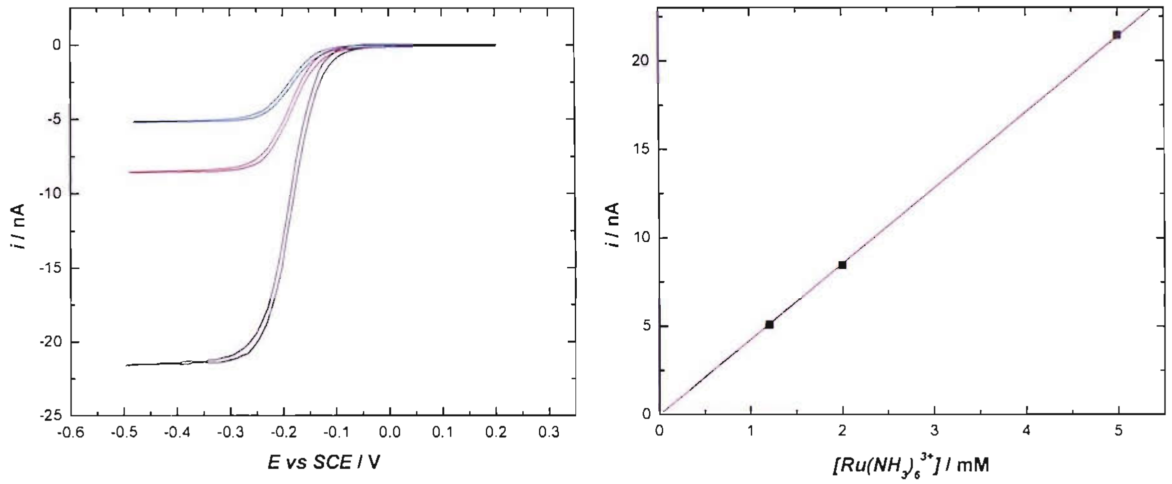

Figure 9. Recorded with a 25 μm platinum disc recessed by approximately 10 μm. **Left:** cyclic voltammetry in Ru(NH$_3$)$_6$Cl$_3$ (—— = 5 mM, —— = 2 mM and —— = 1.2 mM) in 0.25 M KCl (T = 25 °C, purged with Ar). Sweep rate = 5 mV s^{-1}. **Right:** Plot of i_L vs [Ru(NH$_3$)$_6$$^{3+}$] used to calculate the response of the electrode to Ru(NH$_3$)$_6$$^{3+}$ (i.e. the gradient of the slope).

Good agreement between the depths estimated using the Bartlett and trigonometric methods was observed (see figure 4). Although, it should be noted that great care had to be taken at each stage of the measurement process. The electrodes must be fully characterised before and after etching by ESEM and voltammetry in 1 M sulphuric acid and ruthenium hexamine; to ensure that they are clean and to verify the shape and size of the microdiscs. Careful adjustment of the electrodes in the ESEM sample chamber is required to position the surface as close to horizontal (with respect to the detector) as possible, so that accurate measurements of all the angles and lengths can be made from this reference point. Electrodes must be held firmly in position while measurements are made as any tiny movements will distort the image and introduce errors. The etched electrodes must be cycled in 1 M sulphuric acid after etching to remove and debris from the recess before the voltammetry in ruthenium hexaamine can be performed. If many ruthenium hexaamine voltammograms are to be recorded the concentration of the solution may vary and this must also be accounted for.

The recess depths, as estimated using the Bartlett method, were also compared to values obtained from the Bond equation. As predicted the agreement improves as the recess depth increases[178] (Table 1).

Electrode	$d_{Bond.}$ / µm	$d_{Bartlett.}$ / µm	% difference between d_{Bond} and $d_{Bartlett}$
1	0.05	0.03	66.7
2	0.67	0.47	42.6
3	3.15	2.71	16.2
4	3.57	3.11	14.8
5	4.18	3.73	12.1
6	4.67	4.24	10.1
7	5.01	4.59	9.2
8	6.23	5.80	7.4
9	7.27	6.85	6.1
10	12.60	12.26	2.8
11	16.60	16.35	1.5
12	18.50	18.70	-1.1
13	22.60	22.70	-0.4
14	59.00	59.50	-0.8

Table 1. Comparison of recess depth as estimated using the Bond and Bartlett equations. All measurements made on 25 µm diameter platinum microdiscs (recessed using the method described above 5.2.1) by cyclic voltammetry in solutions of ruthenium hexamine (5, 2 and 1.2 mM in 0.25 M KCl, see 5.2.4 determination of f_{ss}). Electrodes arranged in ascending depth as estimated by the Bartlett method. % difference between d calculated from the Bond equation and those calculated from the Bartlett equation = $(d_{Bond} - d_{Bartlett})/d_{Bartlett} \times 100$.

5.2.5 Conclusions:

It has been possible to fabricate recessed platinum microdisc electrodes by electrochemical etching of platinum microwires sealed in soda glass. The resulting electrodes appear to be recessed evenly and without significant roughening of the surface. It should be possible to control the recess depth by monitoring the charge passed during etching.

It was possible to estimate the depth of the microdiscs by imaging them in an environmental electron microscope. The values of d obtained using this method agree well with those obtained from electrochemical measurements (where the equations 8 and 9 were applied).

5.3 Filling Recesses with Mesoporous Metals

5.3.1 Electrodeposition of Mesoporous Platinum:

Mesoporous platinum was deposited onto recessed microdiscs in much the same way as for polished, inlaid microdiscs. Electrodes were cleaned prior to deposition by voltammetry in 1 M sulphuric acid; then the electrodes were rinsed with distilled water, and stored in distilled water, before applying the plating mixture. Extra time and care was taken, when applying the plating mixture to the surface of the recessed electrodes, to fill the cavity fully and completely cover the microdisc. Figure 10 shows a current time transient for the deposition of mesoporous platinum onto a recessed platinum disc.

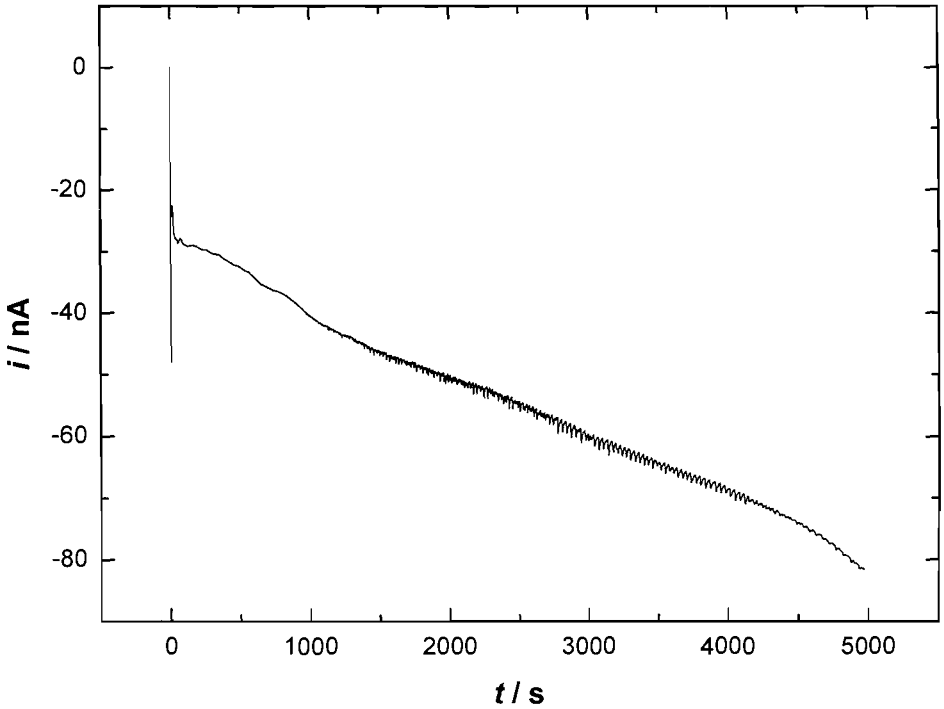

Figure 10. Chronoampreometry for deposition of mesoporous platinum onto a 25 μm diameter platinum disc recessed by 5.22 μm. Plating mixture: water, HCPA, Brij® 56 (1:1:1.5 by weight). Applied potential = -0.1 V vs SCE. Charge passed = 0.27 mC.

This result is fairly typical and is similar to deposition on inlaid electrodes in that there is an initial spike when the potential is first applied (due to charging current), and the current increases with time. However with inlaid electrodes a peak is also usually seen in the first

50-100 seconds, with the current rising and falling briefly before the steady increase at longer timescales.

Through trial and error with different recess depths (all around 5 μm) it was found that a charge of approximately 24 μC was required for each μm of mesoporous film desired. Using this value it was possible to consistently deposit mesoporous platinum very close to the limit of the recesses without overspill.

The theoretical deposition charge, calculated from the volume of platinum required to fill a 1 μm recess of 12.5 μm diameter, is 15.8 μC μm^{-1} (assuming a pore radius of 1.25 nm and pore spacing of 2.5 nm, which gives approximately 22,673,157 pores over the entire microdisc area for a perfect hexagonal arrangement). Therefore 24 μC μm^{-1} corresponds to a Faradiac efficiency of approximately 66 % (somewhat higher than the 43 % efficiency for mesoporous platinum deposition onto inlaid microdiscs, as calculated from surface area measurements in section 3.2.2).

This Faradiac efficiency of 66% is less than the value of 75 % reported for macroelectrodes[21], but higher than the value of 43% observed for inlaid microdiscs of 25 μm diameter (section 3.2.2). As mentioned in section 3.2.2, the efficiency is dependent on the rate of mass transport of platinum(IV) and the intermediate platinum(II) species, to and from the electrode surface[23] (i.e. diffusion of Pt(II) away from the electrode, before it can be fully reduced to platinum metal, leads to a reduced Faradiac efficiency, and this is more pronounced at the microdisc electrodes due to their high rates of mass transport).

As a microdisc is recessed its mass transport regime changes from highly efficient radial diffusion to less efficient planar diffusion, as seen at large electrodes. A recessed microdisc should behave more like a macroelectrode than an inlaid microdisc, and should display a reduced rate of mass transport; therefore one would expect an improvement in the Faradaic efficiency for H_I-ePt reduction. Note that for deeper recesses the Faradiac efficiency of H_I-ePt deposition should tend towards the 75 % reported for macroelectrodes.

5.3.2 Characterisation of Mesoporous Films by ESEM:

Figure 11 below shows ESEM images of a recessed 25 µm diameter platinum disc before and after deposition of mesoporous platinum.

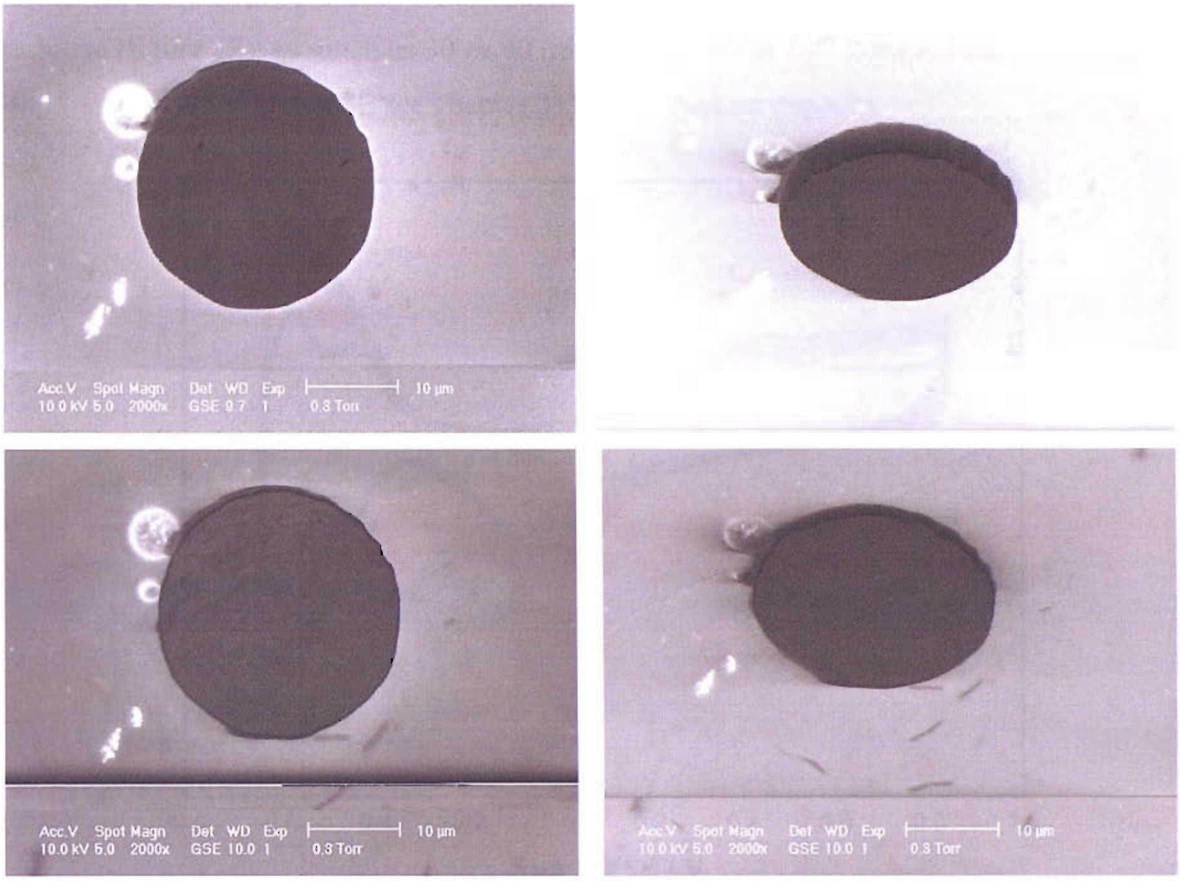

Figure 11. ESEM images of a 25 µm diameter platinum microdisc recessed by approximately 4.4 µm). **Top**: before deposition of the mesoporous platinum. **Bottom**: after passing a charge of 70 µC in the plating mixture. **Left:** viewed perpendicular to the GSE detector. **Right:** tilted by an angle of 42.7°.

The mesoporous platinum deposits evenly across the microdisc, and generally appears quite smooth although there are very subtle ripples and shallow undulations on its surface. In figure 11 above, the mesoporous platinum is not deposited to the very top of the recess (there is approximately 1.7-1.8 µm left). It is important to note that if the same charge (70 µC) was passed at an inlaid electrode the film would spread out and be thinner (see figure 2).

5.3.3 Characterisation of Mesoporous Films by Cyclic Voltammetry in Sulphuric Acid:

After deposition of the H_I-ePt phase, the electrodes were cleaned by soaking in distilled water (as for the polished electrodes) and then by voltammetry in 1 M sulphuric acid. However, for the thick mesoporous films, it took much longer for the voltammetry to stabilise (figure 12); as much as 30 or 40 minutes (at 200 mV s^{-1} between the usual limits: -0.65 V to +1.85 V vs SMSE see chapter 3) for the thickest deposits.

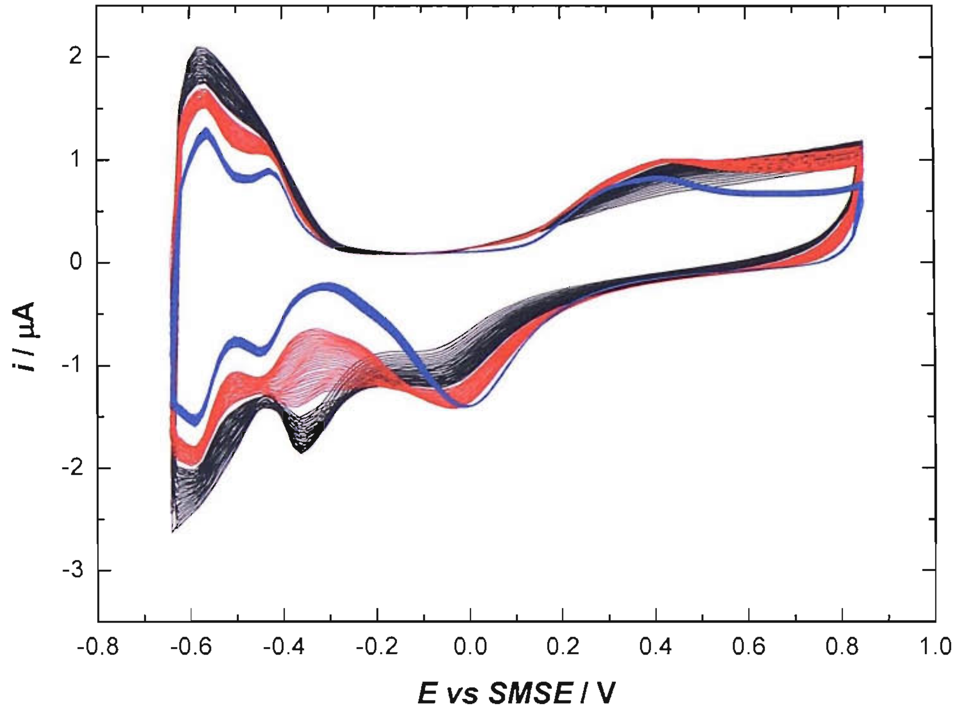

Figure 12. Cyclic voltammetry in 1 M sulphuric acid, T = 25 °C, purged with argon for 15 minutes. WE = 25 μm diameter platinum disc recessed by approximately 5.57 μm, after deposition of approximately 3 μm of H_I-ePt (i.e. 94 μC). Sweep rate = 200 mV s^{-1}. (—) 1st 32 cycles, (-) next 32 cycles recorded ~ 3 minutes later, (—) last 32 cycles recorded ~10 minutes later.

Initially there is no definition to the platinum features and there is an extra peak, at -0.35 V. Slowly this peak decreases in size as the platinum oxide peak grows and the hydrogen adsorption region de-convolutes to two clear peaks.

The surface areas of the nanostructured electrodes were estimated using the charge underneath the hydrogen adsorption/desorption peaks. However they were not as high as one might expect and seemed to reach a limiting value for film depths of about 5 μm and above (figure 13). It would seem that this is, at least in part, due to the fact that the entire surface is not accessible during the timescale of the voltammetry. If the sweep rate is reduced the surface area observed increases (figure 14); except for thinner films i.e. <4 μm where it remains constant.

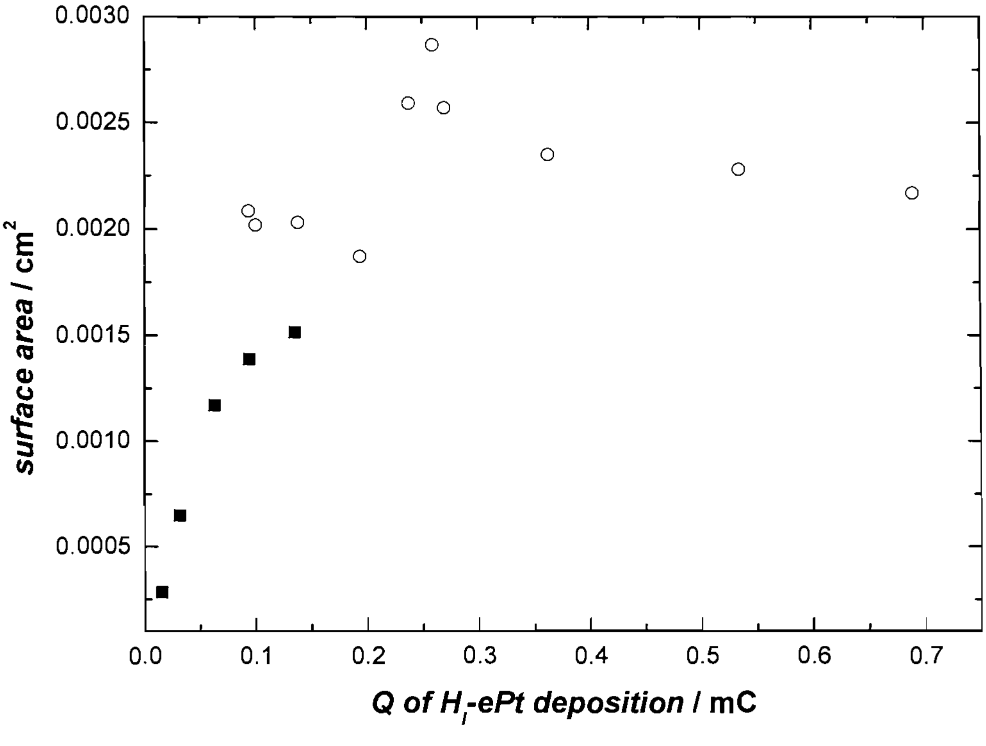

Figure 13. Electrode surface area (as estimated from hydrogen desorption peaks of voltammetry in 1 M sulfuric acid at 200 mV s^{-1}) vs charge passed during deposition of mesoporous film. ■ = mesoporous films on polished platinum discs; ○ = mesoporous films on recessed platinum discs (all electrode diameters 25 μm).

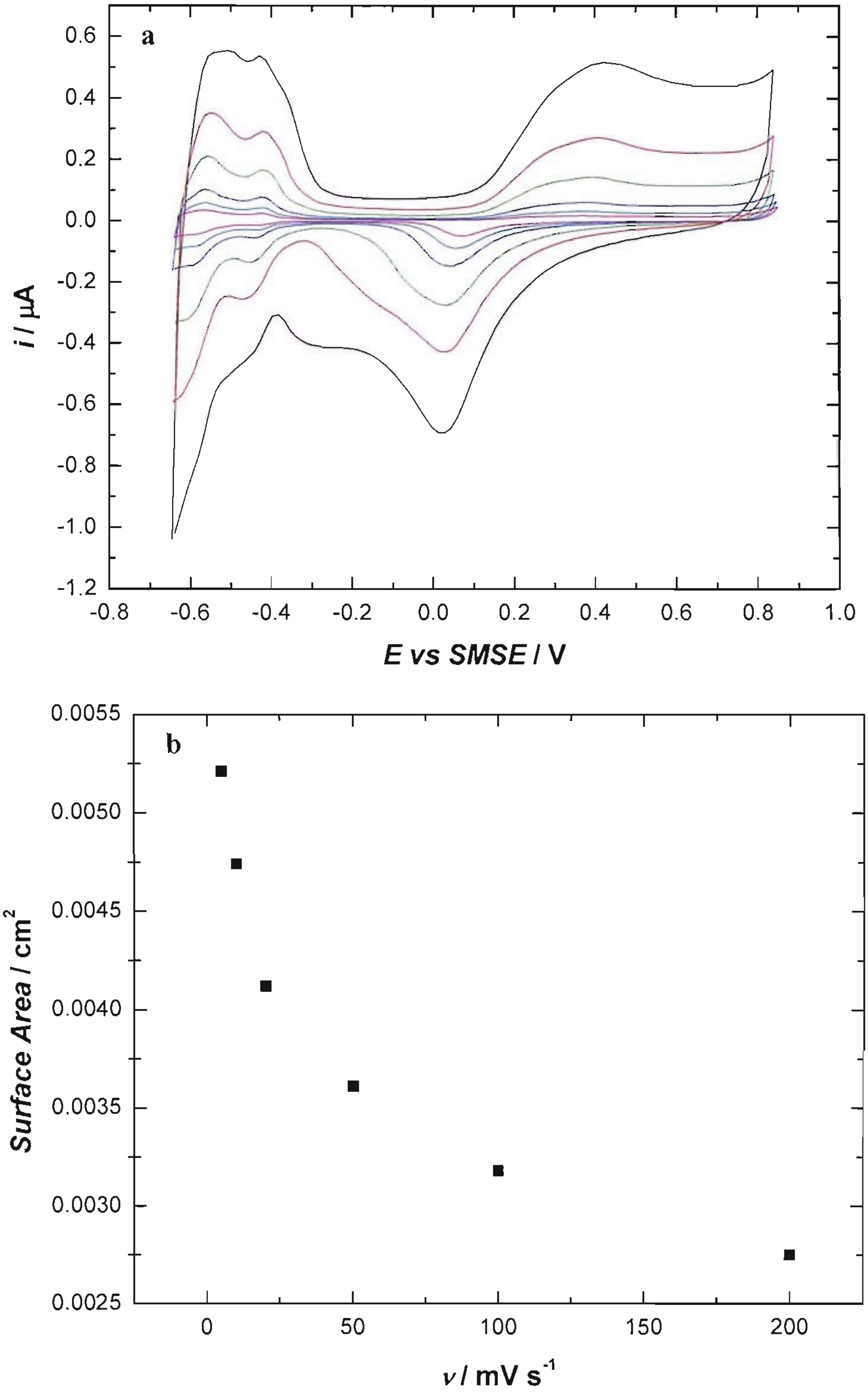

Figure 14. **a)** cyclic voltammetry in 1 M sulphuric acid (T = 25 °C, purged with argon for 20 minutes). WE = 25 μm platinum disc recessed by 10.5 μm and modified with a 10.5 μm mesoporous platinum deposit. Sweep rate: — = 200, — = 100, — = 50, — = 20, — = 10 and — = 5 mV s^{-1}. **b)** platinum surface area (as calculated from the voltammetry) vs sweep rate.

For the thicker mesoporous deposits, reducing the sweep rate alters the shape of the voltammetry (in sulphuric acid) and the measured surface area increases exponentially (figure 14b). It is likely that at the higher sweep rates there is not enough time for a double layer to establish throughout the pores, and so not all of the mesoporous platinum surface is "seen" in the voltammetry.

The accessibility of platinum mesopores was studied using impedance spectroscopy by Elliott and Owen[22]. They provide an equation to calculate the volumetric surface area of the nanostructured metal (equation 11).

$$f = \frac{4\pi r}{\sqrt{3}(2r+w)^2} \qquad \mathbf{11}$$

Where: r = (pore radius) 1.25 nm; w = (wall thickness) 2.5 nm then f = (volumetric surface area) 0.36 × 107 $cm^2\ cm^{-3}$.

Therefore it is possible to calculate a theoretical surface area of the electrodes from the volume of mesoporous platinum deposited. Using slow voltammetry (i.e. slow enough that the charge under the hydrogen adsorption/desorption peaks does not vary with further reduction in sweep rate) the surface areas of the mesoporous platinum deposits in the recessed electrodes was calculated (see chapter 3 for details of surface area measurement). This is compared to the theoretical surface area (calculated from equation 3) in table 2.

Film thickness / μm	Surface area$_{cv}$ / cm^2	Surface area$_{theoretical}$ / cm^2	SA_{cv}/SA_t
10.7	0.00650	0.0190	0.34
10.5	0.00520	0.0186	0.28
7.2	0.00344	0.0127	0.27
6.5	0.00280	0.0114	0.25
4.9	0.00430	0.0086	0.50
3.3	0.00206	0.0058	0.36
2.9	0.00243	0.0051	0.48

Table 2. Comparison of theoretical and observed platinum surface areas for mesoporous deposits of different thicknesses (corresponding to the depth of the recesses the films are deposited into). All electrodes used were 25 μm in diameter.

The observed surface areas are consistently smaller than the theoretical values. There may be several reasons for this: 1) the mesoporous films are not perfect hexagonal nanostructures with totally uniform pore diameters, 2) there may be portions of the film that are unstructured or that have a different structure due to phase changes in the plating mixture as platinum is depleted, 3) there could be different crystal domains in the plating mixture where pores would not line up or change direction sharply preventing or hindering diffusion into the structure or 4) tiny air bubbles in the plating mixture could lead to gaps in the structure.

It is worth noting that Brij® 56 is not an ideal surfactant for this kind of template directed deposition; since it consists of a mixture of surfactant molecules and the resulting liquid crystal phases are not as well defined as they would be for a pure surfactant. Better agreement between theoretical and observed surface areas is seen for mesoporous deposits where pure surfactant (e.g. octaethyleneglycol monohexadecyl ether) was used as a template[21].

Electrochemistry within the pores is further complicated by the fact that there may not be sufficient space for a complete double layer to form. This will depend on the ionic strength of he solution as studied by Boo *et al.*[188]. They state that for a porous electrode the effective surface area will depend on the ratio of the pore diameter (r) to the Debye length (κ^{-1}); i.e. if $\kappa^{-1} > r$ then there is insufficient room in the pore for the double layer to form and only the exterior surface of the electrode will be available for electrochemical reaction. Boo *et al.* calculate κ from equation 12:

$$\kappa = (3.29\times10^{7})zC^{*\frac{1}{2}} \qquad \mathbf{12}$$

where C^* is the bulk $z{:}z$ concentration in mol L^{-1} and κ is given in cm^{-1}.

Equation 12 is fine for symmetrical electrolytes[189] but for electrolytes of a mixed valency (such as the sulphuric acid used in these experiments) a different expression is needed. The more general form of the equation is[190]:

$$\kappa = \left(\frac{e^2 \sum n_i z_i^2}{\varepsilon \varepsilon_0 k_B T} \right)^{\frac{1}{2}} \qquad \mathbf{13}$$

Where e is the absolute value of electronic charge; n_i is the number of ions, of type i, per m^3; z_i is the valency of the ions of type i; ε is the dielectric constant of the solvent (78.3 F m^{-1}); ε_0 is the permittivity of free space (8.85×10^{-12} F m^{-1}); k_B is the Boltzmann constant (1.38×10^{-23} J K^{-1}) and T is the temperature (298 K).

Therefore using equation 13 and the concentration of the acid used in the experiments to measure the electrode surface areas (1 M), a theoretical Debye length (κ^{-1}) of approximately 0.17 nm is expected. This is less than the internal diameter of the pores in the mesoporous films (r = 1.25 nm) and suggests that the entire surface of the platinum is active during voltammetry in 1 M sulphuric acid.

It is worth noting that the equations above refer to planar electrode surfaces and can therefore only be used as an approximation inside the pores if the double layer is much shorter than the pore diameter. The modelling for a cylindrical, nanopore, surface is more complicated and has been considered in many publications[191-193].

It should also be taken into consideration that the number of hydrogen ions is greatly exceeded by the number of platinum surface sites in the pores. The number of hydrogen ions within the pores can be estimated (assuming a pore radius of 1.25 nm and hydrogen ion concentration of 2 M) as 9.82×10^{-21} moles per µm, and the amount of hydrogen ions required to completely cover the platinum is 1.71×10^{-19} moles per µm of pore length. Therefore there are approximately 17 times more platinum sites than hydrogen ions within the pore.

This suggests that there will be a drastic increase in pH within the pore during the cathodic sweep as hydrogen ions are adsorbed. However this will be rapidly redressed by diffusion of bulk ions into the pores. Even for a film thickness of 10 µm (NB the pores, if continuous, will be somewhat longer due to their tortuousity[22]) and a hydrogen ion diffusion coefficient of 9.5 x 10^{-5} cm^2 s^{-1}, it will only take 10.5 ms for hydrogen ions to travel the full length of the pores. At a sweep rate of 200 mV s^{-1}, the hydrogen adsorption/desorption process will take approximately 3.2 s (significantly longer than 10.5 ms). This explains why, even at the fastest sweep rate of 200 mV s^{-1}, the hydrogen adsorption/desorption peaks in figure 14 are only slightly separated, despite the fact that the mesoporous film was 10.5 μm thick.

While the momentary pH change in the pores accounts for the separation of the hydrogen adsoption/desorption peaks, it is not clear what is causing the shoulder on the oxide stripping peak (-0.2 to -0.35 V figure 14). Since this only occurs at the higher sweep rates it could be due to reduction of some species generated during the anodic sweep; something which has time to diffuse out of the pores at slower sweep rates.

5.3.4 Characterisation of Mesoporous Films by Cyclic Voltammetry in Ruthenium Hexaamine Solution:

One of the reasons for depositing mesoporous platinum into recesses was to try and produce very thick structured films without altering the geometry of the electrode. Imaging of the electrodes using ESEM shows that, if the right charge is passed during deposition, the films can be grown to the edge of the recess (or very close) without spilling over onto the glass. Voltammetry in ruthenium hexamine solution confirms that the radii of these electrodes are unaltered (figure 15).

The limiting current for a microdisc (i_L) is related to its radius by the equation 14:

$$i_L = 4nFDca \qquad \textbf{14}$$

Where n = (number of electrons) 1; F = (the Faraday) 96485 C mol^{-1}; c = (concentration of $Ru(NH_3)_6Cl_3$) 3.1 × 10^{-6} mol cm^{-3}; a = (electrode radius) 12.5 × 10^{-4} cm and D = (diffusion coefficient) values for $Ru(NH_3)_6Cl_3$ in 0.1 M KCl range from 8.5 -9.1 × 10^{-6}

$cm^2 s^{-1}$ typically[194]. Taking $D = 8.5 \times 10^{-6}$ $cm^2 s^{-1}$ gives a predicted i_L of 12.71 nA which agrees well with the observed current 12.6 ± 0.1 nA.

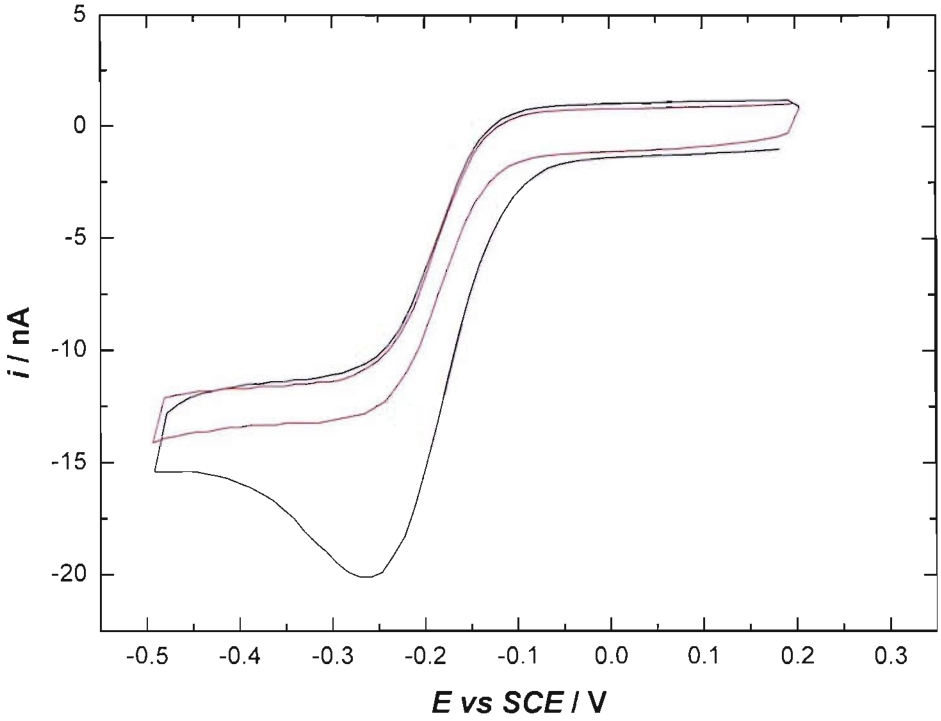

Figure 15. Voltammetry in 3.1 mM $Ru(NH_3)_6Cl_3$ / 0.2 M KCl (purged with argon). Working electrode = 25 μm diameter platinum disc recessed by ≈ 7.17 μm and filled with mesoporous platinum. Sweep rate = 5 mV s^{-1}. (—) = 1st sweep; (—) = 2nd sweep.

The peak at -0.2 V is only present on the first sweep and (like the charging current) is closely related to the observed surface area. This peak is not seen at all for polished microdiscs and seems to be due to reduction of platinum oxide. The oxide layer forms naturally if the electrode is stored in water, but peak size is dependent on time and it takes several days for a full oxide layer to build up.

The nature of the peak was verified by voltammetry in 0.2 M KCl in the absence of the ruthenium complex (figure 16).

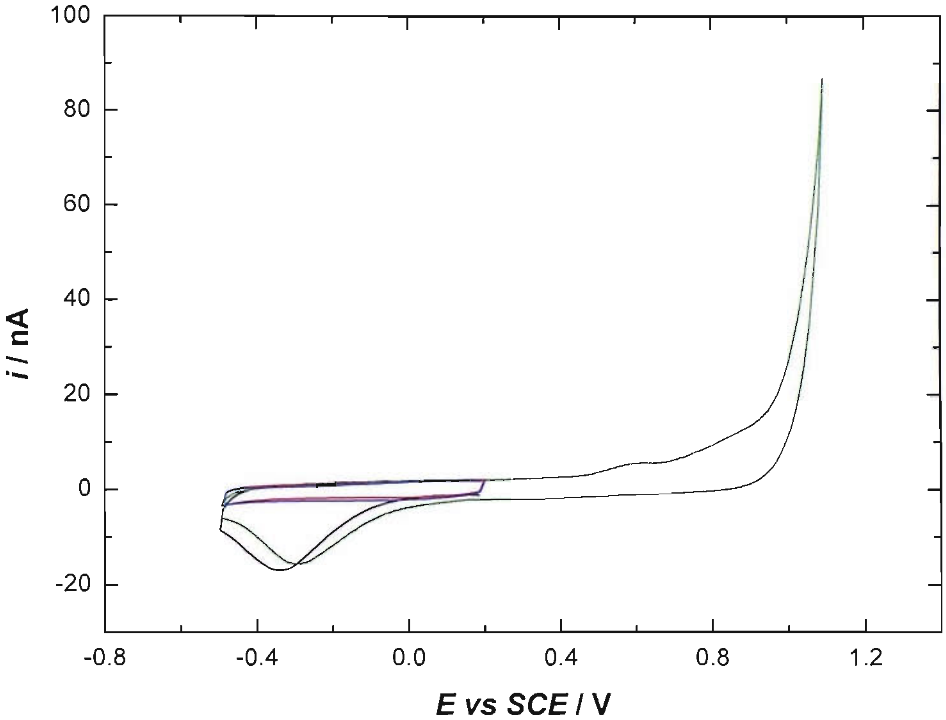

Figure 16. Voltammetry in 0.2 M KCl (purged with argon). Working electrode = 25 μm diameter platinum disc recessed by ≈ 10.6 μm and filled with mesoporous platinum. Sweep rate = 5 mV s^{-1}. (—) = 1^{st} sweep; (—) = 2^{nd} sweep; (—) = 3rd sweep; (—) = 4th sweep.

The peak is present on the first sweep (black line) since the electrode had previously been stored for a week in distilled water. However, once the oxide has been stripped off, only charging current is visible on the second sweep (red line). On the third sweep (green line) the positive limit is increased from + 0.2 V vs SCE to + 1.1 V (sufficient overpotential to fully oxidise the platinum surface) and the peak returns. Then on the fourth and final sweep (blue line) the positive limit was restored to +0.2 V and once again only charging current was observed. A similar experiment was performed in a solution containing the ruthenium complex and differed from figure 16 only in that there was also a ruthenium redox wave present.

5.3.5 Effect of Polishing on Mesoporous Deposits:

The mechanical stability of the mesoporous deposits, within the recesses, was investigated. Two 25 μm platinum disc electrodes were recessed and then the space was filled with mesoporous platinum and rhodium. These electrodes were polished in stages and voltammetry in sulphuric acid and ESEM were used to investigate the effect of each polishing. Figure 17 shows the mesoporous platinum electrode after initial deposition of the nanostructure and after each polishing.

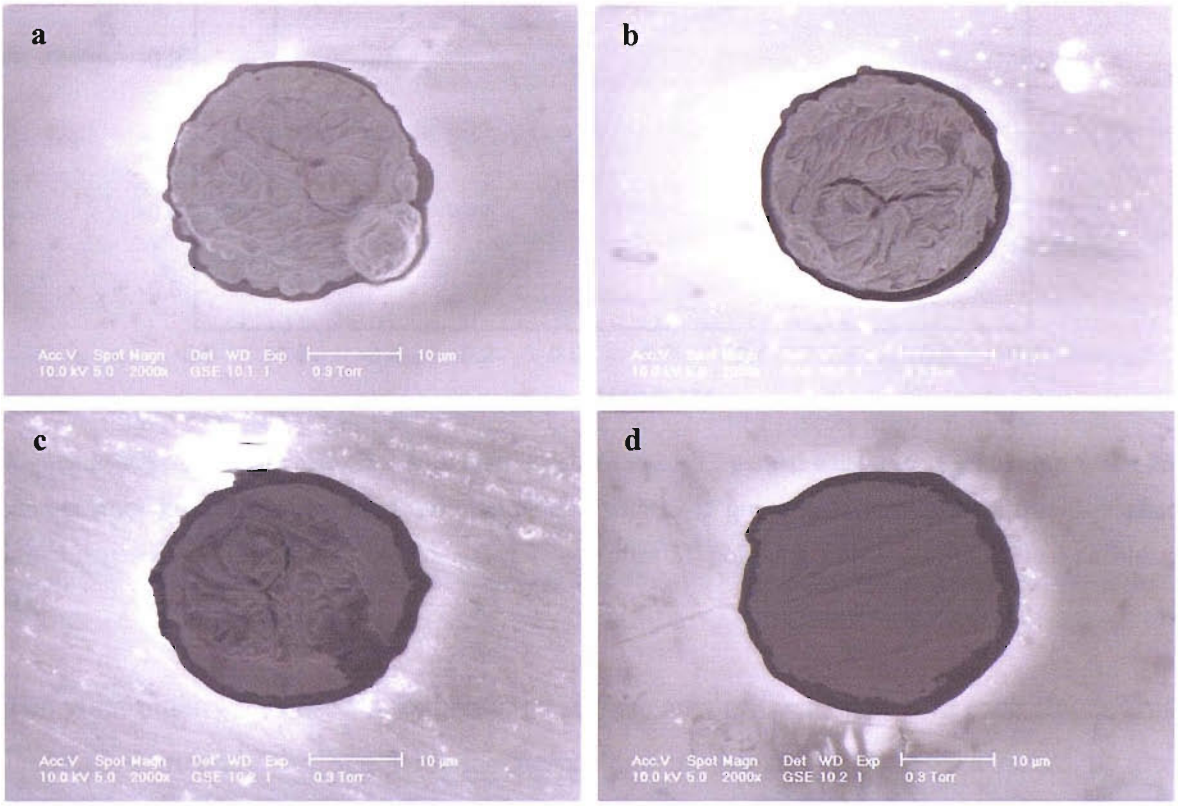

Figure 17. ESEM images of a 25 μm platinum disc recessed by 5 μm and electroplated with a ~ 5 μm mesoporous platinum film. Taken with a Philips XL30 ESEM. **a**) Immediately after deposition. **b**) after polishing on wet 0.3 μm lapping film (~ 1 min). **c**) after polishing on wet 1200 grit silicon carbide paper (~ 30 s) and wet 0.3 μm lapping film (~ 1 min). **d**) after polishing on wet 1200 grit silicon carbide paper (~ 30 s) and wet 0.3 μm lapping film (~ 1 min).

The surface of the mesoporous film is quite uneven and it is the thicker portions that are first affected by the polishing.

Voltammetry in sulphuric acid was recorded at each stage and shows how the surface area of the platinum varies (figure 18).

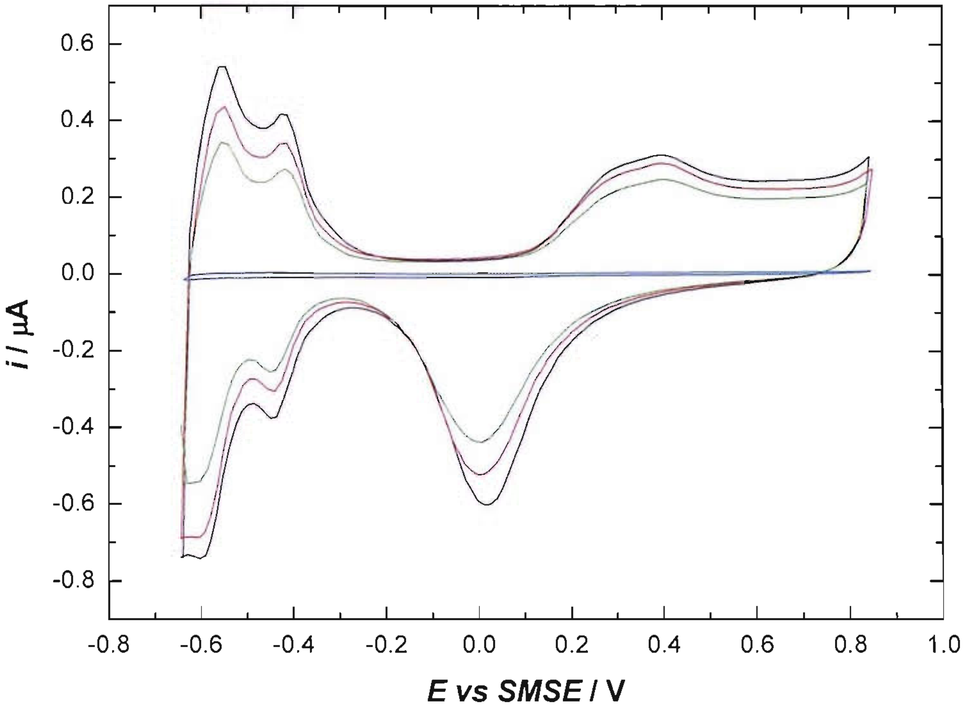

Figure 18. Cyclic Voltammetry in 1 M sulphuric acid (T = 25 °C, purged with argon for 20 min). WE = 25 μm platinum disc recessed by 5 μm and electroplated with a ≈ 5 μm mesoporous platinum film.— = after initial deposition. — = after 1st polishing stage. — = after 2nd polishing stage. — = after final polishing stage.

The voltammetry was used to estimate the surface area of the electrode at each stage. This is detailed in table 4 along with the percentage of the surface that is affected by the polishing (this was estimated from the ESEM images using the area calculation function in SigmaScan® Pro).

Stage	Platinum surface area / cm^2	% of initial surface area	% surface polished
After initial deposition	2.43×10^{-3}	100	0
After 2nd polishing	1.81×10^{-3}	74.5	23
After 3rd polishing	1.43×10^{-3}	59	38
After 4th polishing	1.82×10^{-5}	0.7	100

Table 4. Variation of mesoporous platinum surface area with polishing compared with the percentage of the surface affected by polishing.

The effect of the initial polishing stages appears quite minimal from the ESEM images, and most of the mesoporous structure remains. However the total surface area decreases in proportion to the geometric surface that is polished; suggesting that the pores are no longer accessible where the surface has been damaged. Platinum is quite malleable and it seems that the mechanical forces of polishing smear the metal rendering the nanopores inaccessible. The structure was not re-opened by cycling in acid or even by applying the same electrochemical etching procedure used to recess the electrodes originally.

In the case of the rhodium electrode the nanostructure was grown well above the depth of the recess (figure 19 left). And then the electrode was polished in order to try and remove the excess rhodium and leave a 25 μm disc.

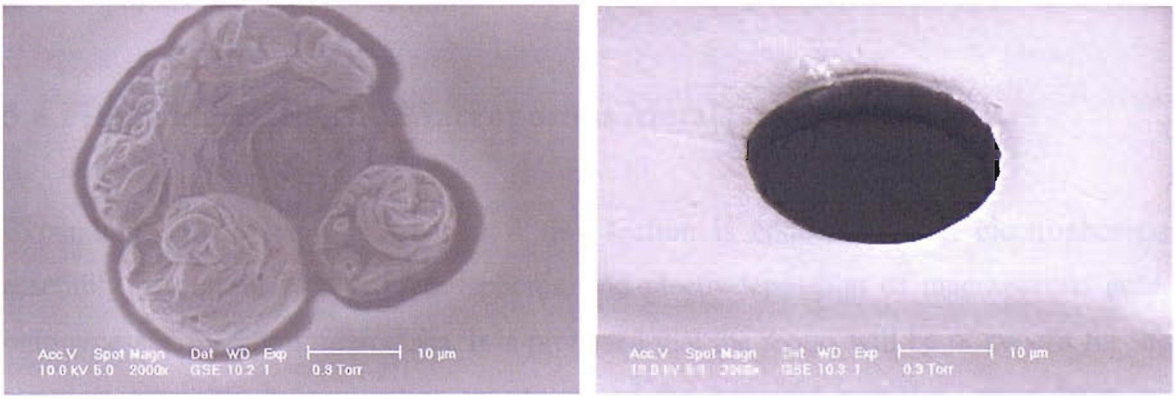

Figure 19. ESEM images of a 25 μm platinum disc recessed by ~ 6.6 μm. **Left**: after deposition of excess mesoporous rhodium. Viewed perpendicular. **Right**: after polishing the modified electrode on a Buhler polishing cloth with a slurry of 1 μm alumina. Viewed at an angle of 44.5 °. Depth estimated as ~ 6.2 μm.

The ESEM image taken after polishing shows a disc of 25 μm diameter recessed by ~ 6.2 μm. It would appear that the rhodium deposit has been pulled out of the cavity in one clean lump during polishing. This is not surprising since the most of the volume of rhodium was outside of the cavity. Voltammetry in sulphuric acid suggests that some small, residue of mesoporous rhodium remains; as there is a rhodium oxide stripping peak comparable to the platinum stripping peak in size.

5.3.6 Conclusions:

In this section it has been shown that mesoporous platinum and rhodium can be electrodeposited onto recessed microdiscs. Thus it is possible to deposit thick structured films without altering the geometrical surface area of the substrate disc, as confirmed by ESEM and cyclic voltammetry in ruthenium hexaamine solution. The mechanical stability of the mesoporous films is improved provided most or all of the metal is deposited below the mouth of the recess. However, while the recessed mesoporous deposits could be polished without displacing them from the substrate electrode, the pores were closed off and could not be reopened. This led to significant reductions of the specific surface area, which were proportional to the percentage of the film surface that was polished.

The electroplating is performed in the same way as previously reported for deposition of mesoporous metals at inlaid microdiscs (Chaper 3), but proceeds with increased Faradaic efficiency due to the decreased rate of mass transport within the recess (at least in the case of mesoporous platinum deposition).

5.4 Filling Recesses with Macroporous Metals

Expanding on the work in Chapter 4 this section is concerned with electrophoretic assembly of colloidal polystyrene spheres, and electrodeposition of macroporous gold, onto recessed platinum microdiscs. It is proposed that the recess will be of benefit for the template assembly by preventing movement of the colloidal particles, away from the electrode surface, during drying.

5.4.1 Electrophoretic Assembly of Polystyrene Latex Spheres:

500 nm polystyrene spheres were assembled at a recessed platinum discs (25 μm diameter) by electrophoresis in a 0.01 wt. % suspension in ethanol. This method allowed spheres to be placed specifically inside the recess. Ethanol was used instead of water here (in contrast to the experiments in Chapter 4) as it evaporated faster once the working electrode was removed from the cell; this seemed to reduce the amount of sphere movement during drying (although this was not quantified). Figure 20 shows a current time transient for a typical assembly experiment.

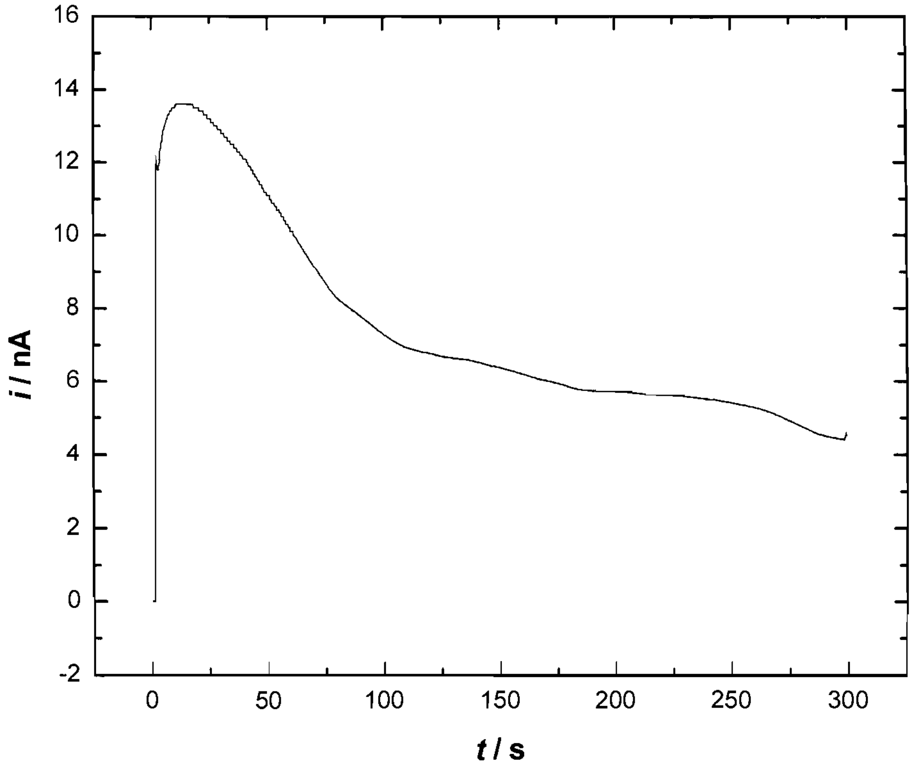

Figure 20. Chronoamperometry in a suspension of 500 nm polystyrene spheres (0.01 wt % in ethanol). WE = 25 μm platinum disc recessed by ≈ 2.9 μm. Applied potential = + 1.5 V vs platinum gauze pseudo reference/counter electrode.

Similar results to those shown in Chapter 4 were obtained although the confinement of the spheres at the electrode after deposition was better (Figure 21). This is probably due to the restricted mobility inside the recess.

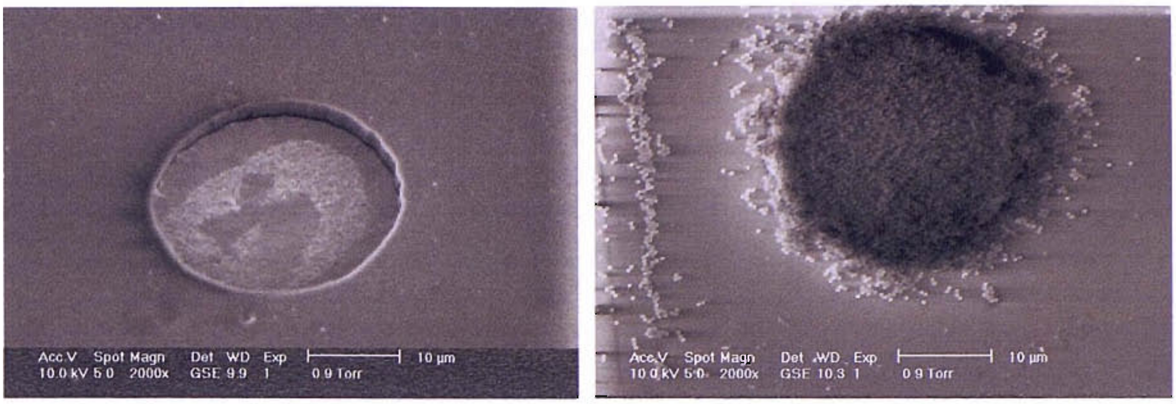

Figure 21. ESEM images of a 25 µm platinum disc recessed by ≈ 2.9 µm. Taken with a Philips XL30 ESEM. **Left:** before assembly of 500 nm polystyrene spheres viewed at an angle of 39.5° to the electron beam. **Right:** after assembly of 500 nm polystyrene spheres. Viewed perpendicular to the electron beam.

5.4.2 Electrodeposition of Macroporous Gold:

The same procedure as that reported in Chapter 4, for macroporous gold deposition at platinum, was employed here. The current transient for gold reduction, onto the electrode pictured in figure 21, is shown in figure 22.

The packing efficiency for a perfect array of monodisperse, close packed spheres is 74 %. However even for the most carefully assembled colloidal arrays the true packing efficiency will be lower. Therefore assuming a sphere packing efficiency of 70 % it was estimated that it would take around 6 µC of charge to completely fill the recess with gold. Less charge was passed (2.7 µC) in order to prevent deposition above the template. Figure 23 differs from the gold deposition transients in Chapter 4 in that there is no undulation in the current. This suggests that the electrophoretically assembled template is less crystalline than the sedimented templates; as regular layers of spheres are needed in order for the current to vary periodically (see section 4.5.1).

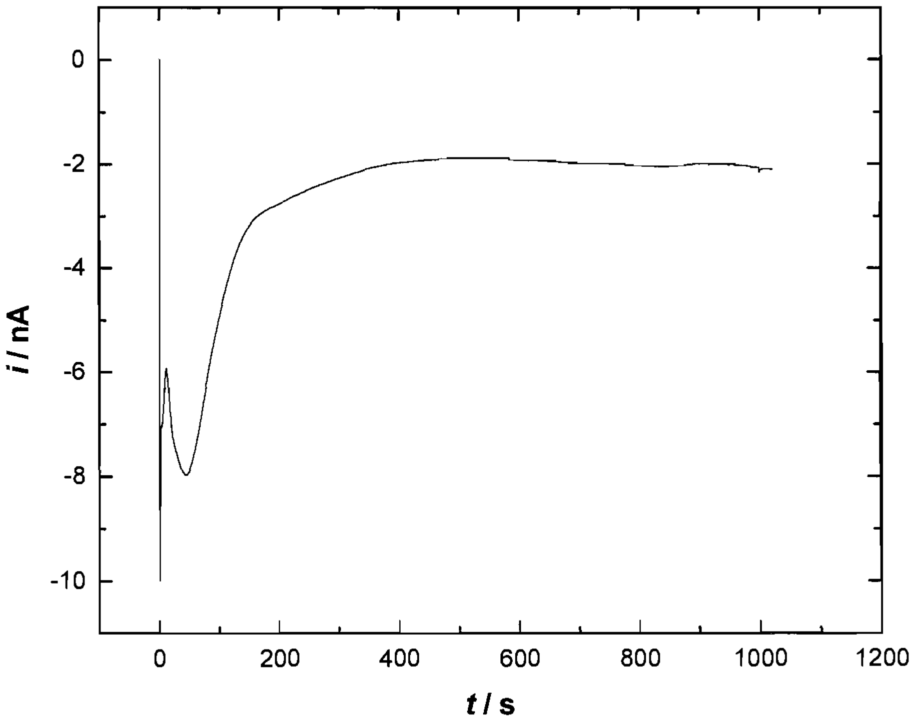

Figure 22. Deposition of macroporous gold onto a 25 μm platinum disc recessed by ≈ 2.85 μm. Solution was a commercial gold plating bath (Techni gold 25) supplied by Technic Inc ($T = 25$ °C). Applied potential = -0.84 V vs SCE. Charge passed = 2.7 μA.

After deposition the electrode was soaked in THF to remove the spheres. However upon imaging in the ESEM it was clear that the template was still present. Soaking the electrode overnight was not enough to dissolve the spheres so other solvents such as DMSO and toluene were tried, but each time the electrode was imaged the spheres (although more distorted) were still visible. Figure 23 shows the electrode after gold deposition and several attempts to remove the template in the three different solvents. Comparison of this image with figure 21 (before gold deposition) indicates that the spheres have been swollen and plasticised.

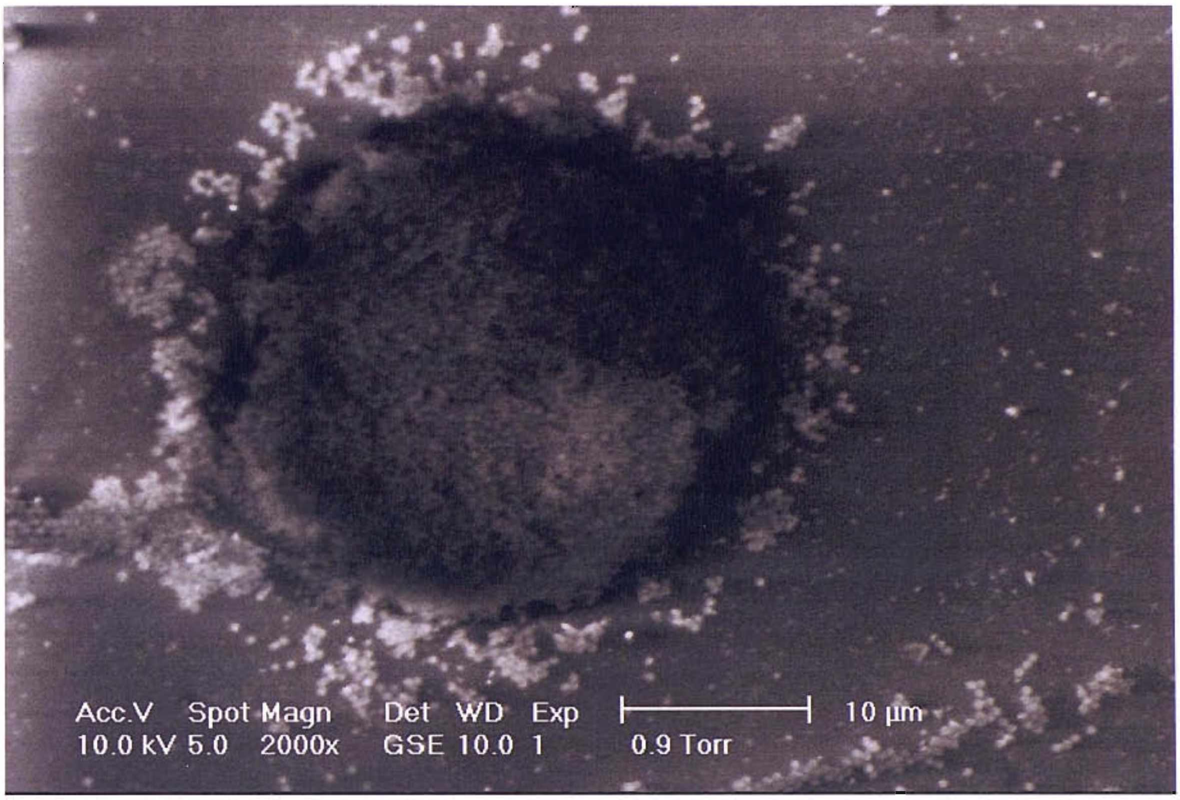

Figure 23. ESEM images of a 25 μm platinum disc recessed by ~ 2.85 μm. After electrophoretic assembly of 500 nm polystyrene latex spheres (see figure 21); deposition of gold (see figure 23) and soaking in THF (12 hours) DMSO (30 min) and toluene (1 hour). Taken with a Philips XL30 ESEM.

Usually the spheres dissolve quite readily in THF or toluene and when the solvents (used on the electrode in figure 23) were mixed with aqueous suspensions of the same 500 nm spheres, the polystyrene dissolved very rapidly.

It is possible that the polymer was rendered insoluble by the electron beam when the template was imaged for the first time (in figure 21). Electron beams are sometimes used to cure polymers by causing the carbon chains to crosslink[195].

It was consistently found here that when the templated electrodes were imaged in the ESEM then the spheres could not be dissolved either before or after gold deposition. It was possible to electrophoretically assemble 500 nm spheres at a recessed platinum disc, deposit gold through the structure and dissolve the template in THF if it was not first imaged in the ESEM. However this meant that the quality and depth of the template could not be checked before gold deposition. Nonetheless, as figure 24 shows, porous gold was deposited on the recessed electrodes.

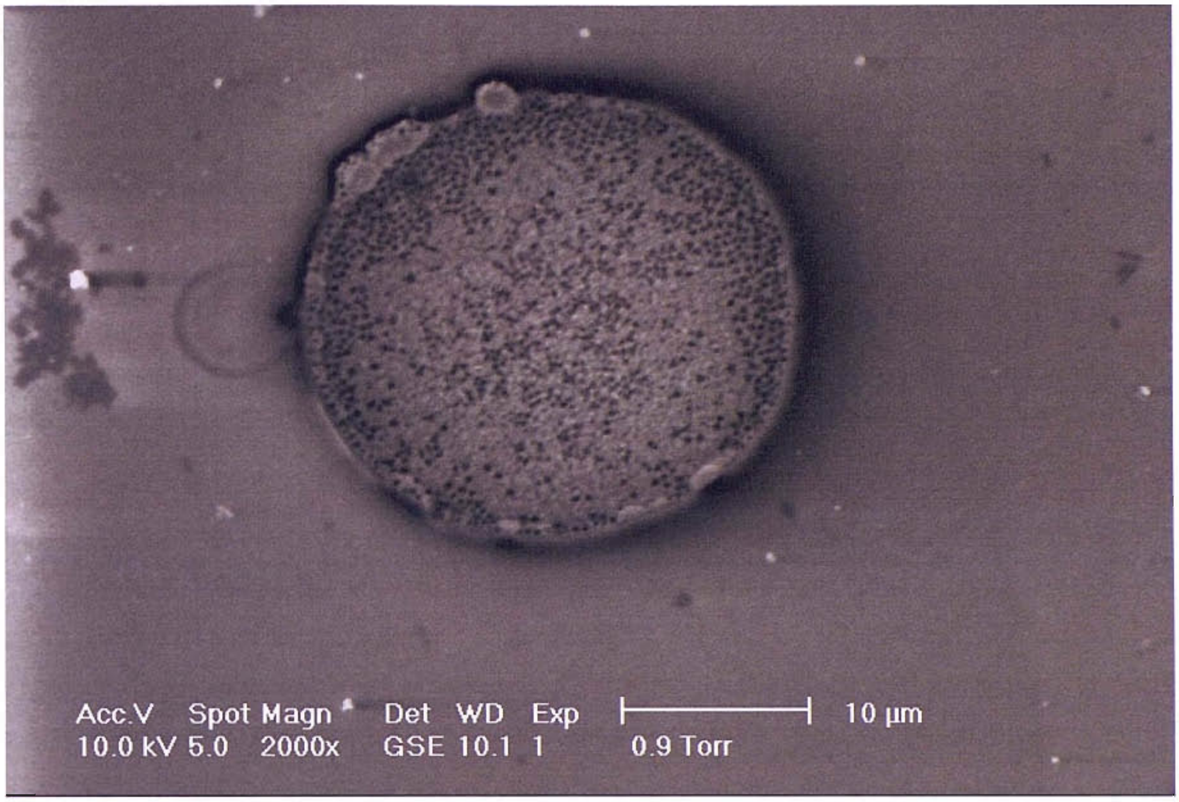

Figure 24. ESEM images of a 25 µm platinum disc recessed by ~ 1.85 µm. After electrophoretic assembly of 500 nm polystyrene latex; deposition of gold (charge passed = 2.8 µC) and soaking in THF (15 min). Taken with a Philips XL30 ESEM.

Gold was deposited to the limits of the recess of the electrode imaged in figure 24, and there are portions where the metal has overgrown the template. However voltammetry in sulphuric acid shows that the structure is open.

5.4.3 Characterisation of Macroporous Gold by Cyclic Voltammetry in Sulphuric Acid:

Voltammetry of the recessed macroporous electrodes in sulphuric acid shows both gold[156] and platinum[123,196] features (similar to the macroporous gold films deposited onto 0.5 mm diameter platinum discs in Chapter 4). The peaks are labelled 1-6 and correspond to platinum oxidation, gold oxidation, gold oxide reduction, platinum oxide reduction, hydrogen adsorption and hydrogen desorption respectively.

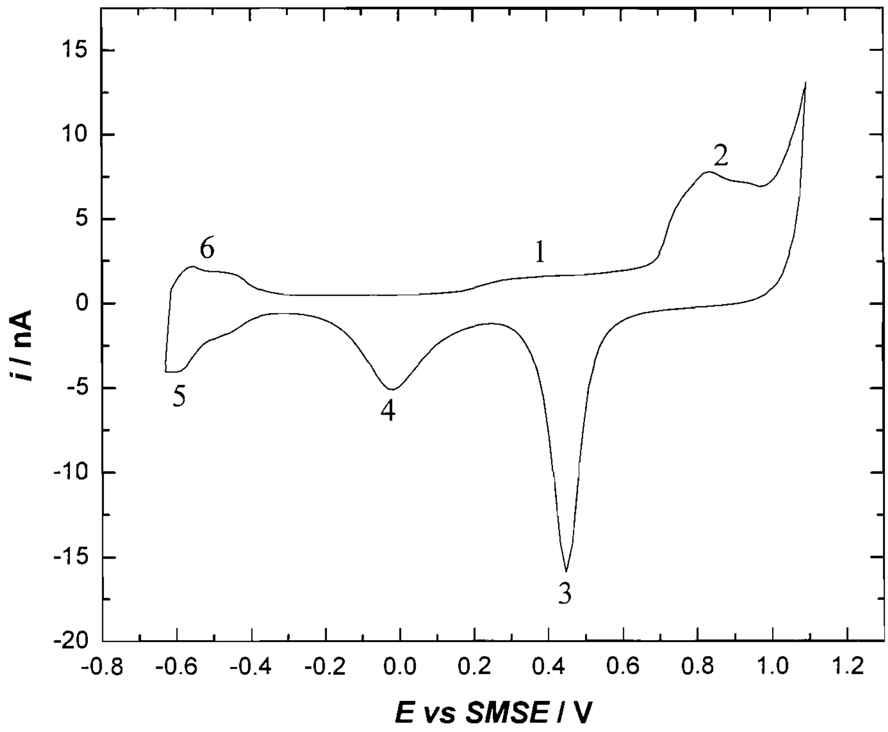

Figure 25. Cyclic voltammetry in 1 M sulphuric acid (T = 25 °C, purged with argon for 20 min). WE = 25 μm diameter platinum disc recessed by ≈ 2 μm, plated with structured gold (500 nm cavities) Q=0.93 μC. Sweep rate = 200 mV s^{-1}.

The platinum and gold surface areas were estimated for several electrodes modified in this way (table 5). All of the electrodes appeared to have open gold structure when viewed in the ESEM (as in figure 24) although the number of spheres and the thickness of the films was quite variable.

Au deposition Q / μC	Pt surface area / cm^2	Au surface area / cm^2
2.8	1.71×10^{-5}	1.97×10^{-5}
2.79	7.92×10^{-6}	1.73×10^{-5}
0.93	5.91×10^{-6}	1.84×10^{-5}
0.93	1.18×10^{-5}	1.25×10^{-5}
1.0	8.32×10^{-6}	2.24×10^{-5}

Table 5. Comparison of gold and platinum surface area with gold deposition charge for recessed 25 μm platinum discs modified with macroporous gold.

There is no correlation between gold surface area and the deposition charge; this is probably due to a lack of crystallinity in the electrophoretically deposited template. The amount of exposed platinum is also quite variable. Assuming the area of contact between the spheres and the platinum to be 5×10^{-10} cm^2 (see table 2 Chapter 4) and near perfect packing at the electrode, the theoretical platinum surface area is 1.13×10^{-6} cm^2. This is much lower than the values calculated from the acid voltammetry (more than 10 times less in some cases).

For a less crystalline template there will be a higher proportion of platinum covered during gold deposition, so one would expect the observed platinum surface areas to be less than the theoretical value. This is odd since the ESEM images show no gaps in the structured films where extra platinum might be exposed. One possible explanation might be that the template is not wetting completely; if there were air bubbles on the microdisc surface then more platinum would be exposed after gold deposition.

5.4.4 Conclusions:

It is possible to electrophoretically assemble 500 nm polystyrene latex spheres at recessed platinum microdiscs, form a colloidal suspension in ethanol. These particle assemblies can be used as templates for the deposition of macroporous gold. ESEM images of the templates, the lack of oscillation in the gold deposition current and voltammetry in sulphuric acid after gold deposition all suggest that these electrophoretically assembled arrays are less crystalline and less well ordered than the templates assembled by sedimentation in Chapter 4. However a macroporous network of open interconnected gold can be formed within the recess above the substrate electrode.

5.5 Summary

It is possible to recess platinum microdiscs by electrochemical etching with some control over the depth. Quite aggressive potential pulsing is required to dissolve the platinum, although the resulting electrodes appear to be recessed evenly and without significant roughening of the surface. The deepest recess generated in this work was approximately 60 µm. However this took over an hour to produce and required periodic sonication of the electrode (in the etching solution) to remove black deposits, of what were assumed to be platinum salts, from the cavity. If these etching products are not removed then the recessing seems to become self limiting at around 20 μm.

The recesses can be filled (completely or partially) with mesoporous metals like platinum and rhodium. These mesoporous deposits do not alter the geometrical surface area of the electrodes in the way that deposition onto polished microdiscs does.

Electrodeposition of mesoporous platinum into recesses proceeds with higher Faradaic efficiency than deposition onto polished, inlaid electrodes (66 % compared to 43 % respectively). This is thought to be due to the restricted diffusion if the recess reducing the loss of the intermediate, Pt(II), reduction product.

Here it has been possible to plate mesoporous metals to depths, and therefore thicknesses, of 10 μm to produce microelectrodes of very high specific surface area. Although the surface areas calculated from voltammetry in sulphuric acid are somewhat less than the theoretical values (25-50 % fairly typical for Brij® 56 templates), these could, almost certainly, be improved by using a better surfactant (i.e. octaethyleneglycol monohexadecyl ether). While these mesoporous films are less prone to damage or removal than films deposited onto polished electrodes, they are not robust enough to withstand polishing, as it would seem that the soft malleable metal structure smears and distorts, rendering the pores inaccessible.

Electrophoretic assembly of polystyrene latex spheres at the recessed platinum microdiscs was more successful than at polished platinum microdiscs. This is probably due to the restricted mobility of the spheres during drying. Spheres immobilised this way were used to deposit macroporous gold films onto the microelectrodes. However preliminary experiments suggest that there is little long range order to the structures.

References

(1) Collings, P. J. *Liquid Crystals: Natures Delicate Phase of Matter* **1990**, *Princeton University Press, Princeton.*

(2) Collings, P. J.; Hird, M. *Itroduction to Liquid Crystals* **1997**, *Taylor and Francis, London.*

(3) Laughlin, R. G. *Aqueous Phase Behaviour of Surfactants* **1996**, *Accademic Press, London.*

(4) Guerin, S. *PhD Thesis, Department of Chemistry, University of Southampton* **1999**.

(5) Attard, G. S.; Bartlett, P. N.; Coleman, N. R. B.; Elliott, J. M.; Owen, J. R. *Langmuir* **1998**, *14*, 7340-7342.

(6) Raimondi, M. E.; Seddon, J. M. *Liq. Cryst.* **1999**, *26*, 305-339.

(7) Richardson, J. W.; Vogt, E. T. C. *Zeolites* **1992**, *12*, 13-19.

(8) Davis, M. E.; Saldarriaga, C.; Montes, C.; Garces, J.; Crowder, C. *Nature* **1988**, *331*, 698-699.

(9) Estermann, M.; McCusker, L. B.; Baerlocher, C.; Merrouche, A.; Kessler, H. *Nature* **1991**, *352*, 320-323.

(10) Beck, J. S.; Vartuli, J. C.; Roth, W. J.; Leonowicz, M. E.; Kresge, C. T.; Schmitt, K. D.; Chu, C. T. W.; Olson, D. H.; Sheppard, E. W.; McCullen, S. B.; Higgins, J. B.; Schlenker, J. L. *J. Am. Chem. Soc.* **1992**, *114*, 10834-10843.

(11) Kresge, C. T.; Leonowicz, M. E.; Roth, W. J.; Vartuli, J. C.; Beck, J. S. *Nature* **1992**, *359*, 710-712.

(12) Monnier, A.; Schuth, F.; Huo, Q.; Kumar, D.; Margolese, D.; Maxwell, R. S.; Stucky, G. D.; Krishnamurty, M.; Petroff, P.; Firouzi, A.; Janicke, M.; Chmelka, B. F. *Science* **1993**, *261*, 1299-1303.

(13) Cheng, C. F.; Luan, Z. H.; Klinowski, J. *Langmuir* **1995**, *11*, 2815-2819.

(14) Behrens, P.; Stucky, G. D. *Angew. Chem.-Int. Edit. Engl.* **1993**, *32*, 696-699.

(15) Hue, Q. S.; Margolese, D. I.; Ciesla, U.; Feng, P. Y.; Gier, T. E.; Sieger, P.; Leon, R.; Petroff, P. M.; Schuth, F.; Stucky, G. D. *Nature* **1994**, *368*, 317-321.

(16) Attard, G. S.; Glyde, J. C.; Goltner, C. G. *Nature* **1995**, *378*, 366-368.

(17) Attard, G. S.; Edgar, M.; Goltner, C. G. *Acta Mater.* **1998**, *46*, 751-758.

(18) Attard, G. S.; Goltner, C. G.; Corker, J. M.; Henke, S.; Templer, R. H. *Angew. Chem.-Int. Edit. Engl.* **1997**, *36*, 1315-1317.

(19) Attard, G. S.; Bartlett, P. N.; Coleman, N. R. B.; Elliott, J. M.; Owen, J. R.; Wang, J. H. *Science* **1997**, *278*, 838-840.

(20) Elliott, J. M.; Birkin, P. R.; Bartlett, P. N.; Attard, G. S. *Langmuir* **1999**, *15*, 7411-7415.

(21) Elliott, J. M.; Attard, G. S.; Bartlett, P. N.; Coleman, N. R. B.; Merckel, D. A. S.; Owen, J. R. *Chem. Mater.* **1999**, *11*, 3602-3609.

(22) Elliott, J. M.; Owen, J. R. *Phys. Chem. Chem. Phys.* **2000**, *2*, 5653-5659.

(23) Gollas, B.; Elliott, J. M.; Bartlett, P. N. *Electrochim. Acta* **2000**, *45*, 3711-3724.

(24) Guerin, S.; Attard, G. S. *Electrochem. Commun.* **2001**, *3*, 544-548.

(25) Whitehead, A. H.; Elliott, J. M.; Owen, J. R.; Attard, G. S. *Chem. Commun.* **1999**, 331-332.

(26) Bartlett, P. N.; Birkin, P. N.; Ghanem, M. A.; de Groot, P.; Sawicki, M. *J. Electrochem. Soc.* **2001**, *148*, C119-C123.

(27) Nelson, P. A.; Elliott, J. M.; Attard, G. S.; Owen, J. R. *J. New Mat.Electrochem. Syst.* **2002**, *5*, 63-65.

(28) Bartlett, P. N.; Marwan, J. *Microporous Mesoporous Mat.* **2003**, *62*, 73-79.

(29) Bartlett, P. N.; Gollas, B.; Guerin, S.; Marwan, J. *Phys. Chem. Chem. Phys.* **2002**, *4*, 3835-3842.

(30) Bartlett, P. N.; Marwan, J. *Phys. Chem. Chem. Phys.* **2004**, *6*, 2895-2898.

(31) Attard, G. S.; Leclerc, S. A. A.; Maniguet, S.; Russell, A. E.; Nandhakumar, I.; Gollas, B. R.; Bartlett, P. N. *Microporous Mesoporous Mat.* **2001**, *44*, 159-163.

(32) Evans, S. A. G.; Elliott, J. M.; Andrews, L. M.; Bartlett, P. N.; Doyle, P. J.; Denuault, G. *Anal. Chem.* **2002**, *74*, 1322-1326.

(33) Park, S.; Chung, T. D.; Kim, H. C. *Anal. Chem.* **2003**, *75*, 3046-3049.

(34) Birkin, P. R.; Elliott, J. M.; Watson, Y. E. *Chem. Commun.* **2000**, 1693-1694.

(35) Marwan, J. *PhD Thesis, Department of Chemistry, University of Southampton* **2003**.

(36) Vincent, C. A.; Scrosati, B. *Modern Batteries: An Introduction to Electrochemical Power Sources* **1997**, *Edward Arnold.*

(37) Al-Saleh, M. A.; Sleem Ur, R.; Kareemuddin, S.; Al-Zakri, A. S. *J. Power Sources* **1998**, *72*, 159-164.

(38) Kiros, Y.; Schwartz, S. *J. Power Sources* **2000**, *87*, 101-105.

(39) Narayanan, S.; Sreekanth, G. *React. Kinet. Catal. Lett.* **1993**, *51*, 449-458.

(40) Bardosova, M.; Tredgold, R. H. *J. Mater. Chem.* **2002**, *12*, 2835-2842.

(41) Stober, W.; Fink, A.; Bohn, E. *J. Colloid Interface Sci.* **1968**, *26*, 62-69.

(42) Sanders, J. V. *Nature* **1964**, *204*, 1151-1153.

(43) Sanders, J. V. *Acta Crystallogr. Sect. A: Found. Crystallogr.* **1968**, *24*, 427-334.

(44) Vlasov, Y. A.; Astratov, V. N.; Baryshev, A. V.; Kaplyanskii, A. A.; Karimov, O. Z.; Limonov, M. F. *Phys. Rev. E* **2000**, *61*, 5784–5793.

(45) Woodcock, L. V. *Nature* **1997**, *385*, 141-143.

(46) Norris, D. J.; Arlinghaus, E. G.; Meng, L. L.; Heiny, R.; Scriven, L. E. *Adv. Mater.* **2004**, *16*, 1393-1399.

(47) Dushkin, C. D.; Lazarov, G. S.; Kotsev, S. N.; Yoshimura, H.; Nagayama, K. *Colloid Polym. Sci.* **1999**, *277*, 914-930.

(48) Nagayama, K. *Colloid Surf. A-Physicochem. Eng. Asp.* **1996**, *109*, 363-374.

(49) Kralchevsky, P. A.; Denkov, N. D.; Paunov, V. N.; Velev, O. D.; Ivanov, I. B.; Yoshimura, H.; Nagayama, K. *J. Phys.-Condes. Matter* **1994**, *6*, A395-A402.

(50) Fustin, C.; Glasser, G.; Spiess, H. W.; Jonas, U. *Langmuir* **2004**, *20*, 9114-9123.

(51) Dimitrov, A. S.; Nagayama, K. *Langmuir* **1996**, *12*, 1303-1311.

(52) Jiang, P.; Bertone, J. F.; Hwang, K. S.; Colvin, V. L. *Chem. Mater.* **1999**, *11*, 2132-2140.

(53) Soukoulis, C. M. *Nanotechnology* **2002**, *13*, 420-423.

(54) John, S. *Phys. Rev. Lett.* **1987**, *58*, 2486-2489.

(55) Yablonovitch, E. *Phys. Rev. Lett.* **1987**, *58*, 2059-2062.

(56) Jin, C. J.; Han, S. Z.; Meng, X. D.; Cheng, B. Y.; Zhang, D. Z. *J. Appl. Phys.* **2002**, *91*, 4771-4773.

(57) Cornelius, C. M.; Dowling, J. P. *Phys. Rev. A* **1999**, *59*, 4736-4746.

(58) Li, Z. Y.; El-Kady, I.; Ho, K. M.; Lin, S. Y.; Fleming, J. G. *J. Appl. Phys.* **2003**, *93*, 38-42.

(59) Cassagneau, T.; Caruso, F. *Adv. Mater.* **2002**, *14*, 1629-1633.

(60) Lee, K.; Asher, S. A. *J. Am. Chem. Soc.* **2000**, *122*, 9534-9537.

(61) Reese, C. E.; Asher, S. A. *Anal. Chem.* **2003**, *75*, 3915-3918.

(62) Jiang, P.; Cizeron, J.; Bertone, J. F.; Colvin, V. L. *J. Am. Chem. Soc.* **1999**, *121*, 7957-7958.

(63) Kulinowski, K. M.; Jiang, P.; Vaswani, H.; Colvin, V. L. *Adv. Mater.* **2000**, *12*, 833-838.

(64) Holland, B. T.; Blanford, C. F.; Stein, A. *Science* **1998**, *281*, 538-540.

(65) Vlasov, Y. A.; Yao, N.; Norris, D. J. *Adv. Mater.* **1999**, *11*, 165-169.

(66) Zakhidov, A. A.; Baughman, R. H.; Iqbal, Z.; Cui, C. X.; Khayrullin, I.; Dantas, S. O.; Marti, I.; Ralchenko, V. G. *Science* **1998**, *282*, 897-901.

(67) Vlasov, Y. A.; Bo, X. Z.; Sturm, J. C.; Norris, D. J. *Nature* **2001**, *414*, 289-293.

(68) Gu, Z. Z.; Hayami, S.; Kubo, S.; Meng, Q. B.; Einaga, Y.; Tryk, D. A.; Fujishima, A.; Sato, O. *J. Am. Chem. Soc.* **2001**, *123*, 175-176.

(69) Abdelsalam, M. E.; Bartlett, P. N.; Baumberg, J. J.; Coyle, S. *Adv. Mater.* **2004**, *16*, 90-+.

(70) Bartlett, P. N.; Baumberg, J. J.; Birkin, P. R.; Ghanem, M. A.; Netti, M. C. *Chem. Mat.* **2002**, *14*, 2199-2208.

(71) Bartlett, P. N.; Baumberg, J. J.; Coyle, S.; Abdelsalam, M. E. *Faraday Discuss.* **2004**, *125*, 117-132.

(72) Bartlett, P. N.; Birkin, P. R.; Ghanem, M. A. *Chem. Commun.* **2000**, 1671-1672.

(73) Bartlett, P. N.; Birkin, P. R.; Ghanem, M. A.; Toh, C. S. *J. Mater. Chem.* **2001**, *11*, 849-853.

(74) Sumida, T.; Wada, Y.; Kitamura, T.; Yanagida, S. *Langmuir* **2002**, *18*, 3886-3894.

(75) Sumida, T.; Wada, Y.; Kitamura, T.; Yanagida, S. *Chem. Commun.* **2000**, 1613-1614.

(76) Xu, L. B.; Zhou, W. L. L.; Frommen, C.; Baughman, R. H.; Zakhidov, A. A.; Malkinski, L.; Wang, J. Q.; Wiley, J. B. *Chem. Commun.* **2000**, 997-998.

(77) Stein, A.; Schroden, R. C. *Curr. Opin. Solid State Mat. Sci.* **2001**, *5*, 553-564.

(78) Nowak, I. *Colloid Surf. A-Physicochem. Eng. Asp.* **2004**, *241*, 103-111.

(79) Biswas, R.; Sigalas, M. M.; Subramania, G.; Ho, K. M. *Phys. Rev. B* **1998**, *57*, 3701-3705.

(80) Busch, K.; John, S. *Physical Review E* **1998**, *58*, 3896-3908.

(81) Coyle, S.; Prakash, G. V.; Baumberg, J. J.; Abdelsalem, M.; Bartlett, P. N. *Appl. Phys. Lett.* **2003**, *83*, 767-769.

(82) Prakash, G. V.; Besombes, L.; Kelf, T.; Baumberg, J. J.; Bartlett, P. N.; Abdelsalam, M. E. *Opt. Lett.* **2004**, *29*, 1500-1502.

(83) Tessier, P. M.; Velev, O. D.; Kalambur, A. T.; Rabolt, J. F.; Lenhoff, A. M.; Kaler, E. W. *J. Am. Chem. Soc.* **2000**, *122*, 9554-9555.

(84) Yan, H. W.; Blanford, C. F.; Holland, B. T.; Parent, M.; Smyrl, W. H.; Stein, A. *Adv. Mater.* **1999**, *11*, 1003-1006.

(85) Ben-Ali, S.; Cook, D. A.; Evans, S. A. G.; Thienpont, A.; Bartlett, P. N.; Kuhn, A. *Electrochem. Commun.* **2003**, *5*, 747-751.

(86) Zoski, C. G. *Electroanalysis* **2002**, *14*, 1041-1051.

(87) Ewing, A. G.; Dayton, M. A.; Wightman, R. M. *Anal. Chem.* **1981**, *53*, 1842-1847.

(88) Dayton, M. A.; Brown, J. C.; Stutts, K. J.; Wightman, R. M. *Analitical Chemistry* **1980**, *52*, 946-950.

(89) Bond, A. M.; Fleischmann, M.; Robinson, J. *J. Electroanal. Chem.* **1984**, *168*, 299-312.

(90) Bond, A. M.; Lay, P. A. *J. Electroanal. Chem.* **1986**, *199*, 285-295.

(91) Cassidy, J.; Khoo, S. B.; Pons, S.; Fleischmann, M. *J. Phys. Chem.* **1985**, *89*, 3933-3935.

(92) Scott, A. O. *Biosensors for Food Analysis* **1998**, *Published by The Royal Society of Chemistry.*

(93) Gábor, H. *Sensors in Biomedical Applications: Fundamentals, Technology and Applications* **2000**, *Technomic Publishing Co. Inc.*

(94) Bartlett, P. N.; Caruana, D. J. *Analyst* **1992**, *117*, 1287-1292.

(95) Cosnier, S. *Biosens. Bioelectron.* **1999**, *14*, 443-456.

(96) Foulds, N. C.; Lowe, C. R. *Journal of the Chemical Society-Faraday Transactions I* **1986**, *82*, 1259-1264.

(97) Jimenez, C.; Bartrol, J.; deRooij, N. F.; KoudelkaHep, M. *Analytica Chimica Acta* **1997**, *351*, 169-176.

(98) Divya, P. S.; Savitri, D.; Mitra, C. K. *J. Biosci.* **1998**, *23*, 131-136.

(99) Godet, C.; Boujtita, M.; El Murr, N. *New J. Chem.* **1999**, *23*, 795-797.

(100) Wang, J.; Angnes, L. *Anal. Chem.* **1992**, *64*, 456-459.

(101) Gale, E. A. M. *Diabetes* **2001**, *50*, 217-226.

(102) Clark, L. C., Jr.; Lyons, C. *Ann. NY Acad. Sci*, *102*, 29-45.

(103) Clark, L. C.; Lyons, C. *US Patent 33,539,455* **1970**.

(104) Wang, J. *Electroanalysis* **2001**, *13*, 983-988.

(105) Guilbault, G. G.; Lubrano, G. J. *Anal. Chim. Acta* **1973**, *64*, 439-455.

(106) Malitesta, C.; Palmisano, F.; Torsi, L.; Zambonin, P. G. *Anal. Chem.* **1990**, *62*, 2735-2740.

(107) Murphy, L. J. *Anal. Chem.* **1998**, *70*, 2928-2935.

(108) Gough, D. A.; Lucisano, J. Y.; Tse, P. H. S. *Anal. Chem.* **1985**, *57*, 2351-2357.

(109) Wang, J.; Lu, F. *J. Am. Chem. Soc.* **1998**, *120*, 1048-1050.

(110) Yamazaki, T.; Kojima, K.; Sode, K. *Anal. Chem.* **2000**, *72*, 4689-4693.

(111) Bindra, D. S.; Zhang, Y. N.; Wilson, G. S.; Sternberg, R.; Thevenot, D. R.; Moatti, D.; Reach, G. *Anal. Chem.* **1991**, *63*, 1692-1696.

(112) M. J. Tierney, a, J. A. Tamadaa, R. O. Pottsa, L. Jovanovicb, S. Garg and Cygnus Research Teamc, a *Biosensors and Bioelectronics* **2001**, *16*, 621-629.

(113) Vogel, A. I. *A text book of Quantitative Inorganic Analysis including elementry insrumental analysis*; third ed.; Longmans, 1961.

(114) Wilson, R.; Turner, A. P. F. *Biosens. Bioelectron.* **1992**, *7*, 165-185.

(115) Li, Q.-S.; Ye, B.-C.; Liu, B.-X.; Zhong, J.-J. *Fresenius' J. Anal. Chem.* **1999**, *363*, 246-250.

(116) Hall, S. B.; Khudaish, E. A.; Hart, A. L. *Electrochim. Acta* **2000**, *45*, 3573-3579.

(117) Hall, S. B.; Khudaish, E. A.; Hart, A. L. *Electrochim. Acta* **1999**, *44*, 4573-4582.

(118) Hall, S. B.; Khudaish, E. A.; Hart, A. L. *Electrochim. Acta* **1999**, *44*, 2455-2462.

(119) Hall, S. B.; Khudaish, E. A.; Hart, A. L. *Electrochim. Acta* **1998**, *43*, 2015-2024.

(120) Hall, S. B.; Khudaish, E. A.; Hart, A. L. *Electrochim. Acta* **1998**, *43*, 579-588.

(121) Homa, A. S.; Yeager, E.; Cahan, B. D. *Journal of Electroanalytical Chemistry and Interfacial Electrochemistry* **1983**, *150*, 181-192.

(122) Yeager, E.; O'Grady, W. E.; Woo, M. Y. C.; Hagans, P. *J. Electrochem. Soc.* **1978**, *125*, 348-349.

(123) Jerkiewicz, G.; Vatankhah, G.; Lessard, J.; Soriaga, M. P.; Park, Y. S. *Electrochim. Acta* **2004**, *49*, 1451-1459.

(124) Rand, D. A. J.; Woods, R. *J. Electroanal. Chem. Interfacial Electrochem.* **1971**, *31*, 29-38.

(125) Karyakin, A. A. *Electroanalysis* **2001**, *13*, 813-819.

(126) Johnston, D. A.; Cardosi, M. F.; Vaughan, D. H. *Electroanalysis* **1995**, *7*, 520-526.

(127) Savinova, E. R.; Wasle, S.; Doblhofer, K. *Electrochim. Acta* **1998**, *44*, 1341-1348.

(128) Cere, S.; Vazquez, M.; de Sanchez, S. R.; Schiffrin, D. J. *J. Electroanal. Chem.* **1999**, *470*, 31-38.

(129) Somasundrum, M.; Kirtikara, K.; Tanticharoen, M. *Analytica Chimica Acta* **1996**, *319*, 59-70.

(130) Vazquez, M. V.; Desanchez, S. R.; Calvo, E. J.; Schiffrin, D. J. *J. Electroanal. Chem.* **1994**, *374*, 179-187.

(131) Zen, J. M.; Chung, H. H.; Kumar, A. S. *Analyst* **2000**, *125*, 1633-1637.

(132) Cai, L. T.; Chen, H. Y. *Sens. Actuator B-Chem.* **1999**, *55*, 14-18.

(133) Blackburn, T. R.; Lingane, J. J. *J. Electro-anal. Chem.* **1963**, *5*, 216-235.

(134) Anderson, A. B.; Albu, T. V. *J. Electrochem. Soc.* **2000**, *147*, 4229-4238.

(135) Anderson, A. B.; Albu, T. V. *Electrochem. Commun.* **1999**, *1*, 203-206.

(136) Hayashi, K.; Iwasaki, Y.; Kurita, R.; Sunagawa, K.; Niwa, O. *Electrochem. Commun.* **2003**, *5*, 1037-1042.
(137) Bartlett, P. N.; Wallace, E. N. K. *Phys. Chem. Chem. Phys.* **2001**, *3*, 1491-1496.
(138) Bae, I. T.; Yeager, E.; Xing, X.; Liu, C. C. *J. Electroanal. Chem.* **1991**, *309*, 131-145.
(139) Beden, B.; Largeaud, F.; Kokoh, K. B.; Lamy, C. *Electrochim. Acta* **1996**, *41*, 701-709.
(140) Vassilyev, Y. B.; Khazova, O. A.; Nikolaeva, N. N. *J. Electroanal. Chem.* **1985**, *196*, 105-125.
(141) Wilde, C. P.; Zhang, M. J. *J. Electroanal. Chem.* **1992**, *340*, 241-255.
(142) Ernst, S.; Heitbaum, J.; Hamann, C. H. *Journal of Electroanalytical Chemistry and Interfacial Electrochemistry* **1979**, *100*, 173-183.
(143) Arrigan, D. W. M.; Bartlett, P. N. *Biosens. Bioelectron.* **1998**, *13*, 293-304.
(144) Brumfield, J. C.; Goss, C. A.; Irene, E. A.; Murray, R. W. *Langmuir* **1992**, *8*, 2810-2817.
(145) Huang, M. J.; Watts, J. D.; Bodor, N. *Int. J. Quantum Chem.* **1997**, *65*, 1135-1152.
(146) Caruana, D. J. *PhD Thesis, Department of Chemistry, University of Southampton* **1994**.
(147) Bartlett, P. N.; Tebbutt, P.; Tyrrell, C. H. *Anal. Chem.* **1992**, *64*, 138-142.
(148) Cong, H. L.; Cao, W. X. *Langmuir* **2004**, *20*, 8049-8053.
(149) Vukusic, P.; Sambles, J. R. *Nature* **2003**, *424*, 852-855.
(150) Parker, A. P. *Engineering Fracture Mechanics* **1999**, *62*, 577-591.
(151) Schulze, G. W.; Erdogan, F. *International Journal of Solids and Structures* **1998**, *35*, 3615-3634.
(152) Lee, W. G.; Routh, A. F. *Langmuir* **2004**, *20*, 9885-9888.
(153) Richetti, P.; Prost, J.; Barois, P. *Physics of Complex and Supramolecular Fluids* **1987**, *Wiley, New York, 1987*, 387-411.
(154) Richetti, P.; Prost, J.; Barois, P. *Journal de Physique Lettres* **1984**, *45*, 1137-1143.
(155) Hayward, R. C.; Saville, D. A.; Aksay, I. A. *Nature* **2000**, *404*, 56-59.
(156) Hoare, J. P. *J. Electrochem. Soc.* **1984**, *131*, 1808-1815.
(157) Grundig, B.; Wittstock, G.; Rudel, U.; Strehlitz, B. *J. Electroanal. Chem.* **1995**, *395*, 143-157.
(158) Katakis, I.; Dominguez, E. *Mikrochim. Acta* **1997**, *126*, 11-32.
(159) Schuhmann, W.; Huber, J.; Wohlschlager, H.; Strehlitz, B.; Grundig, B. *J. Biotechnol.* **1993**, *27*, 129-142.
(160) Mano, N.; Kuhn, A. *J. Electroanal. Chem.* **2001**, *498*, 58-66.
(161) Mano, N.; Kuhn, A. *J. Electroanal. Chem.* **1999**, *477*, 79-88.
(162) Mano, N.; Thienpont, A.; Kuhn, A. *Electrochem. Commun.* **2001**, *3*, 585-589.
(163) Min, K. L.; Steghens, J. P. *Biochem. Biophys. Res. Commun.* **1999**, *265*, 273-278.
(164) Southward, C. M.; Surette, M. G. *Mol. Microbiol.* **2002**, *45*, 1191-1196.
(165) Tsien, R. Y. *Annu. Rev. Biochem.* **1998**, *67*, 509-544.

(166) Palm, G. J.; Zdanov, A.; Gaitanaris, G. A.; Stauber, R.; Pavlakis, G. N.; Wlodawer, A. *Nat. Struct. Biol.* **1997**, *4*, 361-365.

(167) Barbosa, M. R.; Real, S. G.; Vilche, J. R.; Arvia, A. J. *J. Electrochem. Soc.* **1988**, *135*, 1077-1085.

(168) Yin, Y. D.; Lu, Y.; Gates, B.; Xia, Y. N. *J. Am. Chem. Soc.* **2001**, *123*, 8718-8729.

(169) Harriman, K.; Gavaghan, D. J.; Houston, P.; Suli, E. *Electrochem. Commun.* **2000**, *2*, 163-170.

(170) Henry, C. S.; Fritsch, I. *Anal. Chem.* **1999**, *71*, 550-556.

(171) Morita, K.; Furuya, E. *Anal. Chem.* **1994**, *66*, 2197-2199.

(172) Morita, K.; Shimizu, Y. *Anal. Chem.* **1989**, *61*, 159-162.

(173) Tokuda, K.; Morita, K.; Shimizu, Y. *Anal. Chem.* **1989**, *61*, 1763-1768.

(174) Bezbaruah, A. N.; Zhang, T. C. *Water Res.* **2002**, *36*, 4428-4432.

(175) McRipley, M. A.; Linsenmeier, R. A. *J. Electroanal. Chem.* **1996**, *414*, 235-246.

(176) Zoski, C. G.; Liu, B.; Bard, A. J. *Anal. Chem.* **2004**, *76*, 3646-3654.

(177) Bond, A. M.; Luscombe, D.; Oldham, K. B.; Zoski, C. G. *J. Electroanal. Chem.* **1988**, *249*, 1-14.

(178) Bartlett, P. N.; Taylor, S. L. *J. Electroanal. Chem.* **1998**, *453*, 49-60.

(179) Belmont, C.; Tercier, M. L.; Buffle, J.; Fiaccabrino, G. C.; KoudelkaHep, M. *Analytica Chimica Acta* **1996**, *329*, 203-214.

(180) Kounaves, S. P.; Deng, W.; Hallock, P. R.; Kovacs, G. T. A.; Storment, C. W. *Anal. Chem.* **1994**, *66*, 418-423.

(181) Seddon, B. J.; Shao, Y.; Girault, H. H. *Electrochim. Acta* **1994**, *39*, 2377-2386.

(182) Kawagoe, J. L.; Niehaus, D. E.; Wightman, R. M. *Anal. Chem.* **1991**, *63*, 2961-2965.

(183) Burnett, D. S. *Finite Element Analysis, From Concepts to Applications* **1987**, *Addison Wesley Pub. Co., USA.*

(184) Ferrigno, R.; Brevet, P. F.; Girault, H. H. *Electrochim. Acta* **1997**, *42*, 1895-1903.

(185) Galceran, J.; Gavaghan, D. J.; Rollett, J. S. *J. Electroanal. Chem.* **1995**, *394*, 17-28.

(186) Kwak, J.; Bard, A. J. *Anal. Chem.* **1989**, *61*, 1221-1227.

(187) Shoup, D.; Szabo, A. *J. Electroanal. Chem.* **1982**, *140*, 237-245.

(188) Boo, H.; Park, S.; Ku, B. Y.; Kim, Y.; Park, J. H.; Kim, H. C.; Chung, T. D. *J. Am. Chem. Soc.* **2004**, *126*, 4524-4525.

(189) Grahame, D. C. *Chemical Reviews (Washington, DC, United States)* **1947**, *41*, 441-501.

(190) Olphen, H. v.; J., M. K. *Physical Chemistry: Enriching Topics From Colloid and Surface Science* **1975**, *Theorex.*

(191) Corry, B.; Kuyucak, S.; Chung, S. H. *Chem. Phys. Lett.* **2000**, *320*, 35-41.

(192) Jamnik, B.; Vlachy, V. *J. Am. Chem. Soc.* **1993**, *115*, 660-666.

(193) Kemery, P. J.; Steehler, J. K.; Bohn, P. W. *Langmuir* **1998**, *14*, 2884-2889.

(194) Banks, C. E.; Rees, N. V.; Compton, R. G. *J. Electroanal. Chem.* **2002**, *535*, 41-47.

(195) Glauser, T.; Johansson, M.; Hult, A. *Polymer* **1999**, *40*, 5297-5302.
(196) Hu, C. C.; Liu, K. Y. *Electrochim. Acta* **2000**, *45*, 3063-3068.

Estimate of charge required to deposit a gold film of half a sphere layer thick:

Volume of unstructured gold = electrode surface area × film thickness

i.e. = $\pi a^2 \times r$, (where r = the diameter of the template spheres e.g. 250 nm).

= 1.963×10^{-3} cm^2 × 2.5×10^{-5} cm

= 4.9×10^{-8} cm^3.

Number of spheres at the electrode surface = (electrode surface area/cross-sectional area of a sphere) × 0.9[i]

= (1.963×10^{-3} cm^2/1.963×10^{-9} cm^2) × 0.9

= 900,000.

Volume of gold deposit occupied by spheres = (number of spheres × volume of sphere)/2

= (900,000 × 6.545×10^{-14} cm^3)/2

= 2.95×10^{-8} cm^3.

Total volume of gold = unstructured gold volume – total sphere volume

= 4.9×10^{-8} cm^3 - 2.95×10^{-8} cm^3

= 1.96×10^{-8} cm^3.

Moles of gold = (total volume of gold × density)/atomic weight

= (1.96×10^{-8} cm^3 × 19.3 g cm^{-3})/196.97 g mol^{-1}.

= 1.92×10^{-9} moles.

Deposition Q = mnF, (where m = moles, n = number of electrons and F = Faraday constant)

= 1.86×10^{-4} C.

---

[i] 2D hexagonal packing efficiency = 91 % (or 79 % for squar packing).

For gold depositions of more than half a sphere height the calculation is complicated by changes in the sphere packing between the surface and the bulk.

The thickness of gold required to deposit half way up the next sphere layer is not simply 1.5 × r, as the spheres do not stack directly on top of each other; instead spheres in subsequent layers nestle between three of the spheres from the lower layer (figure 1).

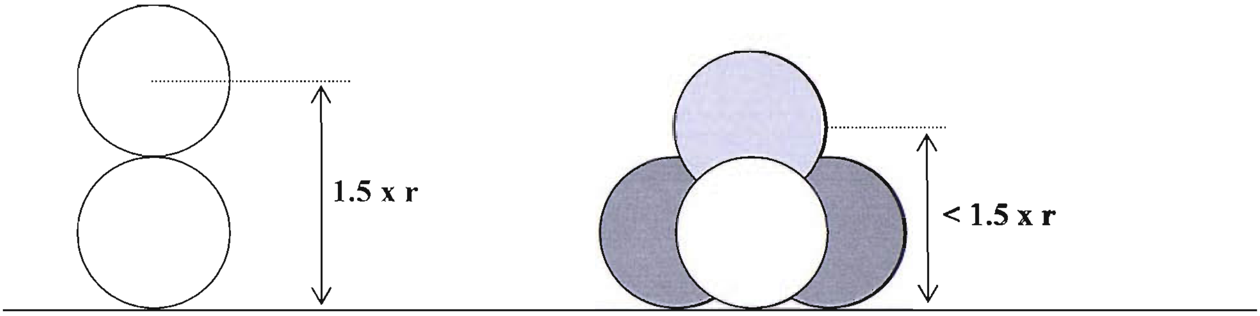

Figure 1. Diagram illustrating the three dimensional packing of spheres.

This height discrepancy can be calculated by considering the relationship between the centres of 4 spheres in contact as in figure 1 above. In this tetragonal arrangement all four spheres are in contact; hence the centres of the spheres form a triangular based pyramid with all the side lengths equal to d (sphere diameter) and all angles 60° (figure 2).

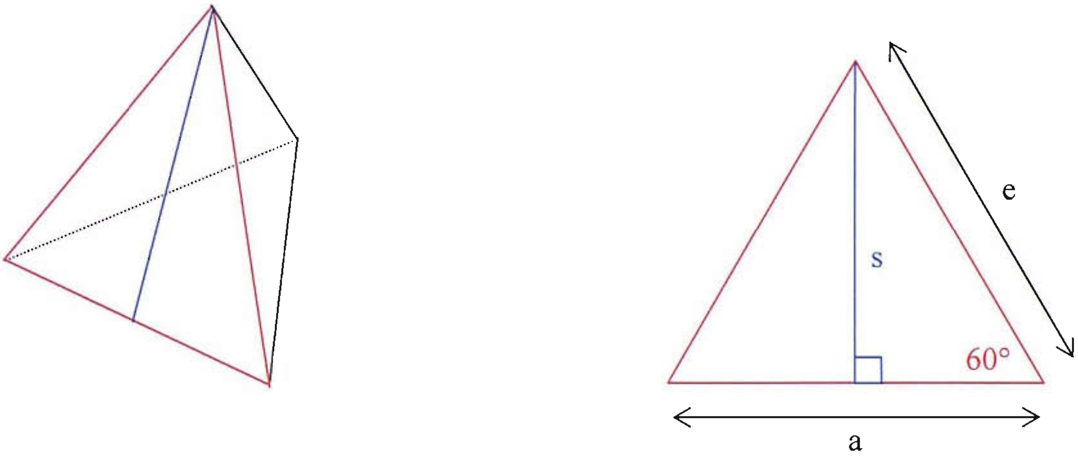

Figure 2. Polyhedron illustrating the tetragonal arrangement of the centres of 4 contacting, close packed spheres.

The height of this pyramid (and thus the discrepancy between the true layer height and 2d) can be calculated from equation 1:

$$h = \sqrt{e^2 - \frac{1}{3}a^2} \qquad \textbf{1}$$

Where h = the pyramid height, e = the edge length and a = the base edge length (both a and e = d here).

NB h can also be calculated by its relationship to the slant height (s):

$$h = \sqrt{s^2 - \frac{1}{12}a^2} \qquad \textbf{2}$$